



Norwegian University of
Science and Technology

Structural Design and Dynamic Analysis of a Tension Leg Platform Wind Turbine, Considering Elasticity in the Hull

Kristian Freng Svendsen

Wind Energy

Submission date: May 2016

Supervisor: Erin Bachynski, IMT

Norwegian University of Science and Technology
Department of Marine Technology

Structural Design and Dynamic Analysis of a Tension Leg Platform Wind Turbine, Considering Elasticity in the Hull

Master of Science Thesis

For obtaining the degree of Master of Science in Offshore Engineering and
Dredging from Delft University of Technology and Master of Science Technology-
Wind Energy from the Norwegian University of Science and Technology

Kristian Freng Svendsen

June 10, 2016

European Wind Energy Master – EWEM

Delft University of Technology

Faculty of Mechanical, Maritime and Materials Engineering

Department of Maritime and Transport Technology

Section of Offshore and Dredging Engineering

Norwegian University of Science and Technology

Faculty of Engineering Science and Technology

Department of Marine Technology



MSC THESIS IN MARINE TECHNOLOGY

SPRING 2016

FOR

STUD.TECHN. Kristian Freng Svendsen

Structural design and dynamic analysis of a tension leg platform wind turbine, considering elasticity in the hull

Background:

The wind industry has developed very fast in recent years, moving from onshore to offshore in shallow water and then in deep water. Many floating wind turbine concepts have been proposed for water depth larger than 100-200 m. Tension leg platform wind turbines (TLPWTs) are among the concepts that are under consideration for deeper water.

Global dynamic analysis of TLPWTs has typically focused on the dynamic loads in the tendons and tower, while structural design of the hull has been based on hydrostatic and hydrodynamic loads in the frequency domain. For the tension leg platform, the flexibility in the hull itself may be important for the global behaviour, and the dynamic loads in the hull due to coupled wind-wave action are of interest. The hydrodynamic loads for large-volume structures depend strongly on frequency, and novel methods are needed to include both flexibility and correct hydrodynamic loads in the global analysis.

In the project work of this candidate, a basic scantling design for an existing 5MW TLPWT design has been made, and an equivalent beam model was developed to represent the cross-sectional stiffness and mass distribution.

Hydrodynamic analysis (using the DNV SESAM packages GeniE and HydroD or using WAMIT) will be carried out with a panel model which is appropriately discretized compared to the beam element model.

By integrating the panel pressure from the hydrodynamic analysis, the frequency-dependent hydrodynamic loads will be included at selected nodes in the beam element model using many

Thesis work description

"SIMO bodies". Simulations of various wind-wave conditions using the resulting multi-body model will be compared to published results for the TLPWT with rigid hull. Load estimates in the tendons and tower will be compared to published results. The loads within the hull structure will be compared to predicted values from the pure hydrodynamic loading, which will highlight possible dynamic amplification in the structure.

Assignment:

The following tasks should be addressed in the thesis work:

1. Literature study on design of tension leg platform wind turbines, methods for coupled analysis of floating wind turbines. The basic theory and methods for wind turbine aerodynamics, floater hydrodynamics as well as coupled dynamic analysis should be studied.
2. Generate a hydrodynamic model of the TLPWT in HydroD with panel discretization corresponding to the beam element model. Compute hydrodynamic added mass, radiation damping, and excitation for the hull structure as a whole and compare to published results.
3. Generate "SIMO body" input of hydrodynamic added mass, radiation damping, and excitation for sections of the TLPWT hull, resulting in a "multi-body" global analysis model. Assistance in integration of the panel pressure in the form of scripts will be provided.
4. Select wind-wave conditions for simulation in SIMO-RIFLEX-AeroDyn using the resulting multi-body model. Compare to published results for the TLPWT with rigid hull.
5. Compare the loads within the hull structure to the loads predicted by pure hydrodynamic frequency-domain analysis. Investigate the effects of dynamic amplification.
6. Evaluate the proposed scantling based on the computed loads.
7. Conclude the work and give recommendations for future work.
8. Write the MSc thesis report.

In the thesis the candidate shall present his personal contribution to the resolution of problem within the scope of the thesis work.

Theories and conclusions should be based on mathematical derivations and/or logic reasoning identifying the various steps in the deduction.

The candidate should utilize the existing possibilities for obtaining relevant literature.

The thesis should be organized in a rational manner to give a clear exposition of results, assessments, and conclusions. The text should be brief and to the point, with a clear language. Telegraphic language should be avoided.

The thesis shall contain the following elements: A text defining the scope, preface, list of contents, summary, main body of thesis, conclusions with recommendations for further work, list of symbols and acronyms, reference and (optional) appendices. All figures, tables and equations shall be numerated.

The supervisor may require that the candidate, in an early stage of the work, present a written plan for the completion of the work. The plan should include a budget for the use of computer and laboratory resources that will be charged to the department. Overruns shall be reported to the supervisor.

The original contribution of the candidate and material taken from other sources shall be clearly defined. Work from other sources shall be properly referenced using an acknowledged referencing system.

The thesis shall be submitted in two copies as well as an electronic copy on a CD:

- Signed by the candidate
- The text defining the scope included
- In bound volume(s)

Drawings and/or computer prints which cannot be bound should be organized in a separate folder.

Supervisors:

NTNU: Erin Bachynski

TU Delft: Frank Sliggers

Deadline: 17.06.2016

Abstract

There is an increasing interest in using offshore wind turbines in deeper waters. The tension leg platform wind turbine (TLPWT) is seen as a promising concept for this. Low production costs and limited motions give the TLPWT concept both economic and dynamic advantages. Previous studies regarding dynamic analysis of floating offshore wind turbines have focused on global dynamic analysis with a rigid hull. Novel methods are needed to include both flexibility and correct hydrodynamic loads in the global dynamic analysis. This study presents a basic scantling design and a new method for including the large-volume hydrodynamic loads.

A 3-D panel model was generated for the hull, and radiation and diffraction pressures from first-order potential theory were computed for each panel using WAMIT. A Matlab script was written in which an algorithm integrates the panel pressures and generates frequency-dependent added mass, damping and excitation input for sections of the hull. The method gave exact translational load component magnitudes and slightly underestimated rotational load component magnitudes with respect to WAMIT's output for the hull as a whole.

In order to examine the effects of hull flexibility, a basic scantling design was made for the hull of an existing 5-MW TLPWT design by following industry guidelines. Finite element software was used to estimate the stiffness and an equivalent beam element model was created for the hull. Implementing the equivalent beam model in a global model of the whole TLPWT makes it possible to investigate the hull elasticity's influence on the system's global dynamic properties and internal loads. As expected, the hull elasticity had more significant effects on vertical motions: Simulated decay tests indicated an increase of the heave and pitch natural periods of 43 % and 18 %, respectively.

Time-domain simulations of the flexible model with the novel hydro-loading approach in combined wind-wave environments indicated dynamic amplification of the nacelle motions, tower base bending moment and the tendon tension. An attempt was also made to investigate the dynamic amplification of internal loads in the hull. The results indicated unexpectedly large amplification for certain frequencies, and more research is needed to draw substantiated conclusions.

Acknowledgements

This thesis work has been carried out at the Department of Marine Technology of the Norwegian University of Science and Technology (NTNU) in Trondheim, Norway. The thesis has been completed as the concluding work for the Offshore Engineering track of the Erasmus Mundus joint Master of Science programme European Wind Energy Master (EWEM), which awards a double Master of Science degree in Offshore Engineering and Wind Energy from NTNU and TU Delft.

The work was supervised mainly by NTNU Associate Professor Erin Bachynski. I am especially thankful to her for guiding me and sharing her knowledge throughout the entire project from design and modelling to simulating and interpreting results. I am grateful to Frank Sliggers for the feedback from TU Delft side, which made me dig even deeper into the topic and improve my understanding and final delivery. I would like to thank Linda Gaffel and the EWEM administration at TU Delft for providing support in handling formalities and facilitating the arrangement of extra-curricular affairs throughout the whole master programme. Last, I would like to thank the other EWEM Offshore students for two great years spent in Denmark, the Netherlands and Norway.



Kristian Freng Svendsen

Table of contents

List of figures.....	xiii
List of tables	xviii
List of symbols and acronyms	xx
1 Introduction	1
1.1 Offshore wind energy.....	1
1.2 Floating wind turbine concepts.....	3
1.3 Research aim and motivation	5
1.4 Related work.....	7
1.5 Thesis outline.....	9
2 Theoretical background and the TLPWT concept.....	11
2.1 Structural dynamics.....	11
2.1.1 TLPWT rigid body mechanics	12
2.1.2 RIFLEX finite element formulation	13
2.2 Environmental loads	15
2.2.1 Hydrodynamic loads.....	16
2.2.2 Hydrostatic load and restoring forces and moments	19
2.2.3 Aerodynamic loads.....	21
2.3 Hydro-aero-servo-elastic coupling.....	24
2.4 TLP concepts	26
2.4.1 TLP concepts for supporting topsides in the oil and gas industry	28
2.4.2 TLP concepts for supporting wind turbines.....	29
2.5 The reference TLP design	32
2.6 Design standards for offshore wind turbines.....	35

3	Basic scantling design for the reference hull.....	37
3.1	Loads accounted for in the final scantling design.....	39
3.1.1	Loads accounted for in the final scantling design for the pontoons.....	39
3.1.2	Loads accounted for in the final scantling design for the main column.....	39
3.2	Scantling design for the pontoons.....	41
3.2.1	Scantling design for the pontoons with ABS MODU, accounting for hydrostatic pressure only.....	42
3.2.1.1	Required plate thickness.....	43
3.2.1.2	Required section modulus for longitudinal stiffeners.....	44
3.2.1.3	Required section modulus for transverse girders.....	45
3.2.2	Final pontoon scantling design.....	45
3.2.3	Evaluating the final pontoon scantling design by checking against DNV-RP-C201 and accounting for both hydrostatic pressure and tendon induced bending stresses.....	49
3.2.3.1	Estimating the tendon induced bending stresses.....	50
3.2.3.2	Evaluating the final pontoon scantling design with DNV-RP-C201.....	51
3.3	Scantling design for the main column.....	52
3.3.1	Calculation of design equivalent von Mises stress.....	53
3.3.1.1	Design axial stress in the shell due to axial forces.....	53
3.3.1.2	Design circumferential stress in the shell due to external pressure.....	53
3.3.1.3	Design bending stress in the shell due to global bending moment and design shear stress in the shell due to shear force.....	54
3.3.2	Shell buckling check.....	55
3.3.3	Panel ring buckling check.....	56
3.3.4	Column buckling check.....	57
3.3.5	Final scantling design for main column.....	58
4	Equivalent beam model for the hull.....	63

4.1	Mass distribution of the flexible design	65
4.1.1	Pontoon mass distribution.....	65
4.1.2	Main column mass distribution	66
4.2	Equivalent stiffness of the flexible design derived from FE analysis	67
4.2.1	Pontoon equivalent stiffness	67
4.2.1.1	Pontoon equivalent bending stiffness	68
4.2.1.2	Pontoon equivalent torsional stiffness	70
4.2.2	Main column equivalent stiffness	72
4.2.2.1	Main column equivalent bending stiffness.....	72
4.2.2.2	Main column equivalent torsional stiffness.....	74
4.2.3	Summary of equivalent stiffness estimations	76
4.3	Natural frequency estimations for the pontoon and main column in the equivalent beam model	76
4.4	Validation of the equivalent stiffness estimations	79
5	First estimation of the natural periods of the fully-flexible TLPWT.....	81
5.1	Natural periods of the reference TLPWT.....	82
5.2	Added mass estimation	83
5.3	Natural period estimation with eigenvalue analysis in RIFLEX	84
5.4	Mode shapes	85
6	Creating the elastic multi-body hull model	89
6.1	Modelling procedure	90
6.2	Generating the 3-D hydrodynamic panel model of the hull	91
6.3	Hydrodynamic loads for the hull as a whole	93
6.3.1	Added mass for the hull as a whole.....	94
6.3.2	Linear radiation damping for the hull as a whole.....	96

6.3.3	First-order wave excitation for the hull as a whole	97
6.4	Hydrodynamic loads for sections of the hull.....	99
6.4.1	Defining the sections of the hull	100
6.4.2	Computing the hydrodynamic loads for each section	103
6.5	Summing the loads over all of the sections and comparing with the WAMIT output for the hull as a whole.....	110
6.5.1	Number of sections used in the comparison	111
6.5.2	Comparing first-order potential theory wave excitation components	113
6.5.3	Comparing first-order potential theory added mass and radiation damping components	117
7	Global dynamic analysis with the elastic multi-body hull model.....	122
7.1	Statically deformed configuration of the hull.....	123
7.2	Wind turbine performance.....	126
7.3	Fundamental natural periods	129
7.3.1	Surge decay simulation.....	131
7.3.2	Heave decay simulation	131
7.3.3	Pitch decay simulation.....	133
7.3.4	Yaw decay simulation	134
7.3.5	Comparing with previous results.....	134
7.4	Simulations in a combined wind-wave environment.....	136
7.4.1	Simulation results in condition 1	137
7.4.2	Simulation results in conditions 2 and 3.....	140
8	Internal loads in the hull.....	141
8.1	Amplification of internal dynamic loads due to hull elasticity	142
8.1.1	Wave-only frequency-domain analysis with a rigid structure	144
8.1.2	Wave-only time-domain analysis with an elastic structure	147

8.1.2.1	Wave-only time-domain analysis with the reduced model	149
8.1.2.2	Wave-only time-domain analysis with the original model	157
8.2	Evaluation of the proposed scantling design based on internal load estimations in a wind-wave environment	163
8.2.1	Evaluation of pontoon design based on the internal bending moment at the base node connection.....	164
8.2.2	Evaluation of main column design based on internal loads at various cross sections on the main column.....	168
9	Conclusions and recommendations for future work	180
9.1	Conclusions	180
9.2	Recommendations for future work	182
	References	186
	Appendix	190
A.	Potential flow and regular wave theory	191
A.1	Potential flow essentials	191
A.2	Linear wave theory for regular waves.....	193
A.3	Irregular waves and wave spectra.....	195
A.4	Wheeler stretching	196
B.	Wind field	197
B.1	Wind shear.....	197
B.2	Tower shadow.....	198
B.3	Atmospheric turbulence	198
C.	Checking the final pontoon scantling design with the LRFD method accounting for tendon induced bending stresses and hydrostatic pressure.....	200
C.1	Design stress components	200
C.2	Forces in the stiffened plate and effective plate width.....	203

C.3	Characteristic buckling strength of stiffeners	204
C.4	Resistance parameters of stiffeners	206
C.5	Interaction formulas for axial compression and lateral pressure	207
D.	Stiffness estimation for the reference design pontoon and main column	209
D.1	Deflections of the reference pontoon and main column derived from FE analysis	209
D.2	Deflections of the reference pontoon and main column estimated with elementary beam theory	210
E.	Time series of simulations in environmental conditions 2 and 3	213
E.1	Condition 2	213
E.2	Condition 3	216
F.	Matlab code	218

List of figures

Figure 1-1: The Hywind Demo [3]	3
Figure 1-2: The WindFloat concept [4].....	4
Figure 1-3: The Damping Pool concept [5].....	4
Figure 1-4: The Blue H TLP concept [6]	5
Figure 2-1: Definition of global coordinate system and degrees of freedom [7]	12
Figure 2-2: Nodal degrees of freedom of beam element [17]	14
Figure 2-3: Environmental loads on offshore wind turbine [19].....	15
Figure 2-4: Visualization of grid for potential flow panel method [20]	19
Figure 2-5: TLPWT model overview [9]	26
Figure 2-6: Four TLP configurations. Top left: CTLP. Top Right: ETLP. Bottom left: Moses TLP. Bottom right: SeaStar TLP	29
Figure 2-7: Selection of mono-column TLP concepts. Left to right: Withee [11], Matha [14], Glostén [31], Garrad Hassan [32]	31
Figure 2-8: Multi-column TLPWT concepts. From left to right: Suzuki et al. [34], I.D.E.A.S [35], Zhao et al. [10]	32
Figure 2-9: Bachynski’s five rigid baseline TLPWT designs [9].....	33
Figure 2-10: TLP parameter definitions [9]	34
Figure 3-1: Stiffened plate panel	42
Figure 3-2: General stiffener cross section dimensions [36].....	45
Figure 3-3: Pontoon scantling design based on hydrostatic pressure, showing the longitudinal stiffeners and the transverse girders.....	48
Figure 3-4: Pontoon tip plate with stiffeners	48
Figure 3-5: Complete pontoon scantling design	49
Figure 3-6: Bending moment in pontoon induced by tendon force	50
Figure 3-7: Hydrodynamic forces on main column from the regular wave over one wave period calculated with the Morison equation	54
Figure 3-8: Main column scantling design showing the wall, the vertical bulkheads and the ring frames	61

Figure 3-9: Complete main column scantling design	61
Figure 3-10: Complete TLP design with bulkheads, stiffeners and girders	62
Figure 4-1: Pontoon mass distribution	66
Figure 4-2: Main column mass distribution	66
Figure 4-3: Meshed pontoon.....	68
Figure 4-4: Cantilever beam bending test setup of pontoon.....	68
Figure 4-5: Deformed shape of the pontoon cantilever beam on top of the undeformed shape in the bending test	69
Figure 4-6: Cantilever beam torsion test setup of pontoon	70
Figure 4-7: Deformed shape of the pontoon cantilever beam on top of the undeformed shape in the torsion test.....	71
Figure 4-8: Meshed main column	72
Figure 4-9: First (left) and second (right) cantilever beam bending test setup of main column ...	73
Figure 4-10: Deformed shape of the main column cantilever beam on top of the undeformed shape in the first bending test	73
Figure 4-11: Cantilever beam torsion setup for main column.....	74
Figure 4-12: Deformed shape of the main column cantilever beam on top of the undeformed shape in the torsion test	75
Figure 5-1: RIFLEX model of the fully-flexible TLPWT	81
Figure 5-2: Local coordinate system of beams in RIFLEX [43]	83
Figure 5-3: Surge fundamental mode shape. Left: side view. Middle: Front view. Right: Top view.	86
Figure 5-4: Heave fundamental mode shape. Left: side view. Middle: Front view. Right: Top view.	86
Figure 5-5: Pitch fundamental mode shape. Left: side view. Middle: Front view. Right: Top view.	87
Figure 5-6: Yaw fundamental mode shape. Left: side view. Middle: Front view. Right: Top view.	87
Figure 6-1: Schematic of the modelling procedure.....	90
Figure 6-2: Meshed GeniE FE model	92

Figure 6-3: HydroD 3-D panel model seen from above (top) and below (bottom) the water surface	93
Figure 6-4: Added mass coefficients for the whole hull	95
Figure 6-5: Radiation damping coefficients for the whole hull.....	96
Figure 6-6: TLP orientation in the x-y plane	97
Figure 6-7: First-order wave force excitation per unit wave amplitude for the whole hull	98
Figure 6-8: Matlab visualization of panels. Top left: Full TLP. Top right: Main column. Bottom left: Base node. Bottom right: pontoons	101
Figure 6-9: Column and base node panels with and without horizontal planes indicating section boundaries.....	102
Figure 6-10: Pontoon panels with and without vertical planes indicating section boundaries ...	103
Figure 6-11: Visualizations of multi-body models corresponding to "dl=2" (top) and "dl=4" (bottom)	112
Figure 6-12: Comparison of translational excitation components.....	113
Figure 6-13: Comparison of rotational excitation components	115
Figure 6-14: Comparison of diagonal translational added mass and damping coefficients.....	118
Figure 6-15: Comparison of selected off-diagonal added mass and damping coefficients	120
Figure 7-1: Static deformation shape of the elastic hull. Displacements due to elasticity are scaled with a factor of 100.....	124
Figure 7-2: Static vertical displacement of all SIMO-body nodes due to hull elasticity	125
Figure 7-3: Top left: Rotor speed. Top right: Mechanical power. Middle left: Rotor thrust. Middle right: Pitch angle. Bottom left: Generator speed. Bottom right: Generator torque.	128
Figure 7-4: Force applied in surge decay test.....	130
Figure 7-5: Time series of the surge decay tests.....	131
Figure 7-6: Time series of the heave decay tests	131
Figure 7-7: Zooming in on the time series of the heave decay test	132
Figure 7-8: Time series of the pitch decay tests	133
Figure 7-9: Zooming in on the time series of the pitch decay tests	133
Figure 7-10: Time series of the yaw decay tests.....	134
Figure 7-11: Time series of motion response in condition 1	137

Figure 7-12: Power spectrum for the bending moment about the y-axis at the tower base in condition 1	139
Figure 7-13: Power spectrum for the tension at the top of each tendon in condition 1	140
Figure 8-1: Selected cross sections for investigation of amplification of internal dynamic loads due to hull elasticity	143
Figure 8-2: RAO computed with WADAM in HydroD for a wave heading of 0 degrees	145
Figure 8-3: Internal dynamic loads computed at each cross section in HydroD	146
Figure 8-4: Reduced (left) and original (right) versions of the elastic multi-body TLPWT model in SIMO-RIFLEX	149
Figure 8-5: Steady state response at waterline for a wave frequency of 0.65 rad/s.....	150
Figure 8-6: Estimated surge, heave and pitch RAOs for the reduced model (right) compared to the rigid model (left)	151
Figure 8-7: Internal dynamic loads in pontoon 1 for rigid (left) and reduced model (right)	153
Figure 8-8: Internal dynamic loads in main column for rigid (left) and reduced model (right)..	155
Figure 8-9: Estimated amplifications for the reduced model with respect to the rigid model	157
Figure 8-10: Estimated surge, heave and pitch RAOs for the original model.....	158
Figure 8-11: Internal dynamic loads in pontoon 1 for rigid (left) and original model (right).....	159
Figure 8-12: Internal dynamic loads in main column for rigid (left) and original model (right)	161
Figure 8-13: Estimated amplifications for the original model with respect to the rigid model ..	163
Figure 8-14: Time series of bending moment at the base of each pontoon. Top: condition 1. Middle: Condition 2. Bottom: Condition 3	165
Figure 8-15; Free body diagram for statically loaded pontoon	167
Figure 8-16: Time series of main column axial force at various elevations. Top: condition 1. Middle: Condition 2. Bottom: Condition 3	169
Figure 8-17: Time series of main column shear force at various elevations. Top: condition 1. Middle: Condition 2. Bottom: Condition 3	171
Figure 8-18: Time series of main column bending moment at various elevations. Top: condition 1. Middle: Condition 2. Bottom: Condition 3	172
Figure 8-19: Main column stress components in condition 1. Top left: Axial stress due to axial force. Top right: Bending stress due to bending moment. Bottom left: Circumferential stress due to hydrostatic pressure. Bottom right: Shear stress due to shear force.	174

Figure 8-20: Shell buckling ratio at the four elevations. Top: Condition 1. Middle: Condition 2. Bottom: Condition 3.....	175
Figure 8-21: Panel ring buckling ratio at the four elevations. Top: Condition 1. Middle: Condition 2. Bottom: Condition 3	178
Figure A-1: Regular planar wave [48]	194
Figure A-2: The PM and JONSWAP spectra.....	196
Figure B-1: Typical wind shear [23].....	197
Figure B-2: Potential flow around a cylinder [49].....	198
Figure B-3: Turbulent inflow seen by the rotor [23]	198
Figure C-1: Stiffened plate panel.....	201
Figure C-2: Parameter definitions used for calculation of moment of inertia contribution from longitudinal stiffeners.....	203
Figure C-3: L-stiffener with effective plate flange [37].....	206
Figure E-1: Time series of motion response in condition 2	213
Figure E-2: Power spectrum for the bending moment about the y-axis at the tower base in condition 2	214
Figure E-3: Power spectrum for the tension at the top of each tendon in condition 2.....	215
Figure E-4: Time series of motion response in condition 3	216
Figure E-5: Power spectrum for the bending moment about the y-axis at the tower base in condition 3	217
Figure E-6: Power spectrum for the tension at the top of each tendon in condition 3.....	217

List of tables

Table 2-1: Dimensions and masses of the components of the reference design	35
Table 3-1: Mass of components resting on main column causing compression	41
Table 3-2: Weight ratios of recent TLPs [28].....	42
Table 3-3: Final pontoon scantling design weight ratios	46
Table 3-4: Number of bulkheads, longitudinal stiffeners and transverse girders per pontoon	47
Table 3-5: Pontoon wall thickness and bulkhead thickness	47
Table 3-6: Dimensions and modulus of pontoon longitudinal stiffeners	47
Table 3-7: Dimensions and modulus of pontoon transverse girders.....	47
Table 3-8: Main column weight ratios and number of ring stiffeners and vertical bulkheads in the final scantling design.....	59
Table 3-9: Dimensions of main column components	59
Table 3-10: Design stresses for main column scantling design.....	60
Table 3-11: Buckling ratios indicating strength of the main column scantling design.....	60
Table 4-1: Masses of pontoon walls, longitudinal stiffeners and girders	65
Table 4-2: Masses of pontoon bulkheads and tip plate	65
Table 4-3: Masses of main column walls, ring frames and bulkheads	66
Table 4-4: Pontoon vertical displacement at $x=L_{beam}/2$ for various mesh sizes	69
Table 4-5: Summary of load magnitude, deflection computed in ABAQUS and derived equivalent stiffness for the pontoons and main column of flexible design	76
Table 4-6: Error in calculated deflection at $x=3L_{beam}/4$ with respect to numerical solution.....	76
Table 4-7: Estimation of first natural frequencies for the equivalent pontoon and main column beams.....	78
Table 5-1: Natural periods of reference TLPWT.....	82
Table 5-2: Natural periods of fully-flexible TLPWT calculated with the inbuilt eigenvalue analysis in RIFLEX.....	84
Table 6-1: Number of sections in each selected section model.....	111
Table 6-2: Maximum error for rotational excitation components	116
Table 6-3: Maximum error for selected off-diagonal added mass and damping coefficients.....	121

Table 7-1: NREL 5-MW offshore baseline turbine key numbers	126
Table 7-2: Magnitude and duration of forces and moments applied in decay tests.....	130
Table 7-3: Comparison of fundamental natural period estimations between the various models	135
Table 7-4: Environmental conditions for global dynamic time-domain simulations	136
Table 7-5: Mean and standard deviation of each steady state motion response in condition 1...	138
Table 8-1: Location of each selected cross sections' center point in the global coordinate system	143
Table 8-2: Mean and maximum values for pontoon bending moments in conditions 1, 2 and 3	166
Table 8-3: Hydrostatic pressure at the four elevations on the main column	173
Table 8-4: Mean, standard deviation and minimum value of the shell buckling ratio	176
Table 8-5: Mean, standard deviation and minimum value of the panel ring buckling ratio	179
Table D-1: Deflections of both the reference and flexible pontoon and main column computed in ABAQUS.....	209
Table D-2: Timoshenko beam theory predicted deflections of the reference pontoon and main column.....	212
Table E-1: Mean and standard deviation of each steady state motion response in condition 2 ..	214
Table E-2: Mean and standard deviation of each steady state motion response in condition 3 ..	216

List of symbols and acronyms

TLP	Tension Leg Platform
TLPWT	Tension Leg Platform Wind Turbine
BEM	Blade Element Momentum
GDW	Generalized Dynamic Wake
CTLP	Conventional TLP
ETLP	Extended TLP
RP	Recommended practice
LRFD	Load and resistance factor design
MWL	Mean water level
A	Added mass matrix
A_c	Cross sectional area
A_e	Effective area of stiffener and plate
A_{ij}	Added mass coefficient from radiation problem
\bar{A}_{ij}	Non-dimensional added mass coefficient from radiation problem
AREA	Panel area
A_s	Stiffener cross sectional area
A_{wp}	Water plane area
B	Damping matrix
B_{ij}	Damping coefficient from radiation problem
\bar{B}_{ij}	Non-dimensional damping coefficient from radiation problem
C	Stiffness matrix due to hydrostatics
C_a	Added mass coefficient in Morison equation
C_d	Drag coefficient
C_{xs}	Effective width factor due to stresses in x-direction of plate
C_{ys}	Effective width factor due to stresses in y-direction of plate
D	Diameter

D_1	Main column diameter
D_2	Base node diameter
E	Modulus of elasticity
G	Shear modulus
H_{hst}	Hydrostatic head
H_w	Wave height
I	Moment of inertia of cross section
J	Torsion constant
K	Stiffness matrix due to mooring system
L	WAMIT length for non-dimensionalization
L_{beam}	Beam length
L_{mc}	Main column length
L_p	Pontoon length
L_w	Wave length
M	Structural mass matrix
M_b	Bending moment
$M_{p,Rd}$	Design bending moment resistance on plate side
$M_{s,Rd}$	Design bending moment resistance on stiffener side
N_E	Euler buckling strength
$N_{kp,Rd}$	Design plate induced axial buckling resistance
$N_{ks,Rd}$	Design stiffener induced axial buckling resistance
N_{Sd}	Design axial force in plate
$P_{\text{load}}, T_{\text{load}}$	Beam load
S_d	Load effect including all relevant load factors
SM	Section modulus
R_d	Design resistance
T_w	Wave period
V	Fluid velocity
V_D	Displaced fluid volume
W_e	Smallest of the effective section modulus on the plate side and the effective section modulus on the stiffener side

W_{ep}	Effective elastic section modulus on the plate side
W_{es}	Effective elastic section modulus on the stiffener side
X_i	Wave excitation from diffraction problem
\bar{X}_i	Non-dimensional wave excitation from diffraction problem
Z_l	Curvature parameter
a	Wave amplitude
c	Stiffener support conditions dependent factor
d_s	Distance from centroid of stiffener to cross section centroidal axis
f_y	Yield strength
f_k	Characteristic buckling strength
f_{ks}	Design characteristic buckling strength
f_E	Euler buckling strength
f_{ksd}	Design buckling strength of shell
g	Acceleration due to gravity
h	Water depth
h_1	Main column height
h_p	Pontoon height
h_w	Stiffener web height
i_e	Effective radius of gyration
k_{asp}	Panel aspect ratio dependent factor
$k_{buckling}$	Effective length factor
k	Wave number
k_{asp}	Parameter which depends on aspect ratio of plate panel
l_s	Stiffener length between supports
m	Mass
n	Unit normal vector
p	Pressure
p_D	Diffraction pressure
\bar{p}_D	Non-dimensional diffraction pressure

p_j	Radiation pressure component
\bar{p}_j	Non-dimensional radiation pressure component
p_0	Equivalent lateral pressure in plate
p_f	Lateral pressure giving yield in stiffener
p_{sd}	Design lateral pressure in plate
q	Material dependent factor
q_{sd}	Design lateral line load in plate
r_p	Distance from pontoon tip to centerline of main column
r_{mc}	Main column radius
s	Stiffener spacing
s_e	Effective plate width
t	time
t_{plate}	Plate thickness
$t_{eq,bn}$	Base node equivalent thickness in reference design
$t_{eq,mc}$	Main column equivalent thickness in reference design
$t_{eq,p}$	Pontoon equivalent thickness in reference design
t_{mc}	Main column wall thickness
t_p	Pontoon wall thickness
t_w	Stiffener web thickness
t_{wall}	Wall thickness
u	Fluid particle horizontal velocity
\dot{u}	Fluid particle horizontal acceleration
w	Fluid particle vertical velocity
w_p	Pontoon width
y	Perpendicular distance to neutral axis of cross section
z	Vertical coordinate
Z_B	Center of buoyancy
Z_G	Center of gravity

δ, θ	Beam deflection
ζ	Shell buckling ratio
ϵ	Wave phase angle
η	Surface elevation
κ	Shear coefficient
$\bar{\lambda}_p$	Reduced plate slenderness
$\bar{\lambda}_s$	Reduced shell slenderness
μ	Geometric parameter
ν	Poisson ratio
ξ	Motion mode
ρ	Fluid density, material density
σ	Bending stress
$\sigma_{a,Sd}$	Design axial stress in shell due to axial forces
$\sigma_{h,Sd}$	Design circumferential stress in the shell due to external pressure
$\sigma_{j,Sd}$	Design equivalent von Mises stress
$\sigma_{m,Sd}$	Design bending stress in the shell due to global bending moment
σ_{xd}	Design membrane stress in the x-direction of plate
σ_{yd}	Design membrane stress in the y-direction of plate
Y_M	Material factor
τ_{Sd}	Design shear stress plate/shell
ϕ	Fluid velocity potential
ω_{nat}	Natural frequency
ω	Frequency

1 Introduction

Due to the world's increasing energy demand and the depletion of fossil fuels, the importance of alternative energy production is increasing. To reduce environmental impact from energy production, it is also necessary that this alternative energy production is clean. Renewable energies, such as wind, solar and hydro, are believed to be significant contributors to a future cleaner energy mix. The direct emissions from wind power generation are basically zero. Also, the emissions associated with manufacturing are much lower than those of conventional coal and gas power plants. In Europe, the EU's renewable energy directive has set a binding target of 20% of final energy consumption from renewables by 2020 and 27% by 2030. Wind energy is a major contributor to renewable energy production in the EU, where it represents more than 30% of all new power production capacity and currently has the capacity to cover 8% of the total energy consumption.

1.1 Offshore wind energy

To reach the renewable energy targets, wind farms are installed not only onshore, but also offshore. Some of the main aspects which make a typical offshore wind farm different from an onshore wind farm are:

- An offshore wind turbine is exposed to aerodynamic loads from the wind and hydrodynamic loads from waves and currents. This results in design requirements which differ from those of a land based turbine, which is not exposed to hydrodynamic loads.
- Offshore wind turbines have a substructure between the tower base and the foundation.
- Installation and maintenance is generally much more costly offshore than onshore because offshore weather conditions can give reduced site accessibility, and installation vessels can have very high day rates.
- All submerged components of an offshore wind farm are exposed to sea water, which provides a very corrosive environment compared to onshore.

- Submarine cables are required to transport the electricity from the offshore wind farm to the grid connection onshore.
- The spatial planning of an offshore wind farm must account for variables such as marine life, shipping routes and fishery.

At the moment, the cost of offshore wind power is relatively high compared to the cost of onshore wind power. This is mainly due to higher installation, operation and maintenance costs. However, there are benefits from developing offshore wind compared to onshore. First, because the wind encounters almost no obstacles offshore, the wind there is generally stronger and steadier than onshore. This means that the wind resource is better offshore than onshore. Second, the human exposure to noise and visual impacts from the turbines is significantly reduced by placing the turbines on the sea.

The first offshore wind farm was installed in Denmark in 1991, and there are currently several installed offshore wind farms in Europe. The current total installed capacity of offshore wind in Europe is roughly 11 GW. All of these farms consist of wind turbines with bottom-fixed substructures and most of them are located in the shallower parts of the North Sea. As more wind farms are planned it may be necessary to move further offshore, which implies deeper waters. Another option is to look to undeveloped coastal waters with good wind resources. In many cases, this also implies deep waters, such as off the Norwegian, Portuguese or Japanese coast. The current commercially available substructures are mainly monopiles, jackets, gravity based and tripods. Monopiles have the largest market share by far. For water depths larger than 40-50 meters, none of these are economically feasible [1]. This is the main motivation for looking into floating concepts, in which a floating platform moored to the seabed is used instead of a bottom-fixed substructure. Additionally, wind farms further offshore are less sensitive to noise restriction, visual pollution and space availability as they can be placed flexibly to avoid shipping lanes and other critical zones. Potential disadvantages of floating turbines, when compared to bottom-fixed turbines, are more transmission loss, more complex control system due to floater body motions, larger inertia loads due to floater accelerations and a more complicated installation process [2].

1.2 Floating wind turbine concepts

The main floating concepts under consideration are the spar buoy, semisubmersible, barge and tension leg platform (TLP). Each of these concepts is briefly described in the following.

Spar buoy

The spar buoy concept consists of an upright floating thin buoy with a small water plane area. The spar buoy is characterized by a large draft and is moored to the seabed with catenary lines. In 2009, Statoil installed the Hywind Demo off the Norwegian coast as a demonstration project. The Hywind Demo is depicted in Figure 1-1. This is a full scale spar buoy 2.3-MW wind turbine which is still in operation. Statoil has announced plans of making a Hywind pilot park in Scotland consisting of five 6-MW turbines.

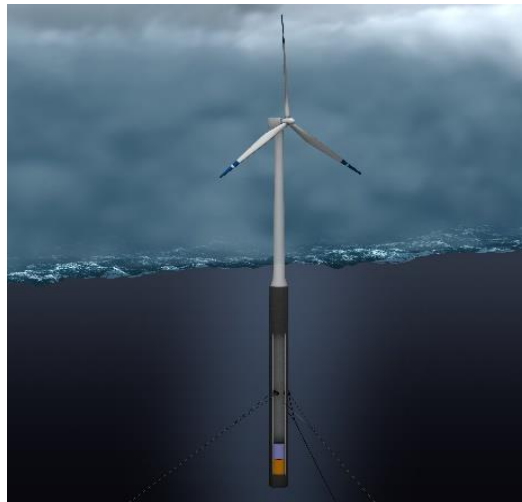


Figure 1-1: The Hywind Demo [3]

Semisubmersible

Semisubmersibles often consist of a deck supported by vertical columns which are interconnected under the water surface. They are characterized by good stability and a medium draft. They are, as the spar buoy, moored to the seabed with catenary lines. In 2011, Principle Power installed the WindFloat prototype off the Portuguese coast. This is a full scale

semisubmersible 2-MW wind turbine. WindFloat has three cylinders and the tower is located on top of one of the cylinders, as depicted in Figure 1-2.



Figure 1-2: The WindFloat concept [4]

Barge

A barge is a flat-bottomed boat with a large water plane area. It is characterized by a small draft and is moored with catenary lines. No full-scale prototype has been made yet. However, the company IDEOL has developed a design called Damping Pool, which is shown in Figure 1-3. This design has a central opening which helps to damp out the floater motions.



Figure 1-3: The Damping Pool concept [5]

Tension leg platform (TLP)

A TLP is characterized by an excess of buoyancy and is pulled down into the water by tendons. This is in contrast to the previously described concepts, which have a catenary mooring system. High stiffness in heave, pitch and roll is characteristic for TLPs, and they are thought to be relatively well suited for intermediate water depths. The tendon system acts as both a stabilizing and station keeping system for the TLP. In 2008, the company Blue H Technologies installed a small prototype of a two-bladed 80 kW TLP wind turbine which was decommissioned less than a year later.

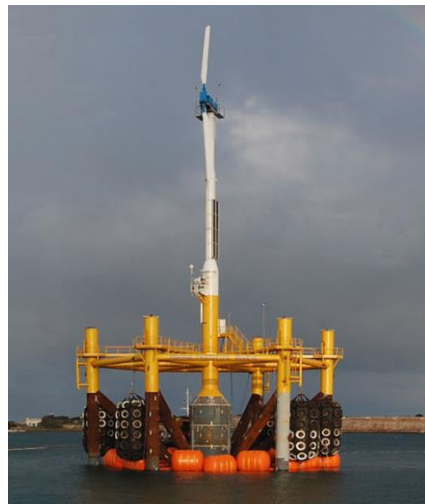


Figure 1-4: The Blue H TLP concept [6]

1.3 Research aim and motivation

Reducing the cost of energy is the primary challenge of today's wind energy industry [7]. Reducing the costs is a necessity for offshore wind energy, and especially deep water offshore wind energy, to be competitive. With this in mind, the TLP concept has been estimated to be one of the most promising floating concepts for wind turbines due to low production costs [8]. It is also assumed that the tendon system makes the TLP concept better suited for shallower waters than concepts with a catenary mooring system and that the high stiffness of the moored TLP, which leads to relatively small motions, is favorable for minimization of structural loading and fatigue damage [7]. Additionally, small pitch motions are favorable for a wind turbine because

the rotor is designed for wind inflow perpendicular to the rotor plane. For these reasons, the TLP concept has both economic and dynamic advantages. At the moment, no multi-MW prototype of any TLP wind turbine (TLPWT) has been made. For an unproven concept, it is desired to carry out numerical analyses with a model which describes the physics of the structure as accurately as possible.

Bachynski [9] performed global dynamic analysis for five selected mono-column TLP designs with a rigid hull. One of the rigid hull designs selected by Bachynski is the starting point for this master thesis. The design comprises the dimensions and mass of the main column and the pontoons. Because the elasticity of the hull could influence the global behavior of the TLPWT it is desired to carry out an analysis with a flexible hull and compare with the results from the analysis which have been carried out with rigid hull. In this way, it can be investigated how the hull elasticity influences the global dynamics of the TLPWT. In this study, a basic scantling design was made for the hull by following industry guidelines. The hull stiffness was then estimated with FE analysis.

The hydrodynamic loads for large-volume structures depend strongly on frequency. Novel methods are needed to include both flexibility and correct hydrodynamic loads in the global analysis. In this study, a new approach was tested by generating an elastic multi-body global analysis model, in which the multi-body analysis tool SIMO is used to represent the hydrodynamic loads for sections of the hull. A SIMO-body can have prescribed data for hydrodynamic added mass, radiation damping and excitation. The essence of the method is to generate this data and insert the SIMO-bodies at the right place in an elastic structural model of the hull. The results were compared to a model of the TLPWT which consists of beam elements with Morison-type loading only and to published results of the TLPWT with rigid hull and frequency-dependent loads from first-order order potential theory.

Previously published papers on dynamic analysis of floating wind turbines focus on global dynamic behavior. In this study, the internal loads in the hull structure were also investigated. A pure hydrodynamic analysis with a rigid hull structure was carried out and the internal hull loads were estimated. The effect of elasticity was investigated by comparing the results from this pure hydrodynamic analysis with the internal loads computed in the global analysis model in a wave-only environment.

Thus, this study has the following three main contributions:

1. Perform hull scantling design and investigate the hull elasticity's influence on the global dynamic properties of Bachynski's TLPWT design.
2. Implement and test a new method for including hydrodynamic loads in a global analysis model.
3. Investigate the effect of elasticity on the internal dynamic loads in the hull.

1.4 Related work

Several papers regarding coupled dynamic analysis of floating offshore wind turbines have been published. Most of these focus on numerical analysis of catenary moored spar floater wind turbines, but some also consider a tension leg platform wind turbine. To this author's knowledge, all previous works on coupled dynamic simulation analysis of TLPWTs have modelled the hull as rigid. However, one study by Zhao et al. [10] indicated that the hull elasticity had a significant influence on the TLPWT's natural frequencies. Furthermore, no studies concerning structural scantling design or internal loads for a TLPWT hull have been discovered. However, there are a number of published studies which deal with coupled global dynamic analysis.

One of the first coupled analyses for a TLPWT was performed by Withee at MIT [11]. His study used the aero-servo-elastic module FAST code in conjunction with the ADAMS software to model and analyze a 1.5-MW TLPWT design. The floater was assumed to be rigid. Withee carried out simulated free decay tests in different modes of motion and evaluated damping coefficients and the natural periods of the system. Additionally, various sources of damping were investigated and typical system responses in a wave-wind environment were presented.

Lee [12] performed frequency-domain response analysis of a 1.5-MW TLPWT. Lee modelled the structure as rigid and found the system to be extremely stiff in the rotational modes and relatively soft in surge and sway. The natural frequencies were found to be outside the high-energy region of typical wave spectra.

Bae et al. [13] performed time-domain coupled dynamic analysis of a 1.5-MW mini TLPWT. They used CHARM3D to develop a dynamic coupling between the floater and mooring lines. Then, FAST was implemented to obtain a so-called rotor-floater-mooring coupled model. The floater was modelled as a rigid body. WAMIT was used to compute the frequency-dependent hydrodynamic coefficients. The hydrodynamic coefficients computed in WAMIT were transferred to CHARM3D for time-domain analysis. The study assessed rotor-floater and floater-mooring coupling effects by comparing the coupled analysis with uncoupled analysis in a co-linear wind-wave environment. The rotor-floater coupling was found to increase the maximum tether tension and to cause high-frequency vibrations on the floater.

Matha [14] conducted fully coupled time-domain aero-hydro-servo-elastic analysis of the current NREL/MIT TLP design and the NREL 5-MW reference turbine. The coupled analysis was performed using FAST, which means that the hull was rigid, and the coupled time-domain hydrodynamics module HydroDyn. Linear frequency-dependent hydrodynamic coefficients were obtained with WAMIT and used as input to HydroDyn. The tower mode shapes were obtained with the multi-body code ADAMS. Loads and stability analysis were carried out for ultimate and fatigue loads, and the loads on the turbine were compared to those of a land-based, a spar-buoy and a barge-type wind turbine. Several findings were documented. An important finding is that a number of instabilities were identified for the TLP for certain load cases. Also, it was concluded that that the loads on all of the offshore type turbines were larger than the loads on the land-based turbine.

A highly relevant previously published study is Bachynski's doctoral thesis from NTNU [9]. Bachynski's work included design and global dynamic analysis of five rigid baseline TLP designs which resemble the SeaStar TLP concept [15]. The designs were intended to support the NREL 5-MW reference turbine and the OC3 Hywind tower design at a water depth of 150 meters. The coupled computer code SIMO-RIFLEX-AeroDyn was used to simulate the behavior of the system in combination with various hydrodynamic load models. The importance of second-order wave forces and third-order ringing forces was investigated for each design. Also, the effect of controller faults, shutdown and wind-wave misalignment was investigated one design.

Ramachandran et al. [16] performed hydro-aero-elastic coupled analysis for a TLP supporting the NREL 5-MW reference turbine. Their model included three-dimensional wave and wind loads which were coupled with the structural response by extending the aero-elastic code Flex5. Morison's equation was used to compute the wave loads, while an unsteady blade element method was used to compute the aerodynamic loads. The aerodynamic model included features such as wind shear, turbulence and moving tower shadow, while the hydrodynamic model accounts for 3-D wave kinematics and directional spreading. The coupled model has 17 degrees of freedom; 11 degrees of freedom for the wind turbine and 6 degrees of freedom for the rigid platform. The loads and responses were validated against simpler models and showed good agreement.

1.5 Thesis outline

The following is an outline of this thesis.

- **Chapter 2:** A theoretical background is given on structural dynamics, floater hydrodynamics and wind turbine aerodynamics. Also, an introduction is given to existing TLP concepts and typical TLP characteristics before Bachynski's selected TLP hull design is presented. Last, relevant design standards are discussed.
- **Chapter 3:** A basic scantling design is made for the hull components (pontoons and main column) by following industry guidelines.
- **Chapter 4:** An equivalent beam model is generated for the hull. FE modelling is used to estimate the stiffness of the hull components, while simple engineering estimations are used to model the mass distribution.
- **Chapter 5:** The equivalent beam model for the hull is implemented in a beam element model of the complete TLPWT. The natural periods and mode shapes of the fully-flexible TLPWT are estimated.
- **Chapter 6:** The hull model is extended by implementing first-order potential theory added mass, radiation damping and excitation for sections of the hull. An elastic multi-body hull model is obtained.
- **Chapter 7:** The elastic multi-body hull model is implemented in the global analysis model of the fully-flexible TLPWT. The performance of the wind turbine is investigated

and decay tests are simulated to estimate the fundamental natural periods of the system. A comparison of the dynamic behavior of the elastic multi-body global analysis model and Bachynski's reference model is presented for selected wind-wave environmental conditions.

- **Chapter 8:** The internal loads in the hull are computed at selected cross sections. The effect of hull elasticity on the internal dynamic loads is investigated. An evaluation of the scantling design from chapter 3 is made.
- **Chapter 9:** Conclusions and recommendations.

2 Theoretical background and the TLPWT concept

This chapter is intended to present the necessary theoretical background information which is needed to model and analyze the TLPWT within the scope of this thesis.

The following is an outline of this chapter.

- Paragraph 2.1 defines the global coordinate system and degrees of freedom of the structure, and presents relevant theory on structural dynamics.
- Paragraph 2.2 discusses the environmental loads. This paragraph both defines the environmental loads which are considered in the present work and how they are estimated.
- Paragraph 2.3 treats the dynamic coupling between structural model, hydrodynamic loads, aerodynamic loads and wind turbine controller logic. Especially the coupling between the structural model and the hydrodynamic loads is essential in the present work.
- Paragraph 2.4 gives an overview of common TLP concepts. Both concepts used in the oil and gas industry and existing TLP designs for offshore wind turbines are presented.
- Paragraph 2.5 presents the TLP designs of Bachynski [9]. An separate paragraph is devoted to this due to its importance to this work. The dimensions of the specific TLP design for which the scantling design is to be made in chapter 3 are given here.
- Paragraph 2.6 presents design standards which are relevant to global and detailed design of offshore wind turbines.

2.1 Structural dynamics

In this study, RIFLEX was used to model the structural dynamics of the wind turbine, floater and tendons. RIFLEX is based on finite element modelling in the time-domain and was developed for analysis of slender marine structures. A detailed description of the theory behind RIFLEX can be found in [17].

This part aims to give an introduction to TLPWT rigid body mechanics (paragraph 2.1.1), and present the essentials of relevant finite element theory (paragraph 2.1.2).

2.1.1 TLPWT rigid body mechanics

For a rigid floating body, one can define three global translational degrees of freedom and three global rotational degrees of freedom. In accordance with common practice, the degrees of freedom will be referred to as surge, sway, heave, roll, pitch and yaw, and can be represented with a motion vector as

$$\xi = [\xi_1(t), \xi_2(t), \dots, \xi_6(t)]^T \quad (2-1)$$

The translational degrees of freedom are surge, sway and heave, while the rotational degrees of freedom are roll, pitch and yaw. Figure 2-1 shows the definition used throughout this thesis for the global coordinate system and degrees of freedom of the TLPWT structure.

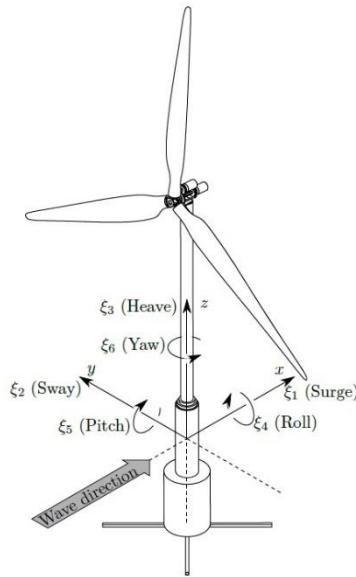


Figure 2-1: Definition of global coordinate system and degrees of freedom [7]

The total mass of the system consists of the structural mass and hydrodynamic added mass. There is hydrodynamic, aerodynamic and structural damping present. The stiffness of the system has contributions from hydrostatic restoring forces and moments, and the mooring system. For linear damping, restoring and excitation forces, the governing dynamic equilibrium can be expressed as a system of differential equations in the following way:

$$(M + A)\ddot{\xi} + B\dot{\xi} + (C + K)\xi = F \quad (2-2)$$

F is a 6-by-1 vector which represents the external excitation forces acting on the structure for each mode of motion. M contains the structural mass components, M_{ij} , while A contains the

added mass components A_{ij} . B contains the damping components, B_{ij} , C contains the hydrostatic restoring components, C_{ij} , and K contains the mooring system restoring components, K_{ij} . M , A , B , C and K are all 6-by-6 matrices. Note that equation 2-2 gives a *linear* description of the system. Including non-linear effects, such as viscous damping according to the Morison formulation, would require additional terms in the equation.

The buoyancy of the TLPWT is larger than its weight. It is pulled downwards into the water by tendons which are fixed to the seabed. Together, the weight and the tendon tension equilibrate the buoyancy. This typically results in a system which is very stiff in heave, pitch and roll, which is characteristic for TLPs. Second-order wave effects related to sum frequencies can therefore be important [18]. In surge, sway and yaw, the TLP is less stiff. The wave and low frequency horizontal forces are important for the surge and sway motions [18].

Some degrees of freedom are coupled to other degrees of freedom due to the nature of the tendon system. For instance, surge and sway motion will induce heave motions because the TLP naturally also moves in the vertical direction if it moves in the horizontal direction. Also, there is coupling between the bending modes of the flexible tower and the platform pitch, as transverse oscillations of the tower will induce pitching of the platform and vice versa [9].

2.1.2 RIFLEX finite element formulation

An improved dynamic model can be obtained by including elastic deflection characteristics. Beam, bar, plate, shell and/or solid elements can be employed to achieve this. RIFLEX allows the employment of non-linear beam elements, which describe deflections of slender structures. In the following, the beam element formulation and solving of the dynamic equilibrium in RIFLEX are briefly described. A detailed description can be found in [17].

RIFLEX beam element formulation

The RIFLEX beam element is formulated with a co-rotated ghost reference description. This means that no transformation of the stress components is necessary and large rotational

deformations allowed. It has three translational and three rotational degrees of freedom at each node, as depicted in Figure 2-2.

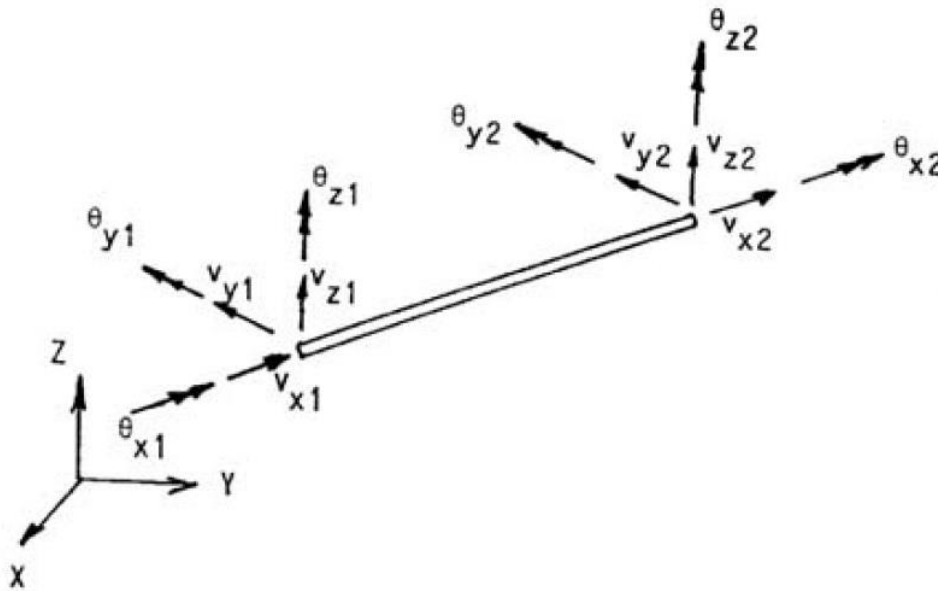


Figure 2-2: Nodal degrees of freedom of beam element [17]

The following assumptions apply for the beam element:

- A plane section normal to the longitudinal axis, remains plane and normal to the longitudinal axis during deformations.
- The strains are small.
- There is no lateral contraction caused by axial elongation.
- There are no shear deformations due to lateral loading.
- There are no coupling effects between torsion and bending.

Solving the governing dynamic equilibrium in RIFLEX

The number of degrees of freedom will in general be higher than for a single rigid body, and they are contained in the motion vector, as previously described. The mass matrices at element level are merged into a global mass matrix. The global mass matrix is consistent, which means that it is based on the same shape functions as the stiffness matrix. The global damping matrix is based

on hydrodynamic damping and mass and stiffness proportional damping. Newton-Raphson iteration is applied for the numerical time integration of the dynamic equilibrium equations.

2.2 Environmental loads

Offshore wind turbines are subjected to a number of different environmental loads. Figure 2-3 illustrates some of the most common ones.

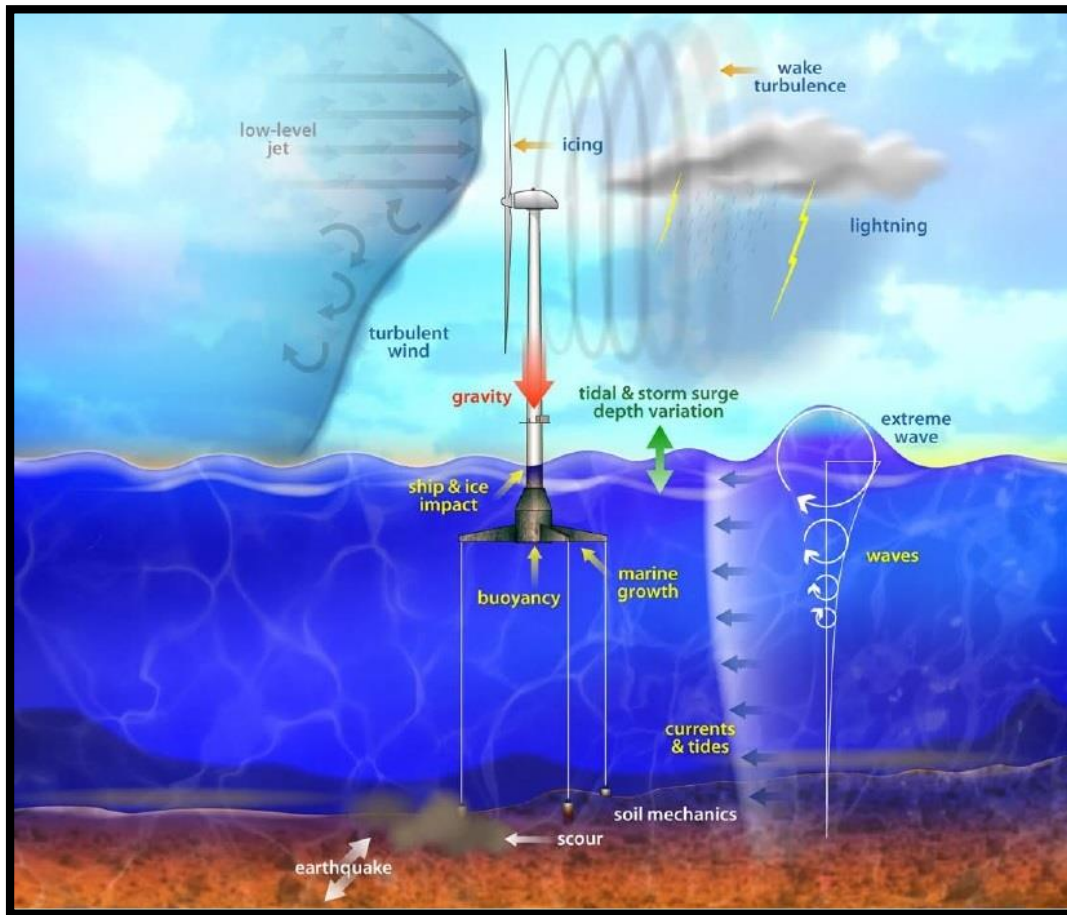


Figure 2-3: Environmental loads on offshore wind turbine [19]

In this study, the main focus is on the implementation of the hydrodynamic loads induced by the waves. Additionally, aerodynamic and hydrostatic loads are considered. Other environmental loads, such as loads due to currents and tides, icing and marine growth will not be considered here.

2.2.1 Hydrodynamic loads

Linear theory is sufficient to describe the wave loads on many offshore structures [20]. In linear theory, the load amplitudes and wave-induced motions of the structure are linearly proportional to the amplitude of the incoming wave. In this study, potential flow theory was assumed to be representative for the fluid. This means that the flow velocity can be defined as the gradient of the velocity potential ϕ . Important features of a potential flow is that the fluid is assumed to be inviscid, irrotational and incompressible. Linear wave theory is applied, which implies that the wave amplitude is small compared to the wave length and that the wave kinematics are valid up to the mean water level only. A summary of first-order potential flow essentials and linear wave theory is given in Appendix A.

The hydrodynamic problem is often divided into two separate sub-problems which are solved independently [20]. When linear theory is used, the forces and moments from these two sub-problems can be superposed to get the total hydrodynamic forces and moments.

- A. The forces and moments on the body from incident waves when the body is restrained from oscillating. These loads are the wave exciting forces and moments. They consist of the Froude-Krylov and diffraction forces and moments. This sub-problem is often referred to as the diffraction problem.
- B. The forces and moments on the body when it is forced to oscillate in initially still water without the presence of waves. These loads are the added mass, damping and restoring forces and moments. This sub-problem is often referred to as the radiation problem.

This implies that also the velocity potential, ϕ , can be decomposed into two components, namely a diffraction component and a radiation component:

$$\phi = \phi_D + \phi_R \quad (2-3)$$

The frequency-dependent wave excitation is found from the diffraction problem. The frequency-dependent added mass and linear radiation damping are found from the radiation problem. The hydrodynamic forces and moments are obtained from integrating the pressure over the instantaneous wetted body surface, S_B . The total pressure in the fluid is given by Bernoulli [21]:

$$p = -\rho \left(\frac{\partial \phi}{\partial t} + \frac{1}{2} |\nabla \phi|^2 + gz \right) \quad (2-4)$$

So the total pressure consists of three terms:

- The first term is the linear dynamic pressure. In complex form, this term can be written as $-i \omega \rho \phi(x, y, z)$, when the potential is described by the product of a space-dependent term and a harmonic time-dependent term: $\phi(x, y, z, t) = \phi(x, y, z)e^{i\omega t}$.
- The second term is the quadratic pressure. This term contributes to the second-order forces.
- The third term is the hydrostatic pressure. This term contributes to the restoring forces.

Wave excitation

The diffraction potential, ϕ_D , is the sum of the potential of the incident wave, ϕ_I , and the potential of the scattered wave field due to the presence of the wave, ϕ_S [21]

$$\phi_D = \phi_I + \phi_S \quad (2-5)$$

The exciting force in direction i is given by integration of the pressure from the diffraction potential over the wetted body surface:

$$X_i = -i\omega\rho \iint_{S_B} \phi_D \mathbf{n}_i dS \quad (2-6)$$

Here, \mathbf{n} is the unit vector normal to the body boundary.

Added mass and radiation damping

The radiation potential can be written as a linear combination of the components corresponding to the degrees of freedom. For a floating rigid body with six degrees of freedom (surge, sway, heave, roll, pitch and yaw), this becomes [21]

$$\phi_R = i\omega \sum_{j=1}^6 \xi_j \phi_j \quad (2-7)$$

where ξ_j and ϕ_j are the amplitude of motion and the unit-amplitude radiation potential in each degree of freedom.

The coefficients for added mass, A_{ij} , and radiation damping, B_{ij} , are found from integration of the radiation potential over the wetted body surface:

$$A_{ij} - \frac{i}{\omega} B_{ij} = \rho \iint_{S_B} \phi_j \mathbf{n}_i dS \quad (2-8)$$

For a body with six rigid body modes, the added mass and radiation damping matrices for a given frequency will be 6-by-6 matrices.

Panel methods

In this study, WAMIT was used to solve the hydrodynamic problem in the frequency domain and obtain the hydrodynamic coefficients for added mass, damping and excitation force. WAMIT is a panel-based diffraction and radiation program, and is commonly used in the offshore oil and gas industry. A brief introduction to the panel method is given here.

Panel methods are numerical methods used to calculate the potential flow around a body. In the panel method, the surface of the structure (and maybe parts of the surrounding water surface too) is divided into discrete elements. These discrete elements are called panels, and each of them fulfill the Laplace equation [20]. Panel methods rely on Green's identity by transforming the three-dimensional Laplace equation into a two-dimensional surface integral equation. The surface of the body is discretized into panels to solve this surface integral equation numerically [18].

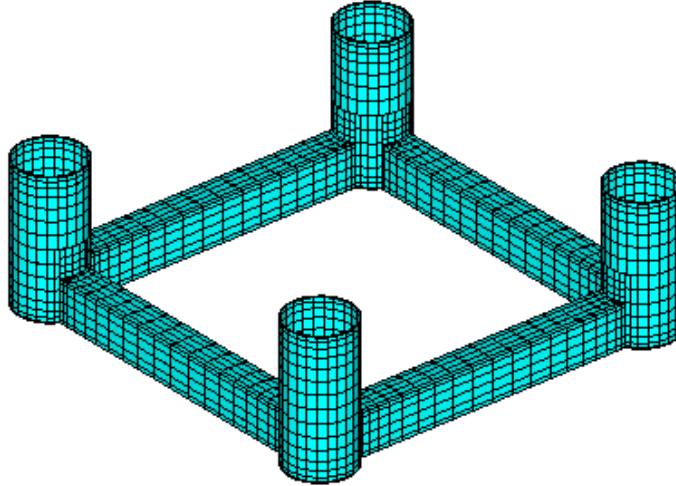


Figure 2-4: Visualization of grid for potential flow panel method [20]

Panel methods are based on potential theory and are commonly used for large-volume structures. Because panel methods are based on potential theory, they cannot accurately predict flow separation and should therefore not be applied to slender structures. Similarly, they cannot accurately predict motions where viscous effects are important, and can only predict damping due to radiation of surface waves [20].

2.2.2 Hydrostatic load and restoring forces and moments

The hydrostatic loading on the submerged part of a structure is the hydrostatic pressure from a fluid at rest. The linear hydrostatic pressure depends only on the vertical coordinate, z . For an incompressible fluid and positive z -direction upwards, this is described as

$$\frac{dp}{dz} = -\rho g \quad (2-9)$$

In equation 2-4, which describes the total fluid pressure, the hydrostatic pressure is represented by the third term. For deeply submerged structural parts, the hydrostatic pressure can represent a significant compressive load. Therefore, the hydrostatic pressure can be important for detailed design when considering buckling of shells and plated structures.

The hydrostatic pressure also contributes to the restoring forces and moments. Therefore, it is generally important for the stability of floating structures. For a freely floating structure, the

hydrostatic pressure completely dictates the structure's stability. For a rigid floating body with six degrees of freedom, the hydrostatic stiffness matrix contains non-zero coefficients for the heave, roll and pitch motions only [18]. For a freely floating body with the x-z plane as symmetry plane for the submerged volume, the non-zero coefficients are generally as described in equations 2-10 through 2-14 [20].

$$C_{33} = \rho g A_{wp} \quad (2-10)$$

$$C_{35} = -\rho g \iint_{A_{wp}} x dx dy \quad (2-11)$$

$$C_{44} = \rho g V_D (z_B - z_G) + \rho g \iint_{A_{wp}} y^2 dx dy \quad (2-12)$$

$$C_{53} = C_{35} \quad (2-13)$$

$$C_{55} = \rho g V_D (z_B - z_G) + \rho g \iint_{A_{wp}} x^2 dx dy \quad (2-14)$$

Here, A_{wp} is the water plane area, V_D the displaced volume, z_B the center of buoyancy and z_G the center of gravity. The hydrostatic restoring forces and moments are important for the stability of TLPs during float-out and installation. However, for a TLP in operational condition, the stability is principally provided by the tendons. A TLPWT in operational condition is not freely floating, but moored and pulled down into the water with tendons. Because of this, there is a significant inequality between the weight of the structure and buoyancy force that the fluid exerts on it. This inequality requires the following modification to the hydrostatic stiffness coefficients for roll and pitch [9]:

$$C_{44} = \rho g V_D z_B - mg z_G + \rho g \iint_{A_{wp}} y^2 dx dy \quad (2-15)$$

$$C_{55} = \rho g V_D z_B - mg z_G + \rho g \iint_{A_{wp}} x^2 dx dy \quad (2-16)$$

2.2.3 Aerodynamic loads

Because of the wind turbine, the TLPWT is subjected to relatively large aerodynamic loads, represented by the rotor thrust force and torque. The thrust force and torque result from integrating the aerodynamic loads acting on the blades over the whole rotor. The thrust force mainly causes the structure to pitch and surge, while the torque causes small roll motions. Additionally, wind flowing in at an angle with respect to the rotor plane can cause sway, roll and yaw motions. Yaw motions can also be caused by an inhomogeneous flow field at the rotor plane. For a three-bladed horizontal axis wind turbine, the rotation frequency of the rotor and the blade passing frequency, commonly known as the 1p and 3p frequencies, are important for tower bending. Last, the spinning rotor can cause so-called gyroscopic loads [22]. The main gyroscopic load is a yaw moment applied by the turbine on the floater which causes yaw motion.

In the following, common methods for computing the aerodynamic loads on a wind turbine are described. There are several different aerodynamic models for wind turbines. The simplest model is the one-dimensional (1-D) momentum balance model for an ideal rotor. On the other hand, also computationally expensive 3-D Navier-Stokes solutions exist. Here, the blade element momentum (BEM) and generalized dynamic wake (GDW) models are briefly described. These two models represent computationally efficient options [9]. Additionally, tower drag and the wind turbine controller is mentioned.

Before the aerodynamic loads can be computed, a description of the wind field is needed. The wind field is discussed in terms of the wind shear, tower shadow and turbulence in Appendix B.

The aerodynamic code applied in this study was developed at MARINTEK to be implemented in RIFLEX, which is used for structural response analysis of slender marine structures. It is a BEM model with additional corrections. A detailed description of the code can be found in [17].

Blade element momentum (BEM) model

In this study, the aerodynamic loads were computed with a blade element momentum method. The blade element momentum method combines momentum theory with blade element theory. A steady BEM model considers steady wind only. This is useful for computing the wind turbine's power and thrust curves as a function of wind speed. However, an unsteady or non-

uniform wind field requires the use of an unsteady BEM model. Additionally, features related to turbine operation and global system dynamics, such as blade pitching and platform motions, may lead to unsteady wind loads which also require an unsteady BEM model to realistically compute the loads.

In the BEM model, the wind flow is modelled as a streamtube which is discretized into annular elements. The model assumes that the force from the blades on the flow is constant in each annular element, which is only true if there are an infinite number of blades. The axial and tangential induction factors are determined iteratively before the local loads on the blade segments are computed. Corrections are needed in order to obtain good results when using BEM. One correction is called Prandtl's tip loss factor and corrects the aforementioned assumption of an infinite number of blades. Another correction is applied to large induction factors for which the momentum theory is no longer valid. For large induction factors empirical relations are used which fit with measurements. Additionally, a hub loss factor can be applied to account for vortices being shed near the hub of the rotor. A detailed description of the blade element momentum theory can be found in Hansen [23]. The BEM model used in this study has implemented Prandtl's tip loss factor and Glauert's correction to large induction factors. However, it does not account for hub losses.

The effect of dynamic wake may also be considered. When the wind speed changes, the blades are pitching or the turbine is yawing, it takes some time for the induced velocities to balance the aerodynamic loads because the induced velocities change relatively slowly in time. The dynamic wake effect can be included by applying a dynamic inflow model which accounts for this. The BEM model used in this study applies a method developed by Stig Øye which filters induced velocities.

Also, dynamic stall effects may be considered. The wind felt locally by a point on a blade is constantly changing during revolution due to turbulence, wind shear etc. Because of this, the angle of attack is also constantly changing. When the angle of attack changes there is a time delay before the aerodynamic loads change. This is called dynamic stall. The applied BEM model uses the Stig Øye model, which gives unsteady lift by filtering the trailing edge separation point.

Generalized dynamic wake (GDW) model

The GDW model is an alternative to the BEM model. The GDW method is based on a potential flow solution to the Laplace's equation and is also known as the acceleration potential method [24]. This solution is used to obtain the pressure distributions in the rotor plane. The main advantage of GDW over BEM is that it includes inherent modelling of the dynamic wake effect, tip losses and skewed wake aerodynamics. Another advantage is that no iteration is required to find the induced velocities in the rotor plane. A drawback of the GDW model is that it only works for lightly loaded rotors and is unstable for low wind speeds because it assumes that the induced velocities are small relative to the mean flow. GDW is not implemented in the aerodynamic code which was used for this study.

Tower drag

In addition to the aerodynamic loads on the rotor, there is also a drag force from the air flow on the tower. The tower drag is usually small compared to the rotor loads. However, in extreme conditions, when the rotor is parked, the tower drag may be important [9]. In this study, no extreme conditions were analyzed. Tower drag was not included in the aerodynamic load computations.

Wind turbine controller

The present work considers a 5-MW horizontal axis wind turbine. A control or regulation system is required to ensure that the turbine operates within its design range. It can also be used to ensure a smooth power output or optimize the power output at low wind speeds. Limiting the power output at high wind speeds is very important. This can be achieved with pitch regulation, stall regulation and yaw regulation.

The controller used in this study was written in Java by Bachynski for the 5-MW NREL Offshore Baseline Turbine and follows the logic described in [25]. It applies a pitch regulated variable speed control. This means that both the blade pitch angle and rotor speed can vary. For wind speeds below the rated wind speed, the blade pitch angle remains unchanged while the

turbine attempts to operate with the optimal tip speed ratio. In this region, the thrust increases quadratically with wind speed, while the power increases cubically. At the rated wind speed, the turbine reaches the rated thrust and rated power. For wind speeds above rated wind speed, the blade pitch angle is regulated in order to limit the power output to the rated power. In this region, the thrust decreases with wind speed while the power stays constant.

Floating turbines can present a challenge to the pitch control system designer. The reason is that floater motions will influence the relative wind speed at the rotor and may cause a conventional pitch controller to amplify these motions, resulting in so-called negative damping. When the turbine is moving into (against) the wind the relative wind speed at the rotor is larger (smaller) than the actual wind speed. For above rated wind speeds, which is the region where the blade pitch mechanism is activated, this results in blade feathering (stalling), which decrease (increase) the thrust force. This in turn leads to amplified motion into (against) the wind. There are several ways to deal with this. However, the stiffness of a TLPWT system is so high that most operational conditions do not require this issue to be addressed [9]. The controller used in this study does not account for this. In other words, the land-based controller is applied.

2.3 Hydro-aero-servo-elastic coupling

For an elastic body, a hydrodynamic load can cause a structural response in the form of an elastic deformation. However, the hydrodynamic load itself also depends on the structural response. In other words, the elastic deformations of the body depend on the hydrodynamic loads and vice versa. This interaction between the elastic response and the hydrodynamic loads is called hydro-elasticity. It is desirable to have a model which captures this effect. In this work, a hydro-elastic model was obtained by coupling WAMIT's hydrodynamic loads from potential theory with the structural formulation in RIFLEX. The hydrodynamic loads computed in WAMIT were implemented in the RIFLEX model by using SIMO-bodies. SIMO is a multi-body time-domain analysis tool which easily can be interfaced with RIFLEX. Thus, the WAMIT output was first transferred to SIMO, which was then coupled to RIFLEX. Implementing and testing this method is one of the major purposes of this study. A detailed explanation on how this was done is presented in chapter 6.

If an aerodynamic model is coupled with a structural model, an aero-elastic model is obtained. Such a model describes the interaction between the structural response and aerodynamic loads. In the aeroelastic model, the aerodynamic loads affect the deflection of the structural components such as the blades and tower. The velocity of the deflected blades and tower change the effective wind velocity at the blades and thus also the aerodynamic loads. Aero-elasticity is thus similar to hydro-elasticity, in that the elastic deformations of the body depend on the aerodynamic loads and vice versa. If the aerodynamic model from paragraph 2.2.3 is coupled with the hydro-elastic model, a hydro-aero-elastic model is obtained. If the controller logic is also implemented, a hydro-aero-servo-elastic model is obtained. A hydro-aero-servo-elastic model couples the interaction between the structural response, the hydro- and aerodynamic loads and the controller. SIMA was used for the coupled dynamic analysis. SIMA is a simulation workbench for dynamic analysis of marine operations and floating systems. SIMA can be used to easily interface RIFLEX, SIMO, the BEM code and the controller logic, and thereby provide a fully coupled simulation environment. Thus, there were five separate codes/software interacting in the hydro-aero-servo-elastic coupled time-domain global dynamic analysis model in this work:

1. RIFLEX (structural dynamics)
2. SIMO (hydrodynamic loads)
3. The BEM code (aerodynamic loads)
4. The wind turbine controller
5. SIMA (workbench which couples the four codes above)

The blades, shaft, tower, hull and tendons were modelled with beam elements. Except for the hull, the structure was modelled exactly as in [9]. The aerodynamic loads were applied at the blades only. The hub, nacelle and tower were not subjected to wind loads in the model. Hydrodynamic loads were applied at the hull and tendons.

Figure 2-5 gives an overview of the structural modelling of the TLPWT and the various load models which may be applied to different parts of the structure.

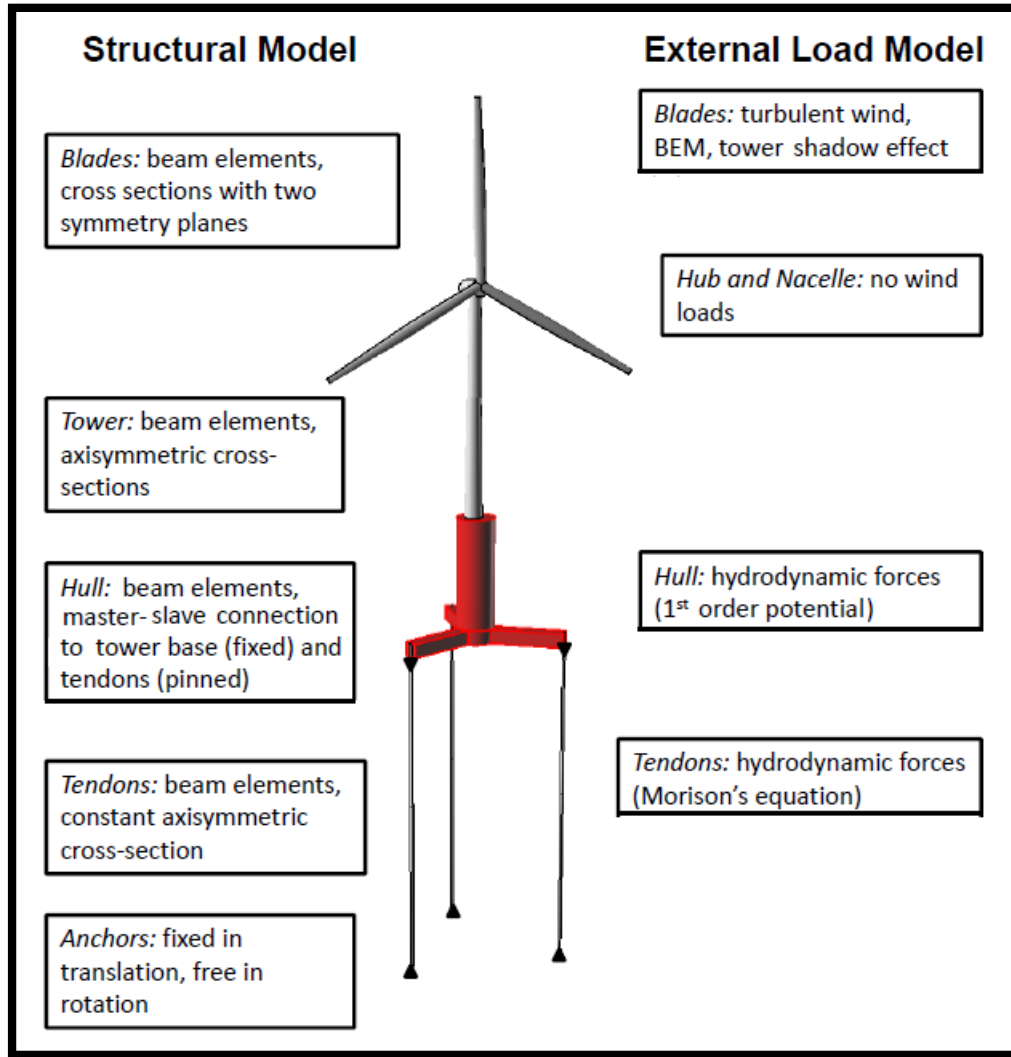


Figure 2-5: TLPWT model overview [9]

2.4 TLP concepts

The TLP concept is largely unproven for wind turbines. However, it is widely used as support structure for topsides in the oil and gas industry. The high stiffness of the tendon system gives small vertical platform motions, which is beneficial for deck operations such as drilling and lifting. For a floating wind turbine, reduced platform motions implies a more steady inflow of wind at the rotor plane. TLPs have been applied in water depths ranging from 150 m to 1,600 m [26].

The hull is hollow and is made up of stiffened plate and shell structures. It is filled with air to provide buoyancy, but can also be used to accommodate ballast tanks. Usually, it is divided into water tight compartments to limit the consequences of a flooding. The hull of TLPs used in oil and gas installations also often accommodates mechanical equipment and pipes. Together, the buoyancy, the total weight and the tendon axial stiffness determine the natural periods of the system. Natural periods in heave, roll and pitch should be less than 4.5 s to avoid resonance in waves [27].

Scantling design for a TLP should take both local and global loads into account. The relatively deep draft of the TLP leads to high hydrostatic pressure which acts normal to the plating and causes large local compressive loads. Fatigue is governing for connections, such as the transition between base node and main column, and for plate thickness transition zones. However, even if fatigue loads do play an important role, it is hydrostatic pressure which is the governing design load for a large portion of the hull [28]. Plate and shell buckling are therefore important factors in TLP scantling design. To avoid local buckling due to the large pressure, stiffeners and girders are added to support the plating and ensure stability. Consequently, an optimized design is a trade-off between plate thickness and the spacing and size of stiffeners and girders.

In addition to large compressive loads due to hydrostatic pressure, the tendon causes a moment which induces large tensile and compressive loads in the pontoons [15]. Especially the plating on the underside of the pontoon is critical, as this is in compression both due to the tendon induced loads and the hydrostatic pressure. Standard thicknesses are used for plates throughout the hull design. The plate thickness is usually one inch or less [29].

Because the main column stretches from the pontoons to above the still water level, the effect of wave hydrodynamics is important. Usually, the main column is large and has a round shape to minimize drag forces [26]. For a TLPWT, it is also important to keep in mind that additional bending and shear stresses are induced in the main column due to the thrust force on the rotor. It has become common practice to use the equivalent design wave approach for dynamic loads in TLP hull structural design and analysis [26]. In the equivalent design wave approach, design checks and response analyses are performed when the structure is exposed to various design waves characterized by a certain wave height and period.

Paragraph 2.4.1 gives a brief introduction to existing TLP designs in the oil and gas industry. Paragraph 2.4.2 gives a brief introduction to existing TLP designs which have the purpose of acting as support structure for wind turbines.

2.4.1 TLP concepts for supporting topsides in the oil and gas industry

There are several different existing TLP hull configurations. Figure 2-6 shows four common configurations: The conventional TLP (CTLP), the extended TLP (ETLP), the Moses TLP and the SeaStar TLP. The CTLP has four columns which are connected under water by a submerged pontoon. The ETLP is similar to the CTLP, but includes a small horizontal extension of the hull at the base of the column. This small extension is where the tendons are attached. Because this increases the separation between the tendons, a reduction in tendon loads is achieved [27]. The ETLP shown in Figure 2-6 is the Magnolia platform located in the Gulf of Mexico. Another existing hull configuration is one which has one or more central columns and a number of cantilever pontoons extending radially. The Moses TLP has four central columns and four radially extending pontoons. The SeaStar TLP has hull configuration which is similar to the Moses TLP. The SeaStar TLP has one central column and three or four radially extending pontoons.

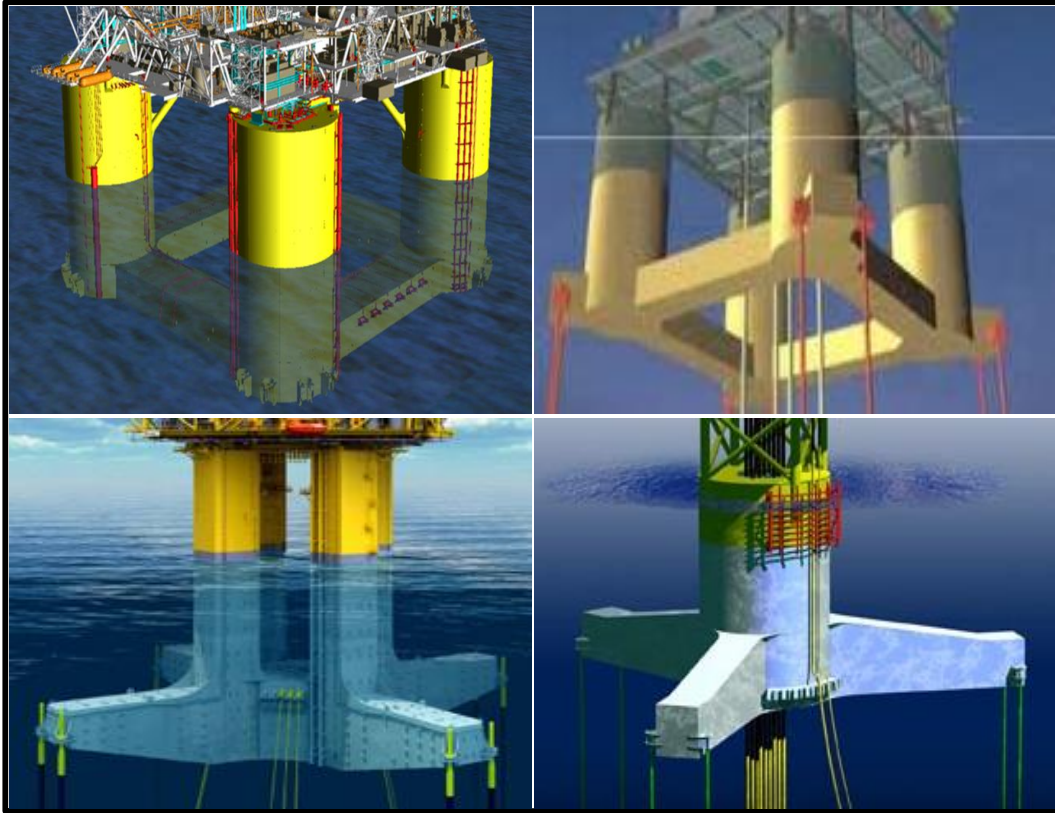


Figure 2-6: Four TLP configurations. Top left: CTLP. Top Right: ETLP. Bottom left: Moses TLP. Bottom right: SeaStar TLP

The SeaStar TLP hull configuration is highly relevant to this master thesis. The weight-to-displacement ratio is a measure of the efficiency of the hull configuration. The smaller the ratio, the more efficient the hull configuration. An advantage of the SeaStar TLP is that it has a relatively efficient hull. On the other hand, it also comes with relatively high installation costs [27]. The scantling design for the Typhoon SeaStar TLP was carried out according to ABS rules [15].

2.4.2 TLP concepts for supporting wind turbines

Most of the TLP concepts that have been developed for supporting offshore wind turbines are mono-column concepts. However, also multi-column concepts have been suggested. The following is a summary of some of the concepts developed to date.

Mono-column concepts

Early work on TLP concepts for wind turbines was performed at MIT. Withee [11] performed coupled dynamic analysis with a mono-column TLPWT, which had four reinforced pontoons with a square cross section. The structure was intended to support a 500 kW turbine. The majority of the buoyancy came from the column. The structure also made use of truss structures between the column and the pontoons to increase the stiffness of the system. Lee [12] presented a three-legged TLP concept intended to support a 1.5-MW turbine. Lee modelled the entire structure as a rigid body.

Matha [14] presented a mono-column concept for a 5-MW turbine on 200 m water depth. The work was based on earlier work carried out at MIT based on parametric optimization. This is the current MIT/NREL design. It is a relatively large structure with four pontoons of 27 m, a waterline diameter of 18 m and a draft of almost 50 m. The design has eight mooring lines with a pretension of 3,931 kN each. The pontoon width and height are not given. However, Lygren [30] back-calculated the required outer radius of the cross section is 1.2 m in order for the maximum stress to be below the steel yield stress.

Some designs have also been developed outside of MIT. Glosten Associates [31] developed a three-legged TLP for a 5-MW turbine. It was designed to be chained to the seabed in environmental conditions found in the UK round 3 development area. The Glosten design has a waterline diameter of 7.2 m and 9 tendons (chains).

Garrad Hassan [32] argued that the TLP is the most suitable floating concept for German waters and presented a three-legged design for a 5-MW turbine. The design was developed for a water depth of 50 m and has draft of 20 m, a column diameter of only 5 m. It has three circular pontoons with a length of 32.5 m and diameter of 4.5 m. The design has three tendons— one per pontoon – and the pretension per tendon is 1,738 kN [9].

Designs have also been developed for even larger turbines. Crozier [33] presented two designs for the NOWITECH 10-MW turbine. One design is stable during towing and operation, while the second is stable during installation only. Both designs had four pontoons, and the main geometric difference between the two designs was the draft, which was significantly larger for the design which is stable during towing and operation.

Bachynski [9] presented five baseline TLPWT designs which resemble the SeaStar TLP. The designs were all made for a 5-MW turbine and modelled with a rigid hull. One of these designs is the starting point for this master thesis. Bachynski's five baseline designs are discussed in more detail in paragraph 2.5.

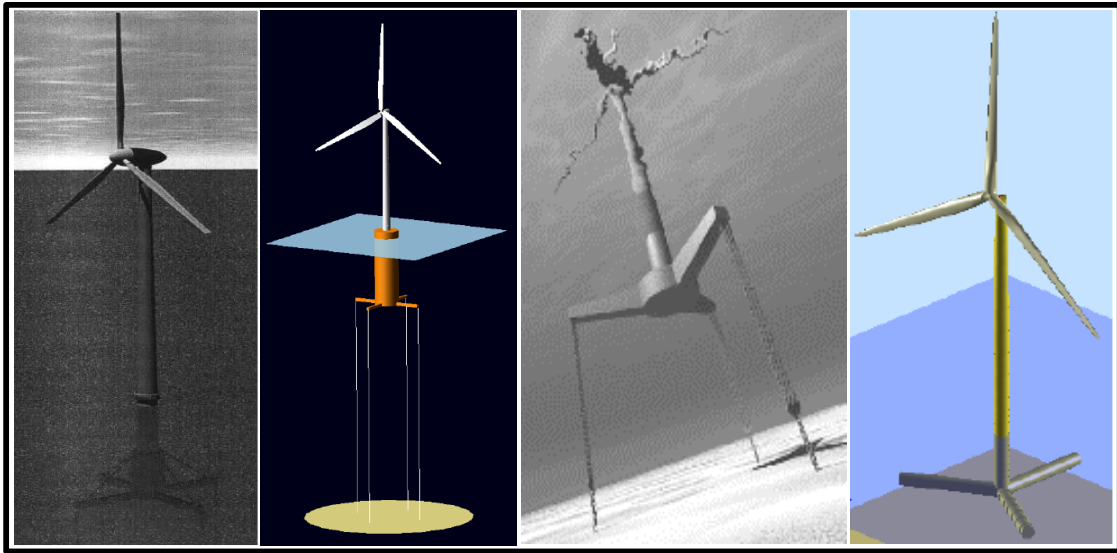


Figure 2-7: Selection of mono-column TLP concepts. Left to right: Withee [11], Matha [14], Glosten [31], Garrad Hassan [32]

Multi-column concepts

Adding more columns can improve the hydrostatic properties of the structure which is beneficial for stability during float-out. However, it also gives rise to increased fabrication complexity. Some of the existing mono-column designs are briefly presented here.

Suzuki et al. [34] developed a TLP for a 2.4-MW turbine. The structure was developed to be situated off the Japanese coast at a water depth of 100 m. The TLP had a center column, three spokes and three corner columns. The analysis included finding the first ten vibration modes, dynamic response in waves and time domain response to seismic loads.

I.D.E.A.S. Inc. [35] presented a design for a 5-MW turbine for 50 m and 100 m water depth. The configuration of the structure includes three inclined columns extending from the central column

at the waterline to some distance below the waterline, forming a triangular base. Additionally, the system has both vertical and lateral mooring lines to minimize offset due to wind, waves and current.

Zhao et al. [10] presented a three-footed concept with a central column and three radiating corner columns. Natural frequencies and mode shapes computed and dynamic response simulations were performed. The natural frequencies of the system were found to be significantly influenced by the elasticity of the turbine system and TLP foundation.

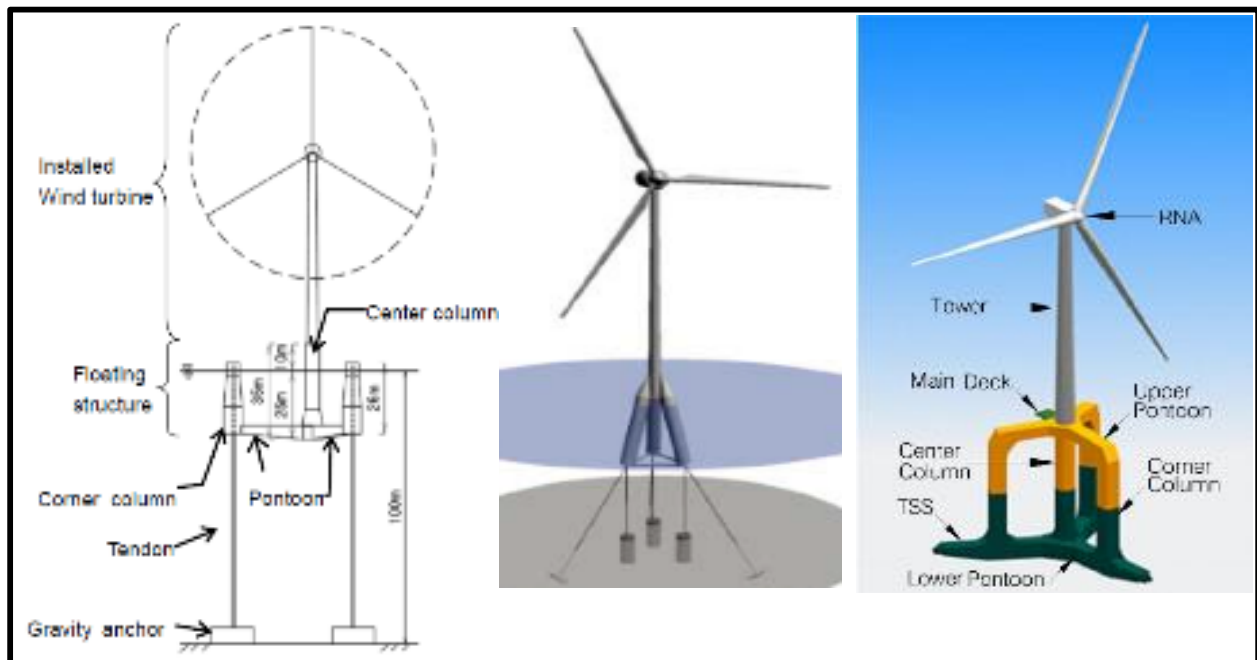


Figure 2-8: Multi-column TLPWT concepts. From left to right: Suzuki et al. [34], I.D.E.A.S [35], Zhao et al. [10]

2.5 The reference TLP design

Bachynski's work included dynamic analysis of 5 baseline TLPWT designs [9]. These designs were not optimized and only intended to give a range of possible geometries. Each design consists of a number of pontoons, one main column and one base node. The base node is located under the main column and can be thought of as the connection node for the pontoons and the main column. The following initial design criteria were used [9]:

1. The surge and sway natural periods should be longer than 25 s in order to avoid first-order wave excitation.
2. The heave, roll/bending, and pitch/bending natural periods should be shorter than 3.5 s in order to avoid first-order wave excitation.
3. In order to limit the angle at the tendon connectors, the mean offset should not exceed 5% of the water depth.
4. The tendon area must be sufficient to prevent yield, within a given safety factor, for tensions up to twice the initial tension.

In addition to these initial design criteria, other criteria, such as minimizing the loads, steel mass and tendon pretension, were taken into account. The tendon pretension and the dimensions of the main column, pontoons and base node were varied. Also, the number of pontoons and their cross sectional shape were varied. Each design has one tendon per pontoon. The designs are depicted in Figure 2-9.

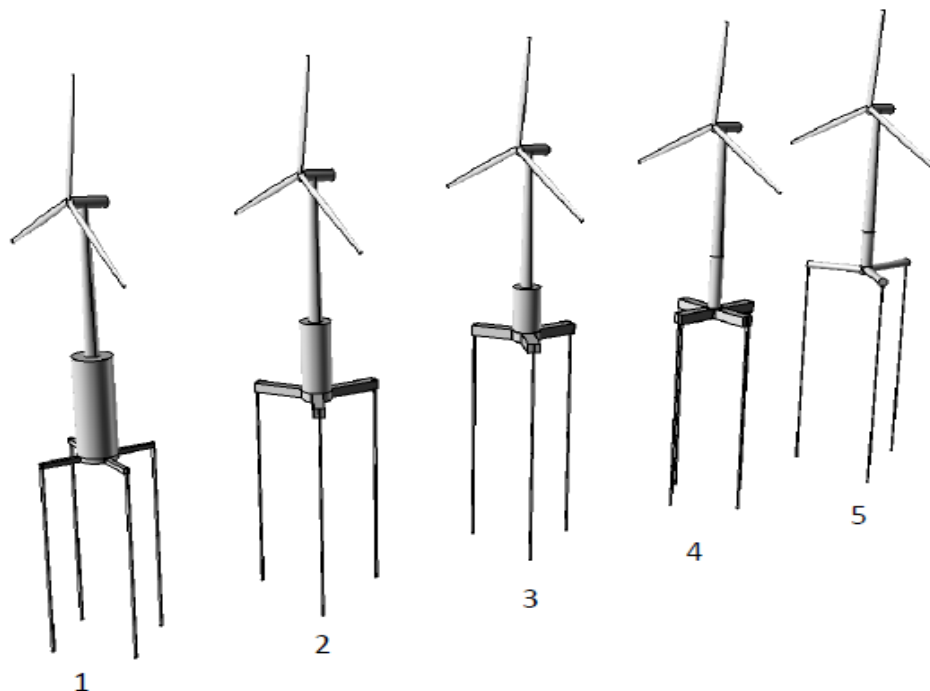


Figure 2-9: Bachynski's five rigid baseline TLPWT designs [9]

The rigid TLP model for which the scantling design was made is the third design in Figure 2-9. This design turned out to be a good compromise between performance and weight (cost). It is an

approximate half-scale version of the Typhoon SeaStar TLP oil platform. It has three rectangular pontoons. The main column and the base node are both cylindrical and have the same diameter. Figure 2-10 gives a parameter definition and closer visualization of the design.

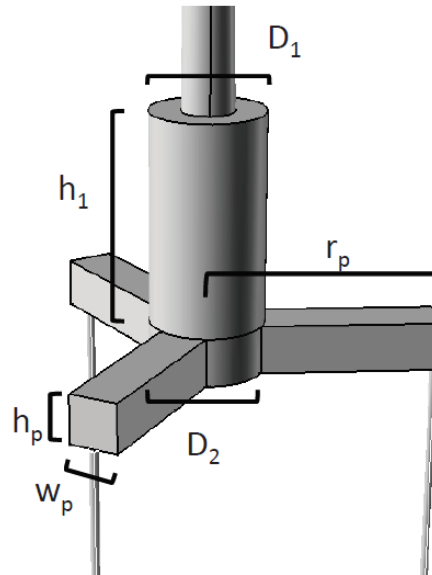


Figure 2-10: TLP parameter definitions [9]

The main column is defined by the diameter D_1 and the height h_1 . The pontoons are defined by their height h_p , width w_p and r_p , which is the distance from pontoon tip to the center of the main column cross section. The base node has diameter D_2 and height h_p . In addition to this, there is an equivalent wall thickness, t_{eq} , related to each part. Throughout the rest of this report, this design will be referred to as the *reference design*. The dimensions and masses of the pontoons and the main column as defined by Bachynski [9] are summarized in Table 2-1.

Table 2-1: Dimensions and masses of the components of the reference design

Main column	
D₁	14 m
h₁	26 m
t_{eq,mc}	5.51 cm
Mass of main column	628,298 kg
Base node	
D₂	14 m
t_{eq,bn}	12.5 cm
Mass of base node	207,131 kg
Pontoons	
r_p	28 m
h_p	6 m
w_p	6 m
t_{eq,p}	3.37 cm

The total mass of the three pontoons is 457,756 kg. The draft of this TLPWT design is 22 m and the tendon pretension is 8,262 kN. The base node accommodates ballast with a mass of 1389,000 kg. The outer tendon diameter is 1.3 m.

It is interesting to compare the reference design with the previously mentioned 5-MW mono-column TLP designs of NREL, Glosten Associates and Garrad Hassan. First, it is noted that the tendon tension is very high, especially when compared to the Glosten and Garrad Hassan designs. When summing up the total tension per tendon group, it is seen that the tension for the NREL design (two lines per tendon group) is only slightly lower than that of the reference design. Second, the central column is considerably smaller than that of the NREL design, but relatively large compared to the Glosten and Garrad Hassan designs. Third, the draft is smaller than that of the NREL design, but similar to the draft of the Garrad Hassan design. Last, it is noted that the pontoons are comparable in length, but relatively thick when compared to the pontoons of the designs of NREL and Garrad Hassan. In chapter 3, a basic scantling design is presented for the pontoons and main column of the reference design.

2.6 Design standards for offshore wind turbines

Standards regarding wind turbines come primarily from the International Electrotechnical Commission (IEC), classification societies and national requirements. This paragraph will first

give a brief summary of available design standards for offshore wind turbines. Next, the design standards which were used in this study are presented.

The IEC has published IEC 61400, which is an international standards regarding wind turbines. Part 3 of this publication (IEC 61400-3) covers issues which are relevant to offshore wind turbines. Det Norske Veritas (DNV) has published various standards regarding offshore wind turbines, such as DNV-OS-J101 (Design of Offshore Wind Turbine Structures) and DNV-OS-J103 (Design of Floating Wind Turbine Systems). Other classification societies, such as the American Bureau of Shipping (ABS) and Germanischer Lloyd (GL) have also published their own standards on both bottom-fixed and floating wind turbines. The standards typically cover topics such as environmental conditions, loads, structural design, corrosion protection, and transport and installation. The standards for floating wind turbines can cover additional topics such as station keeping, design of anchor foundations and floating stability. Often, the design standards require loads to be calculated for a number of design load cases. The design load cases are typically based on combinations of normal, fault, transportation, installation and maintenance design situations with appropriate normal or extreme external conditions.

The only design made in this study was a scantling design for the hull. DNV-OS-J103, which is DNV's standard for floating wind turbine design, refers to other DNV documents for the assessment of buckling of shells, plating, stiffeners and girders. More specifically, it refers to DNV-RP-C202 [36] for designing shells against buckling, and to DNV-RP-C201 [37] for minimum requirements to plate thickness, stiffener section modulus and girders. These are so-called recommended practices, and they apply the load and resistance factor design (LRFD). Both of these RPs were used in this study. According to Zhang, a large portion of a TLP structure is governed by hydrostatic pressure [28]. As previously mentioned, Bachynski's chosen TLP design is an approximate half-scale of the SeaStar TLP oil platform. Because the scantling design for this oil platform was carried out according to ABS rules, it was decided to use ABS rules in this study too. ABS MODU rules [38] for tank boundary shells, flats and bulkheads are used in the scantling design for the pontoons based on hydrostatic pressure in the same way as they are used by Zhang in his parametric study for non-circular pontoons [28].

Chapter 3 gives a detailed explanation of the how the scantling design was carried out.

3 Basic scantling design for the reference hull

This chapter gives a detailed explanation of how the scantling design was performed for the various parts of the reference design hull, which was introduced in the previous chapter. The hull has three different components, namely a cylindrical column, three pontoons with a square cross section, and a base node. In accordance with Bachynski and paragraph 2.5 of this report, the cylindrical column will consistently be referred to as the “main column” throughout the rest of this entire report, even though there is only one column on the entire hull. It is important to note that the design is an ultimate limit state design and that fatigue is not taken into consideration.

Three design codes are used in this chapter.

1. **ABS MODU part 3** is used to create a scantling design for the plated pontoons based on hydrostatic pressure only.
2. **DNV-RP-C201** is used to perform an extra check of the final scantling design, which was obtained with ABS MODU and hydrostatic pressure as the only design load. In this extra check, the tendon induced bending stress in the pontoon plating is included as design load in addition to the hydrostatic pressure. This check is not intended to give rise to design modifications, but merely to give an evaluation basis for the final design, which was obtained with ABS MODU and hydrostatic pressure.
3. **DNV-RP-C202** is used to create a scantling design for the cylindrical main column.

Both DNV-RP-C201 and DNV-RP-C202 use the load and resistance factor design (LRFD) format. This means that the following acceptance criteria is used:

$$S_d < R_d \quad (3-1)$$

where S_d is the load effect including all relevant load factors and R_d is the design resistance. In other words, the design passes the buckling check only if the design resistance is larger than the load effect.

The base node was assumed to have a much higher stiffness than the main column and pontoons because it has a much higher mass per volume. No scantling design was made for the base node. Instead, it was modelled as rigid just as it was in the analyses performed by Bachynski.

The reference design dictates how much steel is available for each component (pontoons and main column). The total pontoon steel mass is given as 457,756 kg. With a steel density of 7,850 kg/m³ the total pontoon steel volume becomes approximately 58.3 m³. This means that roughly 19.4 m³ of steel is available for each pontoon. The total main column steel mass is given as 628,299 kg. With a steel density of 7,850 kg/m³ the total main column steel volume becomes approximately 80.0 m³. The scantling design for the pontoons and the main column was done by distributing the available steel over the walls, while adding stiffeners, girders and bulkheads. The design was then checked against the aforementioned DNV or ABS codes and modified until a satisfactory design was found.

The following is an outline of this chapter.

- Paragraph 3.1 defines the loads which are accounted for in the final scantling design. Paragraph 3.1.1 presents the loads which are accounted for in the final scantling design for the pontoons, while paragraph 3.1.2 presents the loads which are accounted for in the final scantling design for the main column. When the loads have been defined, the actual scantling design can be carried out.
- Paragraph 3.2 presents the scantling design for the pontoons. Paragraph 3.2.1 gives a detailed description of the equations which are applied when using ABS MODU and designing for hydrostatic pressure only. Paragraph 3.2.2 presents the final pontoon scantling design, which is based on hydrostatic pressure only, in terms of tables and figures. Paragraph 3.2.3 presents an estimation of the tendon induced bending stress in the pontoon plating, and an evaluation of the final pontoon scantling design which is based on checking the design against DNV-RP-C201. Checking the design against this RP includes going through a large number of equations. These equations are treated in appendix C.
- Paragraph 3.3 presents the scantling design for the main column. Both the scantling design process, and the final scantling design in terms of tables and figures are presented here.

3.1 Loads accounted for in the final scantling design

This paragraph defines the loads which are accounted for in the final scantling designs of the pontoons and main column. The loads accounted for in the final scantling design for the pontoons are described in paragraph 3.1.1. The loads accounted for in the final scantling design for the main column are described in paragraph 3.1.2.

3.1.1 Loads accounted for in the final scantling design for the pontoons

Part 3 of ABS MODU describes guidelines for hull engineering of mobile offshore drilling units. These rules were adopted in the same way as by Zhang in his parametric study for non-circular pontoons and columns [28]. This means using the ABS MODU rules for tank boundary shells, flats and bulkheads in the scantling design process and taking the maximum hydrostatic pressure as the only design load. The hydrostatic pressure at a depth H_{hst} from a fluid with density ρ was estimated with the following simple formula

$$p = \rho g H_{hst} \quad (3-2)$$

where g is the acceleration of gravity (9.81 m/s^2).

As previously mentioned, the final pontoon design, which is presented in paragraph 3.2.2, was checked afterwards with DNV recommended practice accounting for tendon induced bending stresses in addition to hydrostatic pressure. The estimation of the tendon induced bending stresses is presented together with this additional check in paragraph 3.2.3.

3.1.2 Loads accounted for in the final scantling design for the main column

The scantling of the cylindrical main column was done using DNV-RP-C202. Also for the main column, loads from hydrostatic pressure were accounted for.

The Morison equation was used to calculate the hydrodynamic load on the main column from one design wave. Sea current loads were not accounted for. For a circular cylinder, the Morison equation gives the inline load per unit length with the following equation

$$F = \rho (1 + C_a) \frac{\pi}{4} D^2 \dot{u} + \frac{1}{2} \rho C_d D u |u| \quad (3-3)$$

where \dot{u} and u are the horizontal fluid acceleration and velocity, respectively, D is the cylinder diameter and ρ the fluid density. C_a is the added mass coefficient and C_d is the drag coefficient. Both of these coefficients are empirical. The wave height and period of the regular wave were set to 15 m and 14.1 s respectively [9] and the hydrodynamic forces were estimated with Morison's equation using an added mass coefficient of 1 and a drag coefficient of 0.8 [9]. Linear wave theory was applied to calculate the fluid kinematics. Wheeler stretching was used for the fluid kinematics above the mean water level, where linear wave theory is no longer applicable. Strictly speaking, the Morison equation is only valid if the cylinder diameter is small compared to the wave length. Usually, it is applied in the regime where the wave length is larger than 5 times the diameter [39]. Because the diameter of the main column is 14 m, the wave length of the design wave should be at least 70 m for the Morison equation to be applied. The dispersion relation gives the relation between wave frequency, ω , and wave number, k , for a given water depth, h :

$$\omega^2 = k g \tanh(k h) \quad (3-4)$$

With a water depth of 150 m and a wave period of 14.1 s, the wave number becomes 0.0202 m^{-1} , which corresponds to a wave length of 310 m. Because this is much larger than 70 m, the Morison equation was assumed to be applicable. The inline wave force on the main column will cause a shear force and a bending moment. The wave force thus induces both shear and bending stresses in the main column.

In addition to the wave and hydrostatic loads, the stresses in the main column resulting from the thrust force on the rotor were estimated. The largest thrust force on the rotor is the thrust force at rated wind speed. For the NREL 5-MW wind turbine this corresponds to approximately 660 kN. Because the thrust force acts in the rotor plane and the hub height is 90 m, the thrust force causes a shear force and a bending moment. In this way, also the rotor thrust force induces both shear and bending stresses in the main column.

Last, the rotor, nacelle and tower are resting on the main column and will therefore cause compression. The effect of this was also estimated and accounted for. The masses of these components are given in Table 3-1 [25] [40]. Also the weight of the part of the main column which is located above the still water level was accounted for. The main column is 26 meters high and has a draft of 16 meters. This means that roughly 38 percent of the main column steel volume is located above the still water level. This corresponds to approximately 30.4 m³. With a steel density of 7850 this corresponds to around 240,000 kg. Table 3-1 gives the mass of the four components:

Table 3-1: Mass of components resting on main column causing compression

Component	Mass [kg]
Rotor	111,000
Nacelle	240,000
Tower	250,000
Weight of hull which is above still water level	240,000
Total	841,000

Thus, the following loads were assumed to be governing in the scantling design for the main column:

1. Hydrostatic pressure.
2. Shear and bending stresses induced by a large regular wave.
3. Shear and bending stresses induced by the rotor thrust force.
4. The total weight of the components resting on the main column.

3.2 Scantling design for the pontoons

The final scantling design for the pontoons was made by following guidelines from Zhang for non-circular pontoons and ABS MODU. As previously mentioned, this results in a design which only accounts for hydrostatic pressure. However, the simplicity of the approach made it an efficient tool for obtaining an idea of how to make a design which complies with some minimum requirements. Paragraph 3.2.1 describes the scantling design requirements based on hydrostatic pressure only. The final scantling design, which is based on hydrostatic pressure only, is presented with tables and figures in paragraph 3.2.2. Last, paragraph 3.2.3 presents the additional check of the final design where tendon induced bending stresses are also accounted for. The

result of this additional check is used to evaluate and comment on the quality of the final scantling design.

3.2.1 Scantling design for the pontoons with ABS MODU, accounting for hydrostatic pressure only

The available pontoon steel was distributed over the pontoon walls (side walls and tip plate) and a number of longitudinal stiffeners, transverse girders and transverse vertical bulkheads. Figure 3-1 shows a typical stiffened plate panel stiffeners and girders.

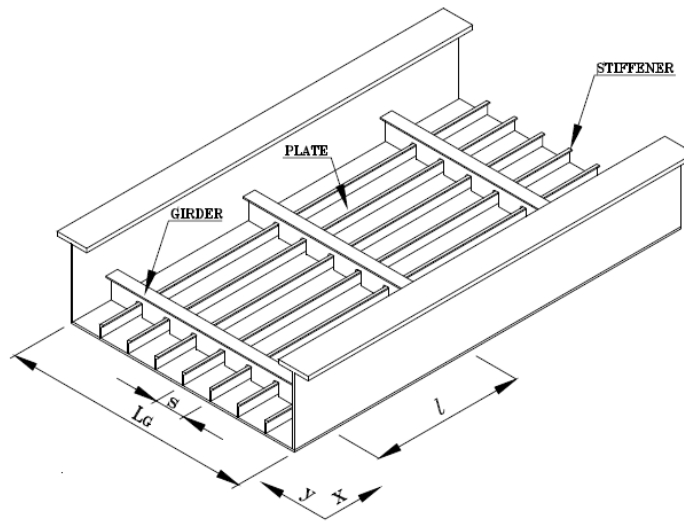


Figure 3-1: Stiffened plate panel

Common TLP weight ratios are given in Table 3-2 [28]. These ranges were used as weight ratios during the first iterations in the design loop, and were later changed to obtain a design which satisfies the constraints with some margin.

Table 3-2: Weight ratios of recent TLPs [28]

Component	Weight ratio [%]
Plates (walls and bulkheads)	45 to 50
Stiffeners	15 to 20
Girders	30 to 35

The plate steel covers both the pontoon walls and the transverse vertical bulkheads. The ABS MODU rules define minimum requirements for the plate thickness, stiffener section modulus and girder section modulus as functions of the hydrostatic design head, stiffener spacing, girder spacing and bulkhead spacing. First, the required plate thickness is treated in paragraph 3.2.1.1. Then, paragraph 3.2.1.2 treats the required section modulus for the longitudinal stiffeners, while paragraph 3.2.1.3 treats the required section modulus for the transverse girders.

3.2.1.1 Required plate thickness

According to ABS, the plate thickness in mm should be no less than what is obtained from the following formula [38]:

$$t_{plate} = s k_{asp} \sqrt{q H_{hst}} / 254 + 2.5 \quad (3-5)$$

Here, s is the stiffener spacing in mm, k_{asp} is a factor which depends on the aspect ratio of the plate panel, q is a factor which depends on the yield and tensile strength of the material and H_{hst} is the design head in meters. The maximum design head for the pontoons is 22 m. For the value of k_{asp} , the aspect ratio of the plate panel was taken to be the longer edge divided by the shorter edge. A plate panel was taken to be the part of a pontoon wall between two bulkheads. Thus, if the distance between two bulkheads is 3 meters and the width of the pontoon is 6 meters, then the aspect ratio is $(6 - 2 t_p) / 3$.

The pontoon wall thickness therefore depends on both the spacing of the longitudinal stiffeners, and the spacing of the bulkheads. An increase in the number of stiffeners and bulkheads will reduce the required wall thickness. The pontoon wall thickness was taken to be uniform. Because stiffeners and bulkheads were given a constant spacing, the design parameters which govern the required wall thickness are the number of stiffeners and bulkheads.

The number of bulkheads was chosen such that the bulkhead thickness is larger than the minimum required plate thickness and smaller than 1 inch in accordance common TLP hull design practice [29].

3.2.1.2 Required section modulus for longitudinal stiffeners

The minimum section modulus in cm^3 of the longitudinal stiffeners was determined with the following equation:

$$SM_{stiffeners} = f c H_{hst} s l_s^2 \quad (3-6)$$

Here, f is 7.8. The supporting conditions determine the value of c . If the stiffener is supported at both ends by girders, then c is 1, otherwise it is 0.9. Again, H_{hst} is the design head in meters. An increase in the hydrostatic pressure gives larger loads and therefore leads to an increase in the minimum required section modulus of the stiffener. Now, s is the stiffener spacing in meters. Larger stiffener spacing means that each stiffener carries more load and therefore leads to an increase in the minimum required stiffener section modulus. l_s is the stiffener length between supports, also this in meters. As the length of a stiffener increases, so does its slenderness. To avoid buckling, the minimum required section modulus must therefore increase if the stiffener length increases. The stiffener length was taken to be equal to the girder spacing, which is constant along the pontoon. Therefore, the design parameters which govern the minimum required stiffener section modulus, $SM_{stiffeners}$, are the number of girders and the number of stiffeners.

Knowing the required section modulus, the shape and dimensions of the stiffener cross section could be determined. For simplicity, flat bar longitudinal stiffeners were chosen, which means that the cross sectional area is determined by the stiffener web height and the stiffener web thickness only. An additional constraint, formulated by DNV, was imposed on the relationship between the web height and the web thickness to avoid local buckling of the flat bar stiffener [36]:

$$h_w < 0.4 t_w \sqrt{\frac{E}{f_y}} \quad (3-7)$$

E is the modulus of elasticity, while the f_y is the yield strength. These were set to 210 GPa and 250 MPa respectively. t_w is the web thickness and h_w is the web height, as shown in Figure 3-2.

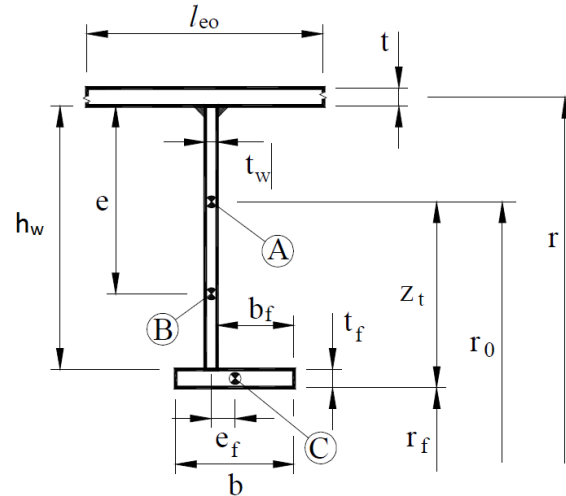


Figure 3-2: General stiffener cross section dimensions [36]

A flat bar stiffener means that there is no dimension b in the figure (no flange).

3.2.1.3 Required section modulus for transverse girders

The minimum section modulus in cm^3 of the transverse girders was determined with the following equation:

$$SM_{girders} = f c H_{hst} s l_s^2 \quad (3-8)$$

Now, f is 4.74. For the girders, the value of c is 1.5. The other parameters are the same as in equation 3-6. Therefore, the design parameters which govern the minimum required girder section modulus, $SM_{girders}$, are the number of girders and the number of stiffeners.

Again, flat bar longitudinal girders were chosen. Also here, the additional constraint to the relation between h_w and t_w was applied to comply with the DNV local buckling requirement.

3.2.2 Final pontoon scantling design

Here, the final scantling design for the pontoons is presented. The design is thus made by applying ABS MODU rules as suggested by Zhang for hydrostatic pressure only. The final design is one which gave relatively large margins for plate thickness, stiffener modulus and girder modulus with respect to the minimum requirements.

Chapter 3: Basic scantling design for the reference hull

A scantling design which complies with all the basic constraints for hydrostatic pressure only was found by varying the following parameters:

- The weight ratios, while trying to stay close to the values given by Zhang (Table 3-2).
- The number of bulkheads
- The number of stiffeners
- The number of girders

The design loop was as follows:

1. Assign weight ratios and number of stiffeners, girders and bulkheads
2. Determine the dimensions of the stiffeners and girders
3. Check the design against ABS MODU

The final design is a result of trying to optimize the design with respect to the ABS MODU minimum requirements for hydrostatic pressure.

A high number of stiffeners will give small stiffener spacing. That means lower required minimum wall thickness and also lower required section modulus for both stiffeners and girders. On the other hand, because the total amount of steel available for the stiffeners is limited by the weight ratio, a high number of stiffeners will also lead to very small stiffeners, which in turn gives a low section modulus for each stiffener. The same logic applies to the girders. However, the effect of the number of girders on the minimum required section modulus is relatively larger because of the l_s^2 -term which is present in both equations.

Several combinations of weight ratios and number of stiffeners and girders turned out to give a design which complies with all the minimum requirements of ABS. The final pontoon scantling design is summarized in Table 3-3 through Table 3-7. This design has a pontoon wall thickness and bulkhead thickness which are both smaller than 1 inch and also have some margin with respect to the required minimum. Also, the section modulus of both girders and stiffeners have some margin with respect to the required minimum.

Table 3-3: Final pontoon scantling design weight ratios

Component	Weight ratio [%]
Pontoon walls	60
Bulkheads	8
Longitudinal stiffeners	20
Transverse girders	12

Compared to the weight ratios for recent TLPs (Table 3-2), this design has a relatively large portion of the steel in the plates (pontoon walls and bulkheads), and a relatively small portion of the steel in the stiffeners and girders.

Table 3-4: Number of bulkheads, longitudinal stiffeners and transverse girders per pontoon

Component	Quantity per pontoon	Spacing [m]
Bulkheads	2	7
Longitudinal stiffeners	20 (5 per pontoon wall)	1
Transverse girders	14	1.4

Thus, the each pontoon has 2 transverse vertical bulkheads, 20 longitudinal stiffeners and 14 transverse girders. The position of the bulkheads are indicated in Figure 3-5.

Table 3-5: Pontoon wall thickness and bulkhead thickness

PLATE THICKNESS	
PONTOON WALL	2.14 CM
BULKHEADS	2.20 CM
MINIMUM REQUIRED WALL THICKNESS	1.80 CM

All of the pontoon plating is thicker than 2 cm and thinner than one inch. Also, the all of the plating has some margin with respect to the ABS minimum required wall thickness. Table 3-6 and Table 3-7 give the dimensions and modulus of the stiffeners and girders.

Table 3-6: Dimensions and modulus of pontoon longitudinal stiffeners

LONGITUDINAL STIFFENERS	
WEB THICKNESS	2.63 CM
WEB HEIGHT	30.53 CM
SECTION MODULUS	409.26 CM ³
MINIMUM REQUIRED SECTION MODULUS	336.336 CM ³

Table 3-7: Dimensions and modulus of pontoon transverse girders

TRANSVERSE GIRDERS	
WEB THICKNESS	2.52 CM
WEB HEIGHT	29.19 CM
SECTION MODULUS	357.57 CM ³
MINIMUM REQUIRED SECTION MODULUS	306.58 CM ³

The final dimensions of the longitudinal stiffeners and transverse girders are very similar. The longitudinal stiffeners are slightly larger. Both the longitudinal stiffeners and the transverse girders have the shape of a flat bar. Therefore, their size are defined by the web thickness and the web height only.

Figure 3-3 shows what the pontoon looks like between the transverse vertical bulkheads.

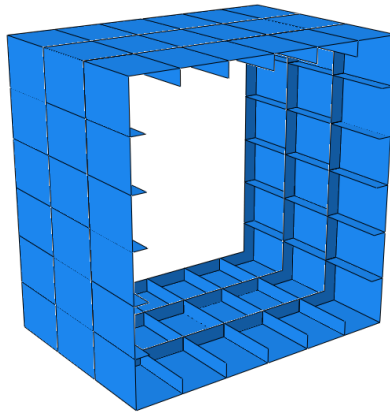


Figure 3-3: Pontoon scantling design based on hydrostatic pressure, showing the longitudinal stiffeners and the transverse girders

The plate at the tip of the pontoon has a thickness of one inch and is also supported by stiffeners. These stiffeners have the same dimensions as the longitudinal stiffeners and there are five of them in both the horizontal and vertical direction. Figure 3-4 gives a visualization of the stiffener pattern.

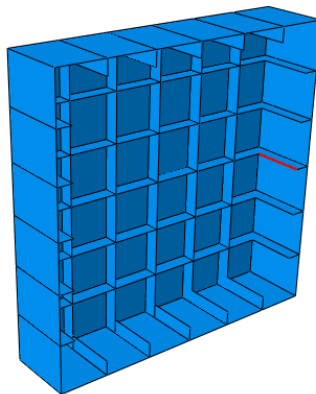


Figure 3-4: Pontoon tip plate with stiffeners

Figure 3-5 shows the complete pontoon

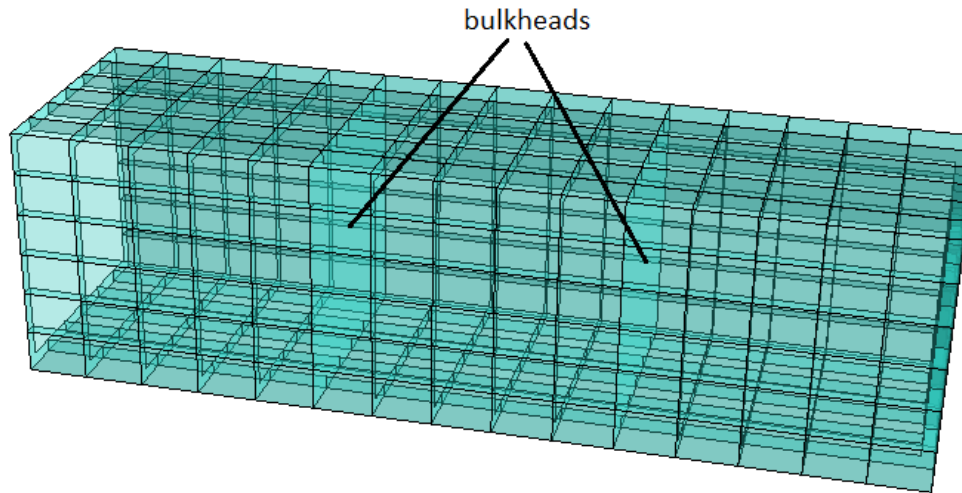


Figure 3-5: Complete pontoon scantling design

The final scantling design for the pontoons has now been completed. In the next paragraph, this design is checked against DNV-RP-C201, accounting for not only hydrostatic pressure, but also for tendon induced bending stresses in the pontoon. The result of this check will give basis for an initial evaluation of the pontoon design which was presented here.

3.2.3 Evaluating the final pontoon scantling design by checking against DNV-RP-C201 and accounting for both hydrostatic pressure and tendon induced bending stresses

Because it might be desirable to include more loads than only hydrostatic pressure, an additional and more detailed check of the resulting scantling design was performed. The final scantling design which was presented in paragraph 3.2.2 was therefore checked against DNV-RP-C201, accounting for both hydrostatic pressure and tendon induced bending stresses in the pontoon plating. This is an extra design check which is only intended to give basis for an evaluation of the previously presented design.

Paragraph 3.2.3.1 describes how the tendon induced bending stress in the pontoon plating was estimated. Paragraph 3.2.3.2 treats the check of the final pontoon scantling design with the

LRFD method according to the DNV recommended practice. Paragraph 3.2.3.2 also presents a discussion regarding the quality of the design.

3.2.3.1 Estimating the tendon induced bending stresses

The bending stress in the pontoon which is induced by the tendon force was estimated with simple beam theory. Figure 3-6 shows the bending moment variation in the pontoon over the pontoon length.

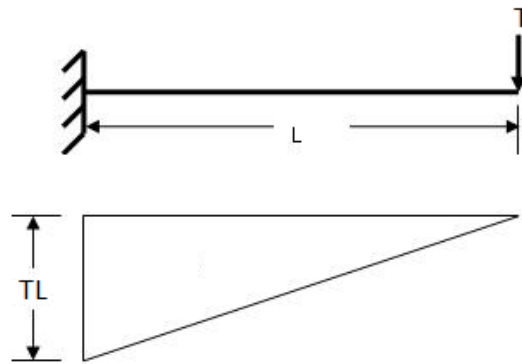


Figure 3-6: Bending moment in pontoon induced by tendon force

The bending moment in the pontoon is largest where the pontoon is connected to the base node. The fact that the connection surface between the pontoon and the base node in reality is curved was not taken into consideration here. Instead it was assumed that a flat surface at a distance of 21 meters from the pontoon tip is representative. With a static tendon tension of approximately 8.3 MN and a pontoon length of 21 m, the bending moment at the base becomes roughly 175 MNm. To calculate the bending stress from this, the following formula for stress in a beam under simple bending was used:

$$\sigma = \frac{M_b y}{I} \quad (3-9)$$

Because the height and width of the pontoon are both equal to 6 meters, the distance from the bottom plate to the neutral axis of the cross section is 3 meters. This is the value of y in equation 3-9. The area moment of inertia depends on the cross section design.

Thus, the following loads were estimated and accounted for in the additional check of the final pontoon scantling design:

1. Hydrostatic pressure acting on the pontoon plating
2. Bending stresses in the pontoon plating induced by the tendon tension

3.2.3.2 Evaluating the final pontoon scantling design with DNV-RP-C201

Section 7 in DNV-RP-C201 treats buckling of stiffened plates and stiffeners and uses the LRFD method [37]. The bending stress induced by the tendon tension was included in addition to the hydrostatic pressure. The pontoon plating is thus subjected to the combined loading of hydrostatic pressure and tendon induced bending of the pontoons.

In this design check, so-called interaction formulae for axial compression and lateral pressure determine whether the design is complying with the stability requirements. A number of steps must be completed before the interaction formulae can be treated. The first step in the design check is to estimate the design stress components. Then, the forces in the stiffened plate and the effective plate width are estimated. Next, the characteristic buckling strength and resistance parameters of the stiffeners are treated. When these steps have been completed, the interaction formulae are considered. In the following, only the outcome of the check will be discussed. For details on the formulas which were used, and comments on how they were used, the reader is referred to Appendix C.

The final pontoon design which was presented in paragraph 3.2.2 has a cross section with an area moment of inertia of approximately 3.8 m^4 . The design stress induced by the tendon force is then almost 140 MPa. This gives an equivalent axial force of 4.1 MN. The design lateral pressure is 0.22 MPa and the stiffener spacing is 1 m. The equivalent line load is then 0.22 MN/m. The effective plate width is approximately 0.9 m. The design satisfies the buckling requirements if the result of all interaction formulae is smaller than 1. The largest value of any of the DNV interaction formulae was 0.90. It should be kept in mind that dynamic effects may lead to larger tendon tension, and hence larger bending moments at the base node connection, than what was checked for here. For bending moments larger than 203 MNm at the pontoon base, the design is no longer in accordance with DNV minimum requirements. This corresponds to an amplification of only 17 % with respect to the estimation made for the static case. In case dynamic effects cause larger bending moments than this, then modifications to the current design is recommended.

An example of such a modification could be redesign of the stiffeners from the current flat bar stiffeners to flanged T-section stiffeners. Another way to improve the design is to have non-uniform stiffener dimensions and wall thickness along the length, making the design increasingly stronger as one moves from the tip to the base of the pontoon, where the bending stresses are largest. Also, having more steel at the bottom of the pontoon than at the top will improve the design's ability to resist compressive stresses at the bottom of the pontoon. Last, in general, having larger pontoon height and width at the base than at the tip could also help reducing the bending stress at the base due to increased area moment of inertia. However, such a change is not in accordance with the dimensions defined in Table 2-1.

Next, a scantling design will be made for the main column.

3.3 Scantling design for the main column

The available main column steel was distributed over the walls, which are taken to be constant over the depth, a number of ring stiffeners and three vertical rectangular bulkheads stretching from the base node to the tower connection at the top of the main column. The vertical bulkheads were included in the design to provide more bending stiffness to the main column, which is subject to large bending moments due to its connection with the wind turbine tower. Section 3.5 in DNV-RP-C202, which treats buckling of ring stiffened shells, was used as guideline for the design. This means that shell buckling, panel ring buckling and column buckling were checked. The goal of this paragraph is to present the essentials of the scantling procedure of the main column. The procedure involves a large number of equations from the DNV-RP-C202, and to avoid redundancy, some of those equations will not be repeated here.

Similarly to the scantling design procedure for the pontoons, the first step in the design loop is to assign initial weight ratios and an initial number of ring stiffeners and bulkheads.

Paragraph 3.3.1 treats the calculation of the design equivalent von Mises stress. Paragraph 3.3.2 treats the shell buckling check. Paragraph 3.3.3 treats the panel ring buckling check. Paragraph 3.3.4 treats the column buckling check, and paragraph 3.3.5 presents the final scantling design for the main column in terms of tables and figures.

3.3.1 Calculation of design equivalent von Mises stress

For the shell to be stable and pass the buckling checks, it is required that the design equivalent von Mises stress is smaller than the design buckling strength. The following formula was used to calculate the design equivalent von Mises stress

$$\sigma_{j,Sd} = \sqrt{(\sigma_{a,Sd} + \sigma_{m,Sd})^2 - (\sigma_{a,Sd} + \sigma_{m,Sd})\sigma_{h,Sd} + \sigma_{h,Sd}^2 + 3\tau_{Sd}^2} \quad (3-10)$$

where

$\sigma_{a,Sd}$: Design axial stress in the shell due to axial forces (paragraph 3.3.1.1)

$\sigma_{h,Sd}$: Design circumferential stress in the shell due to external pressure (paragraph 3.3.1.2)

$\sigma_{m,Sd}$: Design bending stress in the shell due to global bending moment (paragraph 3.3.1.3)

τ_{Sd} : Design shear stress in the shell due to shear force (paragraph 3.3.1.3)

3.3.1.1 Design axial stress in the shell due to axial forces

$\sigma_{a,Sd}$ was calculated by dividing the combined weight of the NREL 5-MW rotor and nacelle, the OC3 Hywind tower and the weight of the part of the TLP hull which is above the still water level (Table 3-1) by the cross sectional area of the main column wall. The total mass of these components was found to be 841 000 kg.

The design axial stress in the shell due to axial forces is then found from

$$\sigma_{a,Sd} = \frac{841,000 * 9.81}{2 \pi r_{mc} t_{mc}} \quad (3-11)$$

Where r_{mc} and t_{mc} are the main column radius and wall thickness respectively.

3.3.1.2 Design circumferential stress in the shell due to external pressure

$\sigma_{h,Sd}$ was calculated based on the maximum hydrostatic pressure on the main column, which corresponds to the hydrostatic pressure of sea water with density 1025 kg/m³ at the bottom of the main column. The draft of the TLP is 22 meters and the base node is 6 meters high. This means that the draft of the main column is 16 meters. The maximum hydrostatic pressure is then approximately 1.61 bar. The main column will be designed as a ring stiffened cylinder.

Therefore, the membrane stress midway between two ring frames should be used. DNV-RP-C202 explains how to do this.

3.3.1.3 Design bending stress in the shell due to global bending moment and design shear stress in the shell due to shear force

The design bending stress, $\sigma_{m,SD}$, and the design shear stress, τ_{SD} , were estimated from the bending moment and shear force at the main column base due to the combination of a large regular wave and the rotor thrust force at rated wind speed. This gives a rather rough estimation, but is helpful to get an idea of the order of magnitude.

As previously described, the Morison equation was applied to estimate the hydrodynamic load from the regular wave. A time series over one wave period of the total wave forces on the cylinder shows that the force is inertia dominated:

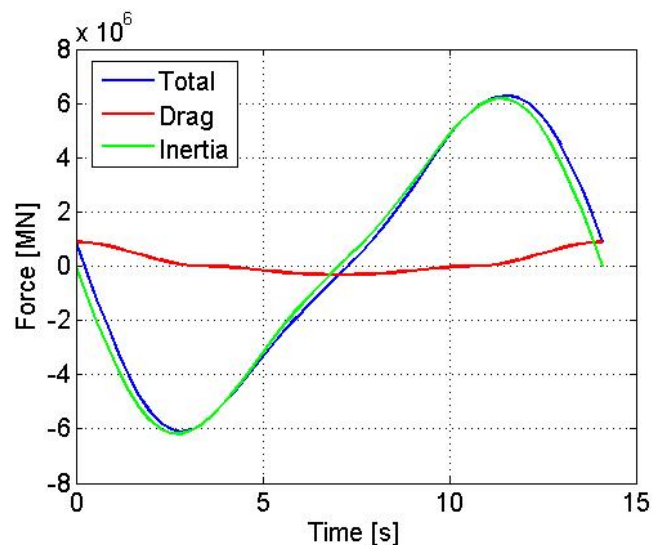


Figure 3-7: Hydrodynamic forces on main column from the regular wave over one wave period calculated with the Morison equation

The maximum total hydrodynamic inline force from the regular wave is 6.29 MN, while the maximum bending moment at the base is 55.41 MNm. These values were taken to be the wave design shear force and the wave design bending moment respectively and are used to calculate the design shear stress and the design bending stress due to waves:

$$\tau_{Sd,wave} = \frac{6.29 * 10^6}{2 \pi r_{mc} t_{mc}} \quad (3-12)$$

$$\sigma_{m,Sd,wave} = \frac{(55.41 * 10^6) r_{mc}}{I_{mc}} \quad (3-13)$$

where I_{mc} is the moment of inertia of the cylinder cross section.

The NREL 5-MW wind turbine has a rotor thrust force at rated speed of 660 kN. This was taken to be the wind design shear force. The hub height is 90 meters, which means that the distance from the hub to the base of the main column is 106 meters. The wind design bending moment is then 76.56 MNm. These values were used to calculate the design shear stress and the design bending stress due to wind:

$$\tau_{Sd,wind} = \frac{0.66 * 10^6}{2 \pi r_{mc} t_{mc}} \quad (3-14)$$

$$\sigma_{m,Sd,wind} = \frac{(76.56 * 10^6) r_{mc}}{I_{mc}} \quad (3-15)$$

The total design shear stress and bending stress due to the combination of wind and waves were estimated by summing up the two contributions:

$$\tau_{Sd} = \tau_{Sd,wave} + \tau_{Sd,wind} \quad (3-16)$$

$$\sigma_{m,Sd} = \sigma_{m,Sd,wave} + \sigma_{m,Sd,wind} \quad (3-17)$$

It is worth noting that torsional moments also can contribute to the design shear stress. Torsional moments were not considered in this initial design, and this introduces additional uncertainty regarding the actual design shear stress.

3.3.2 Shell buckling check

Shell buckling was checked by comparing the design equivalent von Mises stress to the design characteristic buckling strength of the shell. To find the design characteristic buckling strength of the shell, one first needs to find the characteristic buckling strength of the shell. This depends on the reduced shell slenderness and the yield strength, f_y :

$$f_{ks} = \frac{f_y}{\sqrt{1 + \bar{\lambda}_s^4}} \quad (3-18)$$

The reduced shell slenderness depends on the previously described design stresses, the yield strength of the material and the elastic buckling strengths components of circular cylindrical shells subjected to axial compression forces, global bending moments, lateral pressure, and torsional moments and shear forces respectively, $f_{Ea}, f_{Em}, f_{Eh}, f_{E\tau}$:

$$\bar{\lambda}_s^2 = \frac{f_y}{\sigma_{j,Sd}} \left[\frac{\sigma_{a,Sd}}{f_{Ea}} + \frac{\sigma_{m,Sd}}{f_{Em}} + \frac{\sigma_{h,Sd}}{f_{Eh}} + \frac{\tau_{Sd}}{f_{E\tau}} \right] \quad (3-19)$$

These elastic buckling strength components depend on a reduced buckling coefficient which is calculated by using the buckling coefficients in table 3-2 in DNV-RP-C202. Thus, with the elastic buckling strength components the reduced slenderness and the characteristic buckling strength of the shell can be found.

The design characteristic buckling strength, f_{ksd} , of the shell is now found by applying a material factor to the characteristic buckling strength of the shell, f_{ks} . This material factor is determined by the aforementioned reduced slenderness. The final design characteristic buckling strength is then compared to the design equivalent von Mises stress, $\sigma_{j,Sd}$. In general, the stability requirement is satisfied if

$$\sigma_{j,Sd} \leq f_{ksd} \quad (3-20)$$

However, because of the uncertainty related to the design bending stress, $\sigma_{m,Sd}$, and the design shear stress, τ_{Sd} , it was instead attempted to find a design which maximizes the following ratio:

$$\zeta_1 = \frac{f_{ksd}}{\sigma_{j,Sd}} \quad (3-21)$$

Of course, the design does not satisfy the stability requirement if this ratio is smaller than one.

3.3.3 Panel ring buckling check

Panel ring buckling is avoided by proportioning the ring frames such that they satisfy minimum requirements to the cross sectional area and the effective moment of inertia.

The minimum required cross sectional area is defined as

$$A_{req} \geq \left(\frac{2}{Z_i^2} + 0.6 \right) s t_{wall} \quad (3-22)$$

Here, s is the distance between the ring frames, t_{wall} is the wall thickness and Z_i is a curvature parameter. The curvature parameter in turn depends on s , t_{wall} , the Poisson's ratio and the radius of the cylinder. Thus, the required area of the ring frames is governed by two design parameters, namely the distance between the ring frames and the wall thickness.

In general, the minimum required effective moment of inertia is defined by

$$I_R = I_x + I_{xh} + I_h \quad (3-23)$$

The design parameters that control I_x are mainly s and t_{wall} . I_{xh} is also controlled by t_{wall} and s . I_h depends on a number of variables. Among these, the most significant design parameters are s and t_{wall} , and the dimensions of the ring frame itself. The ring frame was designed as a flanged T-stiffener. As with the pontoon stiffeners, the DNV local buckling constraint was applied. For flanged stiffeners this requirement is:

$$h_w < 1.35 t_w \sqrt{\frac{E}{f_y}} \quad (3-24)$$

Also, it was made sure that there is some spacing between the flanges of two neighboring ring frames to allow for welding.

Following the same logic as before, it is attempted to maximize the following ratio.

$$\zeta_2 = \frac{I_{ring\ frame}}{I_R} \quad (3-25)$$

Again, if this ratio is smaller than one, the effective moment of inertia of the ring frames is definitely too small.

3.3.4 Column buckling check

Column buckling should be assessed if

$$\left(\frac{k_{buckling} L_C}{i_C}\right)^2 \geq 2.5 \frac{E}{f_y} \quad (3-26)$$

Here, $k_{buckling}$ is the effective length factor, L_C is the total cylinder length, i_C is the radius of gyration of the cylinder section, E is the modulus of elasticity and f_y is the yield strength. The effective length factor is set equal to 2 because the cylinder is approximated as fixed on one side (the bottom) and free on the other side (the top). The radius of gyration is the only variable here. It is determined by the cylinder wall thickness. Again, it is decided to try to maximize the ratio of the two instead of just complying with the minimum requirement:

$$\zeta_3 = \frac{2.5 \frac{E}{f_y}}{\left(\frac{k_{buckling} L_C}{i_C}\right)^2} \quad (3-27)$$

If this ratio is smaller than one, then an assessment of column buckling is definitely required.

3.3.5 Final scantling design for main column

To summarize, the design procedure was as follows:

1. Assign weight ratios and number of ring stiffeners and bulkheads
2. Determine the design stresses, stiffener cross section properties and thickness of cylinder wall and bulkheads.
3. Check buckling stability

The buckling checks were carried out for various combinations of weight ratios and numbers of ring stiffeners and bulkheads. A combination that gives high values for the aforementioned ratios, ζ_1 , ζ_2 and ζ_3 , was chosen in the final scantling design for the main column. Also, a distance of at least 2 meters between two neighboring stiffener flanges was set as a requirement to allow for fabrication. It was found that the ratio ζ_1 , which is related to shell buckling, is strongly dependent on the weight ratio assigned to the main column wall, while ratio ζ_3 , which is related to column buckling, was a lot less sensitive to varying weight ratios. The ratio ζ_2 on the other hand was, as one could expect, very sensitive to the weight ratio assigned to the ring frames. As with the pontoon bulkheads, the bulkhead weight ratio and the number of bulkheads for the main column was chosen such that the bulkhead thickness was smaller than 1 inch.

Table 3-8 and Table 3-9 summarizes the final scantling design for the main column. Also, the final corresponding design stresses are presented here.

Table 3-8: Main column weight ratios and number of ring stiffeners and vertical bulkheads in the final scantling design

Component	Weight ratio	Quantity
Cylinder wall	0.75	N/A
Ring stiffeners	0.1	8
Vertical bulkheads	0.15	3

Compared to the weight ratios of the pontoon (Table 3-3), it is seen that the main column has a very large proportion of the steel assigned to the walls and bulkheads, and that the stiffeners are accounting for a very low proportion of the total steel.

Table 3-9: Dimensions of main column components

Component dimensions	[cm]
Cylinder wall thickness	5.27
Bulkhead thickness	2.20
Stiffener web thickness	1.68
Stiffener web height	63.37
Stiffener flange thickness	1.68
Stiffener flange width	82.39

The bulkheads of the main column have the same thickness as the bulkheads of the pontoons. The main column wall is more than twice as thick as the pontoon walls. This design gives a ring stiffener spacing of 2.9 meters. The gap between the flanges of two neighboring stiffeners is approximately 2.1 meters.

Because the ring stiffeners in the main column are flanged, the stiffener web height is allowed to be relatively large compared to the web thickness. The longitudinal stiffeners and girders in the pontoon design had a stricter constraint to the relationship between these two dimensions because they are shaped as flat bars. This was made use of in the design and can be seen when comparing the numbers in Table 3-6 and Table 3-7 with the ring stiffener dimensions in Table 3-9.

Table 3-10 shows the design stresses for this design. Note that compressive stresses are negative and tensile stresses are positive.

Table 3-10: Design stresses for main column scantling design

Design stresses	[MPa]
$\sigma_{a,Sd}$	-3.56
$\sigma_{m,Sd}$	-16.46
$\sigma_{h,Sd}$	-21.46
τ_{Sd}	3.00
$\sigma_{j,Sd}$	21.41

The bending stress due to bending moments and the circumferential stress due to external (hydrostatic) pressure are the most significant contributors to the design equivalent von Mises stress. Still, these are much smaller than the estimated tendon induced bending stress in the pontoon, which was roughly 140 MPa even without accounting for dynamic amplification. Based on this, one can conclude that large tendon tensions may actually account for the largest stresses in the whole TLPWT hull.

The values of the buckling ratios ζ_1 , ζ_2 and ζ_3 , which are related to shell buckling, effective moment of inertia of the ring frames and column buckling are given in Table 3-11. The larger the ratio, the stronger the design relative to the minimum requirements set by DNV.

Table 3-11: Buckling ratios indicating strength of the main column scantling design

Ratio	
ζ_1	3.81
ζ_2	17.66
ζ_3	18.88

There turned out to be some room for variation in the main column scantling design and still meet the requirements set by DNV-RP-C202. This could indicate that the amount of steel in the main column can be reduced. On the other hand, the estimations of design bending and shear stresses are quite rough and should be assessed in more detail before any material reduction is actually considered. Figure 3-8 gives a visualization of the design.

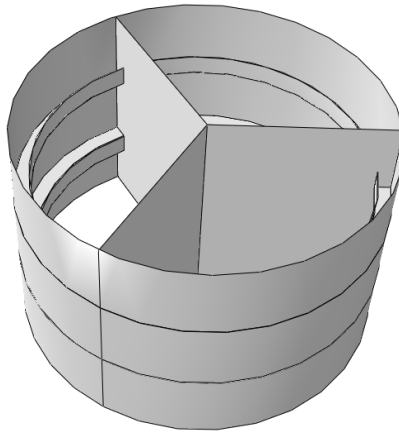


Figure 3-8: Main column scantling design showing the wall, the vertical bulkheads and the ring frames

Figure 3-9 shows the complete main column design

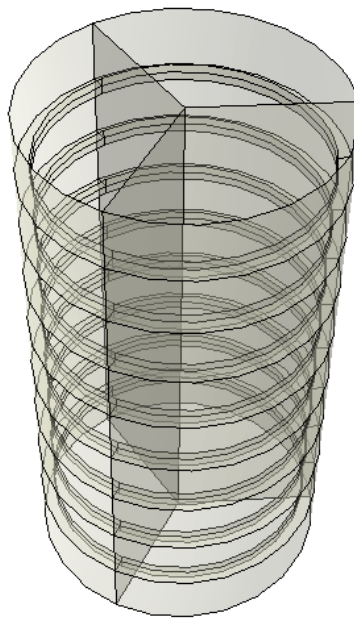


Figure 3-9: Complete main column scantling design

Figure 3-10 shows the complete TLP assembly.

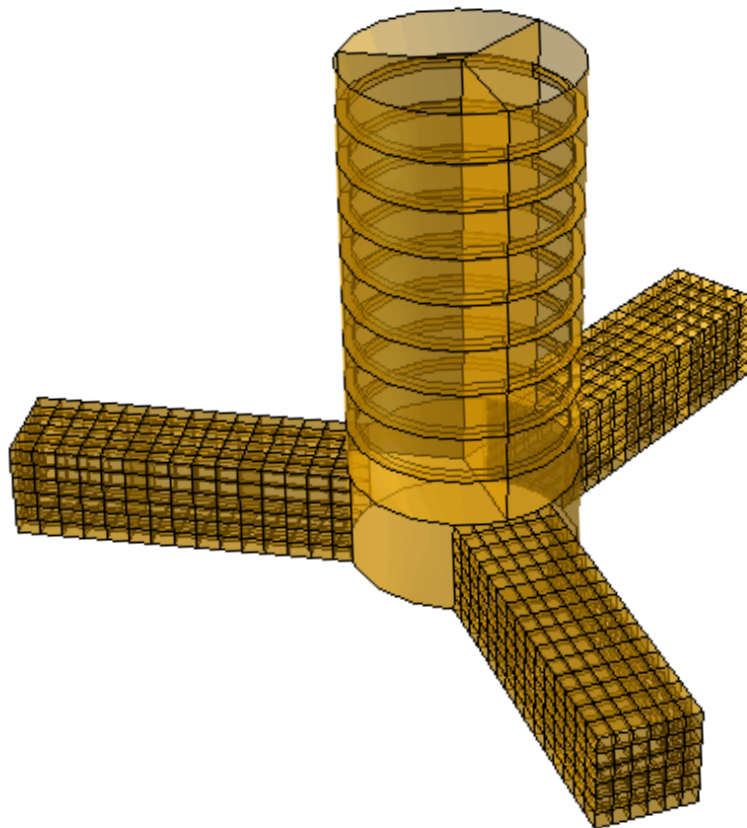


Figure 3-10: Complete TLP design with bulkheads, stiffeners and girders

In the next chapter, the mass distribution and stiffness of the pontoons and main column are estimated to generate an equivalent beam model of the hull.

4 Equivalent beam model for the hull

For convenience, the scantling design made for the pontoons and main column in chapter 3 will be referred to as the *flexible design* throughout the rest of this report. Thus, there is a reference design and there is a flexible design. The flexible design has stiffeners, girders and bulkheads, while the reference design does not. To investigate the influence of the hull elasticity on the global dynamic behavior of the TLPWT, the hull's stiffness and mass distribution are needed. More specifically, the stiffness and mass distributions of the pontoons and main column are needed. As already mentioned, the base node was kept rigid. From now on, the main column and pontoons of the flexible design will be referred to as the flexible main column and pontoons. Similarly, the main column and pontoons of the reference design will be referred to as the reference main column and pontoons.

The global dynamic analysis was to be carried out in RIFLEX with a model that describes the whole system by using beam elements. Therefore, a beam model was required for the hull, and it should represent the mass distribution and stiffness of the flexible design. It will be referred to as the *equivalent beam model*, and consists of two different of beams: one beam which describes the flexible pontoons, and one beam which describes the flexible main column. The beam's stiffness was approximated with an equivalent Euler-Bernoulli stiffness which is constant along the beam length. Together with the mass distribution, the equivalent stiffness of each beam define the equivalent beam model. This chapter describes how the equivalent beam model was generated for the flexible design.

The mass distributions were simplified to consist of uniformly distributed masses and concentrated masses. For the equivalent stiffness estimation, FE models of the TLP components were made in the FE analysis software ABAQUS. The FE models include all of the bulkheads, stiffeners and girders which were defined in the scantling design in chapter 3. The equivalent stiffness was found for each part (pontoon and main column) separately. The part was fixed on one side and a load was applied on the other side, mimicking a tip loaded cantilever beam. The deflection at some distance from the fixation plane was then extracted from ABAQUS.

Chapter 4: Equivalent beam model for the hull

Because of the presence of the stiffeners, girders and bulkheads, both the flexible pontoon and main column have a rather irregular cross section along the length. Therefore, verifying the stiffness from the FE model analytically with classical beam theory is difficult. To work around this problem, an FE model was also made for the reference pontoon and main column (Table 2-1). The reference main column has a uniform circular cross section defined by the outer diameter and the equivalent wall thickness. Similarly, the reference pontoon has a uniform square cross section defined by the pontoon height and width, and the equivalent wall thickness. The stiffness of the reference main column and pontoons were then found in the exact same way as for the flexible main column and pontoons. Because of the simplicity of the reference main column and pontoon, these results are much easier to compare with analytical formulae. It was then assumed that if the numerical output from the FE model of the reference pontoon and main column is consistent with beam theory, then so is the numerical output from the FE model of the flexible pontoon and main column. The numerical output from the FE models of the reference main column and pontoon, and the corresponding comparison with elementary beam theory, is presented in Appendix D. Based on this comparison it was decided whether the stiffness estimations for the flexible main column and pontoon were acceptable.

The following is an outline of this chapter.

- Paragraph 4.1 presents the mass distributions of the flexible main column and pontoon estimated with basic engineering simplifications.
- Paragraph 4.2 presents the equivalent bending and torsional stiffness of the flexible main column and pontoon estimated with FE analysis.
- Paragraph 4.3 presents an attempt to analytically estimate the corresponding fundamental natural bending and torsional frequencies.
- Paragraph 4.4 comments on the validity of the estimated equivalent stiffness based on the results in Appendix D.

4.1 Mass distribution of the flexible design

The mass distribution of the flexible pontoon was modelled as a combination of a uniformly distributed mass due to walls, longitudinal stiffeners and transverse girders, and three concentrated masses due to the two bulkheads and the tip plate.

The mass distribution of the flexible main column was modelled as a uniformly distributed mass due to walls, ring frames and vertical bulkheads.

4.1.1 Pontoon mass distribution

The mass due to pontoon side walls and longitudinal stiffeners was modelled as uniformly distributed over the length of the pontoon. Because the girder spacing of 1.4 m is small compared to the total length of the pontoon, the mass due to the girders was also approximated as uniformly distributed over the length. The masses of these components are presented in Table 4-1.

Table 4-1: Masses of pontoon walls, longitudinal stiffeners and girders

Component	Mass [kg]
Walls	84,373
Longitudinal stiffeners	26,514
Transverse girders	18,310

The two bulkheads and the tip plate are located at 7 m, 14 m and 21 m respectively from the connection to the base node. These were modelled as concentrated masses. The masses of these components are presented in Table 4-2.

Table 4-2: Masses of pontoon bulkheads and tip plate

Component	Mass [kg]
Bulkhead 1	6,103
Bulkhead 2	6,103
Tip plate with stiffeners	11,182

Chapter 4: Equivalent beam model for the hull

The final mass distribution of the pontoon beam was thus approximated as a composition of a uniformly distributed mass over the length and three concentrated masses. The three concentrated masses are located at 7 m, 14 m and 21 m from the connection to the base node.



Figure 4-1: Pontoon mass distribution

The total steel mass of one pontoon is approximately 152,600 kg.

4.1.2 Main column mass distribution

The mass due to the main column wall and vertical bulkheads was modelled as uniformly distributed over the height of the main column. Similarly to the transverse girders of the pontoon, the mass due to the main column ring frames was approximated as uniformly distributed over the height. The masses of the three components are presented in Table 4-3.

Table 4-3: Masses of main column walls, ring frames and bulkheads

Component	Mass [kg]
Walls	471,220
Ring frames	62,830
Vertical bulkheads	94,245

The final mass distribution of the main column beam was thus approximated as uniform over the height.



Figure 4-2: Main column mass distribution

The total steel mass of the main column is approximately 628,300 kg.

4.2 Equivalent stiffness of the flexible design derived from FE analysis

Now that the mass distributions have been defined, only the pontoon and main column equivalent stiffness remained before the equivalent beam model was defined. This paragraph intends to give a detailed description of how the equivalent stiffness of the flexible pontoon and the main column were estimated. First, the estimation for the equivalent bending and torsional stiffness of the pontoon are presented. Then, the estimation for the equivalent bending and torsional stiffness of the main column are presented. The ABAQUS FE models are described in detail together with how the tip loaded cantilever beam tests were carried out. The equivalent stiffness was finally derived from the deflection calculated by ABAQUS and elementary Euler-Bernoulli beam theory. Because all of the features of the design are thin walled, a model consisting of only shell elements was assumed to be representative.

The material that was used was steel with a bending stiffness of 210 GPa and a Poisson ratio of 0.3. The material density was not included in the finite element model in order to avoid gravity loads influencing the deflection.

The equivalent bending and torsional pontoon stiffness estimations is presented in paragraph 4.2.1. The equivalent bending and torsional main column stiffness estimations are presented in paragraph 4.2.2. A summary of the findings is given in paragraph 4.2.3.

4.2.1 Pontoon equivalent stiffness

The equivalent bending stiffness of the pontoon was found by orienting the pontoon horizontally, keeping it fixed on one side, applying a vertical load at the free end, and reading off the vertical deflection. The equivalent torsional stiffness was found in a similar way, namely by applying forces at free end which result in pure torsion, and reading off the angular deflection.

The deflection in the bending test was investigated for different mesh sizes to check that the solution converges. It was assumed that if the deflection in the bending test converges, then the

deflection in the torsion test also converges. The mesh sizes used in the bending test were 7 m, 5 m, 3 m and 1 m. The results for each of these meshes are presented in Table 4-4.

Figure 4-3 shows the pontoon meshed with triangular elements of quadratic geometric order and a characteristic mesh size of 1 m. This is the mesh size which was finally used for the derivation of the equivalent bending and torsional stiffness.

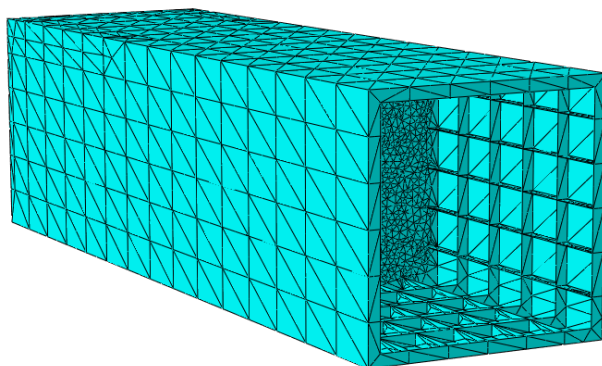


Figure 4-3: Meshed pontoon

4.2.1.1 Pontoon equivalent bending stiffness

The pontoon is 21 meters long. Figure 4-4 shows the cantilever beam test setup. The beam was fixed on the left end and the four concentrated forces are applied in the corners on the right (free) end.

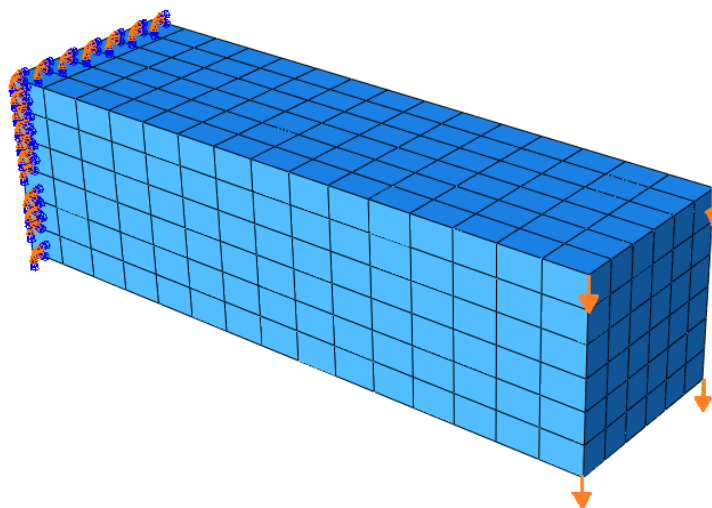


Figure 4-4: Cantilever beam bending test setup of pontoon

The magnitude of each concentrated force is 250 kN, giving a total tip load of 1 MN. Figure 4-5 shows the deformed shape of the pontoon cantilever beam on top of the undeformed shape in the bending test.

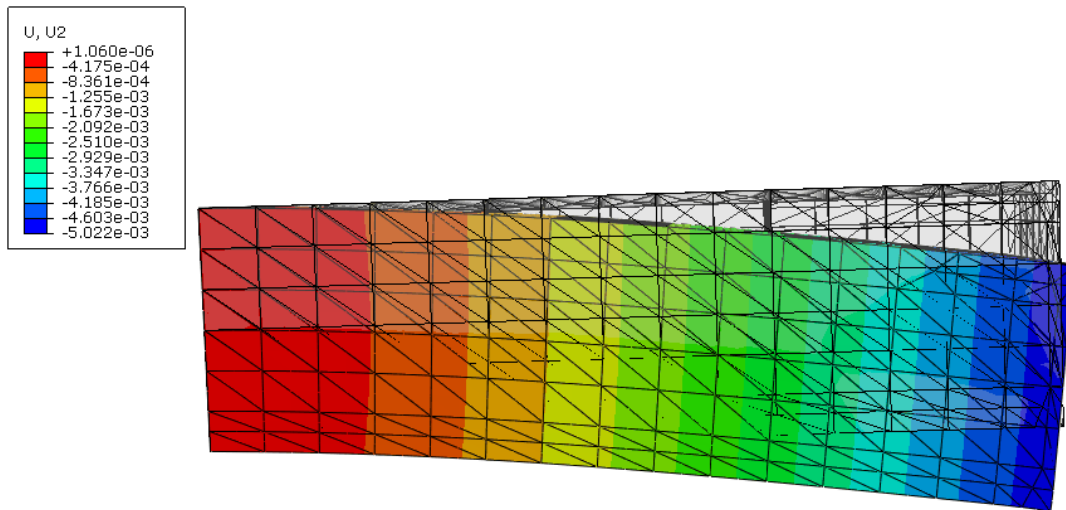


Figure 4-5: Deformed shape of the pontoon cantilever beam on top of the undeformed shape in the bending test

To derive an equivalent bending stiffness, the vertical deflection at the middle of the beam was found and the analytical formula for a tip loaded cantilever Euler-Bernoulli beam was solved with respect to EI :

$$\delta = \frac{P_{load}x^2}{6EI} (3L_{beam} - x) \tag{4-1}$$

Here, P_{load} is the tip load, which in this case equals 1 MN. L_{beam} is the length of the beam and equals 21 m. The middle then corresponds to a vertical line at $x=L_{beam}/2=10.5$ m. The vertical displacement of a node which is located at the middle of this line on the undeformed beam was used for the reverse calculation of the equivalent bending stiffness. Table 4-4 shows the vertical displacement of the corresponding node for all of the aforementioned mesh sizes.

Table 4-4: Pontoon vertical displacement at $x=L_{beam}/2$ for various mesh sizes

Characteristic mesh size [m]	Vertical displacement at $x=L_{beam}/2$ [mm]
7	1.74977
5	1.75059
3	1.75103
1	1.75122

Chapter 4: Equivalent beam model for the hull

The values in the table indicate that the solution converges as the difference in the displacement found for two subsequent mesh sizes is decreasing as the mesh is refined. It also shows that the displacement at the middle of the beam is almost the same for the various mesh sizes. Based on this, the characteristic mesh size of 1 m was assumed to give a result of sufficient accuracy.

The bending stiffness which corresponds to a vertical deflection of 1.75 mm at the middle of the beam is 551 GNm². To get an idea of how representative this bending stiffness is for other points on the pontoon beam, the displacement at $x=3L_{beam}/4$ was back calculated with equation 4-1 by using the estimated equivalent stiffness. This displacement was then compared to the corresponding displacement calculated by ABAQUS. At this distance from the wall ABAQUS computed a displacement of 3.25 mm. The analytical solution for the displacement in this point with the estimated equivalent bending stiffness is 3.54 mm. Thus, at $x=3L_{beam}/4$, the estimated equivalent bending stiffness results in an overestimated displacement with an error of almost 9 % with respect to the numerical solution.

4.2.1.2 Pontoon equivalent torsional stiffness

To find an equivalent torsional stiffness, the characteristic mesh size of 1 m was used. Again, triangular elements of quadratic geometric order were used. Figure 4-6 shows the test setup with one force applied at the center of the bottom edge and one force applied at the center of the top edge of the free end.

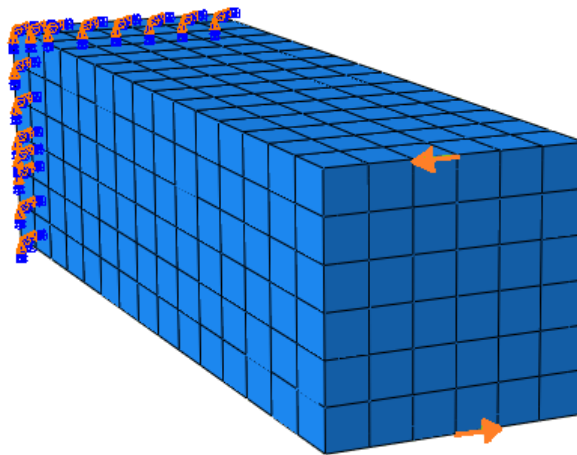


Figure 4-6: Cantilever beam torsion test setup of pontoon

The magnitude of the applied forces was 5 MN, giving a torque of 30 MNm. Figure 4-7 shows the deformed shape of the pontoon cantilever beam on top of the undeformed shape in the torsion test.

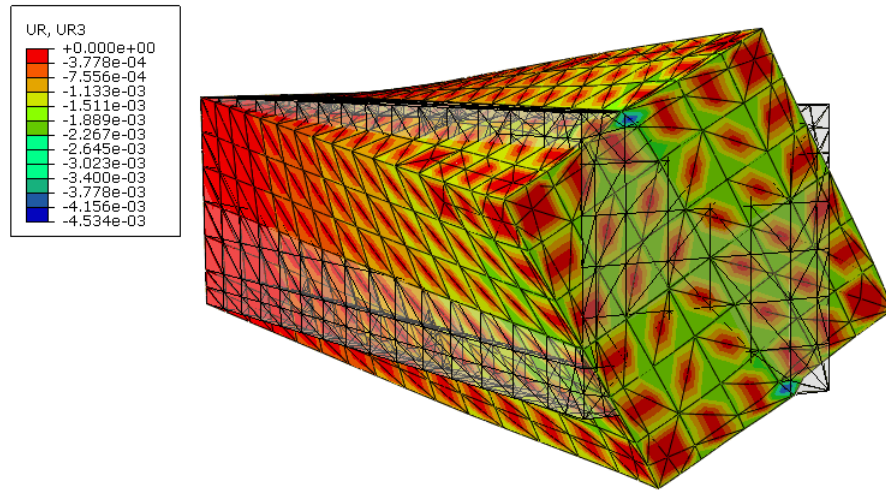


Figure 4-7: Deformed shape of the pontoon cantilever beam on top of the undeformed shape in the torsion test

The deflection of the same node as in the bending test was investigated. Its rotation about the axis going in the longitudinal direction of the pontoon is 0.00083 radians. This twisting angle was used to derive the equivalent torsional stiffness, JG , from the following formula:

$$\theta = \frac{T_{load}x}{JG} \quad (4-2)$$

Here, T_{load} is the applied torque, x is 10.5 m again and θ is the twisting angle. The torsional stiffness which corresponds the computed twisting angle and the applied torque is 380 GNm^2/rad .

Substituting this torsional stiffness back into equation 4-2 and solving for the twisting angle at $x=3L_{beam}/4$ results in a deflection angle of 0.00124 rad. The twisting angle computed by ABAQUS in this point was 0.00130 rad. The estimated equivalent torsional stiffness of 380 GNm^2/rad then results in an underestimated twisting angle with an error of almost 5 % with respect to the numerical solution at $x=3L_{beam}/4$.

4.2.2 Main column equivalent stiffness

The equivalent bending and torsional stiffness of the main column were found in the same way as for the pontoon. Based on the results for the deflection of the pontoon in the bending test, it was assumed that a characteristic mesh size of 1 m is sufficient here too. Again, triangular elements of second geometric order were used. The mesh is shown in Figure 4-8.

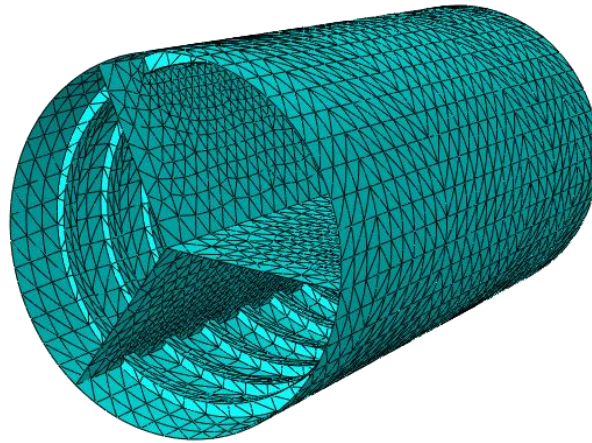


Figure 4-8: Meshed main column

4.2.2.1 Main column equivalent bending stiffness

The test setup of the main column was similar to that of the pontoon, as shown in Figure 4-9. The load was applied at the center of the free end, which corresponds to the intersection point of the three bulkheads. The deflection may depend on how the bulkheads are oriented with respect to the direction of the force. Two different cases were therefore tested: The first case was where one bulkhead is oriented in the same direction as the force, while the second case was where no bulkheads are oriented in the same direction as the force. To be conservative the case which gave the largest deflection was used to estimate the equivalent bending stiffness.

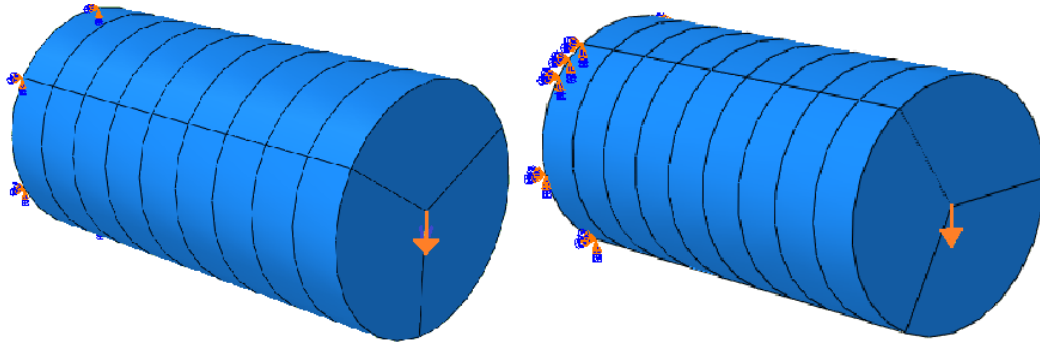


Figure 4-9: First (left) and second (right) cantilever beam bending test setup of main column

Thus, the difference between the two tests was the orientation of the bulkheads relative to the direction of the force.

The magnitude of the load was 5 MN. Figure 4-10 shows the deformed shape of the main column cantilever beam on top of the undeformed shape for the first load case. The deformed shape for the second test case looked very similar. To avoid redundancy, only the deflection for the first test case is depicted here.

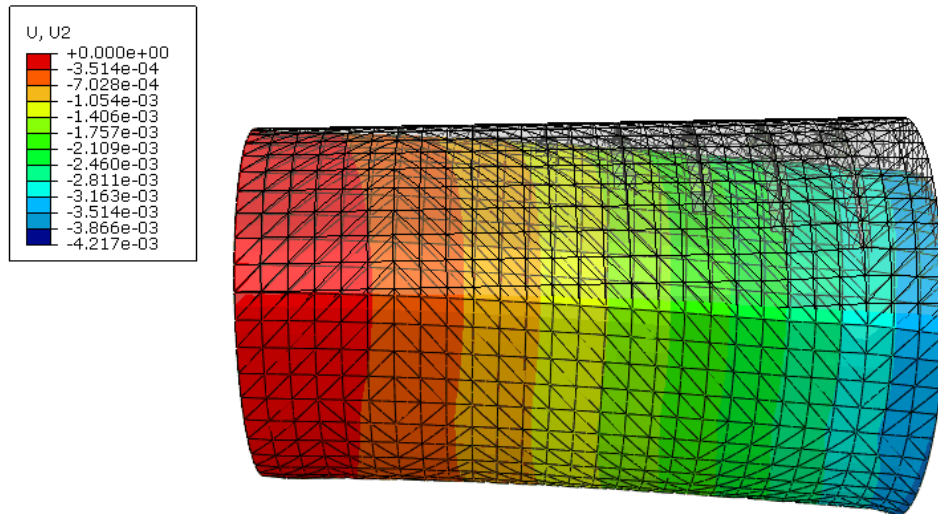


Figure 4-10: Deformed shape of the main column cantilever beam on top of the undeformed shape in the first bending test

The vertical displacement of the nodes at the middle of the beam in the first bending test was 1.24 mm, while it was 1.26 mm in the second bending test. The largest of these gives an equivalent bending stiffness of 7265 GNm².

Substituting this bending stiffness back into equation 4-1 and solving for the vertical displacement at $x=3L_{beam}/4$ gives a value of 2.55 mm. The displacement computed by ABAQUS in this point was 2.27 mm. So the estimated equivalent bending stiffness of 7265 GNm² results in an overestimated deflection with an error of approximately 12 % at $x=3L_{beam}/4$.

4.2.2.2 Main column equivalent torsional stiffness

To apply a torque, three concentrated forces were applied at the edge of the free end. The forces were directed such that they gave a resultant force equal to zero and only caused pure torsion.

Figure 4-11 shows the test setup with the applied forces.

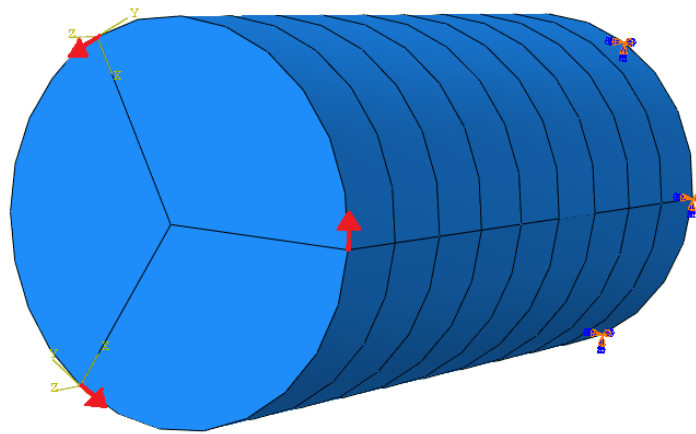


Figure 4-11: Cantilever beam torsion setup for main column

The magnitude of each force was 5 MN, giving a torque of 105 MNm. Figure 4-12 shows the deformed shape of the main column cantilever beam on top of the undeformed shape.

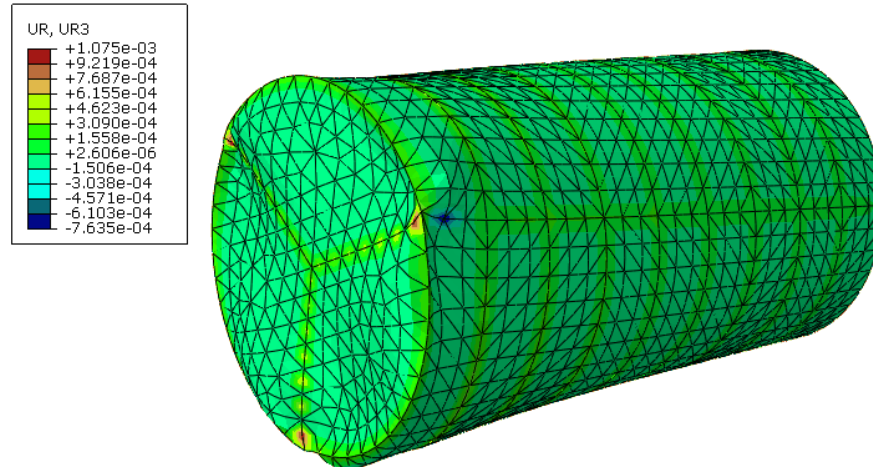


Figure 4-12: Deformed shape of the main column cantilever beam on top of the undeformed shape in the torsion test

The deflection of the same node as in the bending test was investigated. Its rotation about the axis going in the longitudinal direction of the pontoon was 0.00015 radians. This twisting angle corresponds to an equivalent torsional stiffness of 9100 GNm²/rad.

Substituting this torsional stiffness back into equation 4-2 and solving for the twisting angle at $x=3L_{beam}/4$ gives an angle of 0.00023 rad. The twisting angle computed by ABAQUS in this point was 0.00018 rad. Thus, the estimated equivalent torsional stiffness of 9100 GNm²/rad results in an overestimated twisting angle with a rather large error of more than 25 % with respect to the numerical solution. Because of this large error, the same comparison was made at $x= L_{beam}/4$. There, the torsional stiffness of 9100 GNm²/rad resulted in an underestimated twisting angle with an error of 7 % with respect to the numerical solution.

It seems that the equivalent torsional stiffness of 9100 GNm²/rad, which was derived based on the twisting angle at $x= L_{beam}/2$, results in overestimated twisting angles when approaching the free end of the beam where the torque was applied. It also seems to result in underestimated twisting angles as when approaching fixed end. This could be partly caused by nonlinear effects in the vicinity of the applied load, which can be seen in the twisting deformation shape in Figure 4-12. On the other hand, the twisting angle deviation of the pontoon at $x=3L_{beam}/4$ was much lower, even if similar effects can be seen in the twisting deformation shape of the pontoon in Figure 4-7.

4.2.3 Summary of equivalent stiffness estimations

To summarize, the equivalent bending and torsional stiffness were found by carrying out tip loaded cantilever beam tests with the FE models in ABAQUS and looking at the deflection at a distance $x = L_{\text{beam}}/2$ from the fixed end. Table 4-5 summarizes the magnitudes of the loads, deflections and derived equivalent stiffness in both bending and torsion.

Table 4-5: Summary of load magnitude, deflection computed in ABAQUS and derived equivalent stiffness for the pontoons and main column of flexible design

	Pontoon ($L_{\text{beam}}=21$ m)	Main column ($L_{\text{beam}}=26$ m)
Bending load	1 MN	5 MN
Torsion load	30 MNm	105 MNm
Deflection in bending at $x = L_{\text{beam}}/2$	1.75 mm	1.26 mm
Deflection in torsion at $x = L_{\text{beam}}/2$	0.00083 rad	0.00015 rad
Bending stiffness	551 GNm ²	7265 GNm ²
Torsional stiffness	380 GNm ² /rad	9100 GNm ² /rad

Calculating the deflections at $x=3L_{\text{beam}}/4$ by substituting the derived equivalent stiffness into the equation for a tip loaded cantilever Euler-Bernoulli beam resulted in the following errors with respect to the numerical results.

Table 4-6: Error in calculated deflection at $x=3L_{\text{beam}}/4$ with respect to numerical solution

	Pontoon	Main column
Error in vertical displacement	9 % (overestimated)	12 % (overestimated)
Error in twisting angle	5 % (underestimated)	27 % (overestimated)

These errors indicate that the derived equivalent beam stiffness are not able to accurately represent the actual stiffness along the whole length of each part. An improvement could be made by using beam elements which allow for shear deformations and/or stiffness which is not constant along the length.

4.3 Natural frequency estimations for the pontoon and main column in the equivalent beam model

With the mass distribution and equivalent stiffness of each part defined, the corresponding isolated fundamental natural frequencies of each part could be estimated.

Natural frequency estimations for the main column equivalent beam

The main column was thus modelled as a beam with a constant mass per length and constant bending and torsional stiffness along the length. A constant mass per length implies that the cross sectional area is also constant along the length. The first natural frequency for transverse vibration of the main column can be estimated as follows [41]

$$\omega_{nat,main.col,bending} = 3.52 \sqrt{\frac{EI}{\rho A_c L_{mc}^4}} = 95 \text{ rad/s} \quad (4-3)$$

Here, A_c is the cross section area, ρ is the material density and L_{mc} is the length of the main column.

The pontoon mass distribution includes three concentrated masses (Figure 4-1). If the two bulkheads are neglected, then the tip plate is the only concentrated mass left. The first natural frequency for transverse vibration can then be estimated with the following equation [41]

$$\omega_{nat,pontoon,bending} = \sqrt{\frac{3EI}{L^3(m_{tip\ plate} + 0.24\rho A_c L_p)}} = 75 \frac{\text{rad}}{\text{s}} \quad (4-4)$$

where L_p is the length of the pontoon. To estimate the torsional natural frequencies, the polar moments of inertia are needed. For the main column this is estimated as the polar moment inertia of a hollow circular cross section [42]

$$I_{polar,main.col} = \frac{\pi}{2} \left(\frac{D_{mc}}{2}\right)^4 - \frac{\pi}{2} \left(\frac{D_{mc} - 2 * t_{mc}}{2}\right)^4 = 112.2993 \text{ m}^4 \quad (4.5)$$

Where D_{mc} and t_{mc} are the diameter and wall thickness of the main column cross section. Note that the bulkheads and the ring frames have been neglected here. The first torsional natural frequency of the main column is now estimated with the following equation

$$\omega_{nat,main.col,torsion} = \sqrt{\frac{JG}{L_{mc} I_{polar,main.col}}} = 56000 \frac{\text{rad}}{\text{s}} \quad (4.6)$$

where JG is the torsional stiffness of the main column.

Natural frequency estimations for the pontoon equivalent beam

The pontoon polar moment of inertia is estimated as that of a hollow rectangular cross section [42].

$$\begin{aligned}
 I_{polar,pontoon} &= \frac{1}{12} (w_p h_p (w_p^2 + h_p^2)) \\
 &\quad - \frac{1}{12} ((w_p - 2t_p)(h_p - 2t_p) ((w_p - 2t_p)^2 + (h_p - 2t_p)^2)) \quad (4.7) \\
 &= 6.0976 \text{ m}^4
 \end{aligned}$$

Where w_p , h_p and t_p are the width, height and wall thickness of the pontoon cross section. Note that the girders, bulkheads and stiffeners have been neglected here.

Neglecting the bulkheads and the tip plate, the first torsional natural frequency of the pontoon becomes

$$\omega_{nat,pontoon,torsion} = \sqrt{\frac{JG}{L_p I_{polar,pontoon}}} = 55000 \text{ rad/s} \quad (4.8)$$

Summary of natural frequency estimations

Table 4-7 summarizes the natural frequency estimations for the equivalent pontoon and main column beams.

Table 4-7: Estimation of first natural frequencies for the equivalent pontoon and main column beams

	Pontoon	Main column
1 st natural frequency in bending	75 rad/s	95 rad/s
1 st natural frequency in torsion	55000 rad/s	56000 rad/s

The estimation of the transverse natural frequency of the pontoon is quite rough for two reasons. First, the bulkheads were neglected. These would cause reduction of the calculated natural frequency. If the tip plate is also neglected, then the natural frequency would be 94 rad/s. So

including the tip plate therefore causes the natural frequency to decrease by approximately 20% (from 94 rad/s to 75 rad/s). The combined mass of the two bulkheads is almost the same as the mass of the tip plate. However, because they are located closer to the base node, the influence of the bulkheads on the natural frequency must be smaller than that of the tip plate. This gives a lower limit to the pontoon transverse natural frequency of approximately 56 rad/s. Second, there may also be axial forces present in the pontoon because of the tendon force applied at the tip of the pontoon. Including this could also influence the natural frequency. Because this is just a simplified first estimation, both the effect of the bulkheads and the effect of the tendon force were neglected. Similarly, the estimation of the torsional natural frequency of the pontoon is also quite rough. Including the bulkheads and the tip plate will give a reduction of the estimation. However, the estimation does give an idea of the order of magnitude.

4.4 Validation of the equivalent stiffness estimations

Because the cross section of the flexible pontoon and main column are not uniform along the length, it is difficult to check the derived equivalent stiffness against beam theory. Instead, FE models were made in ABAQUS for the reference pontoon and main column too, and the same cantilever beam tests as described before were carried out again. The reference pontoon has a simple constant hollow square cross section. The reference main column has a simple constant hollow cylindrical cross section. Their dimensions were presented in Table 2-1. The cross section properties of the reference pontoon and main column were calculated by hand.

Timoshenko beam theory was then used to predict the deflection analytically. This deflection was then compared to the deflection derived from the FE models. It was assumed that the equivalent stiffness estimations found for the flexible main column and pontoon in paragraph 4.2 are assumed to be representative if the stiffness estimations for the reference main column and pontoon are consistent with beam theory. The numerical and analytical results for the reference design main column and pontoon are presented in Appendix D. It was found that the FE solution corresponded well with Timoshenko beam theory's predicted solution. Because of this, it was assumed that also the numerical solutions obtained for the flexible main column and pontoon are representative. Consequently, the estimated equivalent bending and torsional stiffness derived in paragraph 4.2 were assumed to be representative.

The beams which define the equivalent beam model for the hull are thus described by the mass distributions in paragraph 4.1 and the stiffness estimations in paragraph 4.2. A model of the whole TLPWT with elastic hull can now be made in RIFLEX. This model was used to estimate the natural periods and corresponding mode shapes of the system. This is presented in the next chapter.

5 First estimation of the natural periods of the fully-flexible TLPWT

A system's amplitude of vibration increases significantly when excited at a natural frequency. This leads to increased stress amplitudes, which in turn can damage the system and reduce its life. Because of this, it is important to know the natural frequencies. In this chapter, a first estimation is made for the fundamental natural periods and mode shapes of the TLPWT. The hull was modelled with beam elements according to the equivalent beam model presented in the chapter 4. The rest of the structure was modelled with beam elements according to Bachynski's model. Thus, the whole structure, except for the hull base node, was modelled with flexible elements. Therefore, the model is referred to as the *fully-flexible TLPWT*. As already mentioned in paragraph 2.3, RIFLEX was used to model the structure. A visualization of the RIFLEX model is shown in Figure 5-1.

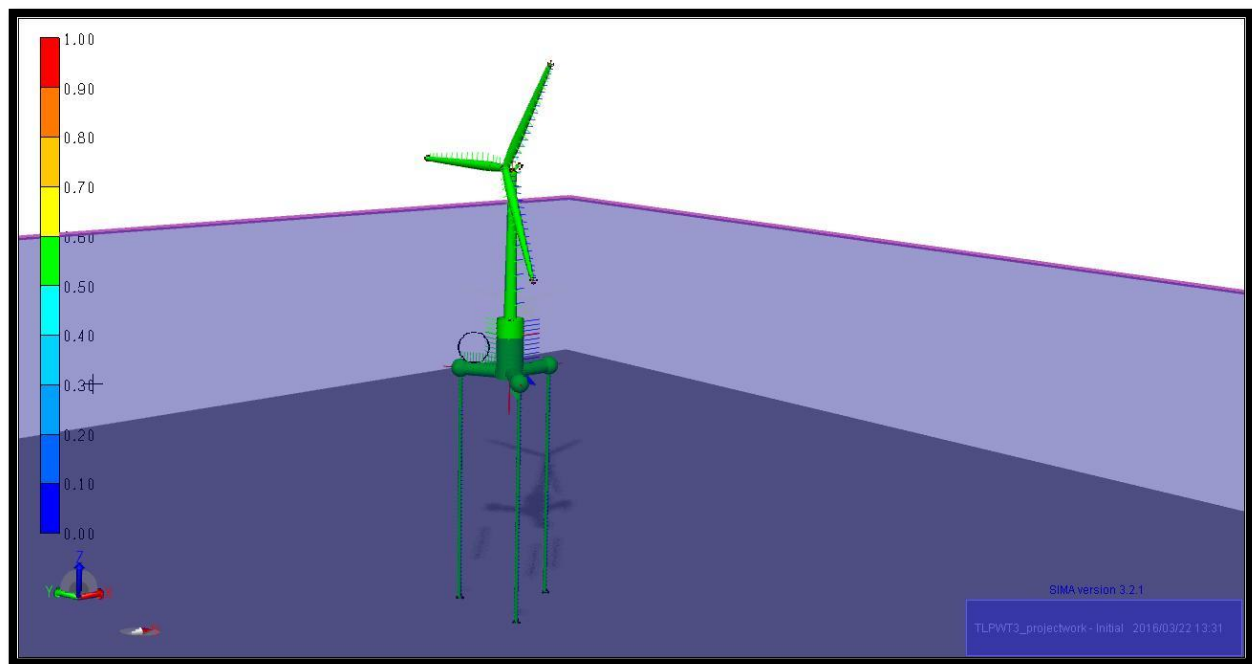


Figure 5-1: RIFLEX model of the fully-flexible TLPWT

RIFLEX has an inbuilt eigenvalue analysis tool which can be used to estimate the natural periods of a large number of modes. This tool was used here.

The following is an outline of this chapter:

- Paragraph 5.1 presents the natural periods of the rigid hull TLPWT which were estimated by Bachynski [9].
- Paragraph 5.2 describes how the added mass was estimated in this eigenvalue analysis.
- Paragraph 5.3 presents the estimated natural periods.
- Paragraph 5.4 presents the corresponding estimated mode shapes.

5.1 Natural periods of the reference TLPWT

It is reasonable to compare the fundamental natural periods of the fully-flexible TLPWT with the corresponding natural periods of Bachynski's rigid hull TLPWT. For convenience, Bachynski's rigid hull TLPWT will be referred to as the *reference TLPWT* from now on. The natural periods of the reference TLPWT are given in Table 5-1 [9]. These were found from simulated decay tests. The tower bending and platform pitch are coupled motions. In a pitch decay test, two frequencies will be present: one frequency for the platform pitch motion and one frequency for the tower bending motion. Therefore, there are two natural periods associated with the pitch motion of the structure. The lower of these is the platform pitch motion, while the higher is the tower bending motion. The sway and roll/bending natural periods are not presented as they are almost equal to the surge and pitch/bending natural periods respectively.

Table 5-1: Natural periods of reference TLPWT

Natural periods of reference TLPWT [s]	
Surge	41.86
Heave	0.60
Pitch/bending	2.76/0.39
Yaw	18.63

Even if the hull of the fully-flexible TLPWT was not modelled as rigid, it is still relatively stiff. Therefore, its natural periods should be somewhat close to the natural periods of the reference TLPWT. An important feature of the eigenvalue analysis in RIFLEX is that it does not include

damping. Therefore, added mass is the only additional parameter which had to be estimated. The added mass estimation is presented in the following paragraph.

5.2 Added mass estimation

It was assumed that the added mass coefficient can be estimated independently for each component with 2-D added mass coefficients. The local coordinate system of the beams in RIFLEX are defined according to Figure 5-2.

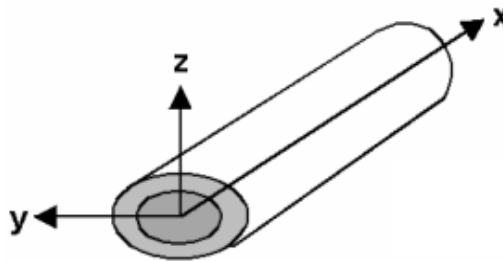


Figure 5-2: Local coordinate system of beams in RIFLEX [43]

The added mass in the x-direction was assumed to be negligible compared to the added mass in the z- and y-directions. Newman [44] gives added mass for 2-D bodies submerged in a fluid with density ρ .

For a circular cross section (main column) with radius a , the added mass per unit length is estimated with

$$m_a = \pi \rho a^2 \quad (5-1)$$

For a square cross section (pontoons) with side length $2a$, the added mass per unit length is estimated with

$$m_a = 4.754 \rho a^2 \quad (5-2)$$

The added mass per unit length for the pontoons and the main column were calculated to be approximately 158,000 kg/m and 44,000 kg/m respectively. Because of symmetry, the added mass in y- and z-direction are the same.

5.3 Natural period estimation with eigenvalue analysis in RIFLEX

The surge, heave, pitch/bending and yaw natural periods of the fully-flexible TLPWT calculated with the inbuilt eigenvalue analysis in RIFLEX are presented in Table 5-2. The column on the right gives the percentagewise increase (+) or reduction (-) with respect to the corresponding natural period of the reference TLPWT (Table 5-1). The natural period of the platform pitch motion, which is coupled to the tower bending motion, could not be isolated and extracted by the RIFLEX eigenvalue analysis. However, the eigenvalue analysis was able to extract the natural period corresponding to the pitch tower bending motion.

Table 5-2: Natural periods of fully-flexible TLPWT calculated with the inbuilt eigenvalue analysis in RIFLEX

Natural periods of fully-flexible TLPWT [s]		Increase/decrease wrt reference TLPWT
Surge	39.70	- 5 %
Heave	0.78	+ 30 %
Pitch/bending	2.79	+ 1 %
Yaw	19.71	+ 5 %

It can be seen that the surge natural period has decreased by roughly 2 s. This indicates that the system has become stiffer in surge and sway. This could partly be explained by how the added mass is estimated, and partly by the absence of damping in the estimation of the natural periods of the fully-flexible TLPWT:

- The natural periods of the reference TLPWT were estimated with frequency-dependent 3-D added mass coefficients, in contrast to the constant 2-D coefficients which were here. This gives a different total mass and therefore influences the natural periods of the system.
- The natural periods of the fully-flexible TLPWT were estimated with the RIFLEX eigenvalue analysis, which neglects damping. However, damping was not neglected in the natural period estimations for the reference TLPWT (decay tests). Including damping in the natural period estimations for the fully-flexible TLPWT would give longer natural periods because damping decreases the oscillation frequency in free vibration.

Because the hull is no longer modelled as rigid, one can expect that the heave natural period increases due to bending of the pontoons. It can be seen from the table that the natural period in heave has increased with 30 % to 0.78 s.

In platform pitch, one may expect the natural period to have an increase similar to the increase in heave natural period. The pitch/bending natural period has increased only slightly with roughly 1% to 2.79 s. The fully-flexible TLPWT and the reference TLPWT have the same tower. The small increase in pitch/bending natural period could therefore indicate that the hull elasticity's influence on the tower bending motion is small.

The yaw natural period has increased with roughly 5 % to 19.71 s. Yaw motion causes bending of the pontoons and twisting of the main column. Because the torsional stiffness of the main column is very high (Table 4-5), the increase in yaw natural period may be assumed to arise mainly from pontoon bending.

When comparing the natural frequencies of the fully-flexible TLPWT with the initial design criteria of Bachynski which were presented in paragraph 2.5, the following conclusions can be drawn:

- The surge and sway natural periods comply with the criteria that they should be longer than 25 s to avoid first-order wave excitation.
- The heave natural period complies with the criteria that it should be shorter than 3.5 s to avoid first-order wave excitation.
- The roll/bending and pitch/bending natural periods comply with the criteria that they should be shorter than 3.5 s in order to avoid first-order wave excitation

5.4 Mode shapes

A Matlab script was provided to read the mode shapes of the whole system from the eigenvalue analysis. The mode shapes are visualized in the following figures from three different views: side view, front view and top view. The blue lines represent the static position of the structure.

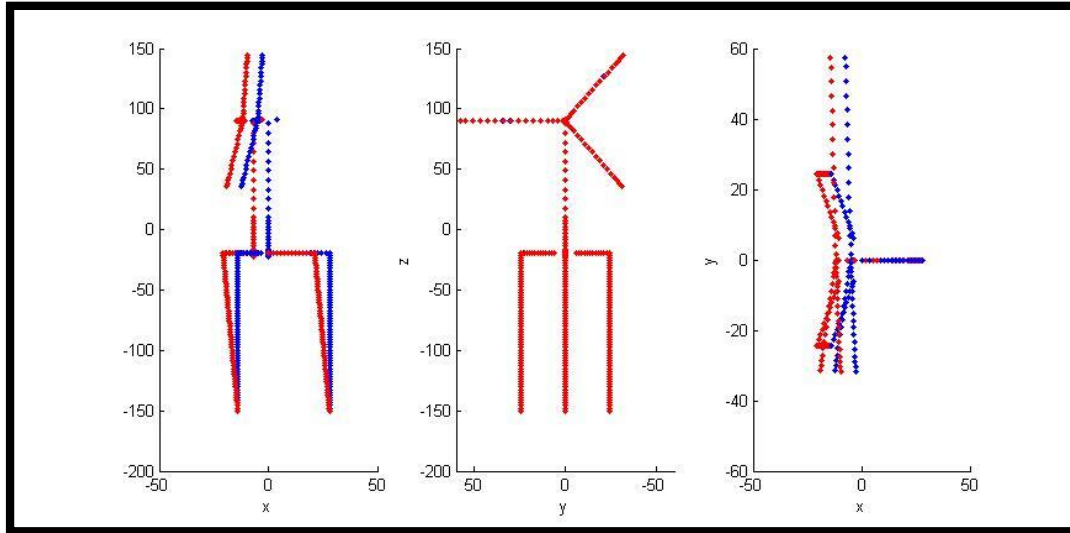


Figure 5-3: Surge fundamental mode shape. Left: side view. Middle: Front view. Right: Top view.

The fundamental mode shape in surge is visualized in Figure 5-3. The shape is best seen from the side view and top view. Because the structure is not moving sideways in surge, the motion cannot be seen from the front view. The side view clearly shows how the tendons are deforming and the tower and rotor is displaced from the static position.

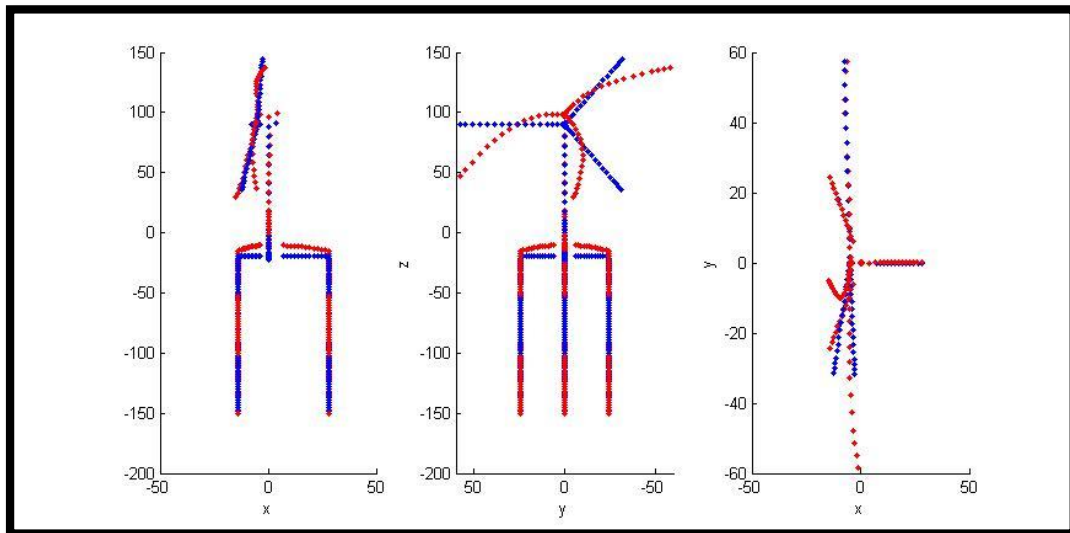


Figure 5-4: Heave fundamental mode shape. Left: side view. Middle: Front view. Right: Top view.

The fundamental mode shape in heave is visualized in Figure 5-4. The shape is best seen from the side view and front view, which clearly show the deformation of the pontoons. Because the heave motion is a vertical motion, the shape cannot be seen from the top view.

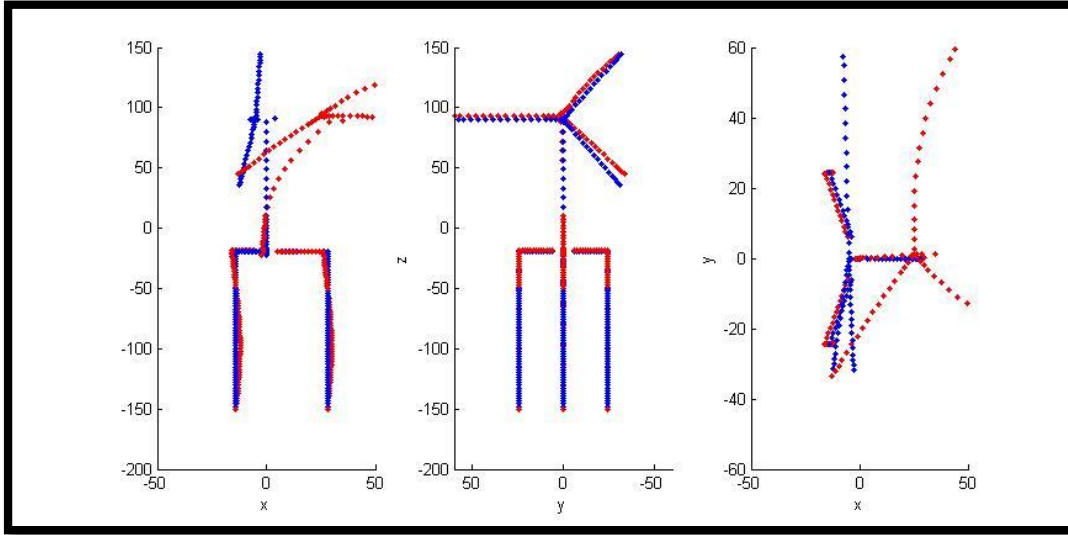


Figure 5-5: Pitch fundamental mode shape. Left: side view. Middle: Front view. Right: Top view.

The fundamental mode shape in pitch is visualized in Figure 5-5. The shape is best seen from the side view and the top view. The side view clearly shows the tower bending shape. Also the tendon bending shape can be seen in the side view.

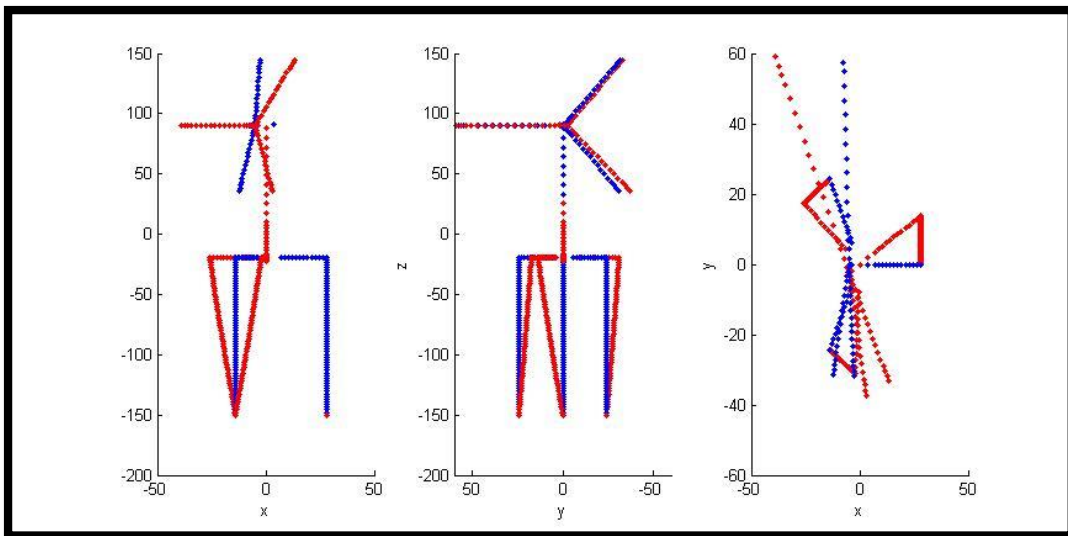


Figure 5-6: Yaw fundamental mode shape. Left: side view. Middle: Front view. Right: Top view.

Chapter 5: First estimation of the natural periods of the fully-flexible TLPWT

The fundamental mode shape in yaw is visualized in Figure 5-6. The shape is best seen from the top view. The top view shows how the pontoons and blades have been displaced due to the rotation of the main column and tower. The side view and front view show the displacement of the tendons which is caused by the displacement of the pontoon tips.

Chapter 6 will show how the RIFLEX beam element model was expanded to an elastic multi-body global analysis model. This was done by including SIMO bodies at selected nodes of the hull which represent frequency dependent 3-D added mass, radiation damping and first-order wave excitation for sections of the hull.

6 Creating the elastic multi-body hull model

As already mentioned in chapter 1, one of the main purposes of this study is the implementation and testing of a new method for including hydrodynamic loads in a global analysis model. The model which was used in chapter 5 is a hydro-aero-servo-elastic coupled global dynamic analysis model which has the ability to include quadratic viscous damping and the previously described 2-D added mass coefficients. However, because the hull of the TLPWT is relatively large, the hydrodynamic loads depend strongly on frequency. Therefore, it is reasonable to assume that the model can be improved by including frequency-dependent added mass, radiation damping and wave excitation from the first-order potential problem. In short, the RIFLEX equivalent beam model of the hull was expanded by implementing radiation and diffraction pressures from potential theory as hydrodynamic load input for sections of the hull by using SIMO-bodies. In this way, the resulting model became an elastic multi-body hull model. A SIMO-body is not required to have any structural mass or volume. In order to not add unwanted weight or buoyancy to the structure, each SIMO-body was given zero mass and zero volume. This chapter is intended to give a thorough stepwise description of how the elastic multi-body hull model was created.

The following is an outline of this chapter.

- Paragraph 6.1 gives an overview of each step in the modelling procedure and how the various software packages were used.
- Paragraph 6.2 describes how the 3-D hydrodynamic panel model of the hull was generated.
- Paragraph 6.3 presents the frequency-dependent added mass, radiation damping and wave excitation computed for the hull as a whole.
- Paragraph 6.4 describes the frequency-dependent added mass, radiation damping and wave excitation computed for the sections of the hull.
- Paragraph 6.5 compares the total hydrodynamic loads from the sections with the computed loads for the hull as a whole.

6.1 Modelling procedure

Various engineering software were used. First, GeniE and HydroD were used to generate a 3-D panel model for the hull. Then, WAMIT was used to solve the radiation and diffraction problems for the whole hull. A Matlab code was written to transform the radiation and diffraction pressures computed in WAMIT into frequency-dependent added mass, radiation damping and wave excitation input for sections of the structure. Last, this section-wise load input was incorporated into the previously presented RIFLEX model by inserting SIMO-bodies at selected nodes. Figure 6-1 shows a schematic of the modelling procedure.

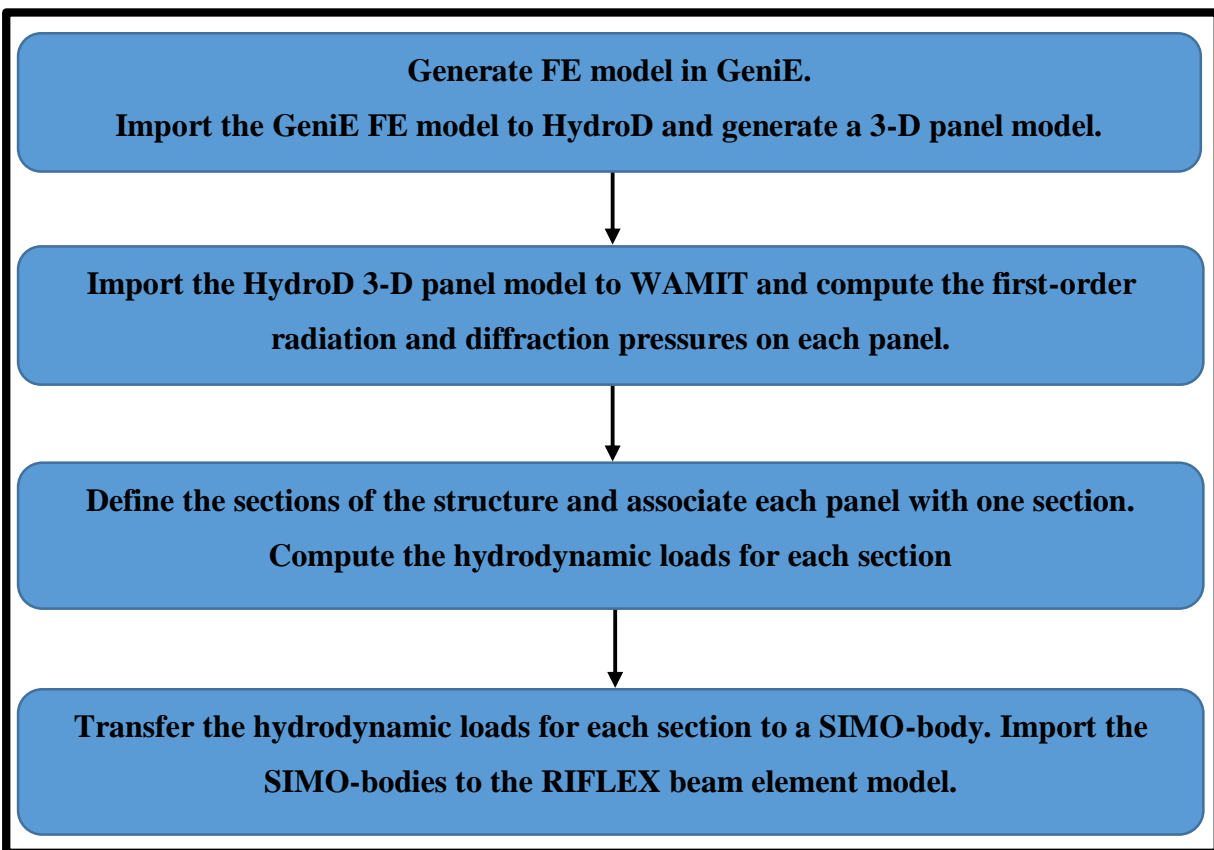


Figure 6-1: Schematic of the modelling procedure

The following paragraphs of this chapter give more details on how each of the steps in the modeling procedure were carried out.

6.2 Generating the 3-D hydrodynamic panel model of the hull

The DNV Sesam package modules GeniE and HydroD were used to generate a 3-D panel model for the hull. In this study, a previously made GeniE FE model was provided up front. This FE model comprises all of the global geometry of the hull, such as the column diameter, pontoon length etc. Defining a mesh was the only task remaining before the model was ready for import to HydroD, where the panel model was generated. A mesh with surface elements of approximately 1 m^2 was chosen. The resulting total number of surface elements was 2664. Importing a meshed GeniE model to HydroD gives a panel model with a number of panels which corresponds to the mesh. Thus, the total number of panels is also 2664. According to Faltinsen, 1000 panels are generally enough [20]. Because there are several structures which are much larger than the TLP in question, 2664 panels was assumed to be sufficient. On the other hand, DNV-RP-C205, which is DNV's recommended practice concerning environmental conditions and environmental loads, suggests that for a low-order panel method (which was used here), the diagonal length of panel mesh should be less than $1/6$ of the smallest wave length in the analysis [45]. The diagonal length of the panels in the model was approximately 1.41 m. According to DNV, the waves in the analysis should then not be shorter than approximately 8.5 m, which gives an upper limit to the wave number of approximately 0.74 rad/m. With the dispersion relation, this gives an upper limit to the wave frequency of roughly 2.7 rad/s. As will be shown later, also waves with wave frequencies higher than this were included in the analysis. Consequently, it is worth keeping in mind that the results for the higher frequencies may be susceptible to lower accuracy than the results for the lower frequencies.

The meshed TLP is shown in Figure 6-2. Because the hull is symmetric with respect to the x-z plane, only half of it needed to be defined and meshed in GeniE.

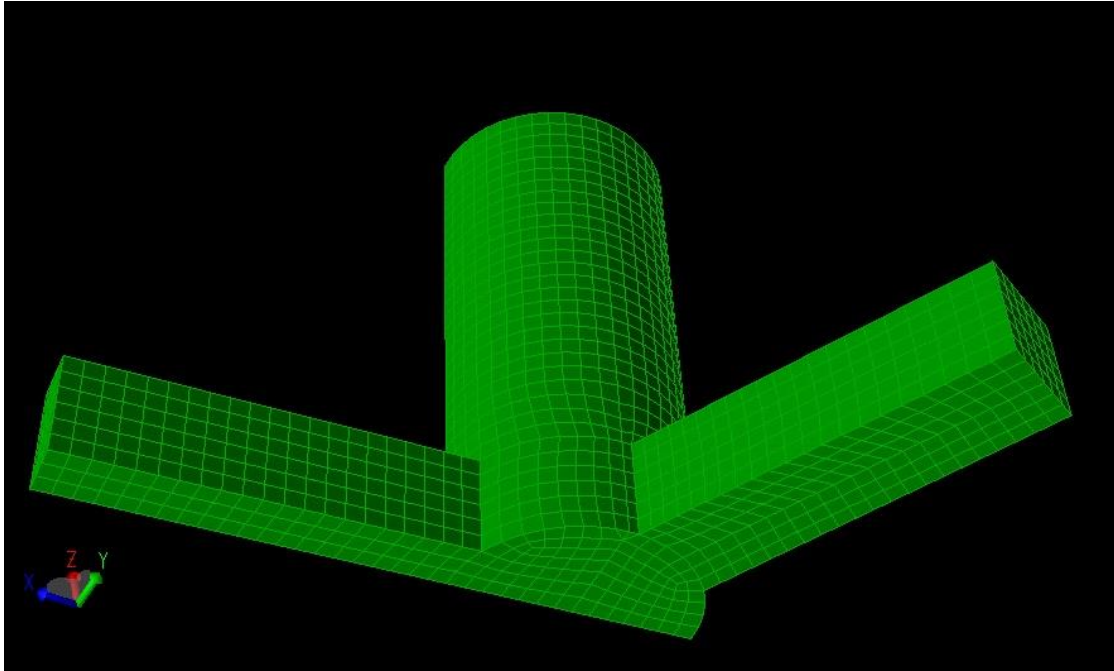


Figure 6-2: Meshed GeniE FE model

Now that a meshed FE model had been created, the hydrodynamic 3-D panel model could be generated in HydroD. However, before doing that, the environment had to be defined in terms of wave frequencies, water depth, density and viscosity. These input variables are needed later when solving the potential problem for the panel model. 59 wave frequencies were chosen, ranging from 0.2 rad/s to 6 rad/s. A water depth of 150 m, a water density of 1025 kg/m^3 and a water kinematic viscosity of $1.19 \cdot 10^{-6} \text{ m}^2/\text{s}$ were chosen.

With the environment defined, the next step is to import the GeniE FE model to HydroD and let HydroD generate the panel model. The geometry and panel distribution are determined by the geometry and mesh of the GeniE FE model. The panel model is shown in Figure 6-3.

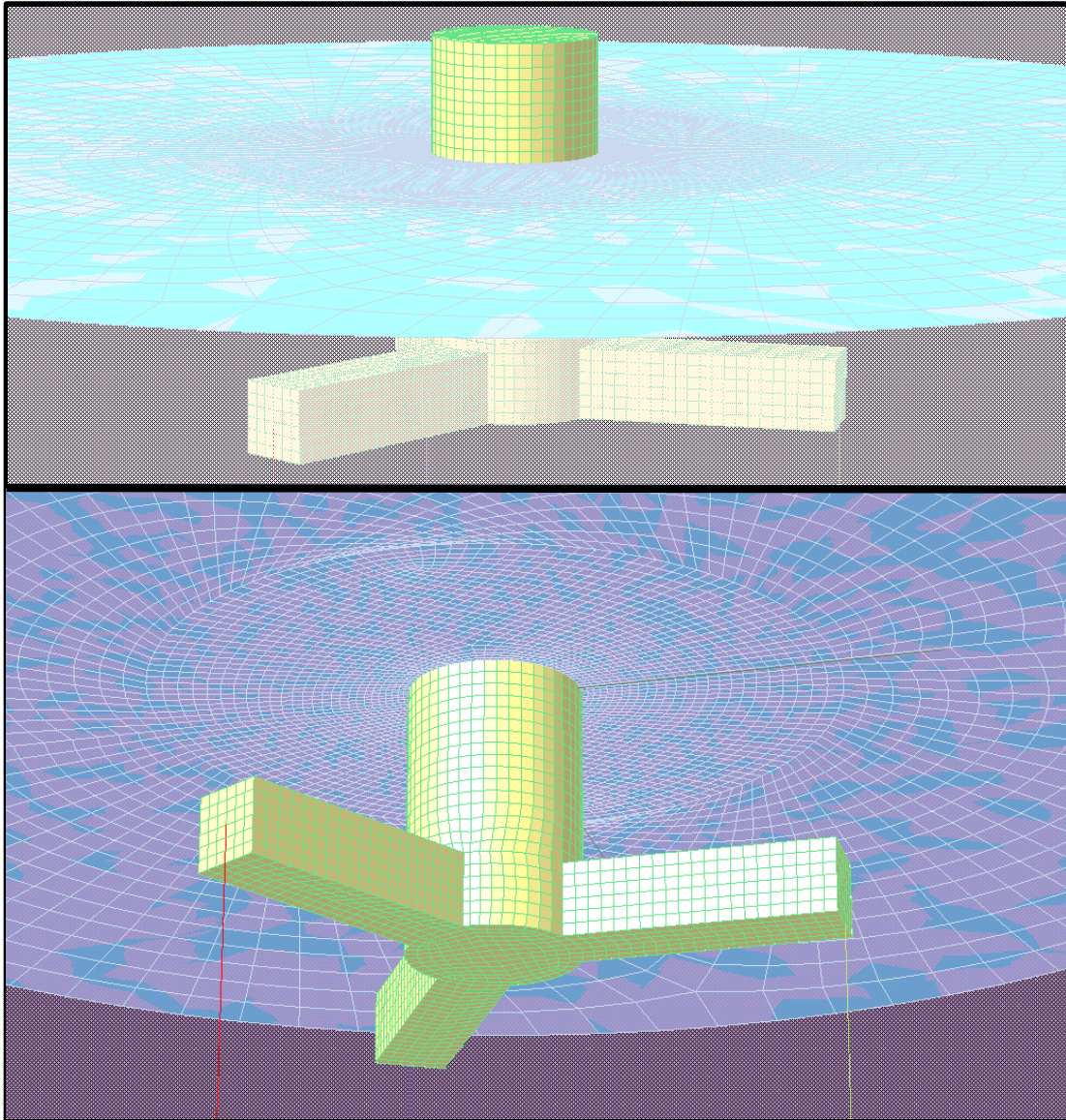


Figure 6-3: HydroD 3-D panel model seen from above (top) and below (bottom) the water surface

Now that the panel model had been created, the radiation and diffraction pressures could be computed in WAMIT. The results from this are presented and discussed in paragraph 6.3.

6.3 Hydrodynamic loads for the hull as a whole

WAMIT was used to solve the first-order potential problem for the 3-D panel model. Solving the first-order potential problem gives the first-order radiation and diffraction pressures. The frequency-dependent added mass and radiation damping can be derived from the radiation

pressure. The frequency-dependent wave excitation can be derived from the diffraction pressure. In WAMIT, the hydrodynamic coefficients are computed for each panel. Summing over all the panels gives the total added mass, linear radiation damping and first-order wave excitation for the hull structure as a whole. Paragraphs 6.3.1 through 6.3.3 present these hydrodynamic quantities. A comparison was made with Bachynski's previously published results for the same hull [9]. Bachynski published results for the added mass and radiation damping coefficients in surge, heave, pitch and yaw, and the first-order wave excitation in surge, heave and pitch. The results found here should be identical to this.

6.3.1 Added mass for the hull as a whole

Figure 6-4 shows the frequency-dependent added mass coefficients in surge, sway, heave, roll, pitch and yaw for the hull as a whole. These coefficients correspond to the diagonal terms in the 6-by-6 added mass coefficient matrix computed by WAMIT.

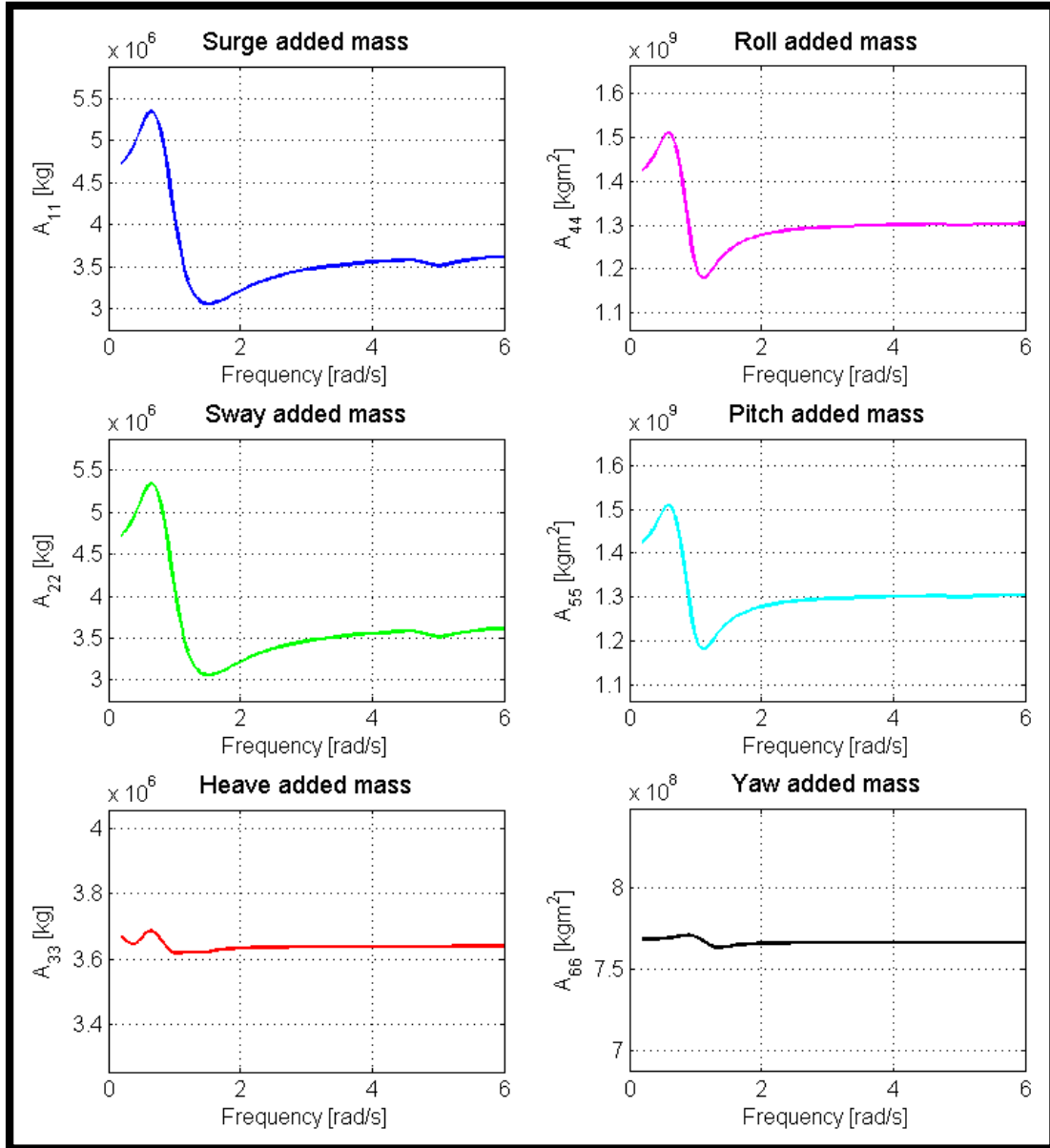


Figure 6-4: Added mass coefficients for the whole hull

Especially the added mass in surge, sway, roll and pitch show frequency variation. Both heave and yaw added mass show a low frequency dependence as they take on approximately the same values over the whole frequency range. The added mass for the translational modes have the same order of magnitude, indicating that the amount of displaced water in these directions is also of the same order of magnitude. The added mass coefficients found here are identical to Bachynski's findings.

6.3.2 Linear radiation damping for the hull as a whole

Figure 6-5 shows the frequency-dependent radiation damping coefficients in surge, sway, heave, roll, pitch and yaw for the hull as a whole. These coefficients correspond to the diagonal terms in the 6-by-6 damping coefficient matrix computed by WAMIT.

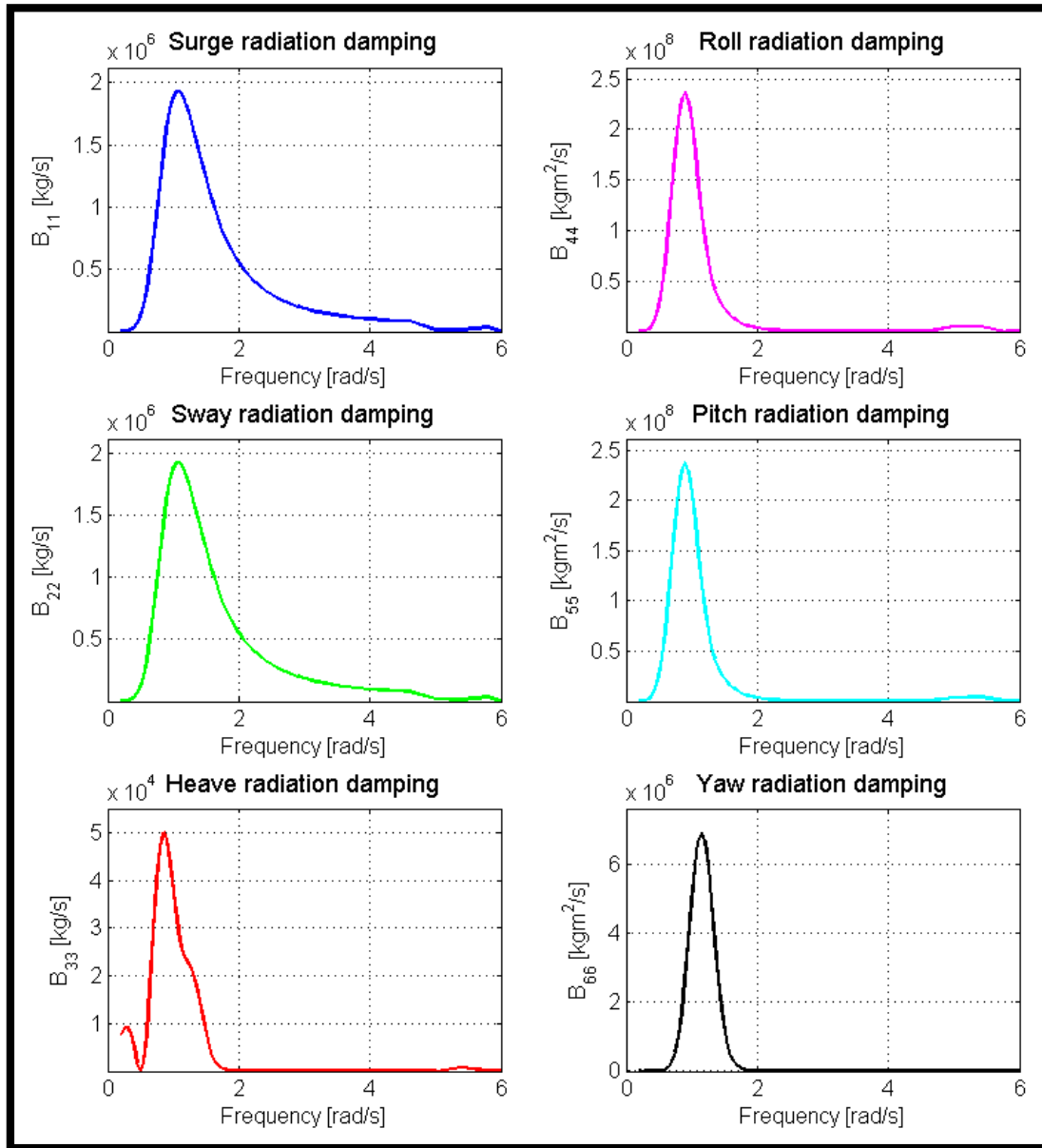


Figure 6-5: Radiation damping coefficients for the whole hull

The radiation damping coefficients show a stronger frequency dependence than the added mass coefficients. All of the four radiation damping coefficients have a peak around 1 rad/s. Also, it

can be seen that they approach zero for both high and low frequencies, which is consistent with theory [44]. The reason for this is that body oscillations at very high or very low frequencies do not generate any free-surface waves, which is necessary in order to carry energy away. Note that this paragraph only concerns the linear radiation damping, and that the global dynamic analysis model will also account for quadratic viscous damping according to the Morison equation.

The radiation damping coefficients found here are identical to Bachynski's findings.

6.3.3 First-order wave excitation for the hull as a whole

The first-order wave force excitation per unit wave amplitude in surge, sway, heave, roll, pitch and yaw were computed for incident waves with three different wave headings: 0 degrees, 45 degrees and 90 degrees. 0 degrees corresponds to the direction of the x-axis, while 90 degrees corresponds to the direction of the y-axis. The origin of the x-axis and y-axis are located at the centerline of the main column. Figure 6-6 shows how the TLP is oriented in the x-y plane. It also shows the numbering of the pontoons. P1, P2 and P3 refer to pontoon 1, pontoon 2 and pontoon 3 respectively. This numbering definition is applied for the sake of convenience and will be used throughout the rest of this report.

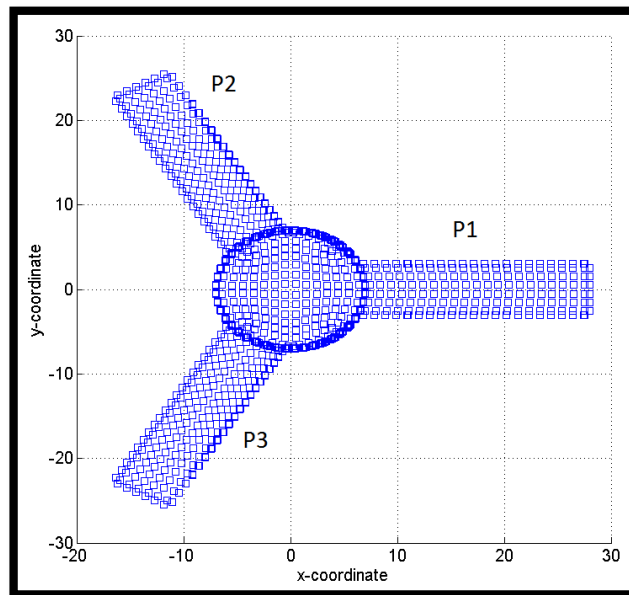


Figure 6-6: TLP orientation in the x-y plane

Figure 6-7 shows the first-order wave excitation per unit wave amplitude as a function of frequency.

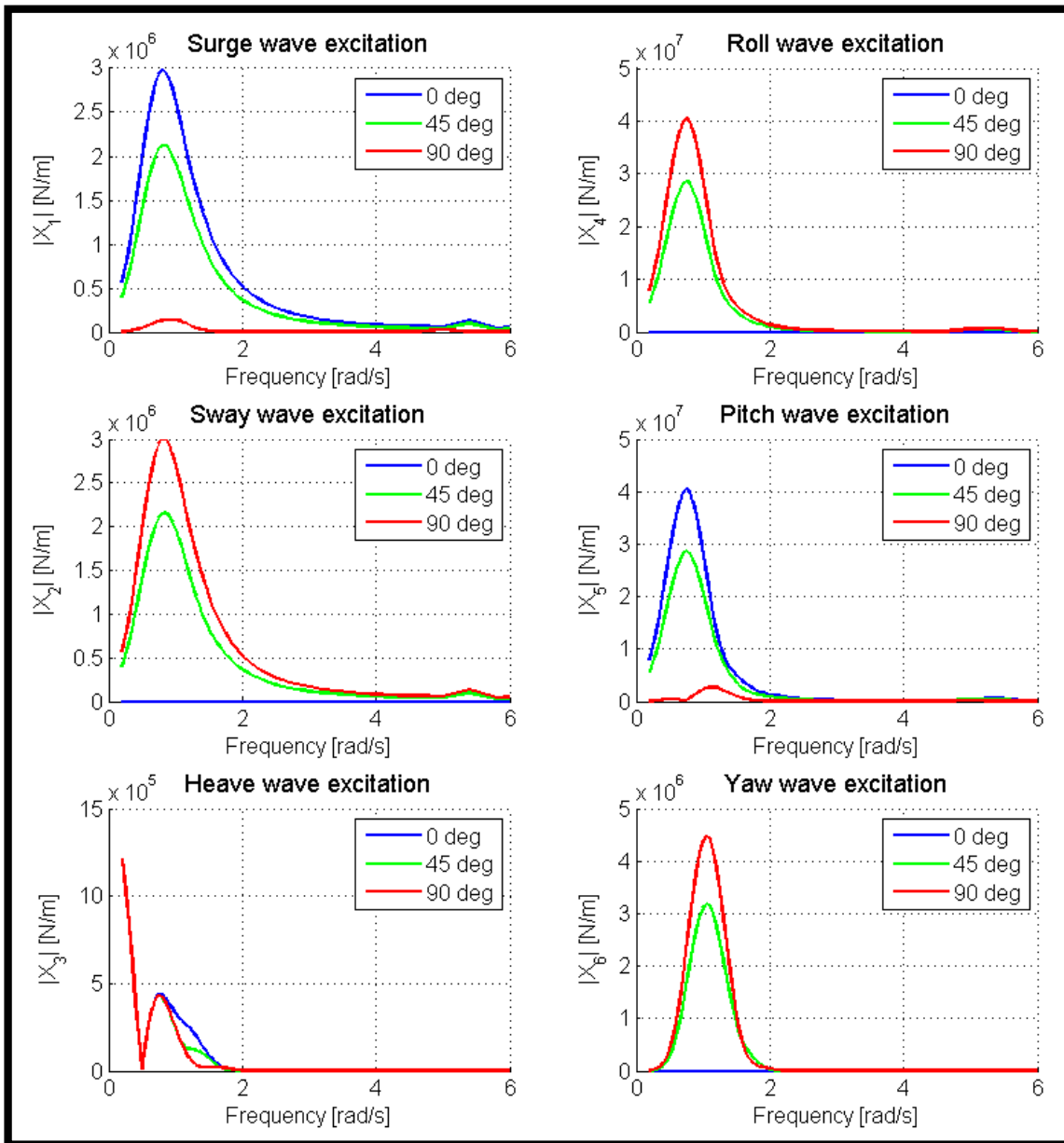


Figure 6-7: First-order wave force excitation per unit wave amplitude for the whole hull

The first-order wave force excitation approaches zero for high frequencies, which is consistent with theory [44]. Physically, this means that several waves will exist along the body which cancel each other out. In all directions except for heave it approaches zero also for low frequencies. Furthermore, in all directions except for heave, the maximum force occurs at a

frequency of approximately 0.8 rad/s. The heave force also has a peak at around 0.8 rad/s, but its maximum occurs at a much lower frequency. The sway and roll excitation are zero for a wave heading of 0 degrees. Because of this, one could expect the surge and pitch excitation to be zero for a wave heading of 90 degrees. As shown in Figure 6-7, this is not entirely the case. To understand why, it is helpful to take another look at Figure 6-6, which shows how the TLP is oriented in the x-y plane. When a wave approaches the hull from 90 degrees (in the positive y-direction), it will be partly blocked by P3 before it reaches P2. Because of this, the wave force on P2 will be smaller than the wave force on P3. Consequently, the problem is no longer symmetric with respect to the y-axis. This gives rise to some resultant surge and pitch excitation even if the wave heading is 90 degrees. For the same reason, the heave excitation shows some wave-direction dependency between 0.8 rad/s and 2 rad/s.

The first-order wave excitation coefficients found here are identical to Bachynski's findings.

6.4 Hydrodynamic loads for sections of the hull

Paragraph 6.3 presented the frequency-dependent first-order potential flow hydrodynamic loads for the hull structure as a whole computed with WAMIT. WAMIT obtained those results by computing the loads from the radiation and diffraction problems on each panel and summing over all of the panels. WAMIT can also give its user the dimensionless hydrodynamic pressure on each panel separately before the loads are computed and everything is summed up. This enables the user to determine himself/herself which panel loads to sum up. Consequently, if the hull is divided into sections, the loads on the panels which correspond to a given section can be summed up to give the total hydrodynamic load for that section. In this way, hydrodynamic load input for sections of the hull can be generated.

Chapter 5 applied a RIFLEX beam element model of the hull for which the mass distributions and stiffness were determined in chapter 4. The goal is to implement hydrodynamic section loads based on potential theory in that RIFLEX beam element model. The result will be a hydro-elastic model which couples hydrodynamic element loads based on potential theory to the RIFLEX beam element description of the hull's elastic behavior.

In the present study, a Matlab script was written which divides the hull into sections and computes the hydrodynamic loads for each section. The essential features of this Matlab script can be found in Appendix F. In the following, a detailed description will be given on how this was done. Paragraph 6.4.1 describes how the hull was divided into sections, while paragraph 6.4.2 describes how the hydrodynamic loads were calculated for each section.

6.4.1 Defining the sections of the hull

As previously mentioned, the hull consists of three main components: main column, base node and pontoons. Sections are defined for each of these main components separately. Thus, the hull consists of three main components, which in turn are divided into sections. WAMIT can output the center-point coordinates of each panel. This can be read by Matlab and used to plot a 3-D Matlab visualization of the complete panel model. Matlab can also conveniently be used to decompose the whole structure into the previously mentioned main components to plot a 3-D visualization of the panel structure for each of the main components separately. Figure 6-8 shows this.

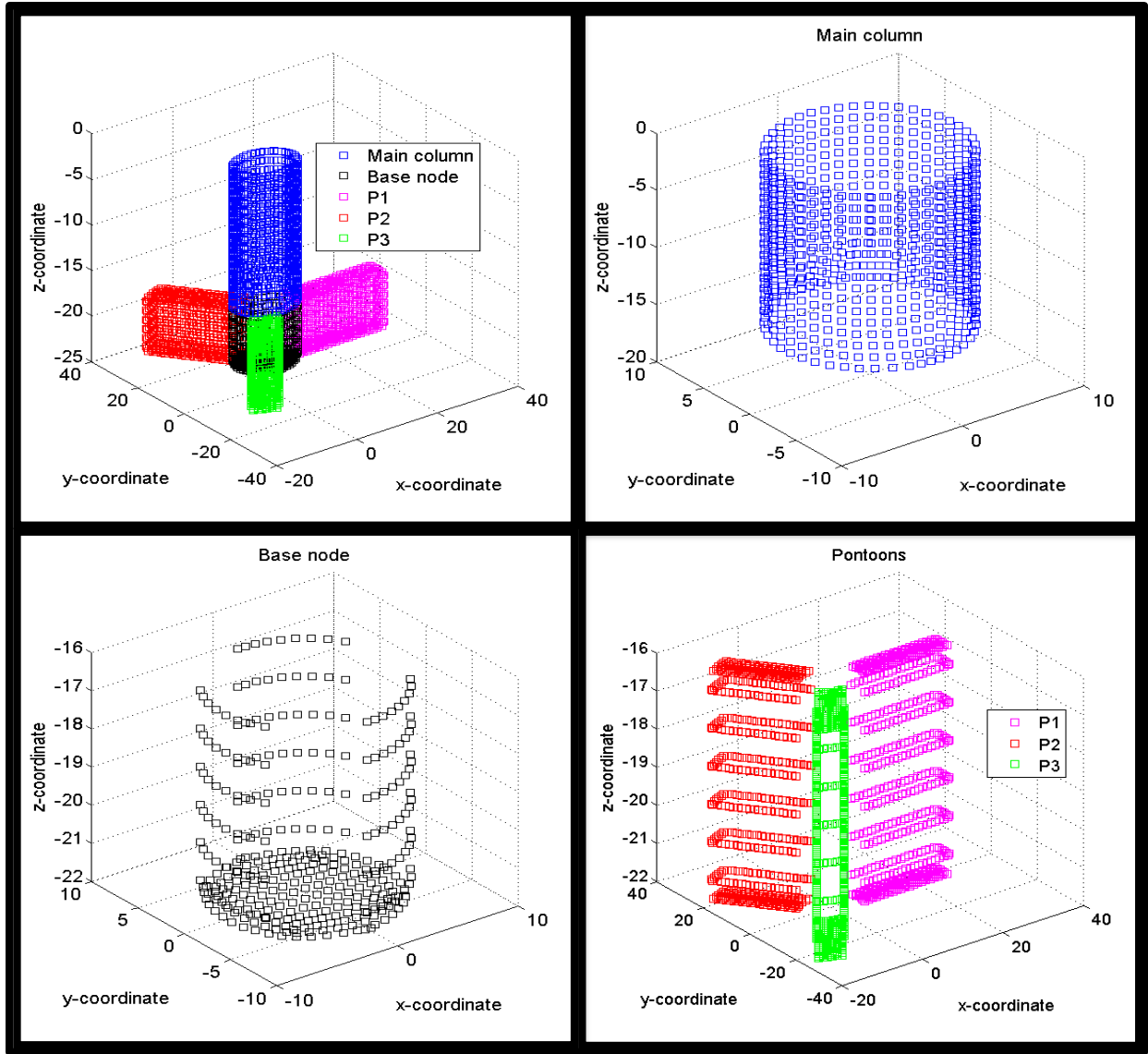


Figure 6-8: Matlab visualization of panels. Top left: Full TLP. Top right: Main column. Bottom left: Base node. Bottom right: Pontoons

Dividing the main column and base node into sections

When the structure is at rest, the main column and base node are oriented vertically with their centerline along the z-axis through the origin of the x-y plane. The main column and base node are represented by beam elements with nodal coordinates $(0, 0, z)$ in the RIFLEX model. The main column and base node should thus be divided into sections by making horizontal cuts along the z-axis. An example of how to make sections of the main column and base node is illustrated

by the yellow planes in Figure 6-9. In this figure, the main column and base node are divided into four and two sections respectively. The section boundaries of the main column and base node are then defined by the z-coordinates of these planes. In the RIFLEX model, each section boundary will correspond to a node.

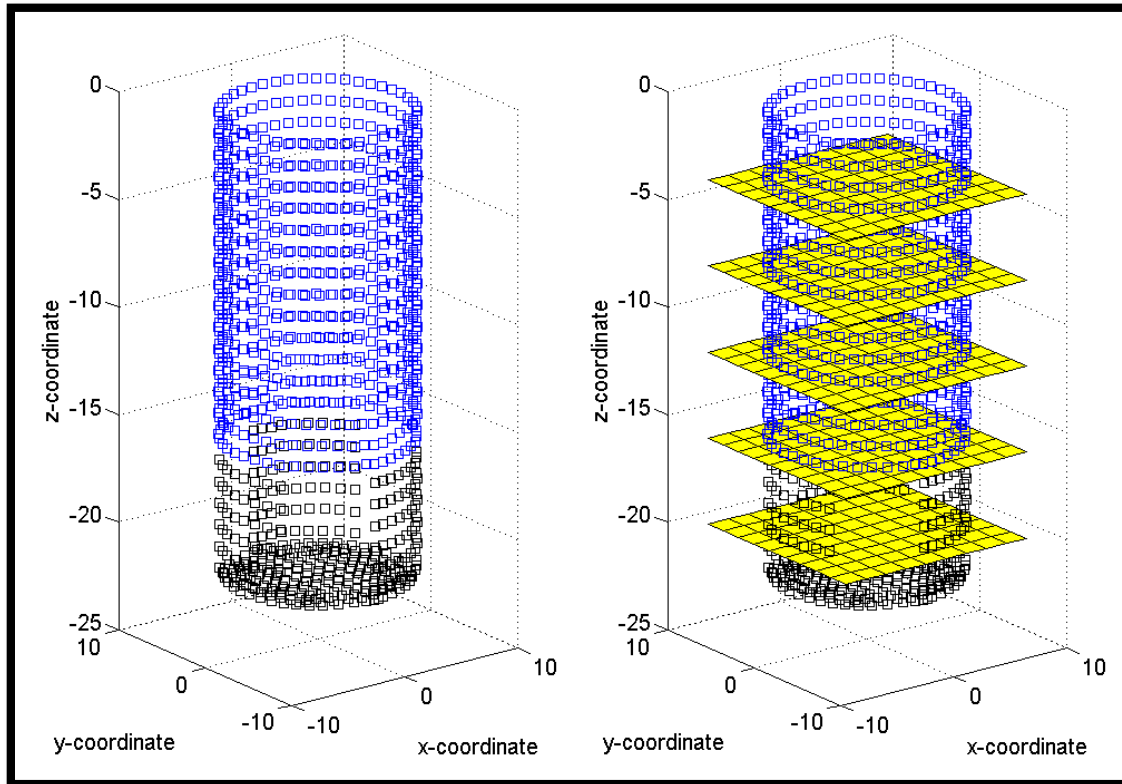


Figure 6-9: Column and base node panels with and without horizontal planes indicating section boundaries

Dividing the pontoons into sections

When the structure is at rest, the pontoons are oriented horizontally at a depth of 19 m. The pontoons are represented by beam elements with nodal coordinates $(x, y, -19)$ in the RIFLEX model. The centerline of each pontoon goes through the origin of the x-y plane where it intersects with the centerline of the main column and base node. A pontoon can be divided into sections by making vertical curved cuts at radial distances from the centerline of the main column and base node. An example of how to make sections of the pontoons is illustrated by the yellow planes in Figure 6-10. In this figure, each pontoon is divided into four sections. The

pontoon section boundaries are thus defined by these cuts' radial distance from the origin of the x-y plane. In the RIFLEX model, each section boundary will correspond to a node.

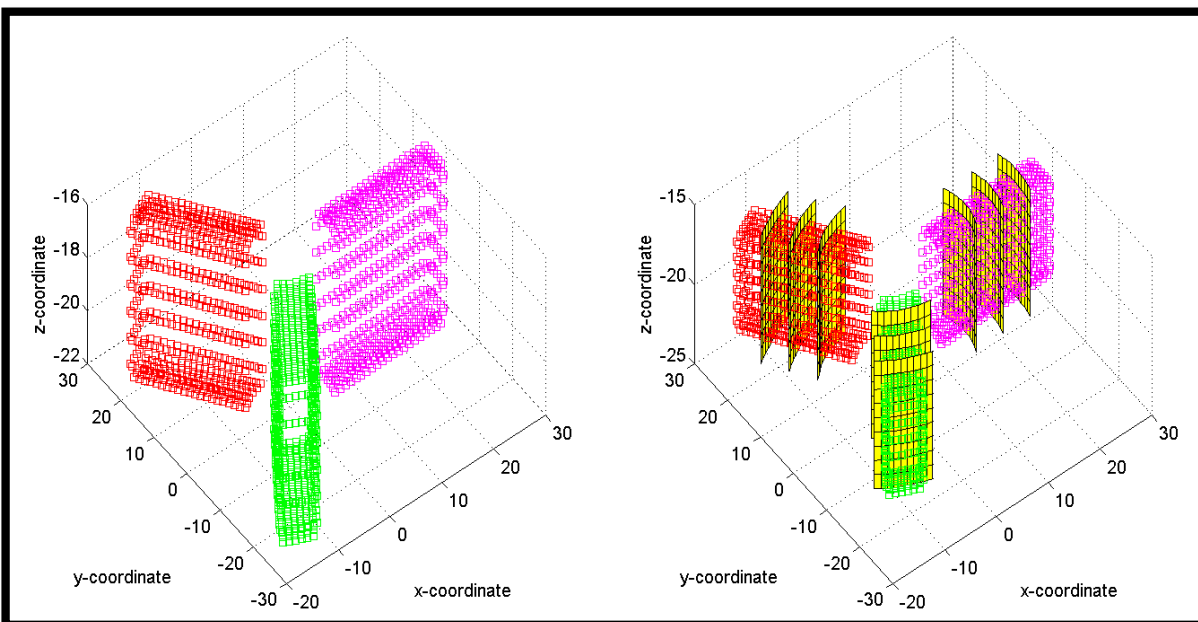


Figure 6-10: Pontoon panels with and without vertical planes indicating section boundaries

Please note that the number of sections shown in Figure 6-9 and Figure 6-10 was chosen with the purpose of illustrating an idea. As will be shown later, the actual number of sections which was applied in the dynamic analyses was higher than this. With the section definition ready, the hydrodynamic loads from first-order potential theory can be computed for each section.

6.4.2 Computing the hydrodynamic loads for each section

An algorithm was used which associates each panel in the model with one of the pre-defined sections. The algorithm does this by looking at the coordinates of each panel's center-point and then determining which section each panel belongs to. For each panel in a section, the following is computed:

- 6-by-6 added mass matrix.
- 6-by-6 linear radiation damping matrix.
- 6-by-1 first-order excitation force vector for wave headings 0, 45 and 90 degrees.

The hydrodynamic loads for a given section is found by summing up the arrays of all the panels which belong to that section. In other words, if there are N panels associated with a section, then the first-order potential flow added mass matrix A , damping matrix B , and excitation force vector X , for that section is found from the following summations:

$$A_{section} = \sum_{n=1}^N A_{panel,n} \quad (6-1)$$

$$B_{section} = \sum_{n=1}^N B_{panel,n} \quad (6-2)$$

$$X_{section} = \sum_{n=1}^N X_{panel,n} \quad (6-3)$$

This means that, for instance, the wave excitation in surge for the whole section, $X_{1,section}$, becomes equal to the sum of the wave excitation in surge for all of the N panels in that section, $X_{1,panel,1} + X_{1,panel,2} + \dots + X_{1,panel,N}$.

The Matlab script which was used to define the sections of the structure and associate every panel with one of those sections, is also used to compute the hydrodynamic loads for each of those sections. The script reads and makes use of the WAMIT non-dimensional pressure component output to do this. Before going into further details on the calculations in the Matlab script, the WAMIT definition of relevant non-dimensional quantities is presented.

WAMIT definition of non-dimensional quantities

WAMIT can provide a number of numeric output files [46]. The OPTN.5P output file contains separate components of the non-dimensionalized diffraction pressure, \bar{p}_D , and the non-dimensionalized radiation pressure components, \bar{p}_j , for each panel. The non-dimensionalized radiation pressure components, \bar{p}_j , correspond to unit motion ($\zeta_j=1$) in each degree of freedom $j=1,2,3,4,5,6$. The OPTN.5P file also contains the components of all panels' unit normal vector. When the non-dimensional pressure is used, the non-dimensional added mass, damping and

excitation coefficients are obtained. On panel level, these non-dimensional quantities are defined in WAMIT as

$$\bar{p}_j = \frac{p_j}{\rho g \xi_j L^n} \quad (6-4)$$

$$\bar{p}_D = \frac{p_D}{\rho g AREA} \quad (6-5)$$

$$\bar{A}_{ij} = \frac{A_{ij}}{\rho L^k} \quad (6-6)$$

$$\bar{B}_{ij} = \frac{B_{ij}}{\rho L^k \omega} \quad (6-7)$$

$$\bar{X}_i = \frac{X_i}{\rho g AREA L^m} \quad (6-8)$$

where *AREA* is the panel area and *L* is the length WAMIT uses to non-dimensionalize. The parameters *k*, *m* and *n* depend on the indices *i* and *j* as described in the following.

The parameter *k* is related to the added mass and damping coefficients and varies with *i* and *j* as follows: *k*=3 for *i,j*=1,2,3, *k*=4 for *i*=1,2,3, *j*=4,5,6 or *i*=4,5,6, *j*=1,2,3 and *k*=5 for *i,j*=4,5,6. In other words, if the 6-by-6 added mass and damping matrices are divided into four quadrants in the same way a 2-D coordinate system is divided into quadrants, then *k*=3 for the 2nd quadrant, *k*=4 for the 1st and 3rd quadrant and *k*=5 for the 4th quadrant:

		j					
		1	2	3	4	5	6
i	1	k = 3			k = 4		
	2						
	3						
	4	k = 4			k = 5		
	5						
	6						

Chapter 6: Creating the elastic multi-body hull model

The parameter m is related to the excitation coefficients and varies with i as follows: $m=2$ for $i=1,2,3$ and $m=3$ for $i=4,5,6$. The parameter n is related to the radiation pressure and varies with the degree of freedom index j as follows: $n=0$ for $j=1,2,3$ and $n=1$ for $j=4,5,6$. In other words, $m=2$ and $n=0$ for translational rigid body modes, while $m=3$ and $n=1$ for rotational rigid body modes.

i	1	$\mathbf{m} = 2$
	2	
	3	
	4	$\mathbf{m} = 3$
	5	
	6	

j					
1	2	3	4	5	6
$\mathbf{n} = 0$			$\mathbf{n} = 1$		

Analytically expressing the hydrodynamic coefficients in terms of the pressure components

In chapter 2, it was shown that the added mass, damping and excitation coefficients can be found from integration of the radiation and diffraction potentials over the wetted body surface. In the following, it will be derived that these coefficients can also be found from integration of the pressures from the radiation and diffraction potentials. This will allow the Matlab script to use the pressure components in the WAMIT OPTN.5P output file when computing the hydrodynamic coefficients.

According to equation 2-4, which describes the total pressure in the fluid, the linear dynamic pressure is related to the time derivative of the velocity potential as follows:

$$p = -\rho \frac{\partial \phi}{\partial t} \quad (6-9)$$

If it is now assumed that the velocity potential can be described by a space-dependent term and a harmonic time-dependent term on the form

$$\phi(x, y, z, t) = \phi(x, y, z) e^{i\omega t} \quad (6-10)$$

then the complex form of the pressure in equation 6-9 becomes

$$p = -i \omega \rho \phi(x, y, z) \quad (6-11)$$

Equation 2-6 showed that the exciting forces can be found from integration of the diffraction potential over the wetted body surface. Rearranging equation 6-11 and substituting it into equation 2-6 allows the exciting forces to be written in terms of the pressure from the diffraction potential:

$$X_i = -i \omega \rho \iint_{S_B} n_i \phi_D dS = \iint_{S_B} n_i p_D dS \quad (6-12)$$

Equation 2-7 defined the radiation potential as follows

$$\phi_R = i \omega \sum_{j=1}^6 \xi_j \phi_j \quad (6-13)$$

By combining equations 6-11 and 6-13, the radiation pressure component p_j can be written as

$$p_j = \omega^2 \rho \xi_j \phi_j \quad (6-14)$$

Equation 2-8 showed that the added mass and damping coefficients can be found from integration of the radiation potential over the wetted body surface. Rearranging equation 6-14 and substituting it into equation 2-8 allows the added mass and damping coefficients to be written in terms of the pressure from the radiation potential:

$$A_{ij} - \frac{i}{\omega} B_{ij} = \rho \iint_{S_B} n_i \phi_j dS = \frac{1}{\omega^2} \iint_{S_B} n_i \frac{p_j}{\xi_j} dS \quad (6-15)$$

It has now been shown that the first-order potential flow added mass, damping and wave excitation can be found from integration of the radiation and diffraction pressures over the wetted body surface. In the following, it will be shown how this was used in the Matlab calculations.

Computing the hydrodynamic coefficients for each panel in Matlab

The non-dimensional pressure components were used to calculate the hydrodynamic coefficients in Matlab. WAMIT version 5 was used to solve the radiation and diffraction problems and to obtain the hydrodynamic pressure components on each panel. This version of WAMIT uses a

lower-order panel method, which means that the potential is assumed constant on each panel. This implies that the pressure is also assumed constant on each panel. The excitation, added mass and radiation damping coefficients for a panel can therefore be computed by simplifying equations 6-12 and 6-15 to

$$X_{i,panel} = AREA n_i p_D \quad (6-16)$$

$$A_{ij,panel} - \frac{i}{\omega} B_{ij,panel} = \frac{1}{\omega^2} AREA n_i \frac{p_j}{\xi_j} \quad (6-17)$$

Equations 6-18 and 6-19 were used to calculate the added mass, damping and excitation forces for each WAMIT panel in Matlab. Those expressions are consistent with equations 6-16 and 6-17 if the non-dimensional quantities which were defined in equations 6-4 through 6-8 are applied. Please note that n with subscript i denotes the unit normal vector, while n without any subscript is the previously discussed parameter that depends on the radiation pressure and the degree of freedom index j . This notation is consistent with the notation in the WAMIT user manual [46].

$$\bar{A}_{ij,panel} - i\bar{B}_{ij,panel} = \frac{AREA}{L^{k-n}} \frac{g}{\omega^2} (n_i \times \bar{p}_j) \quad (6-18)$$

$$\bar{X}_{i,panel} = \frac{AREA}{L^m} n_i \bar{p}_D \quad (6-19)$$

\bar{p}_j represents the radiation pressure components. It is a complex 1-by-6 row vector. n_i is a 6-by-1 column vector, and its matrix product with \bar{p}_i is a complex 6-by-6 matrix. The real parts of this matrix correspond to the added mass coefficients, while the imaginary parts correspond to the damping coefficients. \bar{p}_D is a complex number which represents the diffraction pressure. The modulus and phase angle of the excitation coefficients are described by the complex 6-by-1 column vector \bar{X}_i .

When calculating the loads for each section of the hull, the local origin is at the section center. However, WAMIT calculates all angular quantities about the local origin in the WAMIT model, which is at the still water level. This means that the angular quantities computed by WAMIT cannot be used for the section calculations because they are computed with a different center of rotation. It is assumed that local rotational moments on a small section is much smaller than the

moments from surge, sway and heave forces. Therefore, all pressures due to rotational motions are set to zero. Also, all rotational components of the normal vector n_i were set to zero. In short, p_4, p_5, p_6, n_4, n_5 and n_6 were set to zero for both the diffraction and radiation pressures.

The hydrodynamic section loads' point of application within each section

When the hydrodynamic loads have been computed for all of the panels in a section, equations 6-1 through 6-3 can be applied to obtain the hydrodynamic section loads. Each section is in reality three dimensional. The section loads will be represented by SIMO-bodies in the global analysis model. There will be one SIMO-body per section. The SIMO-bodies will be inserted at selected nodes (points) in the already existing RIFLEX beam element model of the hull. Therefore, the hydrodynamic section loads' point of application within the three dimensional section must be defined for each section. In the present study, the following four rules were adapted:

- For a main column or base node section (Figure 6-9), the loads are assumed to apply in the intersection point between the main column/base node centerline and the section's upper boundary. Thus, if there is a main column section with boundaries at elevations $z=-3$ m and $z=-5$ m, then the loads on the panels belonging to that section are collected and applied in point (0, 0, -3 m).
- The loads on the panels which are located at the bottom of the base node are collected and applied in point (0, 0, -22 m).
- For a pontoon section (Figure 6-10), the loads are assumed to apply in the intersection point between the pontoon centerline and the boundary that is closest to the main column/base node centerline. In other words, if there is a section on pontoon 1 with boundaries at radial distances 10 m and 12 m from the base node wall, then the loads on the panels belonging to that section are collected and applied in point (10 m, 0, -19 m).
- The loads on the panels which are located at the tip of a pontoon are collected and applied at the center point coordinate of the pontoon tip.

It has now been explained how the hydrodynamic loads were computed for each section. It has also been explained in which point the hydrodynamic loads were assumed to apply for each

section. When the hydrodynamic loads had been computed for each section, the data was written to file in WAMIT output file format for each section separately. SIMO can readily read WAMIT output file format. For each section, one SIMO-body was used to represent the hydrodynamic loads. The SIMO-body which represents the hydrodynamic loads for a given section, was inserted in the existing RIFLEX model at a node which corresponds to the hydrodynamic section loads selected point of application for that section. The resulting hull model then becomes an elastic multi-body SIMO-RIFLEX model. The SIMO-bodies have no structural mass, volume or stiffness. Thus, they do not give additional contributions to structural weight, buoyancy or stiffness. Their only function is to represent the frequency-dependent first-order potential flow added mass, radiation damping and wave excitation. The buoyancy, structural stiffness, hydrostatic stiffness and mass distribution are represented by the RIFLEX beam elements. Additionally, the RIFLEX beam elements were subjected to drag loads from the Morison equation.

Summing the section loads across all of the sections should give a result which is close to the WAMIT computations for the hull as a whole (paragraph 6.3). This comparison is presented and discussed in paragraph 6.5.

6.5 Summing the loads over all of the sections and comparing with the WAMIT output for the hull as a whole

The first-order potential added mass and radiation damping matrices, and the first-order wave excitation vector have now been calculated for each section of the structure and transferred to SIMO-bodies. It is desirable to have an idea of how accurately the potential theory loads are transferred to the SIMO-RIFLEX global analysis model. This is investigated in this paragraph.

As already explained, the rotational excitation components were approximated to be zero for each section. In the multi-body model, global rotational moments due to first-order potential theory loads on the hull are caused by translational loads from SIMO-bodies which are located at some distance from the model's global origin. For instance, excitation in the x-direction from a SIMO-body which is located on the base node will cause a moment about the y-axis at the water line. The global moments due to forces in x-, y- and z-directions can be calculated as

$$M_x = F_z y - F_y z \quad (6-20)$$

$$M_y = F_x z - F_z x \quad (6-21)$$

$$M_z = F_y x - F_x y \quad (6-22)$$

The total excitation from the SIMO-bodies was compared to WAMIT’s computed excitation for the hull as a whole. The same was done for the total added mass and radiation damping from the SIMO-bodies. The comparison was made for four different section models of the structure. That is, the total number of sections to divide the structure into was varied during this comparison. This is described in more detail in paragraph 6.5.1.

6.5.1 Number of sections used in the comparison

Table 6-1 presents the number of sections defined for each part of the TLP. The sections are referred to as “dl=1”, “dl=2” etc. This refers to the height of each section on the main column. “dl=2” means that the height of each main column section is approximately 2 m. Within each part of the TLP (main column, base node, pontoons), the dimensions are the same for each section.

Table 6-1: Number of sections in each selected section model

	dl=1	dl=2	dl=3	dl=4
Main column	16	8	5	4
Base node	7	4	3	2
Pontoon 1	15	8	5	4
Pontoon 2	15	8	5	4
Pontoon 3	15	8	5	4
Total	68	36	23	18

Each section on the panel model is represented by one SIMO-body in the SIMO-RIFLEX model. So “dl=1” corresponds to a multi-body model with 68 SIMO-bodies, “dl=2” corresponds to a multi-body model with 36 SIMO-bodies etc. A visualization of the multi-body models which correspond to section models “dl=2” and “dl=4” is shown in Figure 6-11.

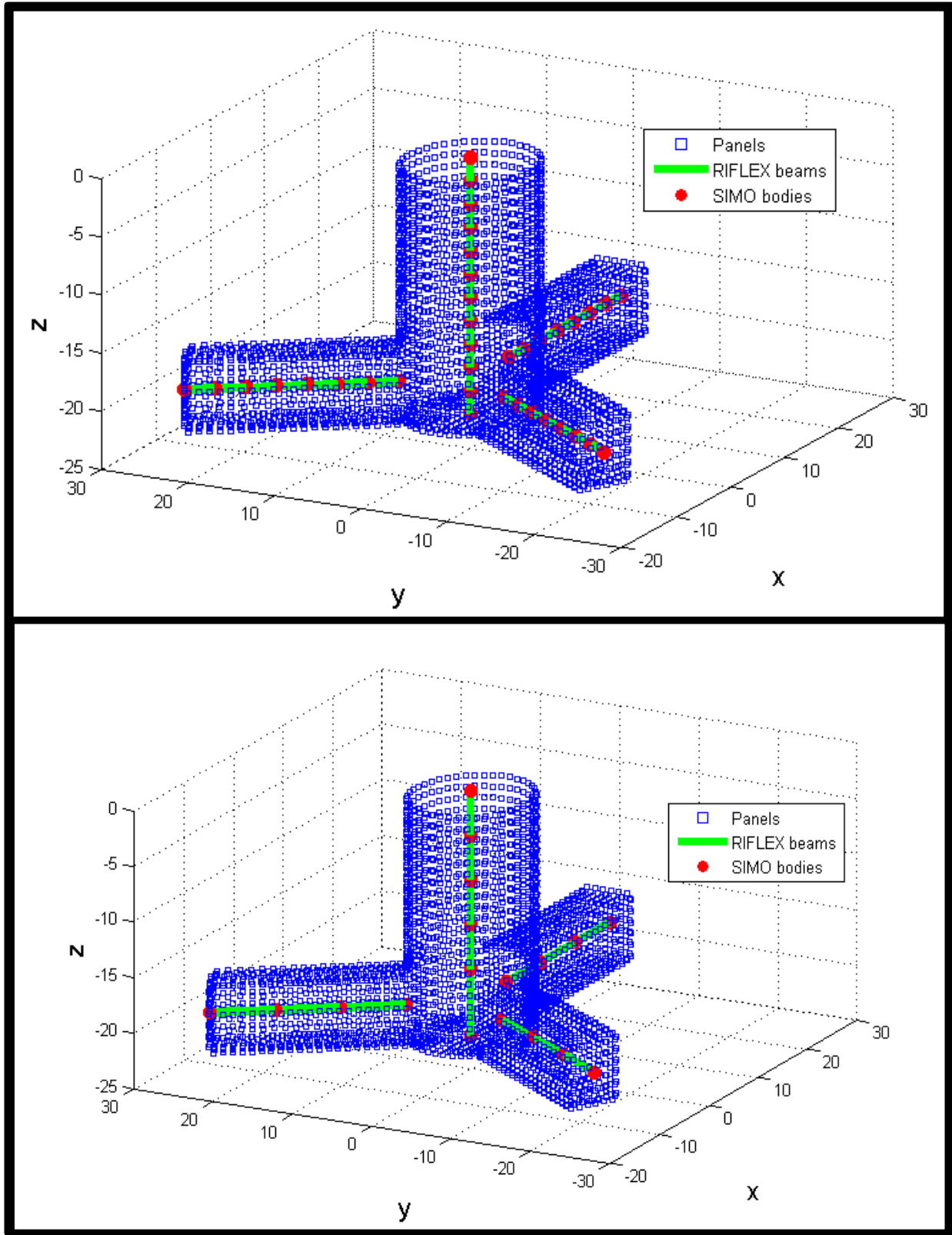


Figure 6-11: Visualizations of multi-body models corresponding to "dl=2" (top) and "dl=4" (bottom)

6.5.2 Comparing first-order potential theory wave excitation components

For a structure with N SIMO-bodies (sections), the excitation component X_i for SIMO-body b can be denoted $X_{i,b}$. The total translational excitation components, $X_{1,2,3}$, are calculated with

$$X_i = \sum_{b=1}^N X_{i,b} \quad \text{for } i = 1, 2, 3 \quad (6-23)$$

Figure 6-12 shows the translational excitation components for each wave heading.

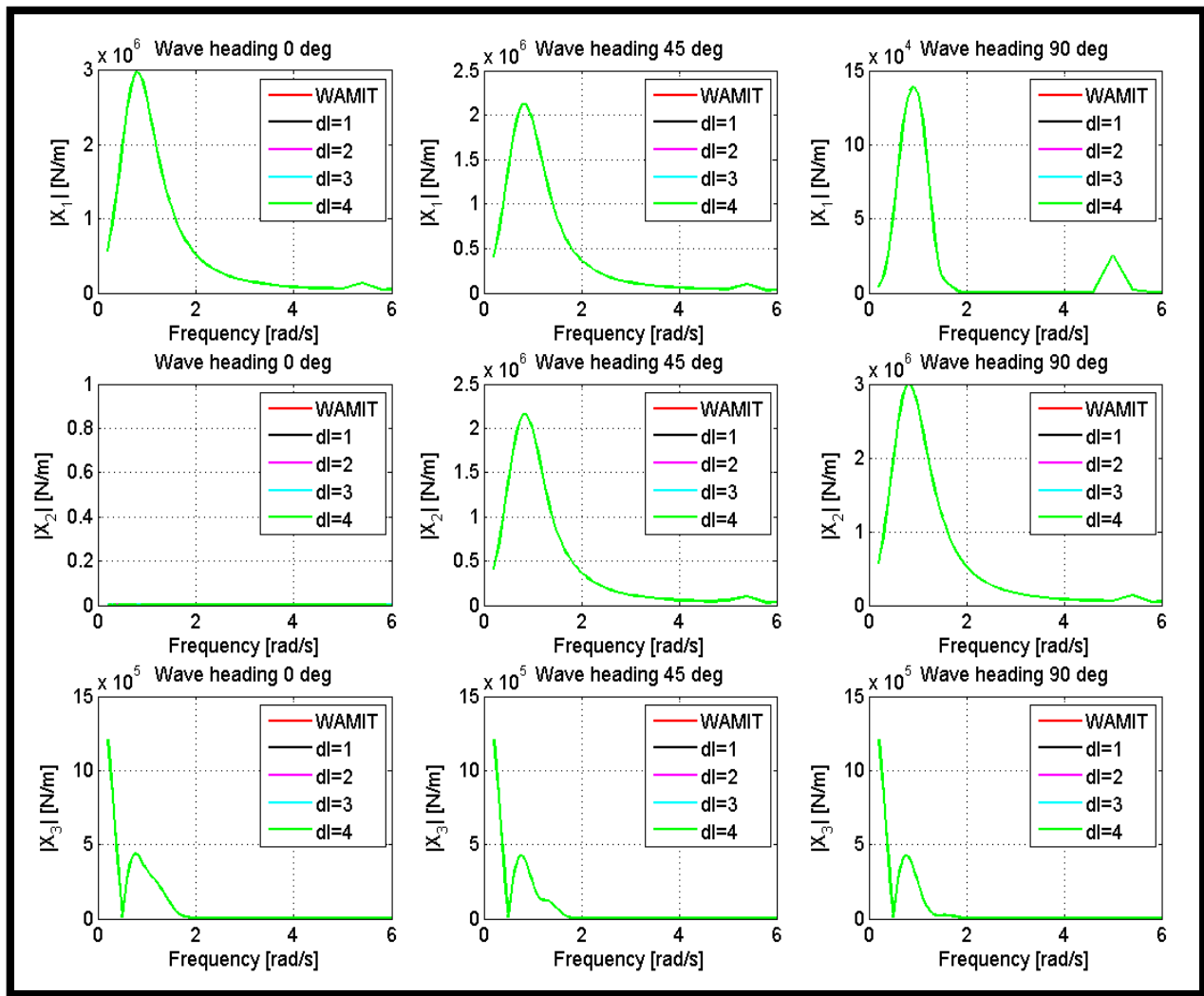


Figure 6-12: Comparison of translational excitation components

It is seen that, for each section model, the sum of the translational excitation from all of the SIMO-bodies give the exact same result as WAMIT's output for the hull as a whole. This is as expected, because the modelling procedure does not give rise to any loss of accuracy in any pure translational component.

In accordance with equations 6-20 through 6-22, the total rotational excitation components, $X_{4,5,6}$, are calculated with

$$X_4 = \sum_{b=1}^N (X_{3,b} y_b - X_{2,b} z_b) \quad (6-24)$$

$$X_5 = \sum_{b=1}^N (X_{1,b} z_b - X_{3,b} x_b) \quad (6-25)$$

$$X_6 = \sum_{b=1}^N (X_{2,b} x_b - X_{1,b} y_b) \quad (6-26)$$

where x_b , y_b and z_b denote the coordinates of the SIMO-body's position. Figure 6-13 shows the rotational excitation components for each wave heading.

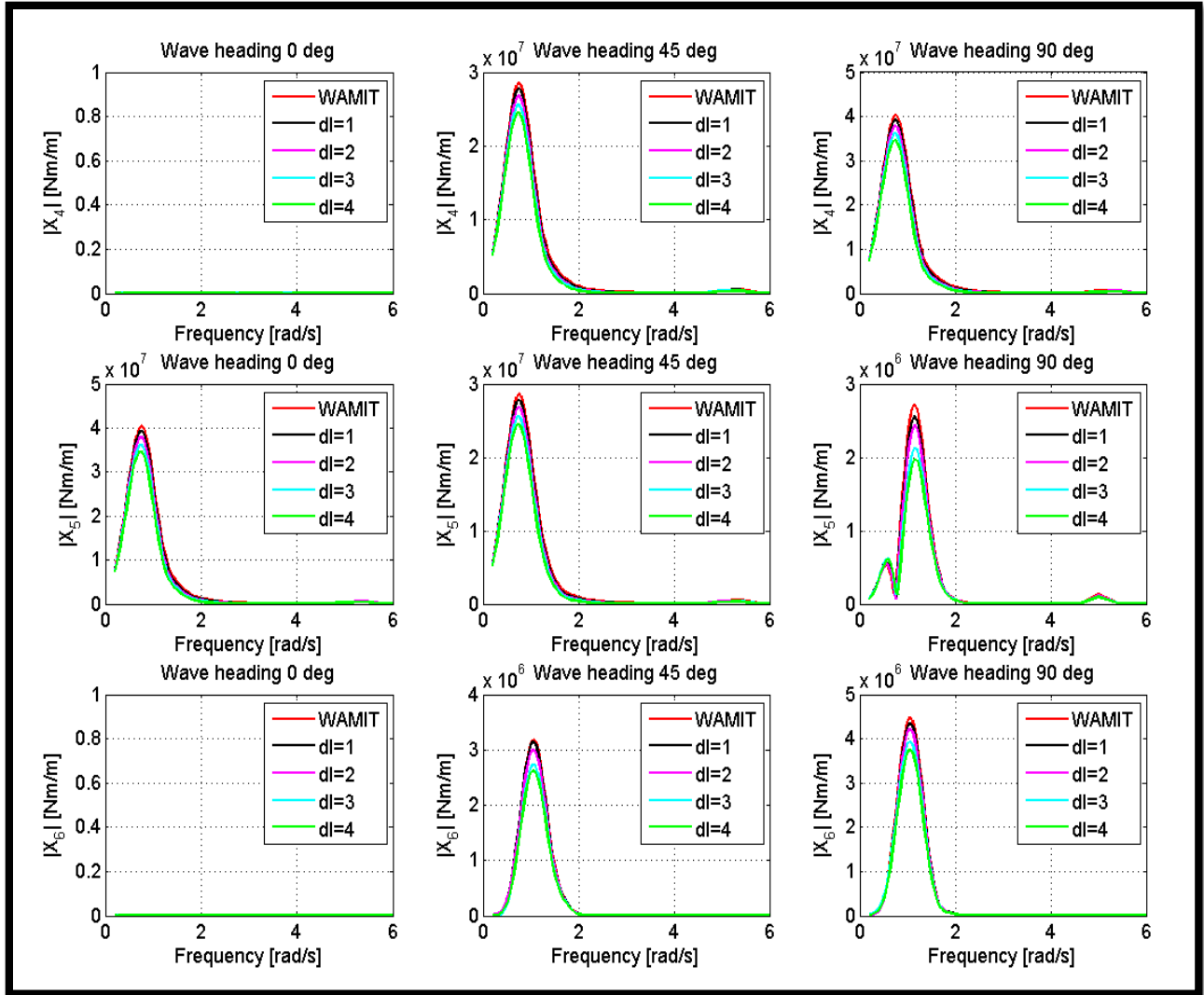


Figure 6-13: Comparison of rotational excitation components

In contrast to the translational components, it is seen that the sum of the rotational excitation from all of the SIMO-bodies is slightly lower than WAMIT’s output for the hull as a whole. This can be explained by the modelling technique. More specifically, it can be explained by the section loads’ selected point of application within each section, which define where the SIMO-bodies are inserted.

On the main column and base node, the section loads’ point of application was assumed to be at the upper boundary of each section. In practice, this means that the forces on the main column and base node are moved slightly upwards and closer to the waterline. The length of each

horizontal force components' vertical moment arm is therefore reduced. This partly explains why the modulus of X_4 and X_5 are lower than what WAMIT computes.

On the pontoons, the section loads' point of application was assumed to be at the boundary which is closest to the main column/base node centerline. In practice, this means that the loads on the pontoons are moved slightly closer to main column/base node centerline. The contributions to X_4 and X_5 from the vertical force component X_3 are therefore reduced too.

X_6 refers to moments about the z-axis. X_6 is caused by horizontal force components on the pontoons. The z-axis coincides with the main column/base node centerline. Therefore, the pontoon section loads' selected point of application result in a smaller modulus for X_6 than computed by WAMIT.

The error in the rotational excitation components can thus be explained by the section loads' selected point of application. Because this determines where the SIMO-bodies are inserted, this error will be inherently included in the SIMO-RIFLEX model. Figure 6-13 shows that increasing the number of sections, which essentially means decreasing the size of each section, results in smaller errors. The largest errors occur at the peaks. Table 6-2 gives the error observed in each model for each component and each wave heading at the peak. The corresponding percentagewise error is given in brackets.

Table 6-2: Maximum error for rotational excitation components

		dl=1	dl=2	dl=3	dl=4
0 degrees	$ X_4 $ [MNm/m]	0 (0 %)	0 (0 %)	0 (0 %)	0 (0 %)
	$ X_5 $ [MNm/m]	1.10 (2.7 %)	2.49 (6.2 %)	4.31 (10.7 %)	5.83 (14.4 %)
	$ X_6 $ [MNm/m]	0 (0 %)	0 (0 %)	0 (0 %)	0 (0 %)
45 degrees	$ X_4 $ [MNm/m]	0.75 (2.6 %)	1.74 (6.1 %)	2.97 (10.4 %)	4.03 (14.3 %)
	$ X_5 $ [MNm/m]	0.77 (2.7 %)	1.75 (6.1 %)	3.02 (10.5 %)	4.08 (14.3 %)
	$ X_6 $ [MNm/m]	0.03 (1.1 %)	0.18 (5.6 %)	0.44 (14.0 %)	0.55 (17.3 %)
90 degrees	$ X_4 $ [MNm/m]	1.07 (2.7 %)	2.50 (6.2 %)	4.27 (10.6 %)	5.79 (14.3 %)
	$ X_5 $ [MNm/m]	0.16 (6.0 %)	0.29 (10.8 %)	0.60 (21.9 %)	0.75 (27.6 %)
	$ X_6 $ [MNm/m]	0.12 (2.7 %)	0.25 (5.6 %)	0.53 (11.9 %)	0.73 (16.4 %)

The largest percentagewise error at the peak is observed for component $|X_5|$ and a wave heading of 90 degrees. For the other non-zero components, the error is fairly stable within each section model.

6.5.3 Comparing first-order potential theory added mass and radiation damping components

Added mass coefficient A_{ij} can be interpreted as the mass which is associated with a force/moment on the body in direction i caused by a unit acceleration of the body in direction j . For instance, added mass coefficient A_{14} can be interpreted as the mass associated with a force in the surge direction due to a unit acceleration in roll. The same logic applies to the radiation damping matrix coefficients B_{ij} .

Similar to equation 6-23, the diagonal translational added mass is calculated with

$$A_{ii} = \sum_{b=1}^N A_{ii,b} \quad \text{for } i = 1, 2, 3 \quad (6-27)$$

The corresponding damping coefficient is calculated in the same way.

Figure 6-14 shows the sum of the diagonal translational added mass and damping coefficients.

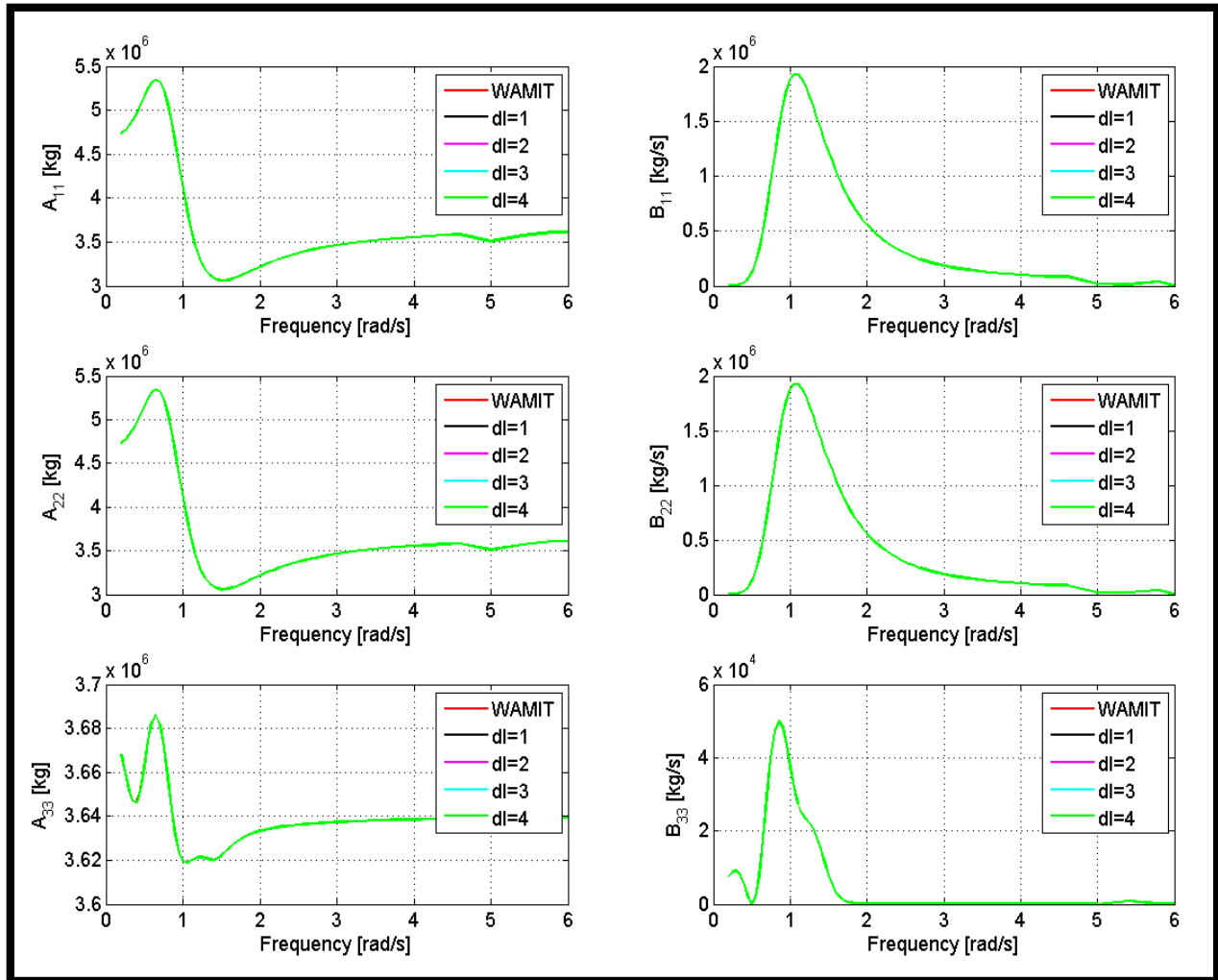


Figure 6-14: Comparison of diagonal translational added mass and damping coefficients

It is seen that, for each section model, the sum of the diagonal translational added mass and damping coefficients from all of the SIMO-bodies give the exact same result as WAMIT’s output for the hull as a whole. As explained before, the modelling technique does not give rise to any errors in pure translational components. Therefore, this is as expected.

The added mass and damping matrices consist of 36 coefficients each. Thus, 33 coefficients remain to be checked. In the modelling procedure, all of the rotational components were set to zero. It is therefore difficult to check any coefficients which result from rotational unit acceleration. In the following, the check for three off-diagonal added mass and damping

coefficients is presented. It was assumed that if these correspond well with WAMIT, then so do the other coefficients. The three off-diagonal coefficients which were checked are:

- Roll added mass and damping due to unit acceleration in sway: A_{42} and B_{42} .
- Pitch added mass and damping due to unit acceleration in surge: A_{51} and B_{51} .
- Yaw added mass and damping due to unit acceleration in sway: A_{62} and B_{62} .

For the elastic multi-body model, these quantities were computed by using the same logic that was used when checking the rotational excitation components. The following equations were applied to calculate the multi-body model's added mass coefficients A_{42} , A_{51} and A_{62} .

$$A_{42} = \sum_{b=1}^N (A_{32,b} y_b - A_{22,b} z_b) \quad (6-28)$$

$$A_{51} = \sum_{b=1}^N (A_{11,b} z_b - A_{31,b} x_b) \quad (6-29)$$

$$A_{62} = \sum_{b=1}^N (A_{22,b} x_b - A_{12,b} y_b) \quad (6-30)$$

The corresponding damping coefficients were calculated in the same way. Figure 6-15 shows the three selected off-diagonal excitation components for each wave heading.

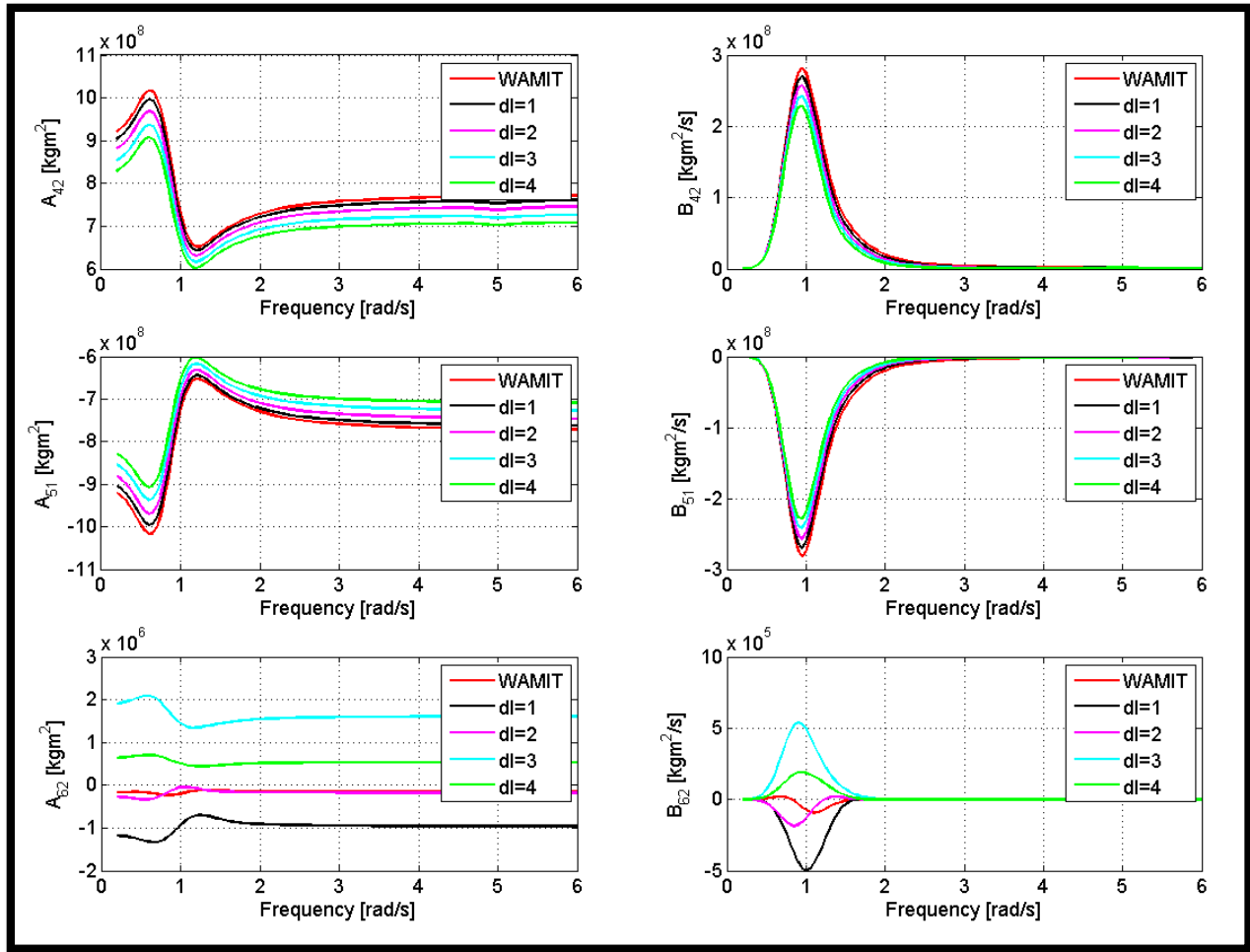


Figure 6-15: Comparison of selected off-diagonal added mass and damping coefficients

The magnitude of the multi-body's A_{42} , B_{42} , A_{51} and B_{51} are slightly lower than what is computed by WAMIT for the hull as a whole. This can be explained with the same reasoning which was used for explaining the differences that were seen in the rotational excitation components. For these coefficients it is also seen that the accuracy is improved by increasing the number of sections.

A_{62} and B_{62} seem to show a more irregular behavior. First, the peaks are not located at the same frequencies as the WAMIT coefficients. Second, the accuracy does not seem to depend on the number of sections. The magnitude of A_{62} and B_{62} are relatively small, and this irregular pattern

could be explained by numerical errors. Of the four section models, dl=2 seems to describe A_{62} and B_{62} the best.

The largest errors for A_{42} and B_{42} occur in the proximity of their respective peaks. Similarly, the largest error for A_{51} and B_{51} occur in the proximity of their respective troughs. Table 6-3 gives the largest error observed in each model for A_{42} , B_{42} , A_{51} and B_{51} . The corresponding percentagewise error is given in brackets. The corresponding values for A_{62} and B_{62} are not included in the table due to the irregular pattern observed for these coefficients.

Table 6-3: Maximum error for selected off-diagonal added mass and damping coefficients

	dl=1	dl=2	dl=3	dl=4
$ A_{42} $ [$\text{kg m}^2 \cdot 10^6$]	21.69 (2.2 %)	49.02 (4.9 %)	81.67 (8.2 %)	111.17 (11.1 %)
$ B_{42} $ [$\text{kg m}^2 / \text{s} \cdot 10^6$]	13.45 (5.8 %)	27.08 (11.6 %)	42.48 (16.5 %)	56.31 (21.9 %)
$ A_{51} $ [$\text{kg m}^2 \cdot 10^6$]	21.49 (2.1 %)	48.42 (4.8 %)	81.35 (8.1 %)	111.11 (11.1 %)
$ B_{51} $ [$\text{kg m}^2 / \text{s} \cdot 10^6$]	13.51 (5.8 %)	26.86 (11.5 %)	42.50 (16.5 %)	56.23 (21.8 %)

As expected, the error at the peak is similar for A_{42} and A_{51} , and for B_{42} and B_{51} respectively. It is also seen that the percentagewise error in damping is larger than the percentagewise error in added mass.

In the next chapter, results are presented from global dynamic analysis with an elastic multi-body hull model corresponding to section model dl=2. dl=2 was chosen because it shows relatively good correspondence in all of the coefficients which were checked, including A_{62} and B_{62} . This means that the multi-body hull model which was used in the global dynamic analysis has a total of 36 SIMO-bodies distributed over the hull: 8 on the main column, 4 on the base node and 8 on each pontoon.

7 Global dynamic analysis with the elastic multi-body hull model

Essential properties of a system's global dynamic behavior can be extracted from basic time-domain simulations. Chapter 6 described how the RIFLEX beam element model of the hull can be expanded with SIMO-bodies which represent hydrodynamic loads from first-order potential theory. This chapter presents and discusses coupled hydro-aero-servo-elastic global dynamic time-domain simulations with the fully-flexible TLPWT system, with the elastic multi-body SIMO-RIFLEX hull model implemented. Also here, the structural modelling which was used in chapter 5 is applied.

In the following, time-domain simulations in three different kinds of environments will be presented and discussed.

1. In still water with steady uniform wind as the only external load. This makes it possible to look at the wind turbine performance and compare it to the NREL 5-MW offshore baseline wind turbine characteristics.
2. In a wind still and still water environment with a temporary pre-defined external nodal force as the only external load. This makes it possible to simulate decay tests from which fundamental natural periods can be estimated.
3. In a combined wind-wave environment with irregular sea and steady uniform wind. This makes it possible to look at the system's behavior in a relatively realistic environment and compare with the behavior of other models.

The following is an outline of this chapter:

- Paragraph 7.1 presents the static deformation of the structure due to hull elasticity when the structure is not subjected to external loads.
- Paragraph 7.2 presents estimations of wind turbine characteristics, such as the generator power and rotor thrust force, as a function of wind speed. A comparison is made with the NREL 5-MW offshore baseline wind turbine characteristics.

- Paragraph 7.3 presents simulated decay tests and an estimation of the fundamental natural periods. A comparison is made with the results of the RIFLEX eigenvalue analysis in chapter 5 and Bachynski's natural period estimations for the reference TLPWT.
- Paragraph 7.4 presents simulations in a combined wind-wave environment. The simulations are first performed with the TLPWT model developed in this study (elastic hull) and then with Bachynski's reference TLPWT model (rigid hull). The results are compared.

7.1 Statically deformed configuration of the hull

The hull deforms also in the static configuration when it is subjected to weight, buoyancy and tendon forces only. The excess buoyancy tries to “pull” the structure up while it is held down by the tendons, which are connected at the tip of each pontoon. If the hull is elastic, the pontoons will bend transversely and the column will deform axially. Consequently, almost every point on the elastic hull will be displaced slightly upwards with respect to the rigid hull, except for the pontoon tips, which are directly connected to the tendons. This deformation effect is not accounted for by a rigid hull.

A rough estimation of the expected static displacement of the pontoon-base node connection can be made analytically. The volume of one pontoon is approximately 750 m^3 . The total volume of the wetted main column and base node is approximately 3400 m^3 . The total volume of the wetted hull (base node, wetted main column and three pontoons) is then roughly 5650 m^3 , and the corresponding mass of the displaced water is about $5790,000 \text{ kg}$. The total steel mass of the hull is around $1293,000 \text{ kg}$, while the ballast and turbine have a mass of $1389,000 \text{ kg}$ and $600,000 \text{ kg}$ respectively. The total mass of the TLPWT structure is then approximately $3182,000 \text{ kg}$. This gives an excess buoyancy force of around 24.6 MN , which is approximately equal to the total downward directed force provided by the three tendons. Each pontoon is thus subjected to a vertical force of roughly 8.2 MN . The pontoon bending stiffness is 551 GNm^2 (chapter 3). With these numbers, equation 4-1 (Euler-Bernoulli bending formula) predicts a displacement of 4.6 cm upwards at the pontoon-base node connection.

Figure 7-1 gives a visualization of the statically deformed configuration of the hull. Note that the actual displacements are scaled with a factor of 100 in this figure. The data points in the figure correspond to the nodes where the SIMO-bodies are inserted. These nodes will be referred to as the “SIMO-body nodes” from now on.

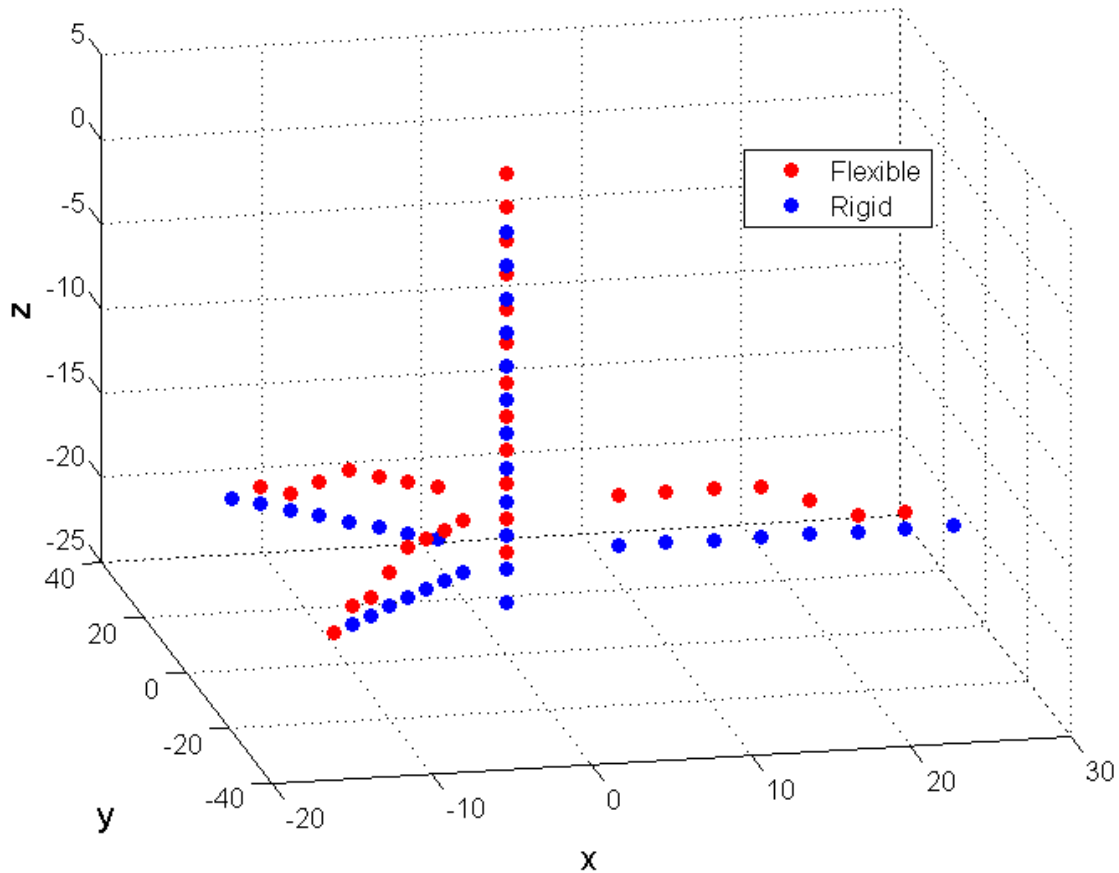


Figure 7-1: Static deformation shape of the elastic hull. Displacements due to elasticity are scaled with a factor of 100.

Figure 7-2 shows the actual vertical displacements which SIMO-RIFLEX has calculated for each SIMO-body node due to the hull elasticity.

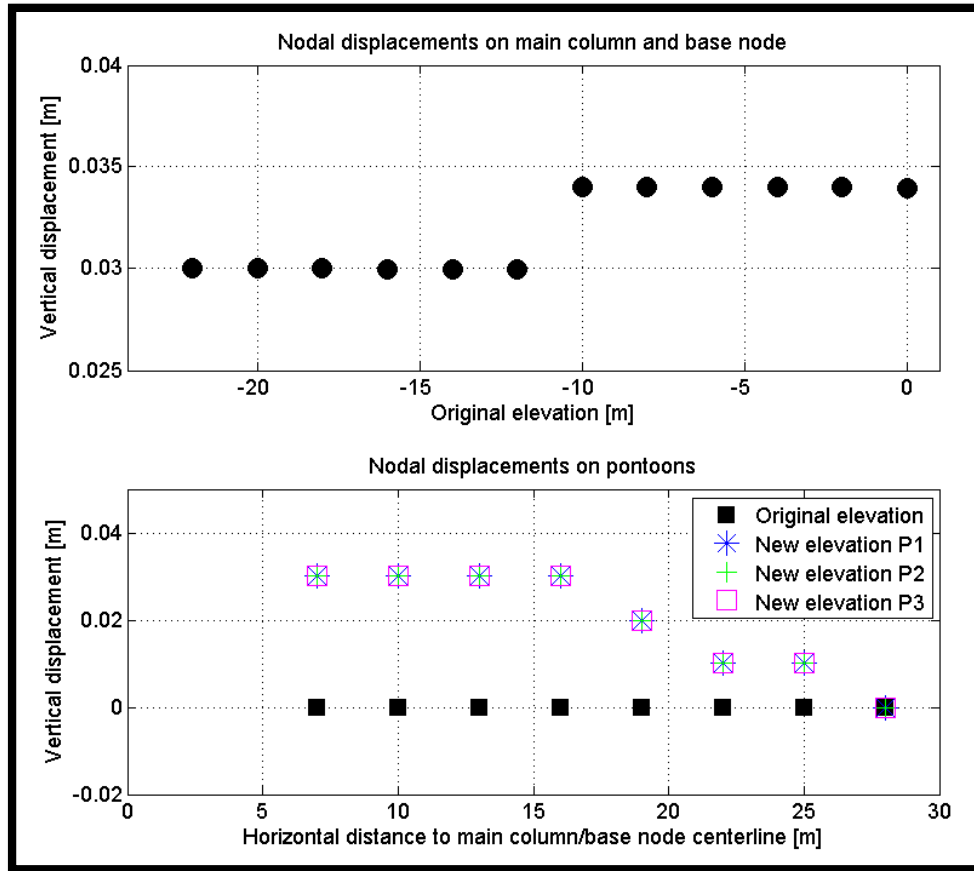


Figure 7-2: Static vertical displacement of all SIMO-body nodes due to hull elasticity

The base node is modelled as rigid. All of the SIMO-body nodes which originally were located between elevations -16 m and -22 m on the main column/base node must therefore have the same displacement. This is confirmed by the figure. The base node has a positive displacement of 3 cm. The SIMO-body nodes which are located close to the waterline on the main column have a larger displacement than the displacement of the SIMO-body nodes which are located on the base node. At the waterline the displacement is 3.4 cm. This indicates that the column deforms (strains) axially.

Each pontoon shows the same deformation pattern. This is logical because each pontoon is modelled in the exact same way and subjected to the same load. The SIMO-body nodes which are located at the tendon connection have zero displacement. The pontoons are rigidly connected to the base node. Therefore, the SIMO-body nodes which are located on the pontoons and close to the base node connection must have the same displacement as the base node. This is confirmed by the figure. The displacement of 3 cm at the pontoon-base node connection is

caused by bending of the pontoons. This is slightly less the 4.6 cm, which was predicted by the analytical estimation. An explanation could be that the analytical estimation did not account for distributed buoyancy and weight over the pontoons, but assumed all forces to apply at the pontoon-base node connection. However, the numerical result does have the same order of magnitude as the analytical estimation.

7.2 Wind turbine performance

To check the performance of the wind turbine, simulations with steady uniform wind and still water can be performed. In this way, the power curve, rotor thrust force and other turbine characteristics can be found as a function of the wind speed. Alternatively, instead of having no waves, a sea state with very small and very long waves can be applied. A sea state with very small and very long waves will give a sea environment which is similar to still water. The version of SIMO-RIFLEX which was used for the simulations in this study requires the environment to have some waves present. Therefore, a sea state with very small and very long waves was chosen. The sea state used here is described by a JONSWAP spectrum with $H_s=0.0001$ m and $T_p=500$ s.

The rotor speed, power curve, rotor thrust force, blade pitch angle, generator speed and generator torque as a function of the wind speed are shown in Figure 7-3. The turbine is intended to perform in accordance with the NREL 5-MW offshore baseline turbine. Table 7-1 gives some key numbers of the NREL 5-MW offshore baseline turbine [25].

Table 7-1: NREL 5-MW offshore baseline turbine key numbers

Parameter	Value
Rated wind speed	11.4 m/s
Rated rotor speed	12.1 RPM
Rated mechanical power	5.296610 MW
Minimum blade pitch angle	0 degrees
Rated generator speed	1173.3 RPM
Gear ratio	97 : 1
Rated generator torque	43.1 kNm

These numbers will, together with the general shape of the curves, be used to determine whether the turbine performance is satisfactory.

As shown in Figure 7-3 the rotor speed is increasing with the wind speed until the rated wind speed of 11.4 m/s is reached. After this, the rotor speed is kept constant at 12.1 RPM, which is the rated rotor speed of the NREL 5-MW offshore baseline turbine. The generator power is increasing with the wind speed until it reaches 5.2966 MW at a wind speed of 11.4 m/s. For wind speeds higher than the rated wind speed, the power is kept constant. 5.2966 MW corresponds well with the rated mechanical power of the NREL 5-MW offshore baseline turbine. Note that the rated mechanical power is slightly higher than 5-MW because generator efficiency losses are not taken into account. The rotor thrust force is increasing until the rated wind speed is reached. After this, the thrust force decreases because the blade pitch angle is increased. The pitch angle is zero, which is also the minimum pitch angle of the NREL 5-MW baseline turbine, for wind speeds lower than the rated wind speed. At the rated wind speed, the blades start to pitch. The pitch angle increases with wind speed for wind speeds higher than the rated wind speed in order to limit the power. The generator speed shows a trend similar to that of the rotor speed and mechanical power. The generator speed is 97 times higher than the rotor speed. This corresponds well with the gear ratio of the NREL 5-MW offshore baseline turbine. The generator speed is kept constant at 1173.3 RPM for wind speeds higher than the rated wind speed. This also corresponds well with the rated generator speed of the NREL 5-MW offshore baseline turbine. The generator torque is increasing until the rated wind speed is reached. After this, it is kept constant at 43.1 kNm, which is also the rated generator torque of the NREL 5-MW offshore baseline turbine.

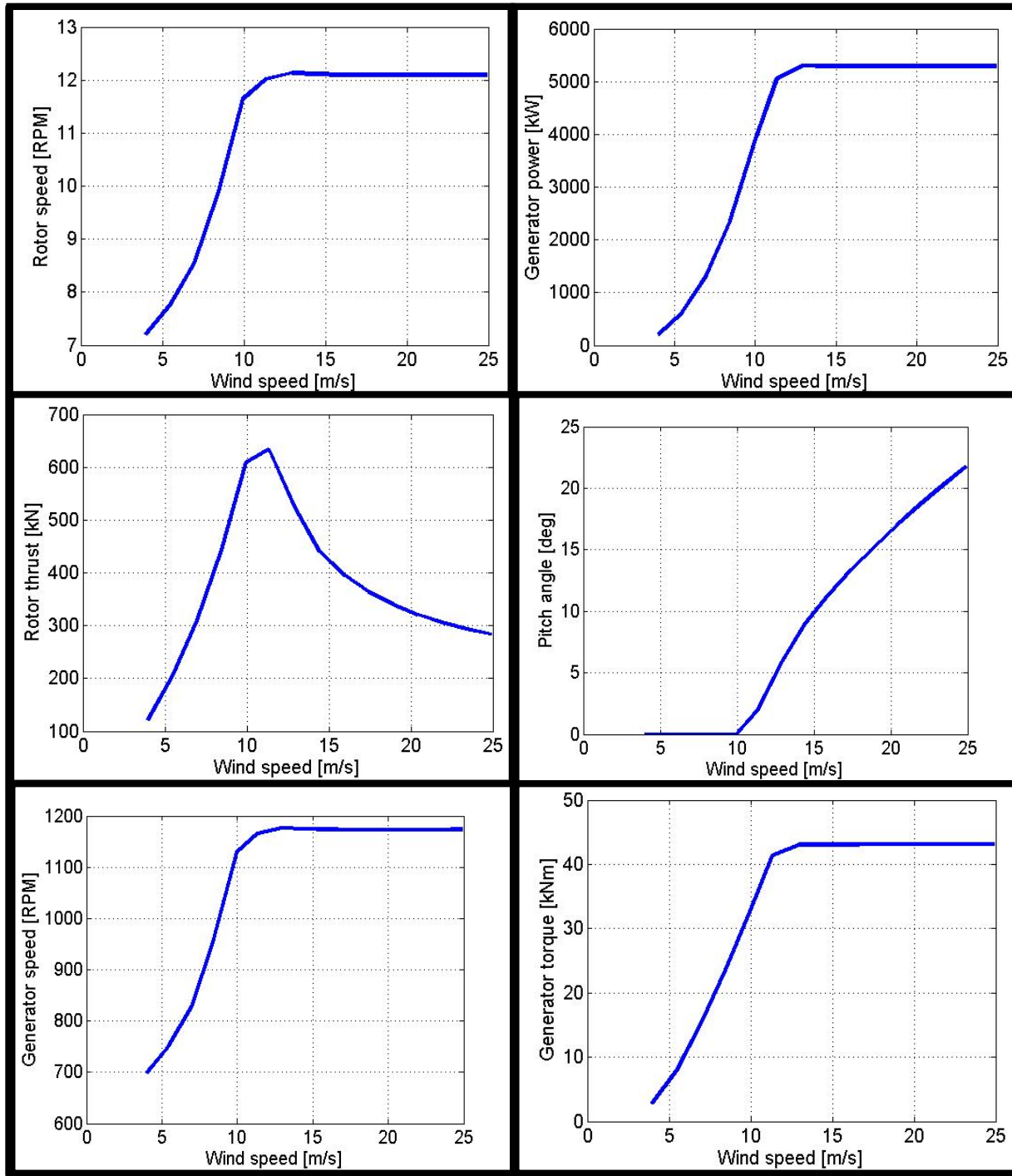


Figure 7-3: Top left: Rotor speed. Top right: Mechanical power. Middle left: Rotor thrust. Middle right: Pitch angle. Bottom left: Generator speed. Bottom right: Generator torque.

Based on the turbine characteristics shown in Figure 7-3 and the accompanying discussions, it is assumed that the turbine is performing in accordance with the NREL 5-MW offshore baseline turbine. Next, the fundamental natural periods of the system are estimated from simulated decay tests.

7.3 Fundamental natural periods

In the absence of an external force, a system tends to oscillate with a period equivalent to its fundamental natural period. Therefore, decay tests can be used to estimate the fundamental natural periods of a system. In this study, the fundamental natural periods for surge, heave, pitch and yaw were estimated from simulated decay tests. The decay tests were performed twice. First without quadratic viscous damping and then with quadratic viscous damping. This means that one decay test includes linear potential damping only while the other includes both linear and quadratic damping. The quadratic damping was calculated according to the drag force in the Morison equation. The drag coefficient was set equal to 0.8, which is the same as in paragraph 3.1.2, for both pontoons and column. The reference area for the pontoons was set equal to the pontoon height. For the column, the reference area was set equal to the column diameter.

Thus, the natural periods derived here correspond to damped natural periods. The decay tests were performed by releasing the structure from an offset position. The natural periods were then derived from the decaying motion of the SIMO-body which is located at the waterline when the structure is at rest. Note that higher natural periods were not investigated here.

To bring the structure to a desired offset position a force or moment was applied at the node at the waterline. For surge and heave decay a force was applied. For pitch and yaw a moment was applied. The force/moment was a combination of a ramp and a constant force/moment. At time 50 s the ramp force/moment was applied. From time 100 s to 200 s the force/moment was kept constant. Figure 7-4 shows the time series of the force used in the surge decay test.

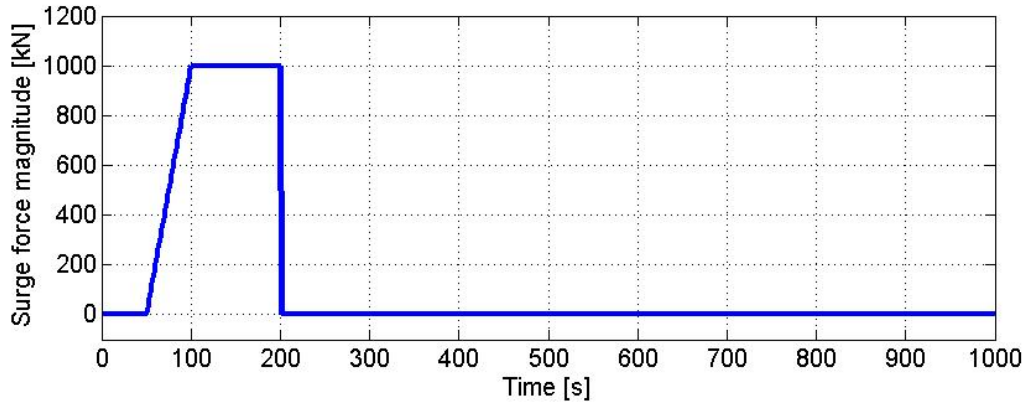


Figure 7-4: Force applied in surge decay test

The force/moment in the other decay tests were similar, only with different magnitudes. Because the system is much stiffer in heave than in surge, the heave force which is required to give the structure a significant initial displacement is relatively large compared to the corresponding surge force. Similarly, because the system is much stiffer in pitch than in yaw, the chosen pitch moment magnitude is relatively large compared to the chosen yaw moment magnitude. The magnitude and duration of the forces/moments applied in each decay test are shown in Table 7-2.

Table 7-2: Magnitude and duration of forces and moments applied in decay tests

Motion	Force/moment magnitude	Ramp duration [s]	Constant force duration [s]
Surge	1000 kN	50 s	100 s
Heave	20 000 kN	50 s	100 s
Pitch	260 000 kNm	50 s	100 s
Yaw	3000 kNm	50 s	100 s

Time series of the motion in each decay test are presented in Figure 7-5 through Figure 7-10.

At time 200 s the force is removed and the structure is released from its offset position. From this moment, the structure shows a decaying oscillating motion. The period of this oscillation is used as an estimate for the natural period.

7.3.1 Surge decay simulation

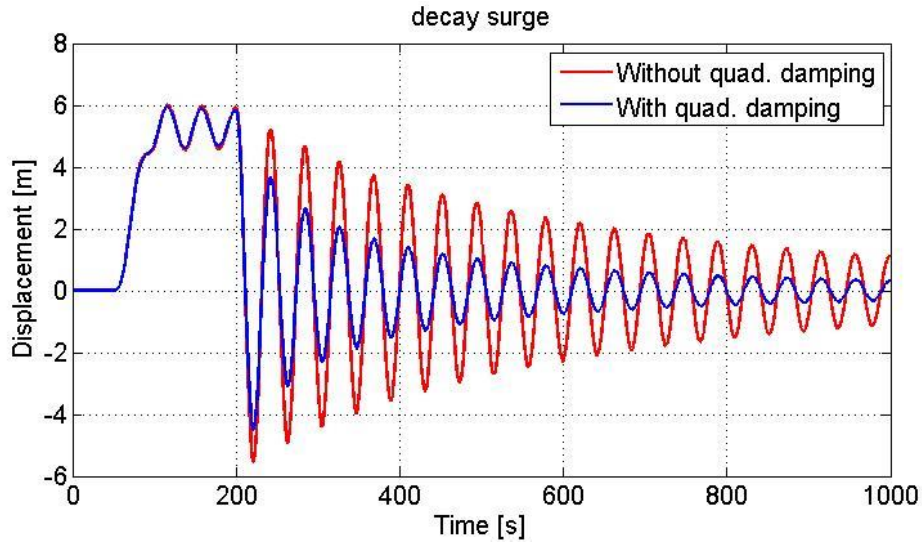


Figure 7-5: Time series of the surge decay tests

Figure 7-5 shows the time series of the surge decay test with and without quadratic damping. The oscillation amplitude is clearly reduced by the presence of quadratic damping. The influence on the oscillation period is much less evident. Without quadratic damping, the oscillation period is 42.03 s. With quadratic damping, it is increased to 42.09 s.

7.3.2 Heave decay simulation

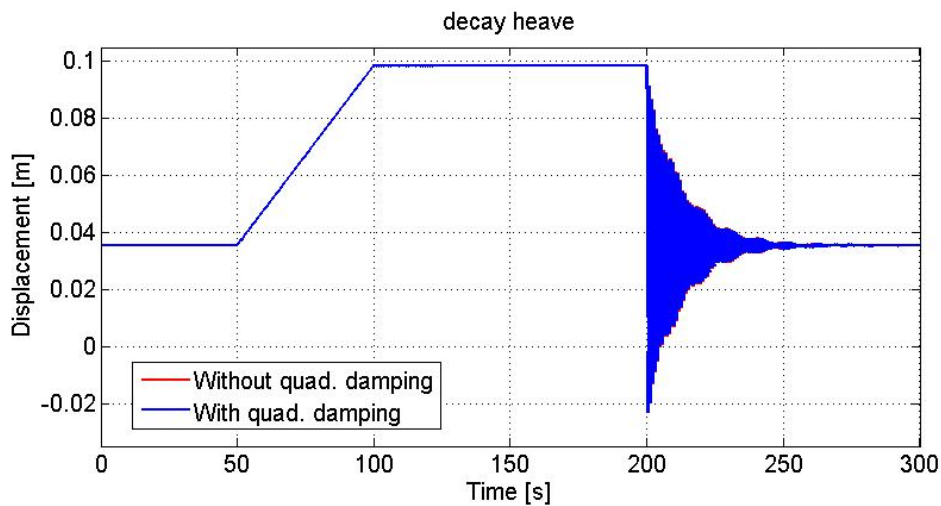


Figure 7-6: Time series of the heave decay tests

Figure 7-6 shows the time series of the heave decay test with and without quadratic damping. It can be seen that the oscillations are damped out faster than in the surge decay test. Also, it can be seen that the body oscillates around an elevation of approximately 3.5 cm, which corresponds well with the findings presented in paragraph 7.1. The heave oscillations are high-frequency oscillations, and the oscillation period is very small compared to the length of the time series. Therefore, zooming in on the time series gives a better picture of the oscillation period.

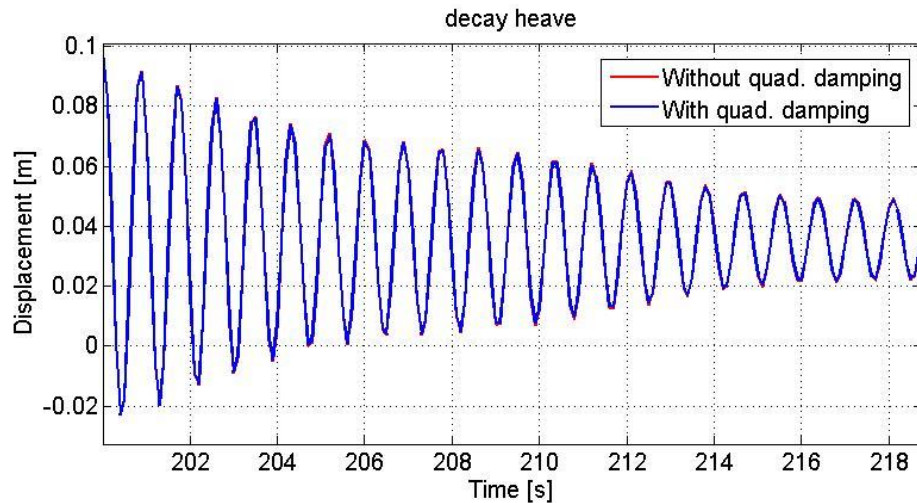


Figure 7-7: Zooming in on the time series of the heave decay test

Figure 7-7 shows the heave oscillations in the heave decay test during the first 10 seconds after the structure is released from its offset position. The influence of the quadratic damping on both oscillation amplitude and period is negligible. In both cases, the oscillation period is 0.86 s.

7.3.3 Pitch decay simulation

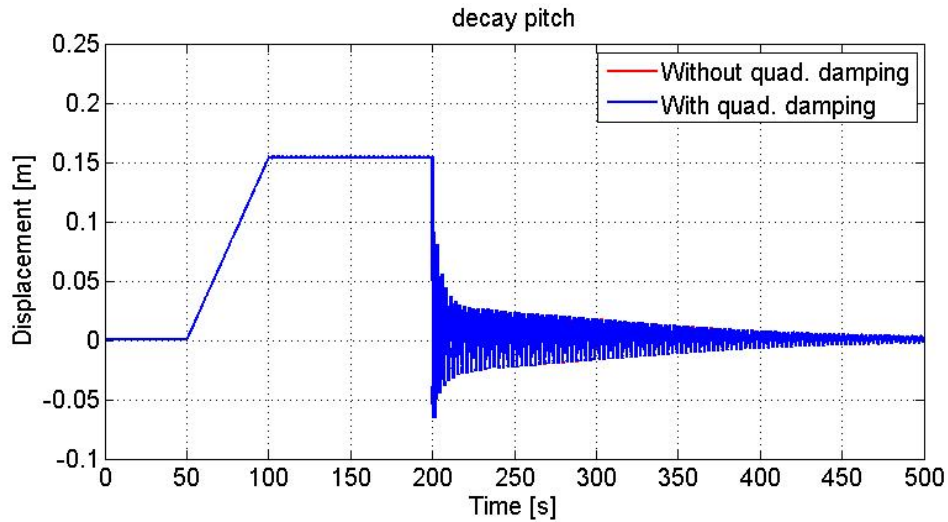


Figure 7-8: Time series of the pitch decay tests

Figure 7-8 shows the time series of the pitch decay test with and without quadratic damping. Similar to the heave decay test, the oscillation period is very small compared to the length of the time series. Again, zooming in gives a better picture of the oscillation period.

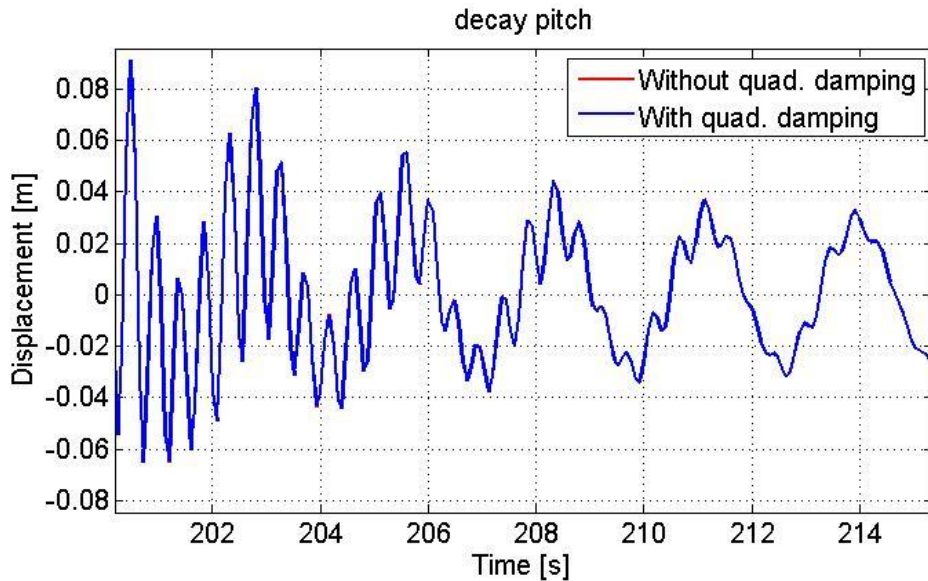


Figure 7-9: Zooming in on the time series of the pitch decay tests

Figure 7-9 shows the pitch oscillations during the first 15 seconds after the structure is released from its offset position. Two oscillation periods can be observed. The lower of these corresponds to the platform pitch motion, while the higher corresponds to the tower bending motion. Again,

the influence of the quadratic damping is negligible. The oscillation period of the platform pitch motion is 0.46 s, while the tower bending oscillation period is 2.79 s.

7.3.4 Yaw decay simulation

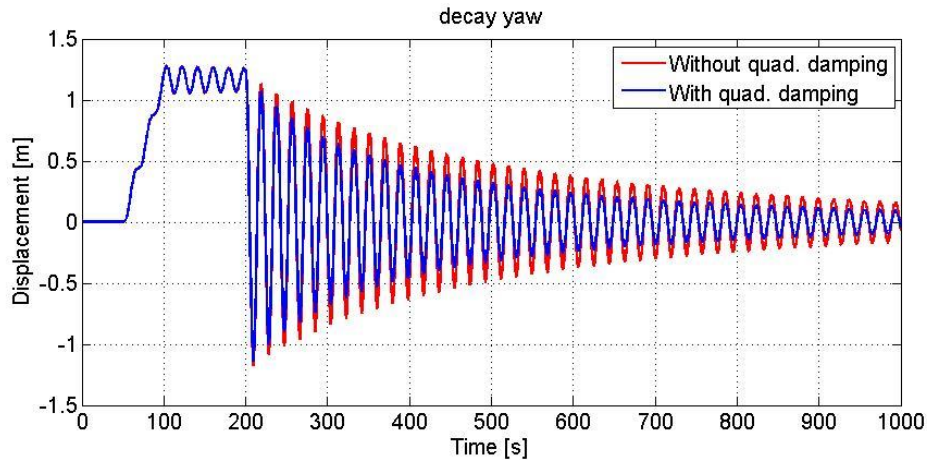


Figure 7-10: Time series of the yaw decay tests

Figure 7-10 shows the time series of the yaw decay test with and without quadratic damping. It can be seen that the quadratic damping reduces the oscillation amplitude. However, the influence on the oscillation period is negligible. In both cases, the oscillation period is 18.90 s.

7.3.5 Comparing with previous results

The fundamental natural periods of the TLPWT have now been investigated with four different hull models:

1. Bachynski's model [9], which is rigid and includes frequency-dependent added mass, radiation damping and excitation.
2. The RIFLEX beam element model of chapter 5, which includes 2-D added mass coefficients, but no damping.
3. The elastic multi-body model of chapter 6, which includes SIMO-bodies that represent frequency-dependent added mass, radiation damping and excitation from WAMIT.
4. The same model as in 3, but also including quadratic damping estimated with the drag equation.

Table 7-3 summarizes the results from all of these models.

Table 7-3: Comparison of fundamental natural period estimations between the various models

	Bachynski's reference model	RIFLEX beam element model	SIMO-RIFLEX elastic multi-body model without quadratic damping	SIMO-RIFLEX elastic multi-body model with quadratic damping
Surge [s]	41.86	39.70	42.03	42.09
Heave [s]	0.60	0.78	0.86	0.86
Pitch [s]	2.76/0.39	2.79	2.79/0.46	2.79/0.46
Yaw [s]	18.63	19.71	18.90	18.90

First, it can be seen that the natural periods of the SIMO-RIFLEX elastic multi-body model without quadratic damping are very similar or identical to the natural periods of the same model with quadratic damping. This indicates that the quadratic damping on the hull has a low influence on the natural periods of the structure.

Bachynski's rigid hull model incorporates hydrodynamic loads from first-order potential theory and quadratic damping. The rigid hull is modelled with one SIMO-body for the whole hull. When comparing the natural periods of Bachynski's reference model with the natural periods of the elastic multi-body SIMO-RIFLEX model, it can be seen that all of the natural periods have increased. The flexibility of the hull can be expected to influence the platform pitch and heave natural periods the most. The largest percentagewise increase is seen in the heave natural period. An increase from 0.6 s to 0.86 s is an increase of 43 %. The platform pitch natural period has increased from 0.39 s to 0.46 s, which is an increase of 18 %. The increase is much less significant in yaw, surge and pitch tower bending motions.

The comparison between Bachynski's reference model and the RIFLEX beam element model was made in chapter 5. The natural periods of the RIFLEX beam element model was performed with RIFLEX' inbuilt eigenvalue analysis tool, which does not account for damping and uses 2-D added mass coefficients. This could be the reason that the RIFLEX beam element models' surge natural period does not correspond particularly well with the surge natural periods of other models, which were estimated with decay tests and 3-D potential added mass and damping coefficients. The RIFLEX beam element model's pitch tower bending natural period is the same as for that of the elastic multi-body SIMO-RIFLEX model. Its yaw natural period is slightly

higher than that of the other models. Its heave natural period is higher than that of the reference model, but lower than that of the elastic multi-body SIMO-RIFLEX models.

In the following, the motions of the elastic multi-body SIMO-RIFLEX model with quadratic damping will be compared to the motions of Bachynski's reference model (1 SIMO-body) in selected wind-wave environments. Note that Bachynski provided her original SIMO-RIFLEX model to the author for this specific comparison.

7.4 Simulations in a combined wind-wave environment

Three different environmental conditions were chosen for comparing the motions predicted with Bachynski's rigid single-body model and the elastic multi-body model. The environmental conditions are not intended to give any basis for extreme value analysis. The purpose is to simply compare the two models' response in relatively basic environmental conditions. The wind is steady and uniform in each condition, while the sea state is described by a JONSWAP spectrum. No current is included. The first condition has below-rated wind speed, the second has rated wind speed and the third has above-rated wind speed. Table 7-4 shows the wind speed, significant wave height and peak period for each condition. The wind and waves have a heading angle of zero degrees in all conditions. Thus, no wind-wave misalignment is considered here.

Table 7-4: Environmental conditions for global dynamic time-domain simulations

	T_p [s]	H_s [m]	Wind speed [m/s]
Condition 1	9.8	2.5	8
Condition 2	11	3.1	11.4
Condition 3	12	4.0	14

In paragraphs 7.4.1 and 7.4.2 the simulation results in each condition are presented for both models, and a comparison is made. The following will be presented and discussed for each condition:

- Time series of the nacelle surge, sway, heave, roll, pitch and yaw motion.
- Power spectrum for the bending moment about the y-axis at the tower base.
- Power spectrum for the tension at the top of each tendon.

7.4.1 Simulation results in condition 1

Motion response

The motion time series are shown in Figure 7-11. The blue line is the rigid single-body model, while the red line is the elastic multi-body model.

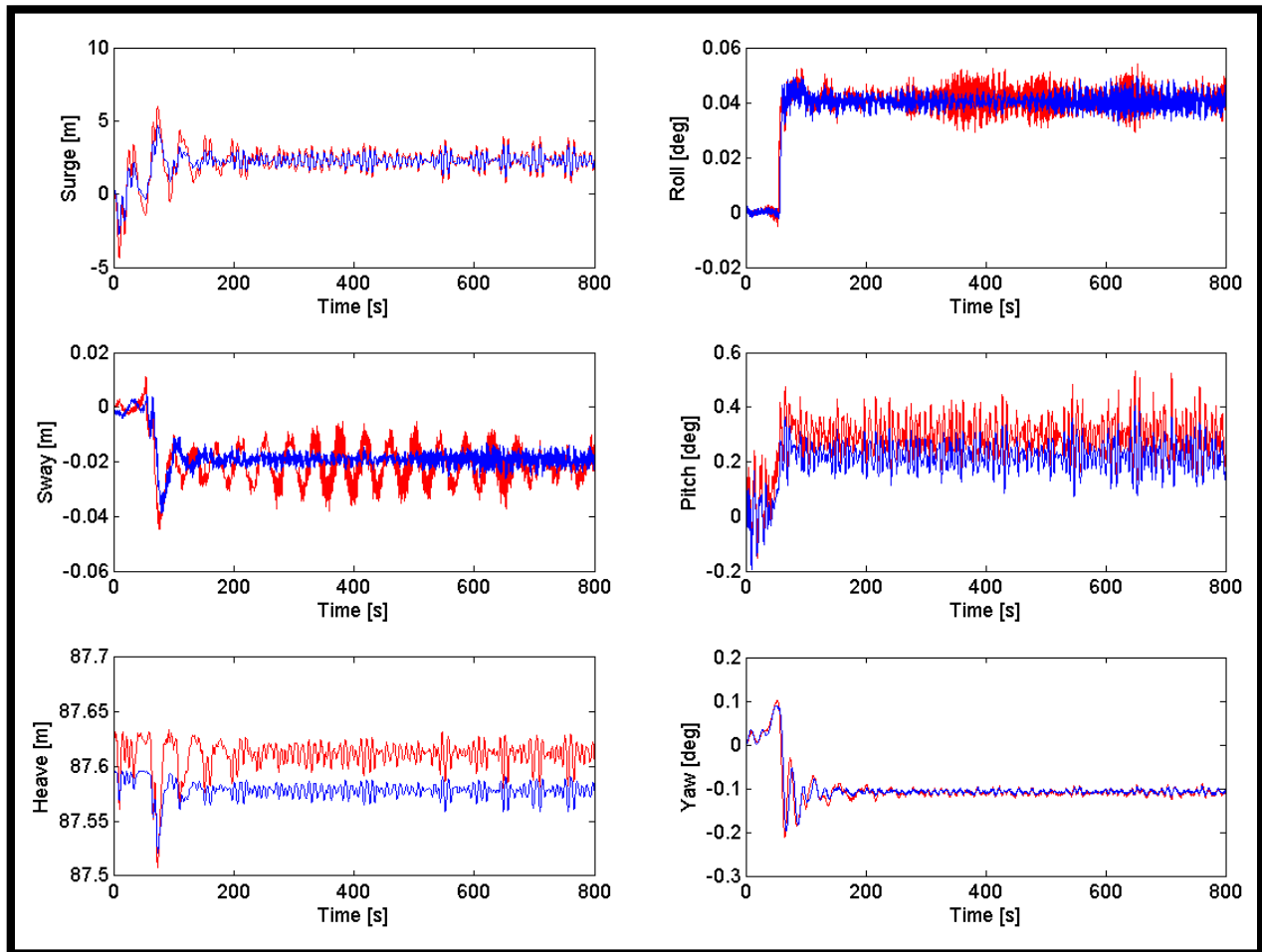


Figure 7-11: Time series of motion response in condition 1

Table 7-5 shows the mean and standard deviation of the last 400 s of each motion response in condition 1. From looking at the time series, the system seems to reach some steady state after approximately 200 s. It was assumed that the last 400 s are representative for the system's steady state response in the given condition.

Table 7-5: Mean and standard deviation of each steady state motion response in condition 1

		Surge [m]	Sway [m]	Heave [m]	Roll [deg]	Pitch [deg]	Yaw [deg]
Elastic multi-body model	Mean	2.315	-0.021	0.012	0.041	0.296	-0.109
	Standard deviation	0.556	0.006	0.009	0.004	0.070	0.006
Rigid single-body model	Mean	2.286	-0.019	-0.022	0.040	0.221	-0.108
	Standard deviation	0.398	0.002	0.006	0.003	0.054	0.004

The surge motions are very similar. Both models oscillate around approximately the same mean position, while the elastic multi-body model has slightly larger oscillation amplitudes around the mean position. The same can be seen in the sway and yaw motion time series. This difference can be explained by the hull elasticity. Because the wind and waves are head on, the surge motion is positive, while the yaw and sway motions are very small. For the same reason, the roll motions are very small. The oscillations in sway and roll can be explained by the rotation of the rotor.

The nacelle heave motion of the elastic multi-body model oscillates around a mean position which is slightly higher than that of the rigid single-body model. This corresponds well with the findings presented in paragraph 7.1. Furthermore, the heave motion of the elastic multi-body model shows larger variation around the mean. This can be explained by the hull elasticity.

The difference in pitch motion shows a trend similar to the difference in heave motion. The pitch motion of the elastic multi-body model oscillates around a mean value which is higher than that of the rigid single-body model. This is due to the elasticity of the elastic hull's main column. A steady wind will cause a steady bending of the hull's main column. In the rigid single-body model, this is not accounted for.

Bending moment about the y-axis at the tower base

The power spectrum for the bending moment about the y-axis at the tower base is presented in Figure 7-12. Again, the red line represents the elastic multi-body model, while the blue line

represents the rigid single-body model. The power spectrum is based on the last 400 s of the time series.

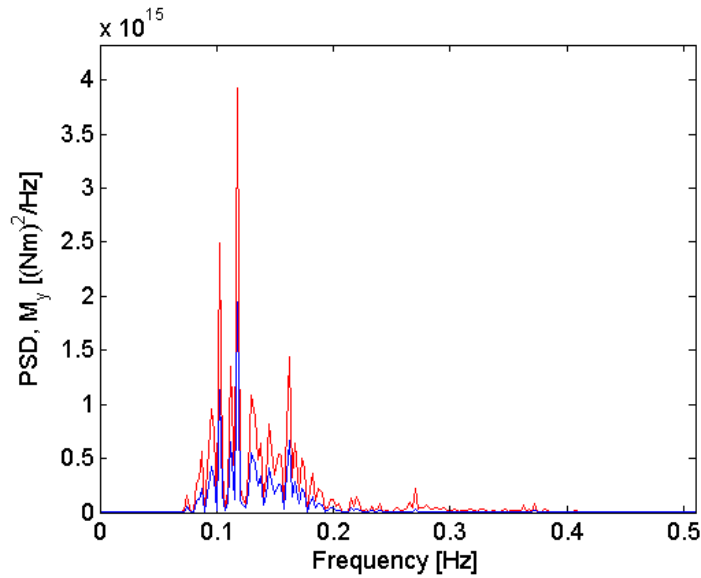


Figure 7-12: Power spectrum for the bending moment about the y-axis at the tower base in condition 1

Figure 7-12 shows that the spectral density is relatively high in the proximity of the wave frequency. Furthermore, it is seen that the spectral density is higher for the elastic multi-body model. This indicates that elastic hull causes bending moment amplification. This observation corresponds well with the time series of the pitch motion in Figure 7-11.

Tendon tensions

Figure 7-13 presents the power spectrum for the tension at the top of each tendon. T_1 denotes the tension in the tendon which is connected to pontoon 1. This tendon will be referred to as tendon 1. The same logic applies for the two other tendons. The power spectra are based on the last 400 s of the time series.

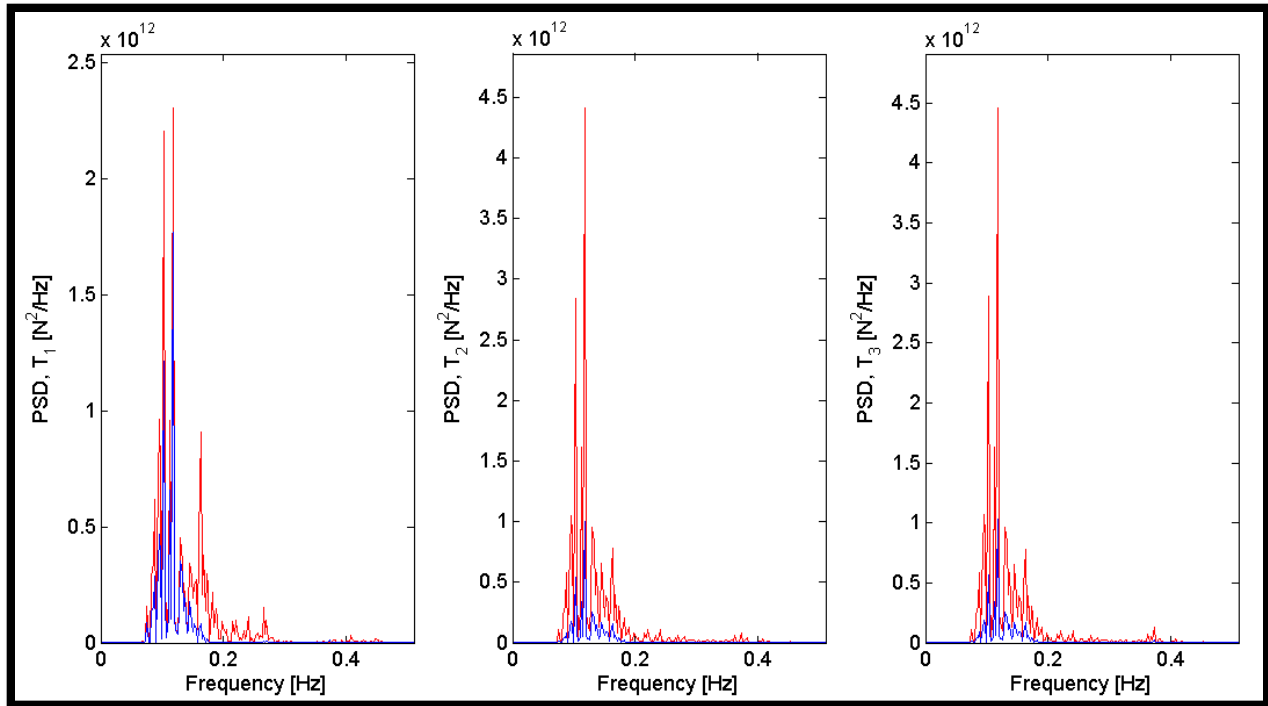


Figure 7-13: Power spectrum for the tension at the top of each tendon in condition 1

Again, the spectral density is high in the proximity of the wave frequency. Also now, the spectral density is higher for the elastic multi-body model. This indicates that the elastic hull causes tendon tension amplification. It is seen that the power spectra of T_2 and T_3 are nearly identical. This can be explained by the very small roll motions.

7.4.2 Simulation results in conditions 2 and 3

The responses in conditions 2 and 3 are very similar to those in condition 1. The same conclusions can be drawn, and they will not be repeated here. The time series and power spectra can be found in Appendix E.

8 Internal loads in the hull

It is important to estimate the internal forces and moments in order to size or design structural parts. The internal loads are often decomposed into axial forces, shear forces and bending moments. An example of an internal load in the TLPWT is the axial force in the main column induced by the weight of the tower and turbine. Other examples are the shear force in the main column due to the aerodynamic rotor thrust force and the bending moment in the pontoon due to the tendon tension. The structural boundary conditions are also important for the internal loads. For instance, a pinned connection, such as the tendon connection, cannot take up any moment. The internal moment in the pontoons can therefore be expected to be much smaller close to the tendon connection than close to the base node connection.

For the static internal loads, the distribution of weight and buoyancy and the location of the tendon connection is important. Therefore, both the distribution of structural mass and the overall design of the TLPWT system are important. For instance, the distance between the pontoon-base node connection and the pontoon-tendon connection is important for the internal static shear force and bending moment in the pontoon.

For the dynamic internal loads, the distribution and amount of mass, damping and stiffness in the system are important. The relationship between these determine the frequency-dependency of the system's response. The internal reaction forces depend on the system's response and are therefore frequency-dependent too. The frequency-dependent added mass and radiation damping from the radiation pressure contribute to the system's mass and damping. In this way, they also influence the internal dynamic loads. The wave exciting forces and moments from the diffraction pressure influence the internal dynamic loads by exciting the system at various frequencies. Together with the added mass, the structural mass determines the amount and distribution of mass in the system. Similarly, the structural damping (which is very low) and the radiation damping determine the amount and distribution of damping in the system. Additionally, there can be contributions from aerodynamic damping. The amount and distribution of stiffness in the system is determined by the tendons' tension and structural properties, the tendons' connection to the hull and the seabed, the hydrostatic restoring forces and the structural description of the

hull, tower and wind turbine. Because the stiffness of the system influences the internal dynamic loads, the use of an elastic hull results in different internal dynamic loads than the use of a rigid hull.

This chapter has two purposes. The first purpose is to look at amplification of internal dynamic loads in the hull due to structural elasticity. Two different kinds of analyses were carried out to do this:

- Dynamic analysis with a rigid structure and wave loading as the only external loading.
- Dynamic analysis with an elastic structure and wave loading as the only external loading.

The second purpose of this chapter is to evaluate the proposed scantling design, which was presented in chapter 3. This evaluation is based on internal loads computed at the base of pontoon 1 and at various elevations on the main column.

Note that the simulations in this entire chapter were carried out for a wave heading of 0 degrees only.

The following is an outline of this chapter:

- Paragraph 8.1 presents the investigation of amplification of internal dynamic loads due to hull elasticity.
- Paragraph 8.2 presents the evaluation of the scantling design. This evaluation is based on the system's response in conditions 1, 2 and 3 from paragraph 7.4.

8.1 Amplification of internal dynamic loads due to hull elasticity

The internal dynamic loads were compared at four different cross sections on the hull. These cross sections are depicted in Figure 8-1. There are two cross sections on the column (yellow) and two cross sections on pontoon 1 (purple). The figure also shows the cross section numbering, which will be used throughout this chapter when referring to the respective cross sections.

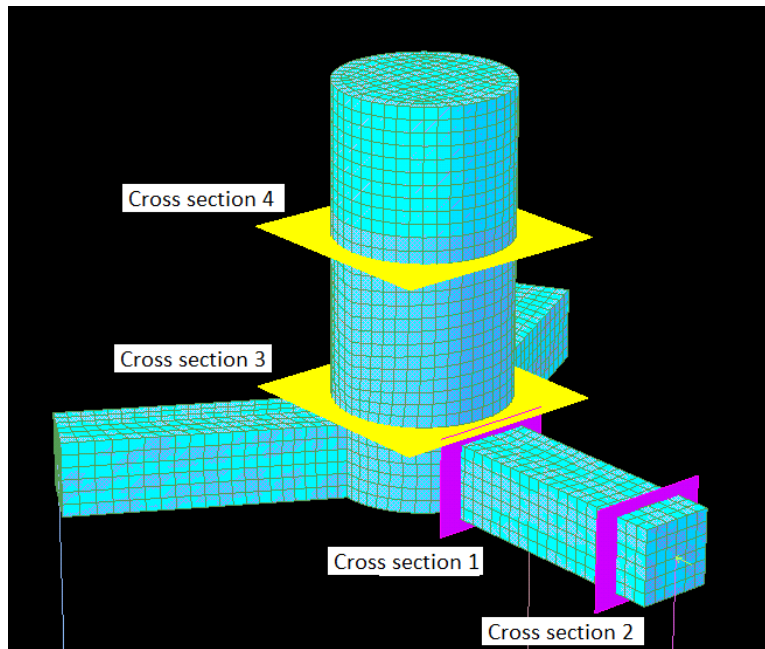


Figure 8-1: Selected cross sections for investigation of amplification of internal dynamic loads due to hull elasticity

Table 8-1 lists the location of the center point of each cross section in the global coordinate system. For each cross section, the internal loads are computed in the center point.

Table 8-1: Location of each selected cross sections' center point in the global coordinate system

	Cross section 1	Cross section 2	Cross section 3	Cross section 4
x [m]	8	25	0	0
y [m]	0	0	0	0
z [m]	-19	-19	-15	-2

Paragraph 8.1.1 presents the results from dynamic analysis with a rigid structure and wave loading as the only external loading. This analysis was performed in the frequency domain, using HydroD. Paragraph 8.1.2 presents the results from dynamic analysis with an elastic structure and wave loading as the only external loading. This analysis was performed in the time domain, using SIMO-RIFLEX and the elastic multi-body model which was developed and tested in previous chapters.

8.1.1 Wave-only frequency-domain analysis with a rigid structure

For the analysis with a rigid structure and wave loading as the only external loading, the WADAM subroutine of the DNV Sesam package module HydroD was applied. WADAM analysis is fully linearized and performed in the frequency-domain. The advantage of linear systems is that they are computationally cheap compared to non-linear systems. However, in many cases, non-linearities are present, such as quadratic viscous damping or non-linear mooring stiffness characteristics. Linear theory is therefore not always able to accurately describe the actual system dynamics. This is important to keep in mind when interpreting the results from WADAM. First-order potential theory was applied for calculating the loads on the structure, using a panel discretization equal to that in paragraph 6.2. Because WADAM is based on WAMIT, the total hydrodynamic loads on the structure are exactly the same here as in chapter 6. In addition to this, linearized Morison loading on the tendons was included. The structure depicted in Figure 8-1 is the model which was applied for the WADAM analysis. The mass of the turbine was included by modelling the “roof” of the TLP hull as very thick, such that the mass of the plating at the top of the TLP hull includes the mass of the turbine. Similarly, the ballast was included by modelling the “floor” as very thick, such that the mass of the plating at the bottom of the TLP hull includes the mass of the ballast. Consequently, the model has the correct total mass, but not the correct mass distribution because the masses of the rotor, nacelle and tower have been concentrated and moved down to an elevation of 10 m above the mean water level. This simplification can be expected to reduce the model’s moment of inertia in pitch and roll especially. Before continuing to the estimated internal loads, it can be useful to study the system’s linear motion transfer function, or Response Amplitude Operator (RAO).

RAO computed in HydroD

An RAO gives a system’s motion response, normalized with the wave amplitude, as a function of frequency for a given wave heading. The RAO computed by WADAM for a wave heading of 0 degrees is presented in Figure 8-2. The RAO was computed for a reference point with coordinates (0,0,0). This means that the RAO is for a point located at the centerline of the main column and at an initial elevation equal to the MWL. Note that the RAO predicts the system’s *linear response to an oscillatory load*.

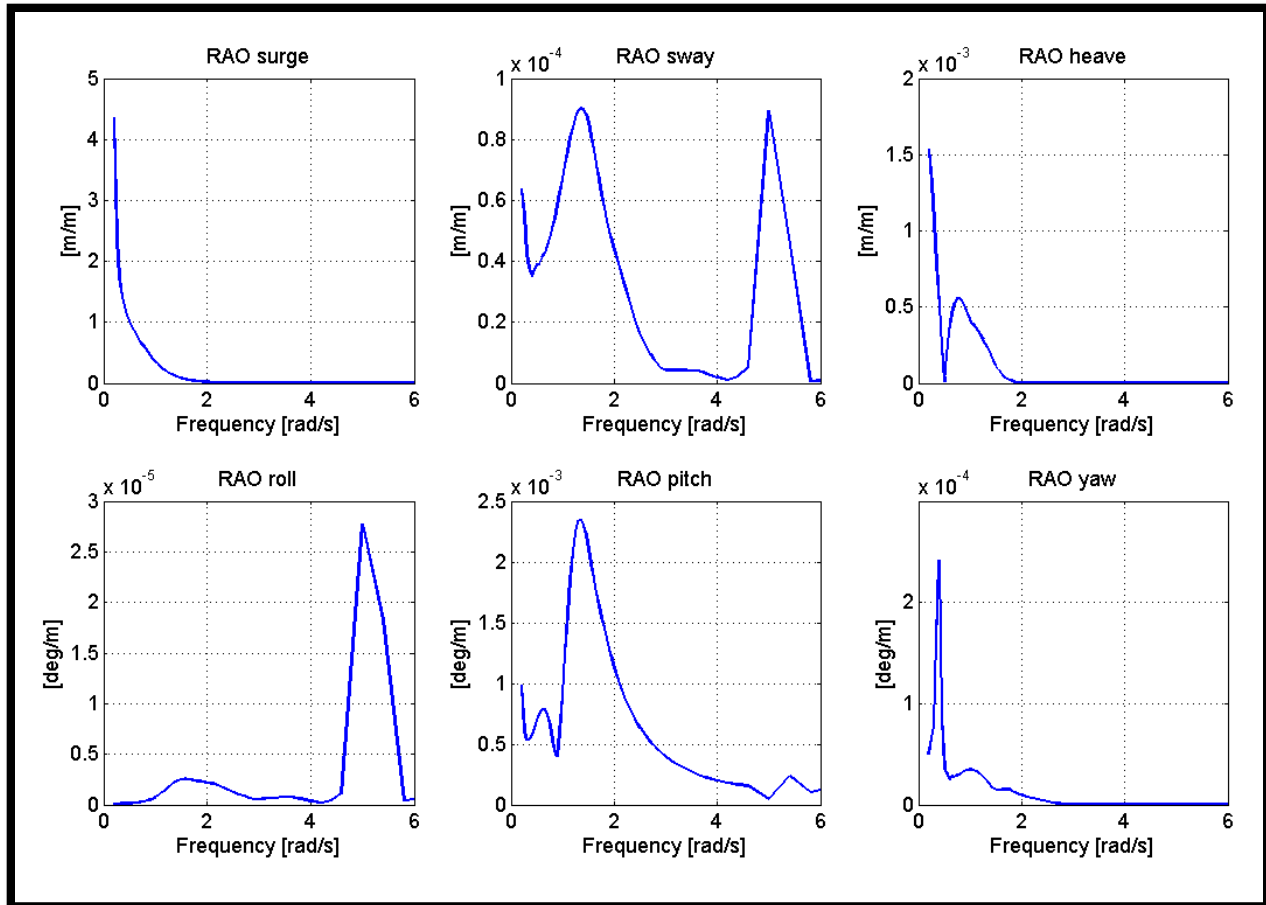


Figure 8-2: RAO computed with WADAM in HydroD for a wave heading of 0 degrees

The figure indicates that WADAM predicts almost no sway, roll or yaw motion. This makes sense because the waves have a heading of 0 degrees. The predicted surge motion is relatively large and rapidly decreasing with frequency for the lower frequencies. This can be explained by the natural frequency in surge located at approximately 0.15 rad/s, and by the rapidly increasing surge damping in this regime (Figure 6-5). The heave motion is relatively large for the lowest frequencies. This is because the heave motion is coupled to the surge motion. Furthermore, it is seen that the predicted frequency-dependency of the heave motion is very similar to that of the heave excitation (Figure 6-7). This can be explained by the very high natural frequency in heave, which results in a stiffness dominated and nearly quasi-static heave response for the frequency range shown here. The predicted heave motion is, as expected, very small, with a maximum displacement of 1.5 mm per meter wave amplitude. Logically, the pitch RAO takes on the largest values of the three rotational motion RAOs. However, the pitch RAO is also very small.

Internal dynamic loads computed in HydroD

Figure 8-3 shows the internal dynamic loads at each of the four cross sections computed in HydroD.

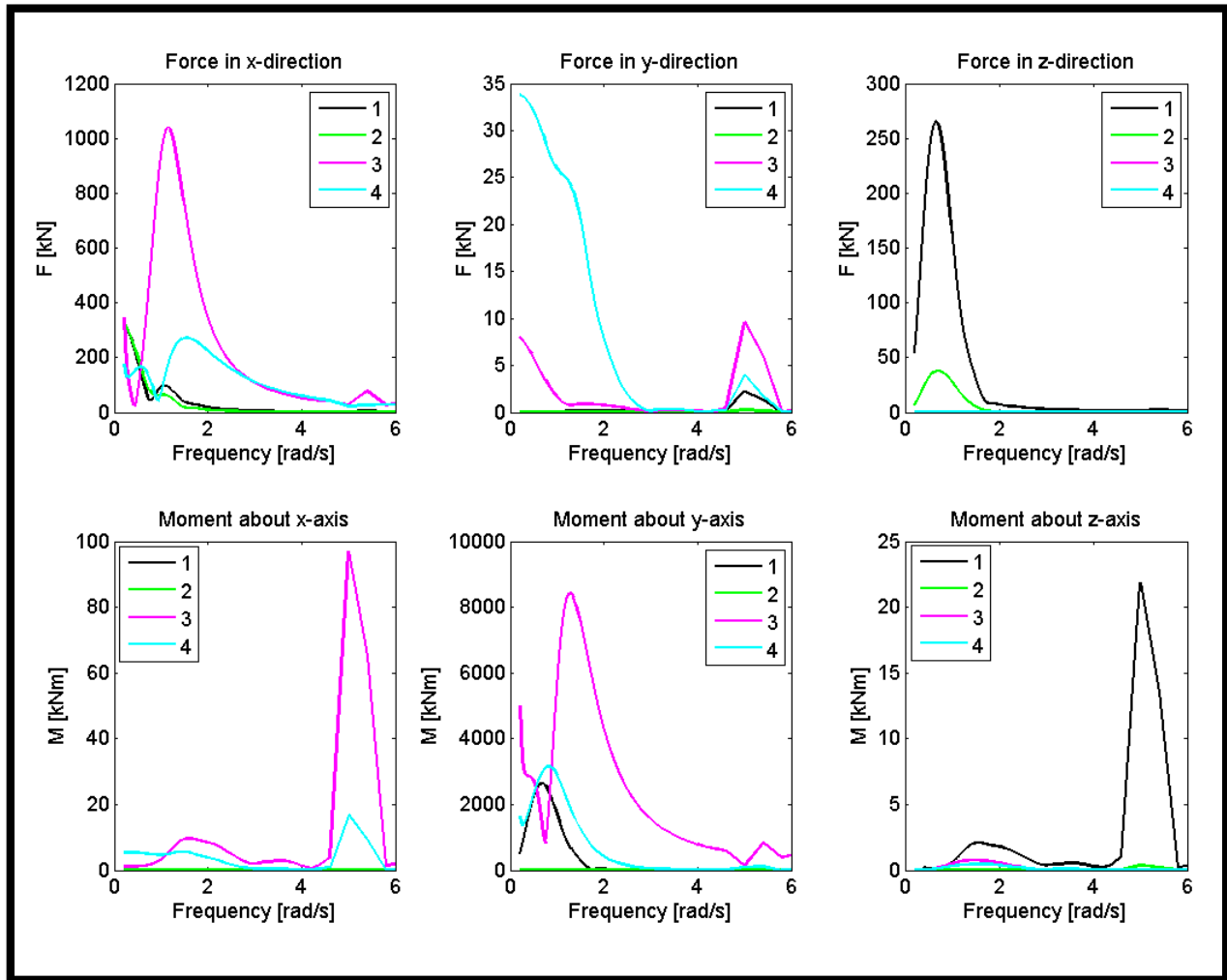


Figure 8-3: Internal dynamic loads computed at each cross section in HydroD

The force in y-direction, F_y , and the moments about the x- and z-axis, M_x and M_z , have relatively small amplitudes. The force in x-direction, F_x , is seen to be larger at the column base than close to the waterline, and approximately the same at both pontoon cross sections. The moment about the y-axis at the bottom of the main column shows a trend very similar to the pitch RAO. The moment about the y-axis is larger at the column base than close to the waterline. Also, it is larger

at the pontoon base than close to the tendon connection, which makes sense because the tendon connection cannot take up any moment. Therefore, all internal moments should decrease as one moves along the pontoon from the base node connection to the tendon connection. Also the shear forces should decrease as one moves along the pontoon from the base node connection to the tendon connection. The reason is that the inertia effects from the base node and main column become less noticeable.

8.1.2 Wave-only time-domain analysis with an elastic structure

SIMO-RIFLEX and the previously developed elastic multi-body model was used to investigate amplification due to the structural elasticity. A SIMO-RIFLEX analysis takes place in the time-domain. To investigate any possible amplification due to structural elasticity at given wave frequencies, a number of time-domain simulations were executed in a windless environment with only one regular wave present in each simulation. The simulations were executed with a simulation time of 800 s. The amplitude of the regular wave was 1 m in each simulation. Amplification was investigated for wave frequencies ranging between 0.2 rad/s, which is the lowest frequency for which the analysis was done in HydroD, and 1.75 rad/s. This frequency range includes common wave periods and has some margin with respect to the natural frequencies of the elastic multi-body TLPWT model (paragraph 7.3). Quadratic damping on the structure was not included, but Morison loading on the tendons was.

Before continuing to the presentation of the SIMO-RIFLEX output and the comparison of this with the corresponding WADAM output, it is important to identify modelling and computational differences between the two software. In this way, one can identify sources which may potentially lead to output differences that cannot be attributed to the structural elasticity.

- First of all, because WADAM analysis is carried out in the frequency-domain, it is able to describe steady-state response only. Therefore, only the steady-state part of the SIMO-RIFLEX response should be used in this comparison.
- The frequency-domain analysis in WADAM is fully linearized. However, the time-domain analysis in SIMO-RIFLEX is not. On the load side, both models account for the same linear loads on the structure due to frequency-dependent added mass, radiation

damping and wave excitation. However, the Morison loading on the tendons in SIMO-RIFLEX was not linearized and includes the quadratic drag term. So the WADAM analysis included linearized drag on the tendons, while SIMO-RIFLEX analyses included quadratic damping on the tendons. It is worth noting that the tendons are located in deeper waters than the hull structure. Because of this, and the fact that they are relatively thin compared to the hull structure as a whole, the difference arising from this linearization may be expected to be small compared to the total hydrodynamic loads on the hull.

- In WADAM, the system structural mass, damping and stiffness matrices are constant throughout the analysis. In SIMO-RIFLEX, these system matrices are generally updated at every time step for incremental dynamic equilibrium. For this particular analysis, geometric stiffness effects introduce non-linearities. In the same way that a cable has an increased lateral stiffness when subjected to an axial tensile force, the transverse stiffness of the RIFLEX beam elements are influenced by axial forces [17]. Because the axial forces are dynamic, and therefore vary in time, the stiffness matrix also becomes time-dependent. The mass matrix is constant in time. The same applies for the damping matrix, which based on proportional damping and the initial mass and stiffness matrices.

In the following, the internal dynamic loads will be presented for two versions of the elastic multi-body TLPWT model. The first version is an imitation of the rigid HydroD model from paragraph 8.1.1. This implies that the rotor, nacelle and tower have been removed and replaced by a point mass at the top of the main column. This version will be referred to as *the reduced model*. The second version is the original full model which was used in chapter 7. This version will be referred to as *the original model*. The difference between the reduced and original models is clearly shown in Figure 8-4.

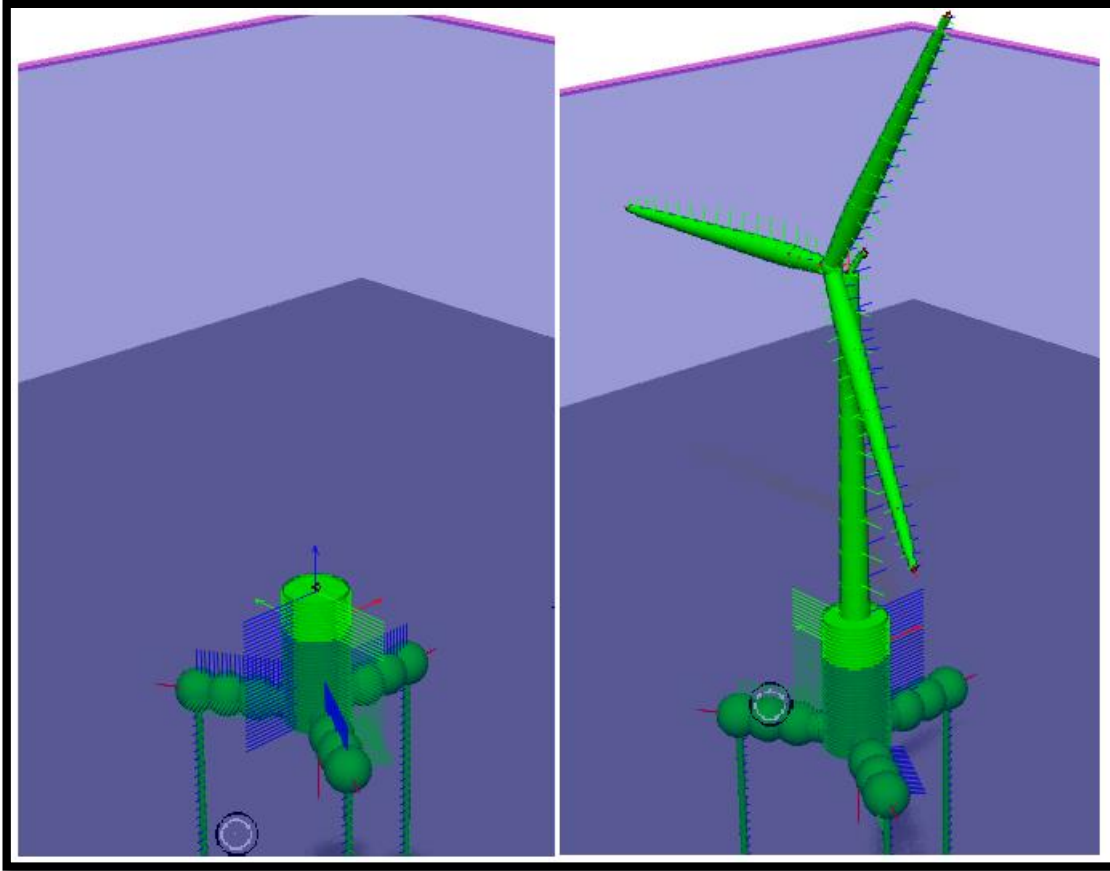


Figure 8-4: Reduced (left) and original (right) versions of the elastic multi-body TLPWT model in SIMO-RIFLEX

For a wave heading of 0 degrees, one can expect the most significant internal dynamic loads to be F_x and M_y for the main column (cross sections 3 and 4) and F_z and M_y for the pontoon (cross sections 1 and 2). Therefore, the focus of the analysis was put on these load components. Additionally, the axial load components (F_z for main column and F_x for pontoon 1) were evaluated. As expected, the other load components were found to be relatively small, and they are not discussed here.

8.1.2.1 Wave-only time-domain analysis with the reduced model

In order to compare the results from the time-domain analysis with the results from the frequency-domain analysis, the steady-state response is needed. In total, time-domain analyses were executed for 15 wave frequencies. These frequencies are almost equally spaced between 0.2 rad/s and 1.75 rad/s. For each wave frequency, the last 100 s of the 800 s time series were

assumed to be representative of the steady-state response. To check this, the time series of the surge, heave and pitch motions of the SIMO-body at the waterline were examined. For each wave frequency, these motions seemed to show a steady-state response during the last 100 s of the time series. The last 100 s of the surge, heave and pitch motion of the SIMO-body at the waterline are shown in Figure 8-5 for a wave frequency of 0.65 rad/s. To avoid redundancy, these motion time series are not shown for the other 14 wave frequencies.

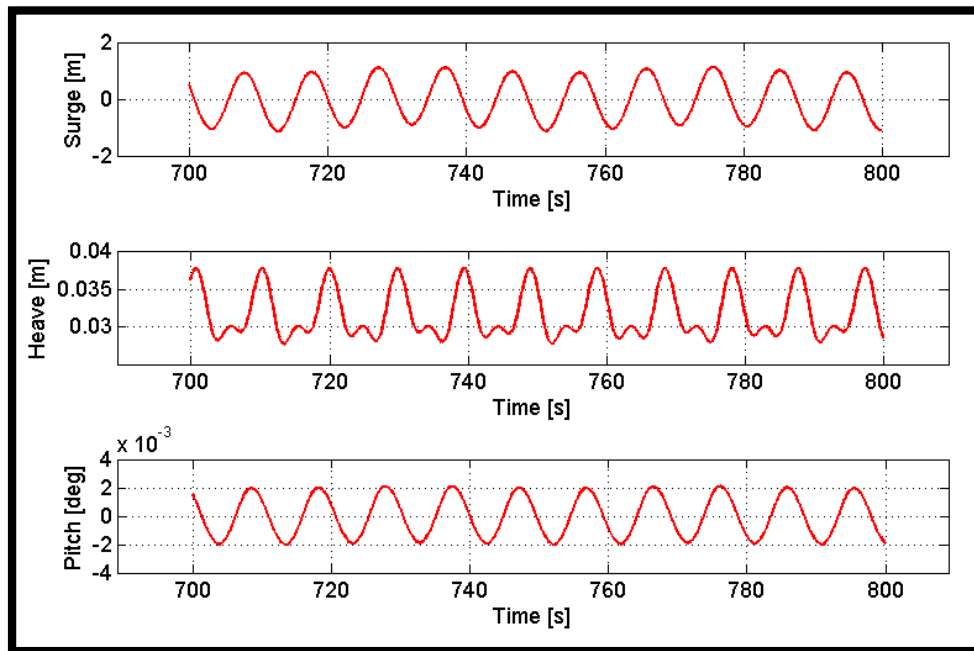


Figure 8-5: Steady state response at waterline for a wave frequency of 0.65 rad/s

During the last 100 s of the time series, the structure is seen to oscillate with a very small variation in amplitude and a period which corresponds to the wave frequency. This was the case for all of the other wave frequencies too. The last 100 s of the time series were therefore assumed to be representative of the steady-state response.

Surge, heave and pitch RAOs for reduced model

An estimation of the surge, heave and pitch RAOs for the reduced model can be made based on the steady-state time-domain results for the surge, heave and pitch motions for all of the 15 selected frequencies. Estimated surge, heave and pitch RAOs for the reduced model are shown in Figure 8-6 together with the corresponding RAOs for the rigid model (Figure 8-2).

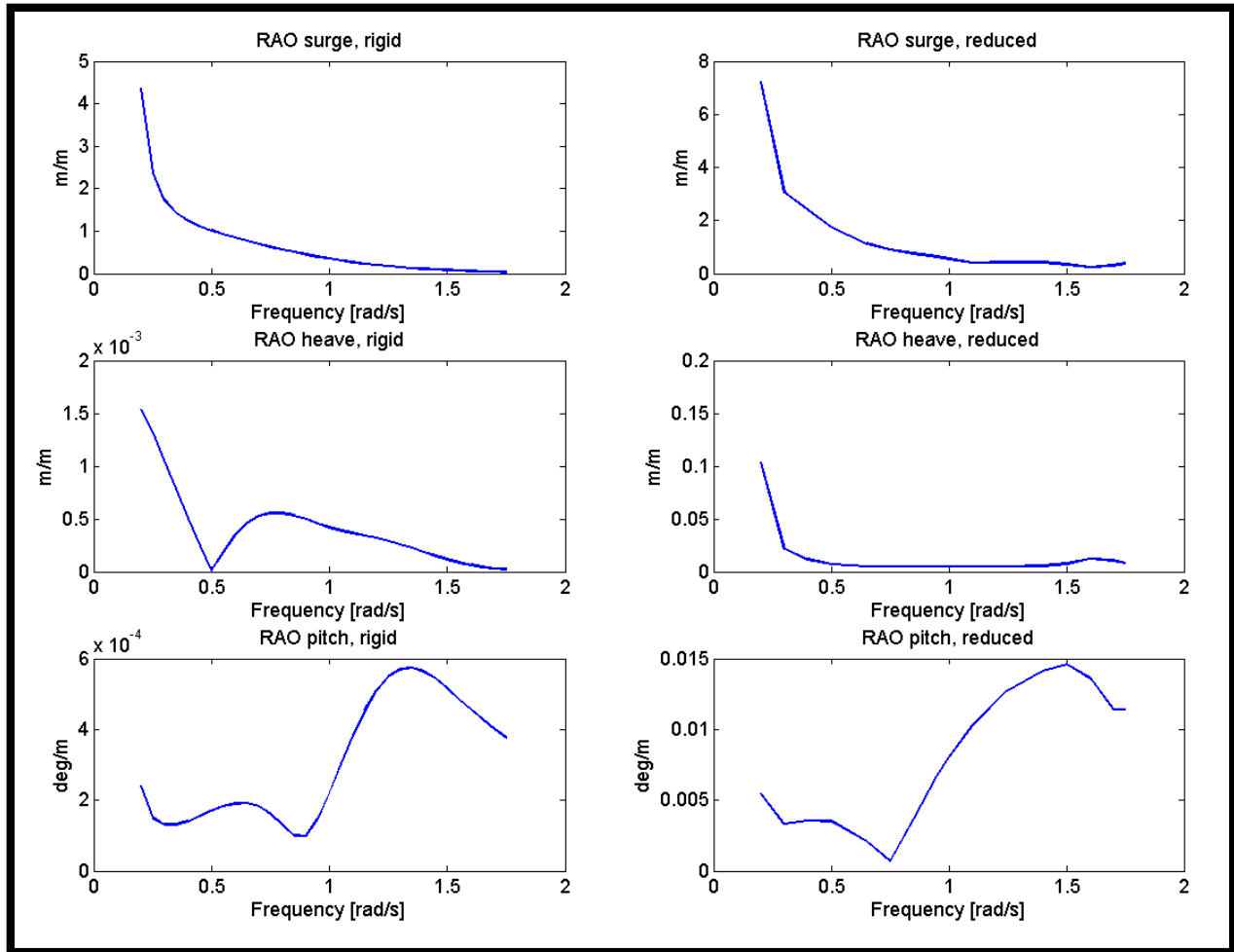


Figure 8-6: Estimated surge, heave and pitch RAOs for the reduced model (right) compared to the rigid model (left)

The surge RAO shows similar trends for the two models. When comparing the amplitudes, it is seen that the surge RAO for the reduced model indicates larger motions than the surge RAO for the rigid model. A closer look at the actual numbers indicate that the surge motion of the reduced model is amplified with a factor of around 1.5 for the lower frequencies. For the higher frequencies, the amplification factor is increasing from 1.5 to a maximum of 10.

Both the heave RAO for the rigid model and the heave RAO for the reduced model indicate relatively large motions for the lowest frequencies. However, the heave RAO for the reduced model does not seem to have the peak around 0.75 rad/s which is seen in the heave RAO for the rigid model. When comparing the amplitudes of the two heave RAOs, it is seen that they both take on small values. However, the heave RAO for the reduced model is many times larger than

the heave RAO for the rigid model for all of the selected frequencies. Again, for the higher frequencies, the amplification is at its largest. The results indicate an amplification factor of more than 300 for the highest frequencies, and a factor of almost 600 for 0.5 rad/s. It is important to keep in mind that the numbers are very small, and therefore quickly show very large amplification.

Like the surge RAO, the pitch RAO shows similar trends for the two models. The pitch RAO for the reduced model indicates larger motions than the pitch RAO for the rigid model. The amplification factor is larger than for the surge RAO, but much smaller than for the heave RAO, and varies mostly between 20 and 30.

In summary, the RAO for the reduced model indicates larger motions than the RAO for the rigid model. This can affect the internal dynamic loads because larger motions may lead to higher inertia loads. In the following, the computed internal dynamic loads at the selected cross sections will be presented.

Internal dynamic loads at the selected pontoon cross sections

The steady-state response of the internal dynamic loads at the two selected cross sections on pontoon 1 are shown in Figure 8-7 together with the corresponding loads computed with WADAM in HydroD (Figure 8-3).

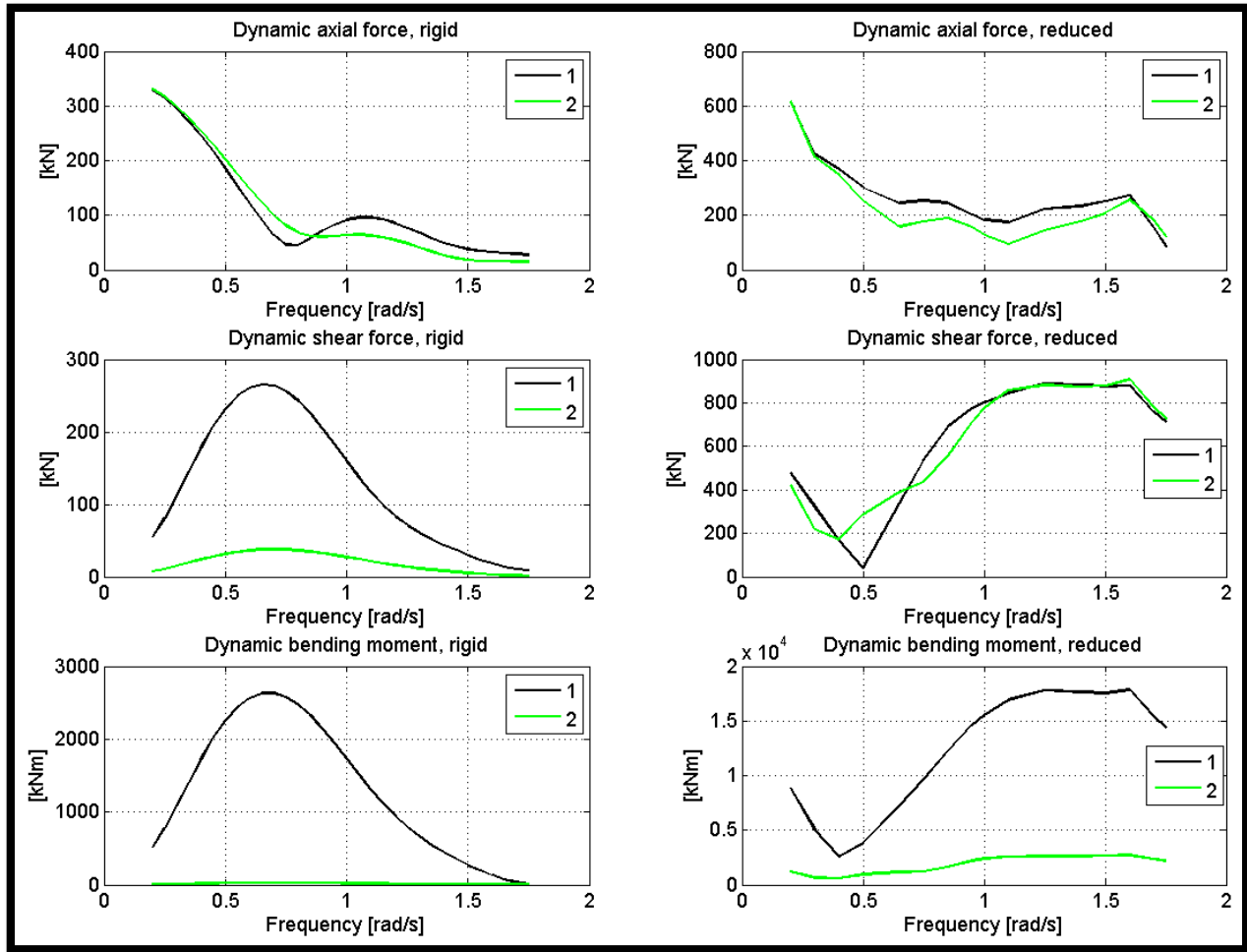


Figure 8-7: Internal dynamic loads in pontoon 1 for rigid (left) and reduced model (right)

The magnitude of the dynamic axial force in the pontoon is similar for both cross sections over the whole frequency range for both the rigid and the reduced model. For both models, the axial force has a decreasing trend for low frequencies before increasing and then decreasing again for higher frequencies. The rigid model shows a peak around 1.1 rad/s. This peak seems to have moved towards a higher frequency in the reduced model.

The magnitude of the dynamic shear force in the pontoon is similar for both cross sections over the whole frequency range for the reduced model. This is in contrast to the rigid model, which has much larger dynamic shear force at the pontoon base (cross section 1) than close to the tendon connection (cross section 2). In the rigid model, the dynamic shear force increases from 0.2 rad/s and peaks at 0.7 rad/s before it approaches zero for higher frequencies. The trend seen in the reduced model is quite different. In the reduced model, the dynamic shear force is

decreasing from 0.2 rad/s to around 0.5 rad/s where it reaches some local minimum. After this it increases and peaks somewhere between 1.3 rad/s and 1.6 rad/s before decreasing again. The results suggest a very large amplification for the higher selected frequencies.

The dynamic bending moment in the rigid model shows a trend similar to the dynamic shear force in the rigid model for both cross sections. This also applies for the reduced model. However, the dynamic bending moment amplitude in the reduced model at cross section 1 is now much larger than at cross section 2. In the reduced model, the curves peak at a frequency for which the curves have almost reached zero in the rigid model. Consequently, the results suggest a very large amplification at both cross sections for the higher selected frequencies.

Internal dynamic loads at the selected main column cross sections

The steady-state response of the dynamic internal loads at the two selected cross sections on the main column are shown in Figure 8-8 together with the corresponding load computed for the rigid model with WADAM in HydroD.

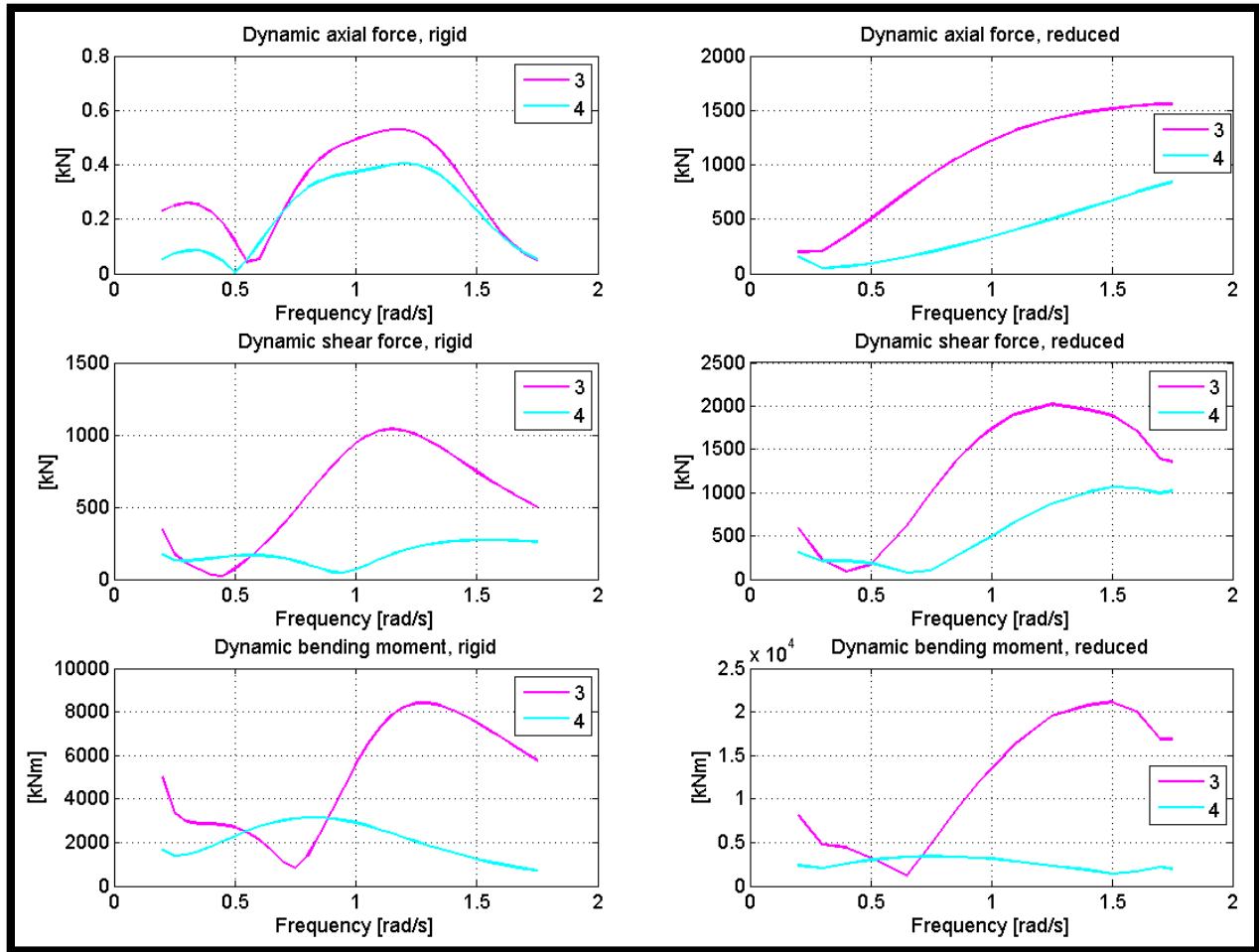


Figure 8-8: Internal dynamic loads in main column for rigid (left) and reduced model (right)

The magnitude of the dynamic axial force is very small for both cross sections over the whole frequency range in the rigid model. In the reduced model, the dynamic axial force is consistently larger at cross section 3 (column base) than at cross section 4 (close to mean water level). In the rigid model, the dynamic axial force is seen to first peak at around 0.3 rad/s and the again at around 1.2 rad/s for both cross sections. The trend seen for the reduced model is very different. In the reduced model, the dynamic axial force first decreases towards 0.3 rad/s before continuously increasing with frequency. As with the dynamic shear force and bending moment in the pontoon, the results indicate a very large amplification of the dynamic axial force in the column for the higher frequencies.

The dynamic shear force at the selected cross sections of the main column shows similar trends in both models. The peaks and troughs are located at approximately the same frequencies and the

overall shape of the curves are similar. This also applies to the dynamic bending moment for both cross sections in both models. The results indicate an amplification which is much smaller than what was seen for the dynamic axial force in the main column.

Summary and discussion of internal dynamic loads comparison between rigid and reduced model

Figure 8-9 depicts the estimated amplification for the surge, heave and pitch RAOs and for all of the discussed internal loads over the selected frequency range. It is hard to say what amplification factors to expect, but one might expect the RAO amplifications to be of the same order of magnitude as that of a simple 1-DOF system, which is typically somewhere between 1 and 4 for frequencies below the natural frequency [47]. Bishop and Price found amplifications in the same range for the bending moment at the middle of a ship hull [48]. Many of the values observed here are much larger than this.

The pontoon axial force, main column shear force and main column bending moment show the smallest amplifications. The figure also indicates that the pitch amplification has a large influence on the amplifications of the dynamic bending moment at cross section 3 and the dynamic shear force at cross section 4.

The main column axial force, pontoon shear force and pontoon bending moment show very large amplification for higher frequencies. Additionally, the main column axial force shows a very large amplification at cross section 4 for a frequency of 0.5 rad/s. The frequencies at which these very large amplifications occur, coincide well with the frequencies at which the heave motion shows very large amplification. When the heave motions are amplified, then so are the inertia loads in the vertical direction. Therefore, the heave motion amplification can partly explain the very large amplifications seen for the dynamic main column axial force, pontoon shear force and pontoon bending moment.

The very large amplification seen at certain frequencies could indicate that the differences between the two models are too large for a comparison to make sense. In this way, the dynamic amplification which is sought for may be covered up by basic differences between the WADAM

and RIFLEX software. Examples of such differences could be the previously mentioned full linearization in WADAM which is not applied in SIMO-RIFLEX.

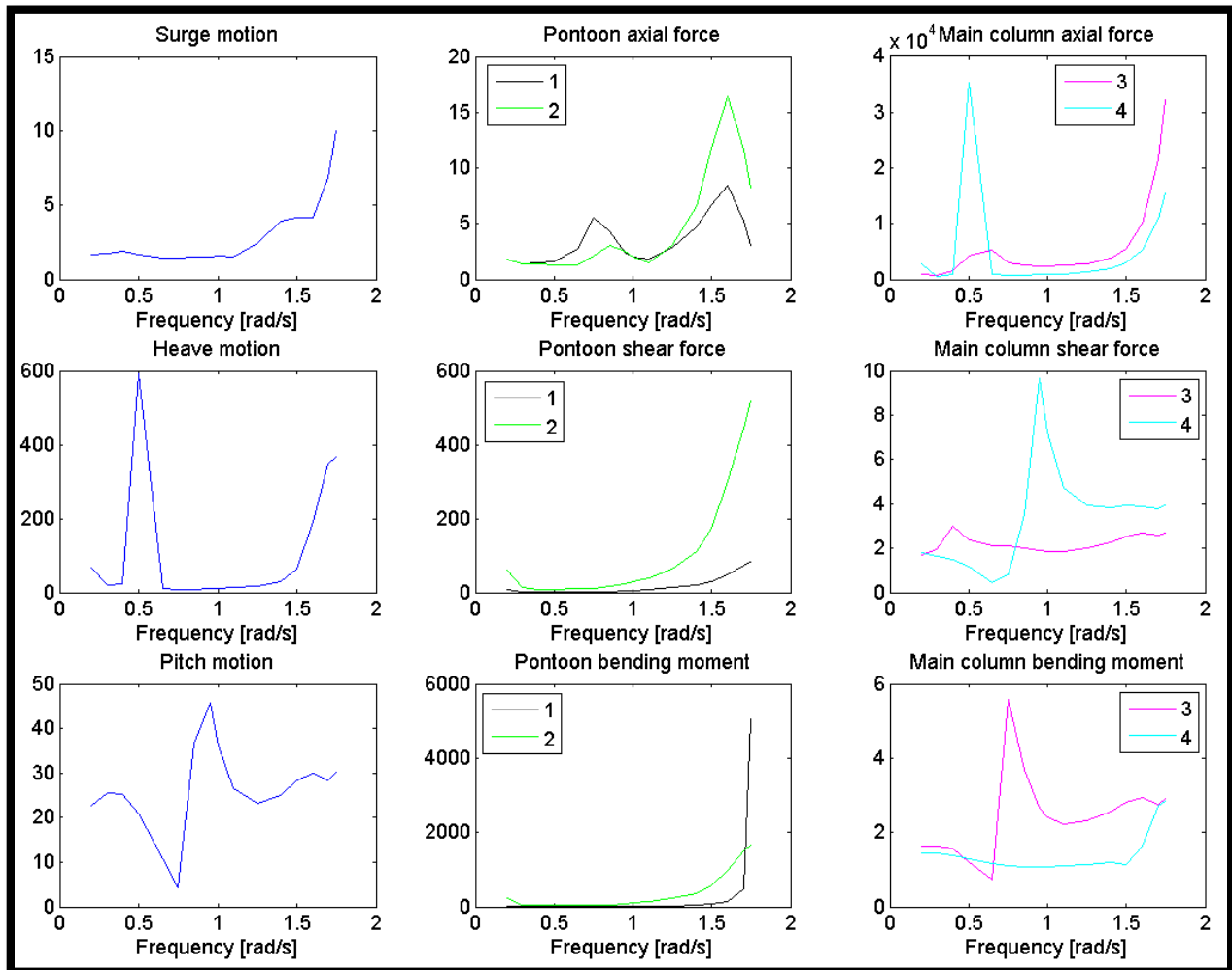


Figure 8-9: Estimated amplifications for the reduced model with respect to the rigid model

8.1.2.2 Wave-only time-domain analysis with the original model

This paragraph presents the time-domain analysis results which were obtained with the original model. The analysis was done with the exact same environmental conditions as in paragraph 8.1.2.1. That is, a windless environment with only one regular wave present in each simulation. Again, the response during the last 100 s of the time series was assumed to be representative for the system's steady-state response.

Surge, heave and pitch RAOs for original model

The estimated surge, heave and pitch RAOs for the original model are shown in Figure 8-10 together with the corresponding RAOs for the rigid model (Figure 8-2).

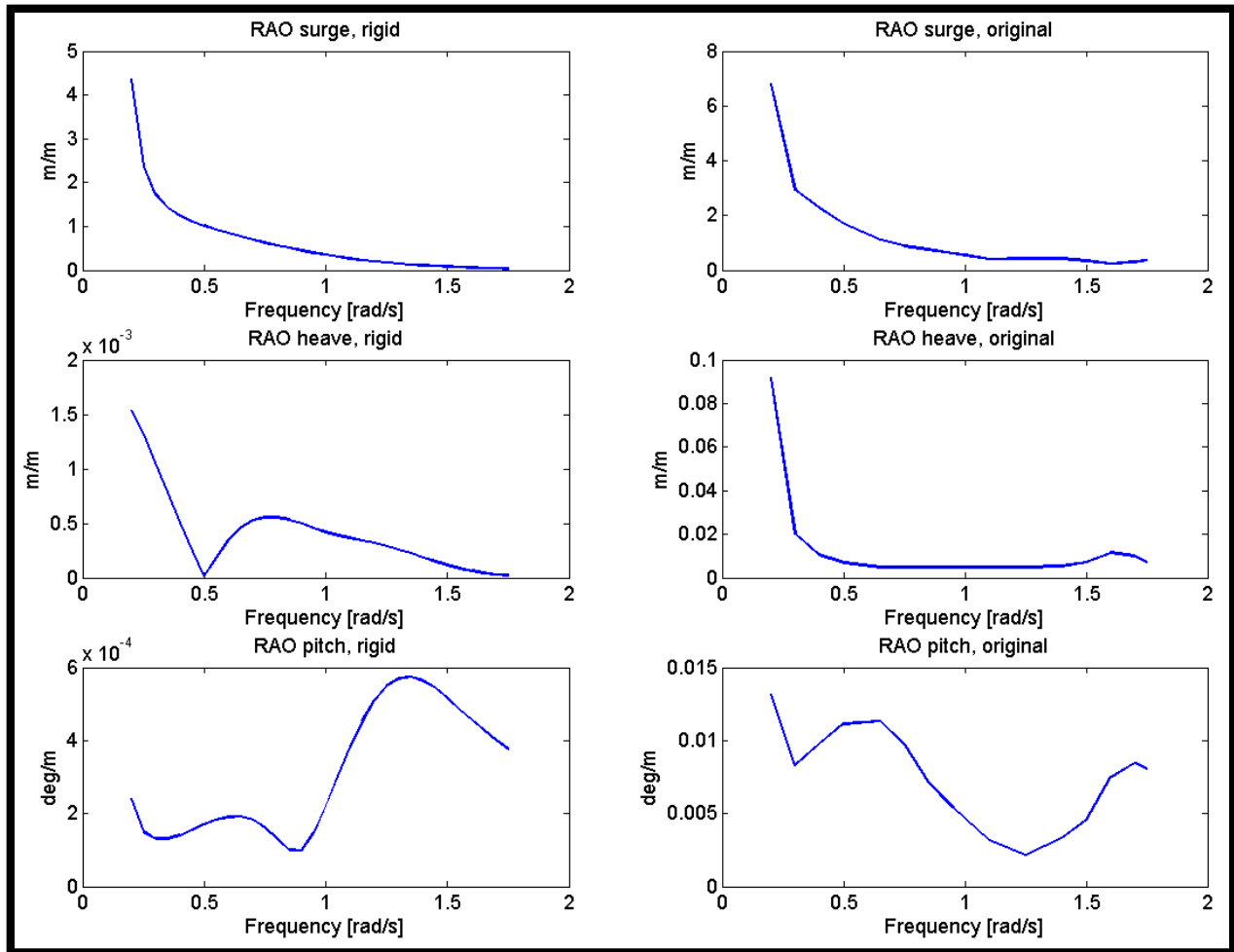


Figure 8-10: Estimated surge, heave and pitch RAOs for the original model

The surge and heave RAOs are very similar to the corresponding RAOs for the reduced model, which were shown in Figure 8-6. However, the pitch RAO now has a shape which is quite different from the pitch RAO for the rigid model. These observations indicate that the rotational inertia from the rotor, nacelle and tower has a large influence on the pitch RAO, and a much smaller influence on the surge and heave RAOs. The further away from the waterline the turbine mass is located, the larger its moment due to inertia forces. This, combined with the elasticity

introduced by the tower reduces the stiffness of the system in pitch. This can explain the alteration of the original model's pitch RAO curve with respect to that of the reduced model.

In the following, the internal loads at the selected cross sections on the main column and pontoon will be investigated for the selected frequency range for the original model.

Internal dynamic loads at the selected pontoon cross sections

The steady-state response of the internal dynamic loads at the two selected cross sections on pontoon 1 are shown in Figure 8-11 together with the corresponding loads computed with WADAM in HydroD (Figure 8-3).

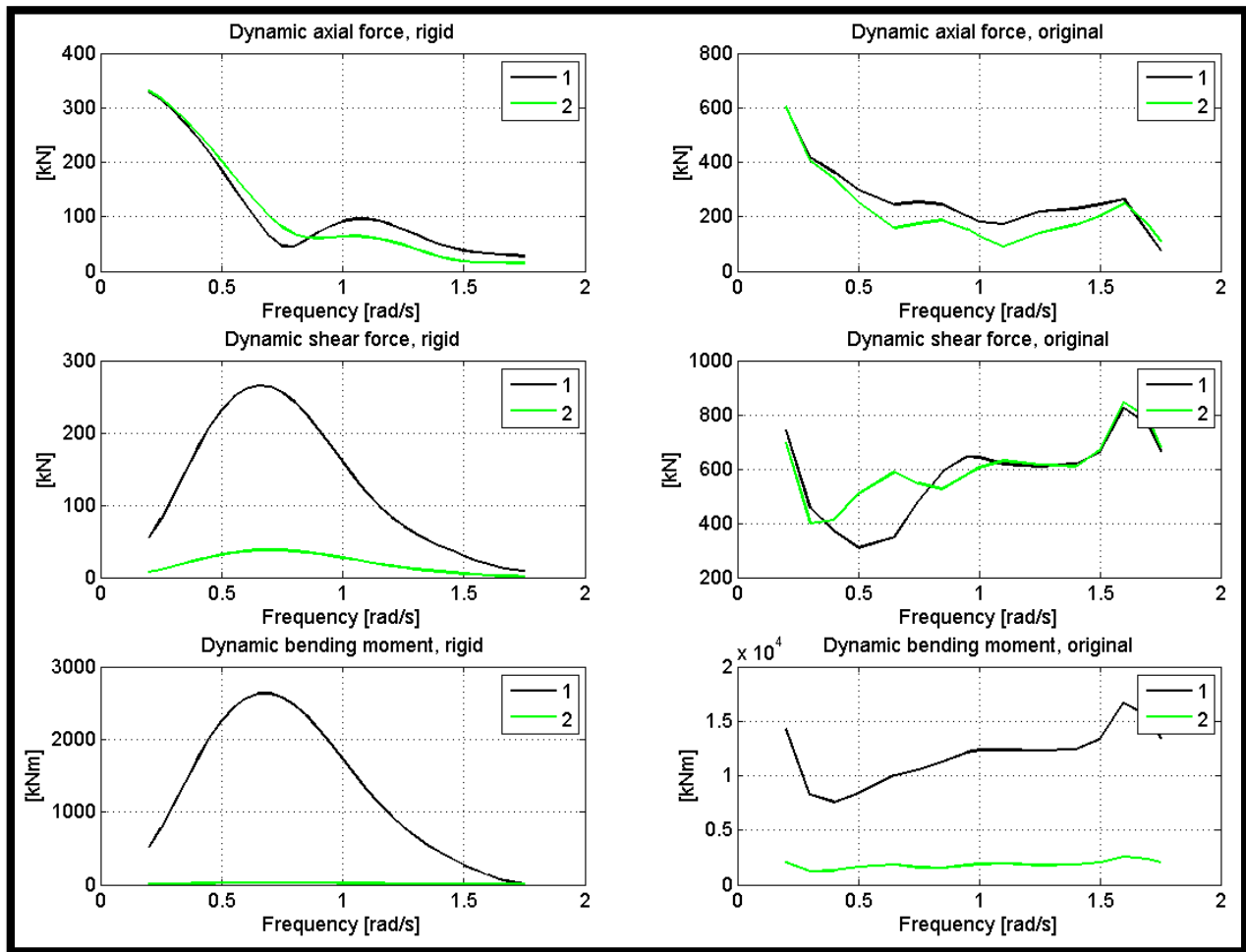


Figure 8-11: Internal dynamic loads in pontoon 1 for rigid (left) and original model (right)

When comparing the dynamic axial force in the pontoon between the rigid and original model, the conclusions which were drawn for the reduced model can be drawn again. Consequently, the rotational inertia from the turbine does not seem have a large influence on the dynamic axial force in pontoon 1.

However, the dynamic shear force looks different now. The overall shape is similar to that of the reduced model. However, the amplitudes for the lower frequencies is larger now. Again, the dynamic shear force is similar at both cross sections. Again, the results indicate a very large amplification for the higher frequencies.

Also now, the dynamic bending moment amplitude at cross section 1 is much larger than at cross section 2, which is in accordance with the rigid model. Similar to what was seen in the reduced model, the curves peak at a frequency for which the curves of the rigid model have almost reached zero. So again, the results suggest a very large amplification at both cross sections for the higher selected frequencies.

Internal dynamic loads at the selected main column cross sections

The steady-state response of the dynamic internal loads at the two selected cross sections on the main column are shown in Figure 8-12 together with the corresponding load computed for the rigid model with WADAM in HydroD.

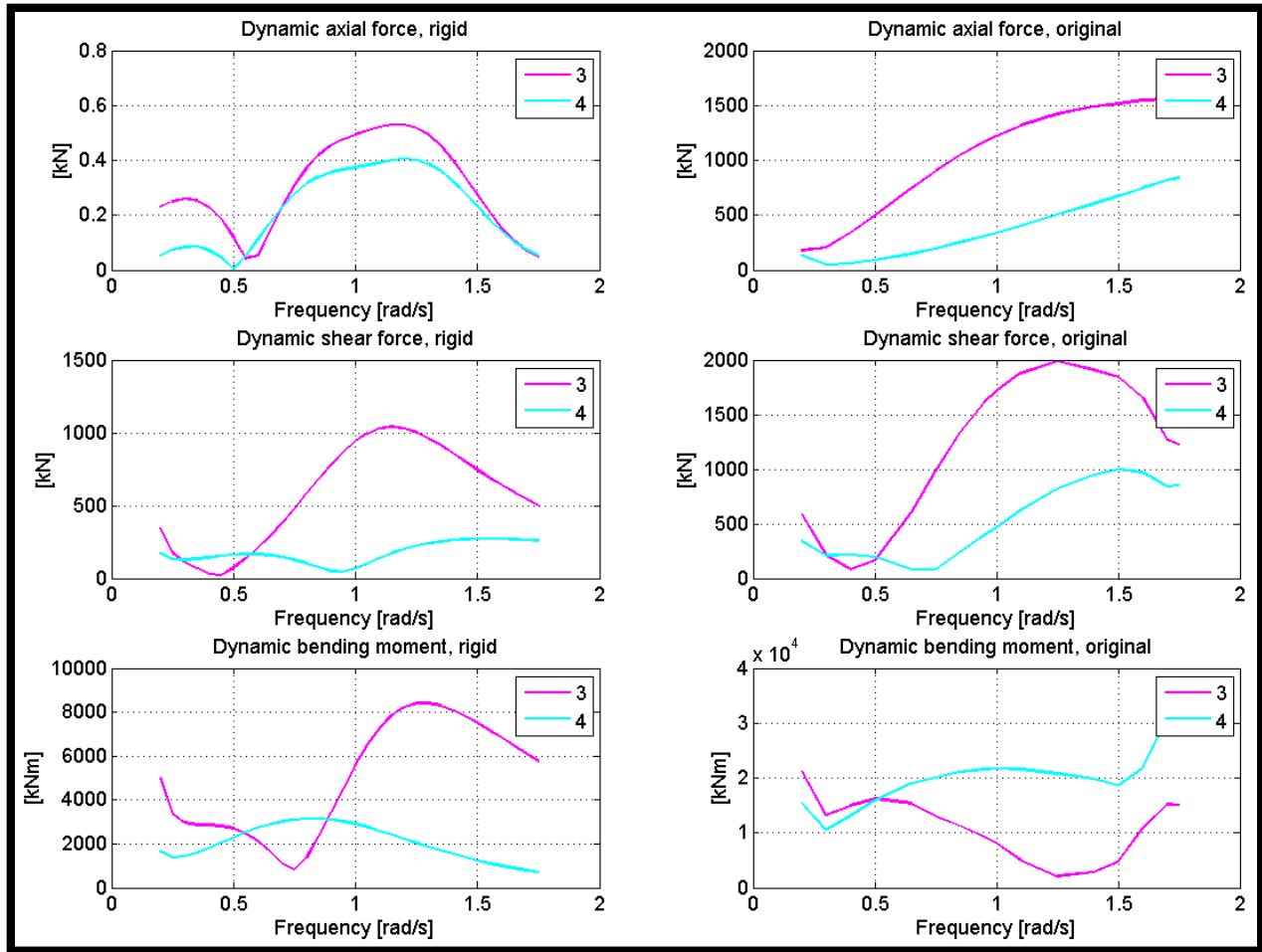


Figure 8-12: Internal dynamic loads in main column for rigid (left) and original model (right)

As for the dynamic axial force in the pontoon, the dynamic axial force in the main column seems to be unchanged. Consequently, the conclusions which were drawn when comparing the dynamic axial force of the reduced and the rigid model can be drawn again. In other words, the rotational inertia of the turbine seems to have little effect on the dynamic axial force in the main column, which is logical because the inertia load in the vertical direction is not affected by this. The same can be said for the dynamic shear force.

The dynamic bending moment, on the other hand, has a very different shape now. The rotational inertia of the turbine is seen to have a noticeable effect on the dynamic bending moment in the main column. For the reduced model, the curve shapes corresponded well with those of the rigid model. Now, it is seen that the peaks and troughs are located at different frequencies. It is also seen that the dynamic bending moment now is larger at cross section 4 for most of the

frequencies. A larger amplification in the dynamic bending moment at cross section 4 is observed.

Summary and discussion of internal dynamic loads comparison between rigid and original model

Figure 8-13 depicts the estimated amplification for the surge, heave and pitch RAOs and for all of the discussed internal loads over the selected frequency range. When comparing with the curves in Figure 8-9, it is seen that only the main column bending moment seems to have been influenced by the turbine rotational inertia. All of the other curves for the internal dynamic loads have the same shape as for the reduced model and take on approximately the same magnitudes.

When looking at the amplification of the internal dynamic bending moment in the main column, it is seen that especially at cross section 4, which is located 2 m below the mean water line, the structure experiences a significant amplification, especially for the higher frequencies. This could indicate that the mode shape corresponding to the pitch tower bending natural frequency (2.25 rad/s) is increasingly excited. The amplification at cross section 3 is peaking around the same frequency as for the reduced model. However, the amplification magnitude at this frequency is almost three times larger now. In contrast to what is seen at cross section 4, the amplification is relatively small for the higher frequencies.

Based on the observations made here, it may be suggested that, for a wave heading of 0 degrees, the rotational inertia of the turbine has little effect on the internal loads in pontoon 1. Future research may be executed for the other pontoons and for various wave headings to see if a simplified model, such as the reduced model in paragraph 8.1.2.1, may be utilized if only the internal loads in the pontoons are of interest. The results also indicate that the rotational inertia of the turbine leads to a larger internal dynamic bending moment close to the waterline than at the main column base for frequencies between 0.5 rad/s and 1.75 rad/s. Again, the amplifications observed for the dynamic axial force in the main column, and the dynamic shear force and bending moment in the pontoon seem unreasonably large.

As previously mentioned, the very large differences between the results for the rigid HydroD model and the elastic SIMO-RIFLEX models may indicate that a comparison across these two software is unsuited for this particular analysis.

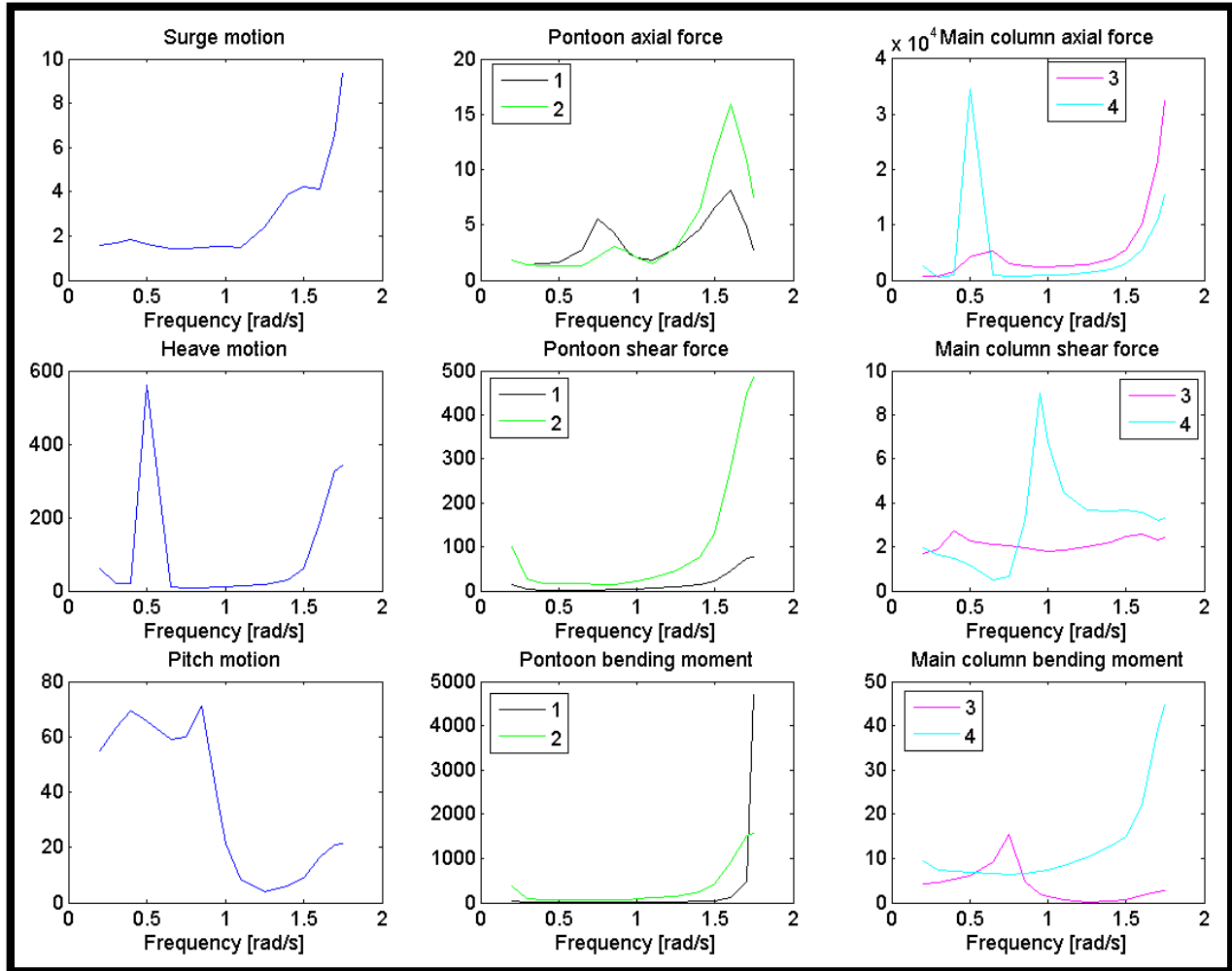


Figure 8-13: Estimated amplifications for the original model with respect to the rigid model

8.2 Evaluation of the proposed scantling design based on internal load estimations in a wind-wave environment

An evaluation of the pontoon and main column scantling design from chapter 3 can be made based on the estimated internal loads. Note that this evaluation should account for both static and dynamic internal loads. The previous paragraphs investigated the amplification of dynamic internal loads only in a wind still environment with loading from regular waves of 1 m amplitude

as the only external loading. An evaluation of the design should be based on the system's response in more realistic environments. In this paragraph, the design will be evaluated based on the system's steady state response in the three conditions from paragraph 7.4. This means that the only external loading comes from aligned head-on wind and waves, and that the sea state is described by a JONSWAP spectrum, while the wind speed is uniform and steady. The "original model", which was also used in paragraph 8.1.2.2 and in chapter 7, was applied for this evaluation.

8.2.1 Evaluation of pontoon design based on the internal bending moment at the base node connection

The pontoon design accounted for hydrostatic pressure only. It was made by following ABS MODU rules and presented in paragraph 3.2.2. The presented design was checked with DNV-RP-C201. This check accounted for tendon induced bending stress in addition to hydrostatic pressure. It was found that the design no longer complies with the minimum requirements of DNV if the bending moment at the pontoon base exceeds 203 MNm. Therefore, redesign is recommended if the simulations indicate pontoon base bending moments higher than this in any of the three conditions. In the following, time series of the pontoon base bending moments for each pontoon in each condition are presented and discussed.

Time series of bending moment at pontoon base

Figure 8-14 shows the time series of the bending moment at the base of each pontoon in each condition.

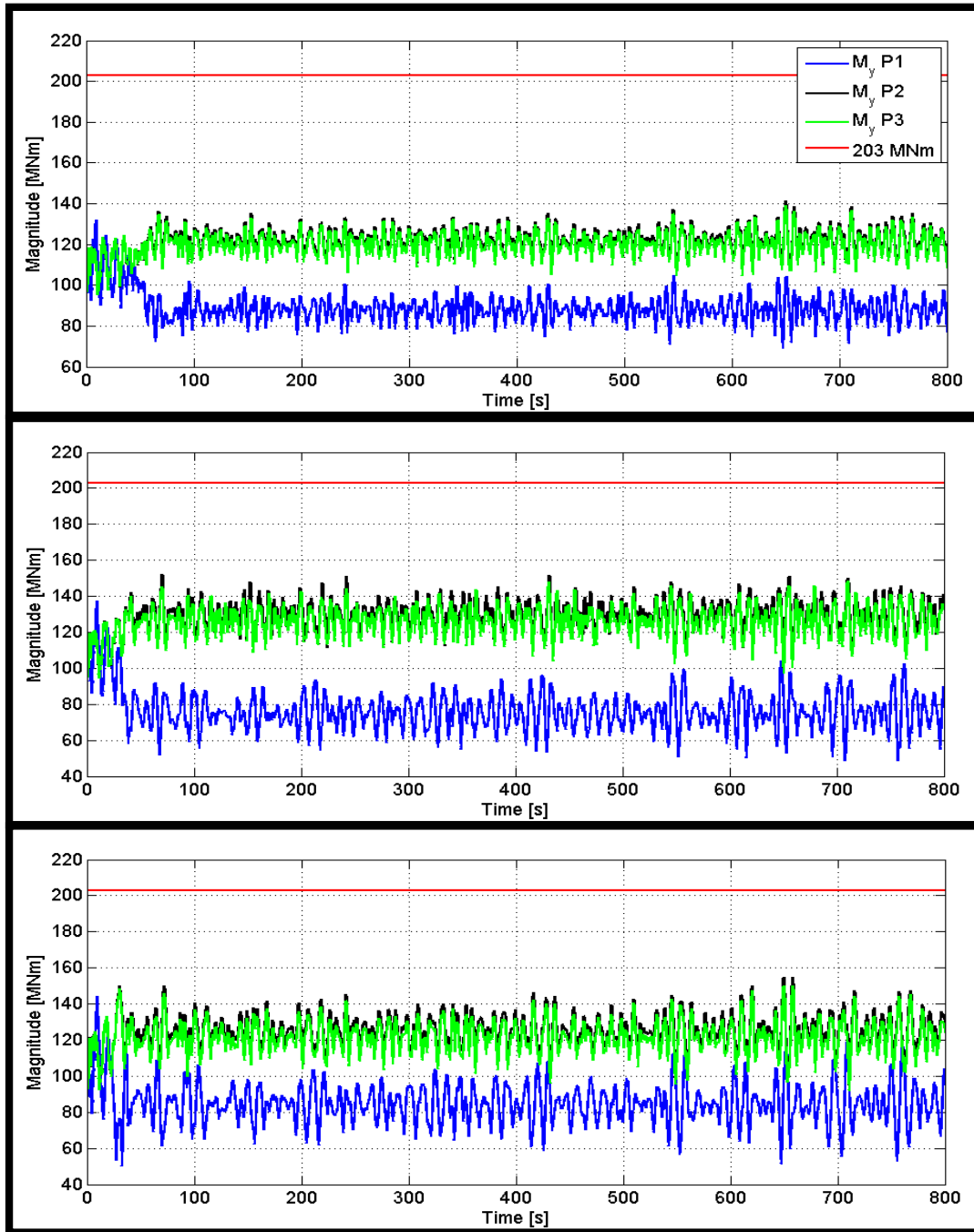


Figure 8-14: Time series of bending moment at the base of each pontoon. Top: condition 1. Middle: Condition 2. Bottom: Condition 3

The time series show that the bending moment at the pontoon base is larger for pontoons 2 and 3 than for pontoon 1. This can be explained by the head on wind and waves which induce positive pitch motion and higher tension in tendons 2 and 3 than in tendon 1. Because the wind and waves are head on, the roll motions are small. This explains why the bending moments in

pontoons 2 and 3 are approximately the same. None of the pontoon base bending moments exceed the critical value of 203 MNm in any of the conditions. This indicates that the pontoon design is not susceptible to buckling in any of these three conditions. More load conditions, including current and turbulent wind as a minimum, are required to make a more general and substantiated judgement about the present pontoon design.

Table 8-2 gives the mean, standard deviation and maximum values for all bending moments in all conditions. Note that these numbers are based on the last 400 s of the time series. This is consistent with paragraph 7.4.

Table 8-2: Mean and maximum values for pontoon bending moments in conditions 1, 2 and 3

	Condition 1	Condition 2	Condition 3
Mean M_y P1 (MNm)	87.3	74.4	83.7
Mean M_y P2 (MNm)	121.6	129.9	124.5
Mean M_y P3 (MNm)	119.9	125.6	120.8
Std M_y P1 (MNm)	5.7	10	11.5
Std M_y P2 (MNm)	5.9	8.5	9.7
Std M_y P3 (MNm)	5.9	8.7	9.6
Max M_y P1 (MNm)	104.9	104.2	119.0
Max M_y P2 (MNm)	141.6	151.7	154.9
Max M_y P3 (MNm)	138.9	148.4	150.2

Positive pitch motion increases the tension in tendons 2 and 3, and decreases the tension in tendon 1, with respect to the static tension. This explains why the mean value of the bending moment in pontoon 1 decreases if the mean value of the bending moment in pontoons 2 and 3 increase and vice versa. Condition 2, which has steady rated wind speed, give the largest mean bending moments. Condition 3, which has the largest significant wave height, gives the largest bending moment variations. The largest bending moment observed is 154.9 MNm (pontoon 2, condition 3). This is roughly 75 % of the estimated maximum allowable bending moment.

Improved estimation for tendon tension induced bending moment

The initial value for the bending moments in the time series in Figure 8-14 are approximately 108 MNm. In paragraph 3.2.3.1 it was assumed that a tendon tension of 8.3 MN would induce a bending moment of 175 MNm at the pontoon base because the pontoon is 21 m long. This

assumption results in a conservative but very inaccurate estimation which is more than 60 % higher than the numerical value. An improved estimation can be made by accounting for distributed buoyancy and weight acting on the pontoon. The main column and base node displace a water volume of 3400 m³. The total steel weight of base node, main column, ballast and turbine is about 2825 tonnes. The upward static force at each of the three base node connections can then be estimated as

$$\frac{(3400 * 1025 - 2825,000) * 9.81}{3} = 2.2 \text{ MN} \quad (8-1)$$

The given pontoon dimensions resulted in a steel mass of about 150 tonnes and a displaced water volume of about 750 m³. The upward force acting on the pontoon due to its own buoyancy and weight can then be estimated as

$$(750 * 1025 - 150,000) * 9.81 = 6.1 \text{ MN} \quad (8-2)$$

In contrast to what was the case in this work, this estimation is generally made before the design is ready. Consequently, the mass distribution can be unknown when this estimation is made. If a uniformly distributed mass along the length had been assumed, the upward resultant force of 6.1 MN would have applied at the middle of the pontoon. The free body diagram in Figure 8-15 gives a more realistic description of the problem for the statically loaded pontoon.

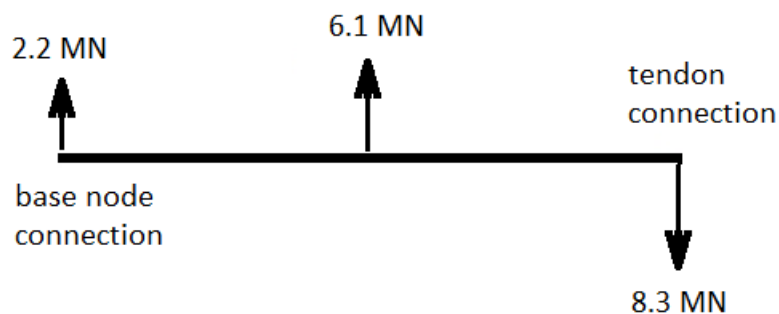


Figure 8-15; Free body diagram for statically loaded pontoon

With this configuration, the estimated bending moment at the base node connection becomes

$$8.3 \text{ MN} * 21 \text{ m} - 6.2 \text{ MN} * 10.5 \text{ m} = 110.0 \text{ MNm} \quad (8-3)$$

which is a considerably improved estimation with respect to the numerical value. With the logic behind the estimation in paragraph 3.2.3.1, the maximum allowable bending moment is reached for a tendon tension of 9.7 MN. This corresponds to an amplification of not even 20 % of the initial tendon tension. The improved estimation presented here predicts that the maximum allowable bending moment is reached for a tendon tension of 12.8 MN. This corresponds to an amplification of more than 50 % of the initial tendon tension.

8.2.2 Evaluation of main column design based on internal loads at various cross sections on the main column

The main column design accounted for the following design loads:

- Hydrostatic pressure.
- Shear force and bending moment induced by wind and waves.
- The axial force resulting from structural weight.

It was made by following DNV-RP-C202 and presented in paragraph 3.3.5. The design was checked for shell buckling, panel ring buckling and column buckling. So-called “buckling ratios” were calculated and used as indicators for the strength of the design. The buckling ratios were presented in Table 3-11. A buckling ratio which is smaller than one indicates that the design is susceptible to buckling.

In this paragraph, the main column scantling design is evaluated based on time series of the buckling ratios. The time series of the axial force, shear force and bending moment at selected elevations on the main column was used as design load input together with the hydrostatic pressure. The hydrostatic pressure was taken to be constant in time and equal to the pressure induced by still water when the structure is at its static position. Strictly speaking, the hydrostatic pressure is also time-dependent because of heave, pitch and roll motions, and time-dependent surface elevation due to waves. These effects were neglected here. Redesign of the main column is recommended if any of the buckling ratios are found to be smaller than 1 during the time series.

Time series of axial force, shear force and bending moment at various elevations on the main column

The time series of the axial force F_z , shear force F_x and bending moment M_y in each condition at four cross sections on the main column are shown in Figure 8-16, Figure 8-17 and respectively. The cross sections are horizontal and defined by the elevation (z-coordinate), just as in paragraph 8.1.

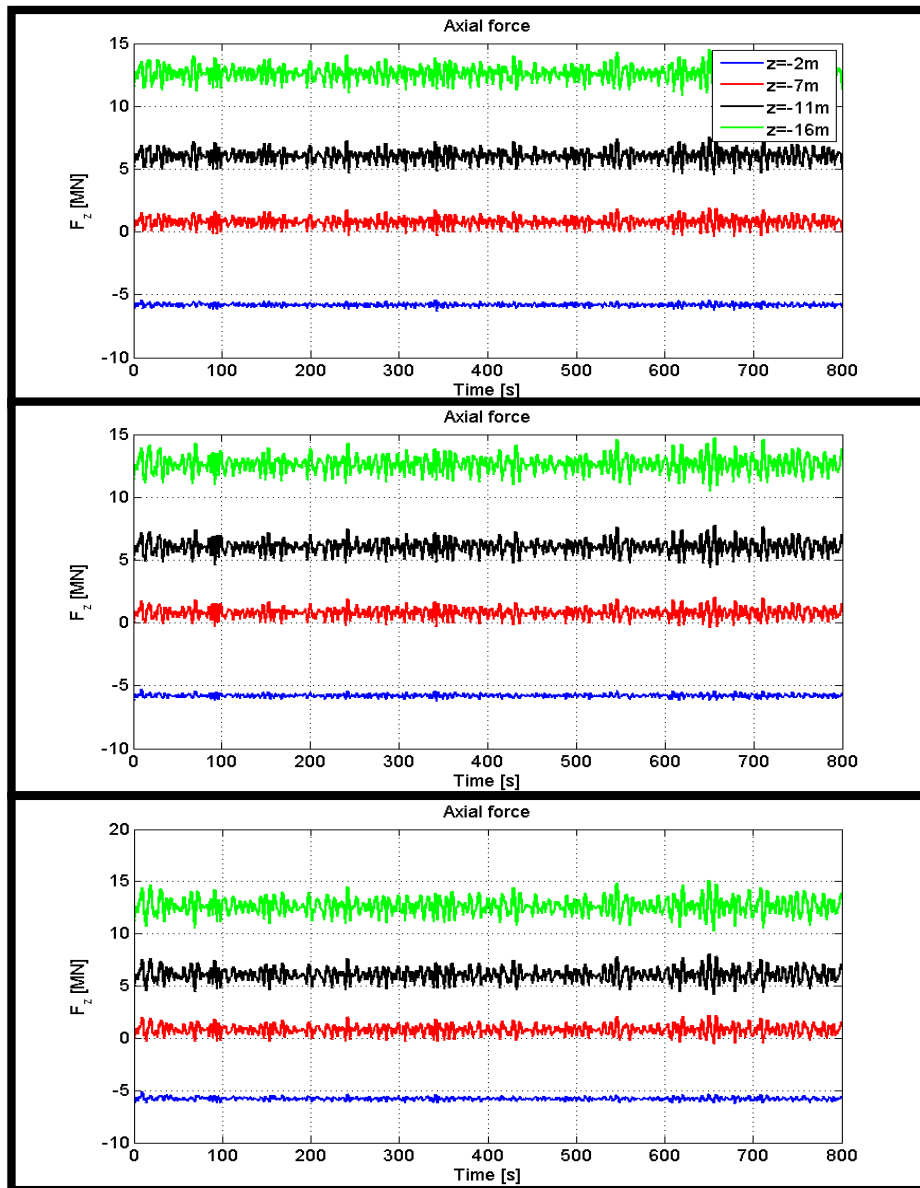


Figure 8-16: Time series of main column axial force at various elevations. Top: condition 1. Middle: Condition 2. Bottom: Condition 3

Chapter 8: Internal loads in the hull

In chapter 3, the axial force was estimated as the compressive force from the weight of the turbine and part of the main column which is above the MWL. The weight of these components correspond to a compressive axial force of 8.24 MN. In Figure 8-16, a positive value indicates tension, while a negative value indicates compression. Only the top cross section is subjected to a compressive axial force. At $z=-7$ m, the axial force is only slightly positive. This indicates that the buoyancy force on the top 7 m of the submerged main column is slightly larger than the weight of everything located above $z=-7$ m. With a diameter of 14 m, the buoyancy force on the part of the main column which is located above $z=-7$ m is

$$\frac{\pi * (14 \text{ m})^2}{4} * 7 \text{ m} * 1025 \text{ kg/m}^3 * 9.81 \text{ m/s}^2 = 10.8 \text{ MN} \quad (8-4)$$

The main column has total mass of 628,000 kg and a length of 26 m. The mass per length is then 24154 kg/m. The structural mass, including the turbine mass of 600,000 kg, which is located above $z=-7$ m results in the following weight

$$(600,000 \text{ kg} + 24154 \text{ kg/m} * 17 \text{ m}) * 9.81 \text{ m/s}^2 = 9.9 \text{ MN} \quad (8-5)$$

This simple hand calculation corresponds well with the numerical result in Figure 8-16, which indicates that the axial force estimation in chapter 3 is very inaccurate for cross sections which are not located close to the MWL.

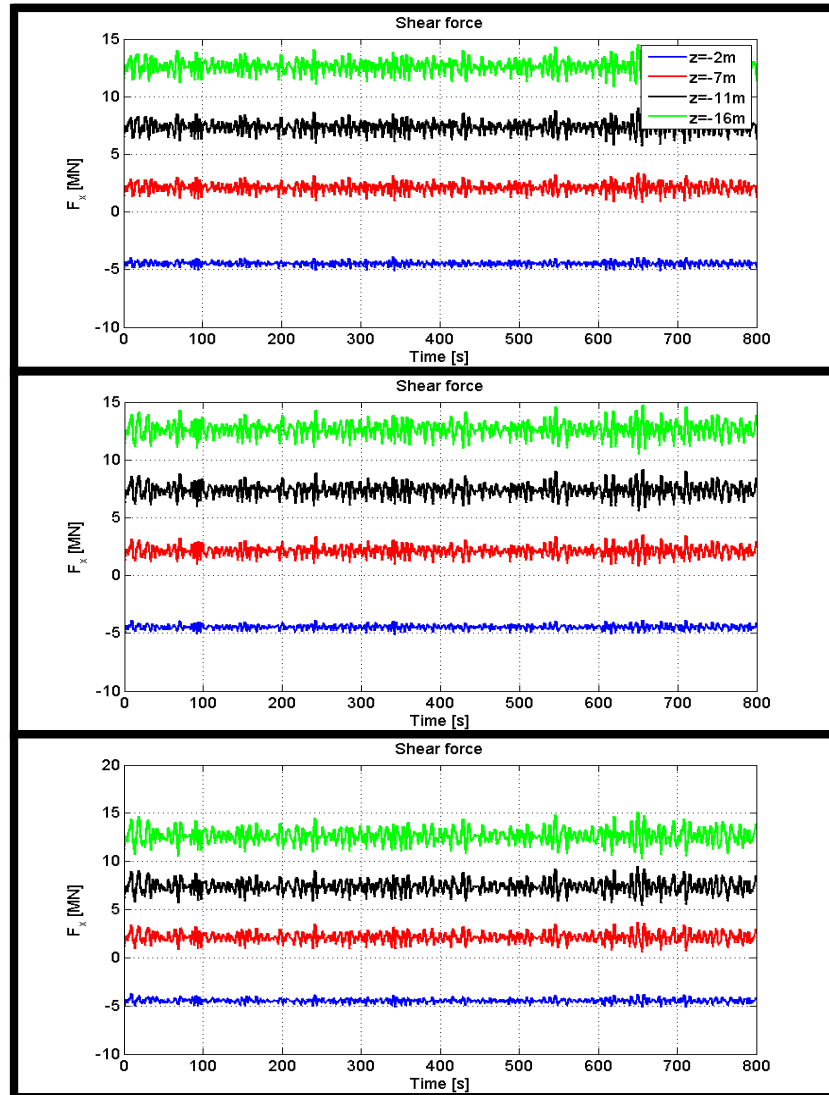


Figure 8-17: Time series of main column shear force at various elevations. Top: condition 1. Middle: Condition 2. Bottom: Condition 3

In chapter 3, the design shear force was estimated as the sum of two components. The first component was the inline force at the main column base from a design wave, computed with the Morison equation. The second component was the aerodynamic rotor thrust force at rated wind speed. They were estimated to be 6.29 MN and 660 kN respectively, which gives a design shear force of 6.95 MN. When comparing this with the numbers in the figure, it is seen that the shear force at the bottom of the main column is larger than this. At $z = -11$ m, the computed shear force is close to the design shear force, while it is smaller at $z = -7$ m and $z = -2$ m. These observations apply to all of the three conditions.

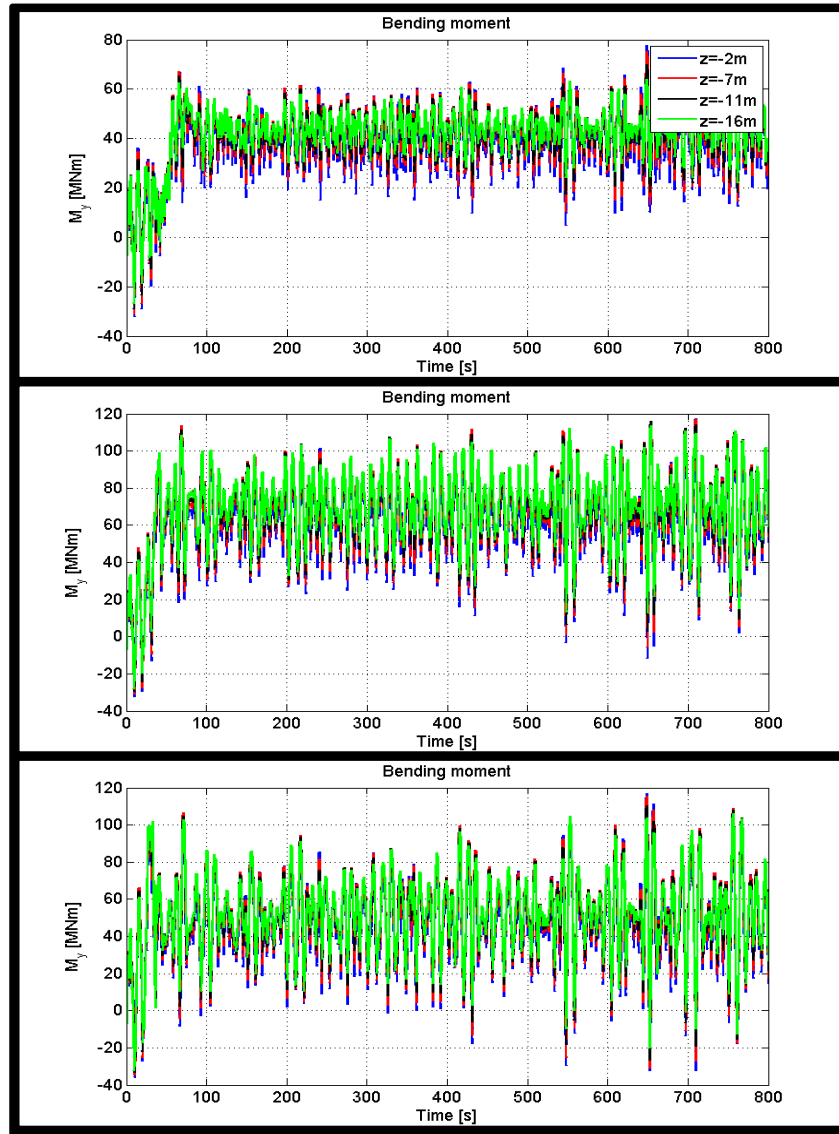


Figure 8-18: Time series of main column bending moment at various elevations. Top: condition 1. Middle: Condition 2. Bottom: Condition 3

In chapter 3, the design bending moment was estimated from the inline force from the design wave and the rotor thrust force. The contributions from these two were found to be 55.41 MNm and 76.56 MNm respectively. This gives a total bending moment of 131.97 MNm. The figure shows that the computed bending moments in conditions 1, 2 and 3 are lower than this at all times at all of the elevations.

Based on the time series of the axial force, a lower axial stress σ_a can be expected than the design axial stress $\sigma_{a, Sd}$ which was predicted in chapter 3. Also the bending stress σ_m can be expected to

be lower than the design bending stress which was predicted in chapter 3. On the other hand, the shear stress τ can be expected to be both higher and lower than the design shear stress τ_{sd} , depending on elevation. Next the hydrostatic pressure is estimated for the various elevations on the main column.

Hydrostatic pressure at various elevations on the main column

The hydrostatic pressure is approximated to be constant in time. Table 8-3 gives the hydrostatic pressure at the different cross sections.

Table 8-3: Hydrostatic pressure at the four elevations on the main column

Elevation	Hydrostatic pressure [bar]
z = -2	0.20
z = -7	0.70
z = -11	1.11
z = -16	1.61

In chapter 3, the hydrostatic pressure was estimated for the column base. This gave the design circumferential stress and was equal to 1.61 bar. For the other cross sections, the hydrostatic pressure is of course lower.

Stress components

Figure 8-19 shows time series of the stress components in condition 1. The stress components were estimated from the previously presented axial force, shear force, bending moment and hydrostatic pressure. The figure also shows the design stress components from Table 3-10. The corresponding figure for conditions 2 and 3 are similar to Figure 8-19, and they are not shown here. Note that a negative value indicates compression.

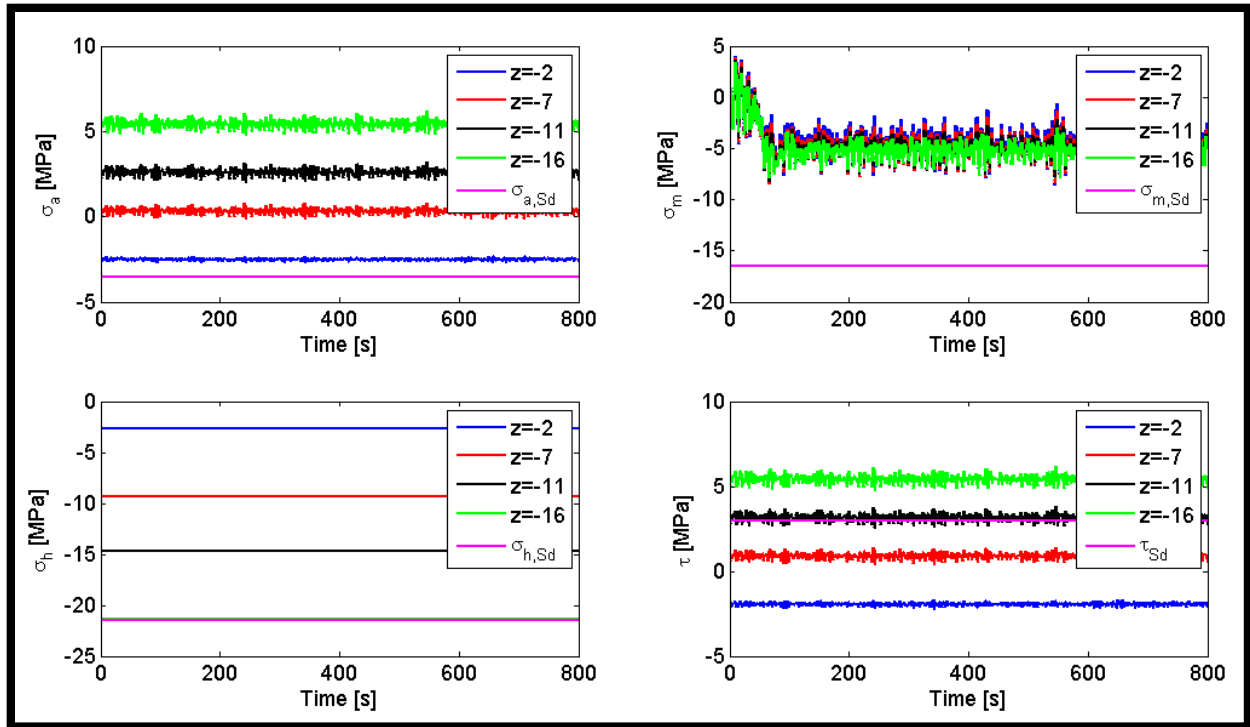


Figure 8-19: Main column stress components in condition 1. Top left: Axial stress due to axial force. Top right: Bending stress due to bending moment. Bottom left: Circumferential stress due to hydrostatic pressure. Bottom right: Shear stress due to shear force.

The design stress components used in chapter 3 give a larger compressive axial, bending and circumferential stress than the stress components calculated here. The shear stress estimated from the time series takes on both larger and smaller values than the design shear stress, depending on elevation.

With the time series of the stress components ready, the buckling ratios can be computed as a function of time. Buckling ratio 3, ζ_3 , is a ratio which indicates whether column buckling should be assessed or not. This ratio depends only on the material properties and the geometry of the structure. Because the material and geometry of the structure has already been determined at this point, this ratio will no longer change. Buckling ratio 3 is therefore not treated here. Buckling ratios 1 and 2 are directly dependent on the loads. The time series for these two buckling ratios are presented in the following.

Buckling ratio 1: Shell buckling

Buckling ratio 1 is related to shell buckling. The design is susceptible to shell buckling if ratio 1 is smaller than 1. If this is the case, then the equivalent von Mises stress σ_j is larger than the characteristic buckling strength f_{ksd} . Both of these parameters depend on the stresses, which were computed from the loads. As previously mentioned, most of the stresses are smaller than the design stresses. Therefore, one may expect the shell buckling ratio ζ_I to be higher than 3.81, which is the value that was calculated with the design stresses. Figure 8-20 shows the time series of the shell buckling ratio ζ_I at the four cross sections (elevations) for each condition.

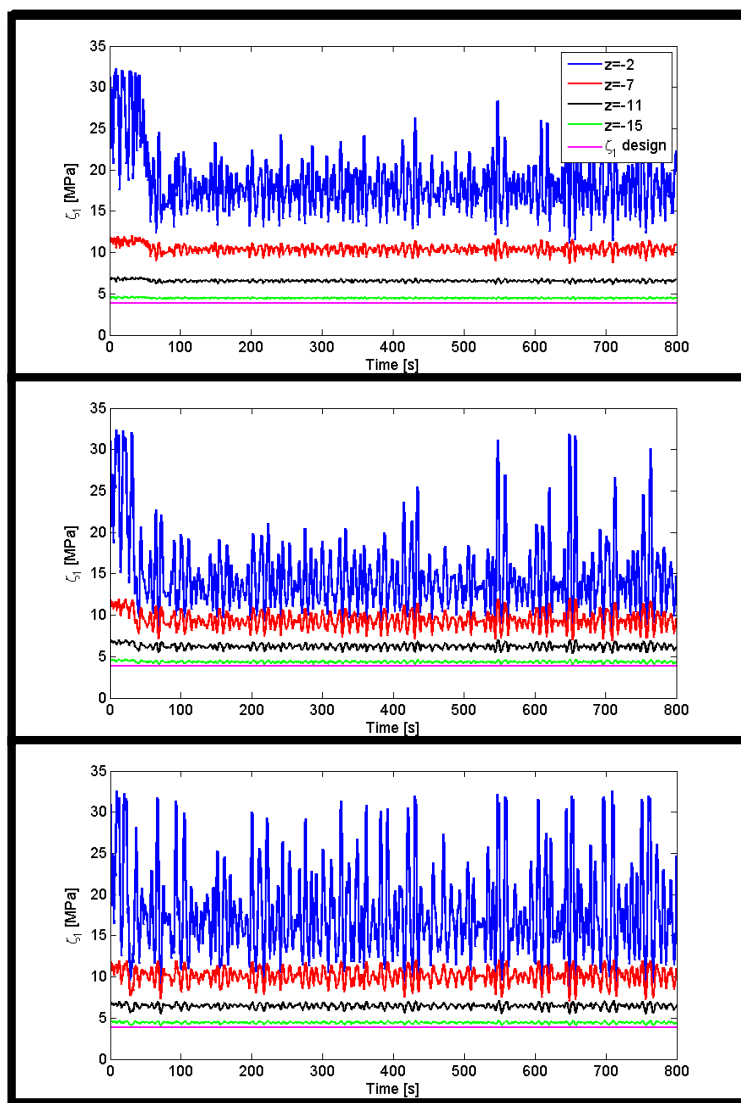


Figure 8-20: Shell buckling ratio at the four elevations. Top: Condition 1. Middle: Condition 2. Bottom: Condition 3

Chapter 8: Internal loads in the hull

The shell buckling ratio is seen to be larger than 1 during the whole time series at all cross sections in each condition. This indicates that the design is not susceptible to shell buckling at any of the cross sections in any of the three conditions. It can also be seen that the ratio at all cross sections is larger than the design ratio of 3.81.

Table 8-4 gives the mean, standard deviation and minimum value of the shell buckling ratio in each condition for each of the four elevations for the last 400 s of the time series.

Table 8-4: Mean, standard deviation and minimum value of the shell buckling ratio

	Elevation	Mean	Standard deviation	Minimum
Condition 1	z=-2	17.52	3.41	11.18
	z=-7	10.32	0.53	8.66
	z=-11	6.55	0.14	6.12
	z=-16	4.47	0.05	4.32
Condition 2	z=-2	14.05	4.09	8.24
	z=-7	9.23	0.99	6.95
	z=-11	6.20	0.31	5.40
	z=-16	4.34	0.11	4.06
Condition 3	z=-2	17.01	5.14	8.27
	z=-7	9.94	1.00	7.01
	z=-11	6.42	0.29	5.48
	z=-16	4.42	0.11	4.09

The ratio decreases as one moves along the main column from the MWL to towards the base. This indicates that the susceptibility to shell buckling is increasing with depth. It is also seen that the buckling ratio's standard deviation is decreasing with depth. This can be explained by the increasing dominance of the hydrostatic pressure.

Buckling ratio 2: Panel ring buckling

Buckling ratio 2 is related to panel ring buckling. The design is susceptible to panel ring buckling if ratio 2 is smaller than 1. If this is the case, then the ring frame moment of inertia $I_{ringframe}$ is smaller than the minimum requirement I_R . $I_{ringframe}$ is determined by the geometry, which has already been defined. I_R is determined by the sum of three components, as was shown in equation 3-23.

The first component, I_x , depends on the axial and bending stress. Figure 8-19 showed that the compressive stresses due to the axial force and bending moment from the time series are smaller than the design axial and bending stresses. Therefore, the minimum requirement to I_x is reduced with respect to the minimum requirement used for the design.

The second component, I_{xh} , depends on the shear stress. Figure 8-19 showed that the shear stress due to the shear force takes on both larger and smaller values than the design shear stress, depending on elevation. Therefore, it depends on the elevation whether the minimum requirement to I_{xh} is reduced with respect to the minimum requirement used for the design.

The third component, I_h , depends on the circumferential stress. As previously shown, the circumferential stress here is equal to the design circumferential stress only at the bottom of the main column.

In summary, the minimum requirements to two of the three components of the moment of inertia are less strict with the current loads than with the design loads used in chapter 3. Figure 8-21 shows the time series of the panel ring buckling ratio at the four elevations for each condition.

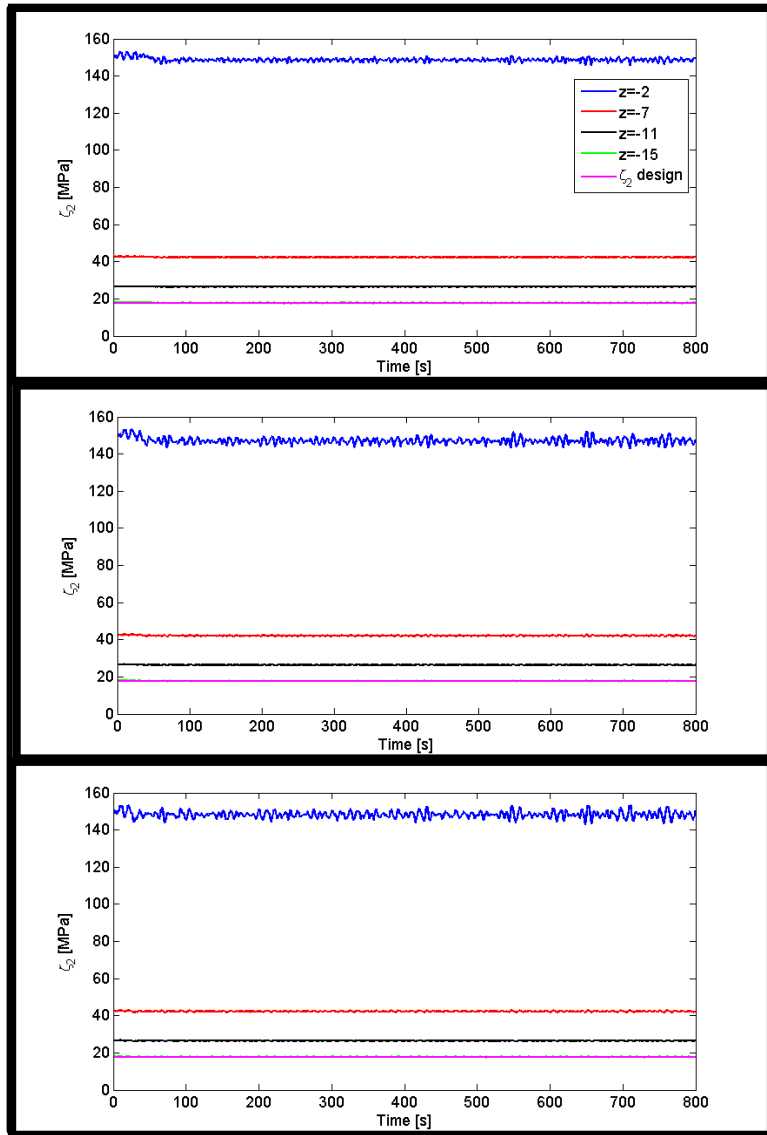


Figure 8-21: Panel ring buckling ratio at the four elevations. Top: Condition 1. Middle: Condition 2. Bottom: Condition 3

The figure indicates a very high panel ring buckling ratio at $z=-2$ m. At the other elevations it is also very high. At $z=-7$ m the ratio is about 42, while it is about 26 at $z=-11$ m. At the bottom of the main column, the ratio is almost equal to the design ratio from chapter 3.

Table 8-5 gives the mean, standard deviation and minimum value of the shell buckling ratio in each condition for each of the four elevations for the last 400 s of the time series.

Table 8-5: Mean, standard deviation and minimum value of the panel ring buckling ratio

	Elevation	Mean	Standard deviation	Minimum
Condition 1	z=-2	148.54	1.01	145.58
	z=-7	42.35	0.13	41.98
	z=-11	26.52	0.06	26.35
	z=-16	17.82	0.03	17.74
Condition 2	z=-2	146.90	1.68	142.77
	z=-7	42.11	0.23	41.56
	z=-11	26.38	0.12	26.10
	z=-16	17.73	0.07	17.57
Condition 3	z=-2	148.08	1.76	142.79
	z=-7	42.28	0.23	41.56
	z=-11	26.48	0.12	26.13
	z=-16	17.79	0.06	17.60

The mean values indicate that the ratio is strongly inverse proportional to the hydrostatic pressure. Also for this ratio, it is seen that the standard deviation is decreasing with depth. These observations indicate that the panel ring buckling ratio is strongly dependent on the hydrostatic pressure. When comparing to the design ratio of 17.66, it is seen that the minimum ratio computed in conditions 2 and 3 are slightly lower than this.

Both buckling ratios were found to be higher than 1 at each elevation in each condition. This indicates that the design is not susceptible to buckling in any of the three conditions. Similar to the pontoon evaluation, more load conditions, including current and turbulent wind as a minimum, are required to make a more general and substantiated judgement about the present main column design.

9 Conclusions and recommendations for future work

This chapter concludes this thesis work and gives the author's recommendations for future work. Paragraph 9.1 summarizes and presents the conclusions. Paragraph 9.2 gives recommendations for future work.

9.1 Conclusions

An initial scantling design for the pontoons and main column of Bachynski's TLPWT design was made based on ultimate limit state design. Design loads were defined and estimated, and the design was then checked for stability with ABS and DNV design codes. An evaluation of the design was made based on numerical results for the internal loads computed in three selected wind-wave conditions. The three selected conditions were defined by a uniform steady wind speed and a sea state described by a JONSWAP spectrum. Both wind and waves were head-on. Both the pontoon and the main column were found to not be susceptible to buckling in any of the three conditions. The numerical results also revealed that some of the design stresses had been largely overestimated in the initial design process/check. The estimated compressive action at the pontoon base due to tendon tension induced bending moment, and at the main column base due to structural weight, did not account for distributed buoyancy forces. This resulted in very inaccurate estimations for the axial stress due to axial forces in the main column, except for close to the MWL, and for the bending stress due to the tendon induced bending moment at the pontoon base.

In order to create a beam element model of the design, the pontoon and main column mass distributions were obtained by simplifying the scantling design. Uniform equivalent Euler-Bernoulli bending and torsional stiffness were estimated using FE modelling. Together the mass distribution and equivalent stiffness of the main column and pontoons define the equivalent beam model for the hull. The base node was modelled as rigid. The derived equivalent stiffnesses were based on the displacement at the middle of the beam in a cantilever beam test with an applied load at the free end. The final estimated equivalent stiffness turned out to give a varying degree of accuracy along the beam length when compared to the numerical solution in

the FE model. Using the derived equivalent stiffness to predict the displacement at another location on the beam resulted in errors of up to 27 % with respect to the numerical solution.

The equivalent beam model for the hull was implemented in a beam model of the complete TLPWT in RIFLEX. Except for the hull base node, the RIFLEX TLPWT beam model consisted of elastic elements only. It is therefore referred to as a fully-flexible TLPWT model. The natural periods of the fully-flexible TLPWT were estimated with the inbuilt eigenvalue analysis tool in RIFLEX. This tool uses constant 2-D added mass coefficients and does not account for damping. The natural periods were compared to Bachynski's estimations for the same TLPWT with a rigid hull and frequency-dependent 3-D added mass and damping coefficients. As expected, the eigenvalue analysis indicated that the elastic hull leads to increased natural periods in heave, pitch and yaw. However, in surge, the natural period decreased with respect to the rigid hull TLPWT. This can be explained by the differences in added mass and damping.

A new approach for implementing added mass, radiation damping and wave excitation from first-order potential theory for sections of the hull structure was tested. A 3-D panel model was made for the hull, and WAMIT was used to compute the radiation and diffraction pressures on each panel. The structure was divided into sections and an algorithm which associates each panel with one of the sections allows the total radiation and diffraction pressures to be computed for each section by integration. The total hydrodynamic load for a section was transferred to the RIFLEX equivalent beam model by using SIMO-bodies. In that way, the RIFLEX equivalent beam model for the hull became an elastic multi-body SIMO-RIFLEX model which can account for frequency-dependent loads from first-order potential theory. The total loads represented by all of the SIMO-bodies together were compared to WAMIT's output for the hull as a whole. All pure translational added mass, damping and excitation components are exactly the same as WAMIT's output. The magnitude of the rotational components which were checked were found to be slightly smaller than WAMIT's output for the hull as a whole. This is partly due to the loads' selected point of application within each section, and partly due to the fact that rotational quantities were assumed to be negligible within each section.

The elastic multi-body model of the hull was implemented in the fully-flexible RIFLEX model of the TLPWT. Due to the elastic hull, the whole structure was found to have displaced upwards with approximately 3.5 cm in static equilibrium. The fundamental natural periods were estimated

from simulated decay tests, both with and without quadratic drag, and compared to Bachynski's estimations for the rigid hull TLPWT. The quadratic drag was calculated with the Morison formulation and was found to have almost no influence on the fundamental natural periods. All natural periods were found to have increased with respect to Bachynski's results for the rigid hull TLPWT. The largest increase was seen in the heave and platform pitch natural periods. With respect to Bachynski's rigid hull TLPWT, these natural periods indicated an increase of 43 % and 18 % respectively. Time-domain simulations in basic combined wind-wave environments were executed for both the elastic multi-body TLPWT and Bachynski's rigid hull TLPWT. The nacelle motions, bending moments at the tower base and tension at the top of each tendon were compared for the two models. The elastic multi-body model predicts larger motions, larger bending moments at the tower base and higher tendon tensions at the top of each tendon.

An attempt was made to investigate the effect of elasticity on the dynamic internal loads in the hull. First, pure hydrodynamic analysis in the frequency-domain was carried out with the WADAM module in HydroD for a "reduced" rigid version of the structure. The reduced structure is characterized by a large concentrated mass located at the top of the main column which represents the turbine mass. The results from this analysis were first compared to the results from time-domain analysis in SIMO-RIFLEX with a correspondingly reduced version of the elastic multi-body TLPWT in a windless environment with regular waves only. Then, the results were compared the results from the same time-domain analysis executed with the full elastic multi-body TLPWT. It was observed that the dynamic axial force in the main column, and the dynamic shear force and dynamic bending moment in the pontoon showed an unexpectedly high amplification at certain frequencies. The estimated RAOs indicate that the motion response is also strongly amplified at these frequencies. A possible explanation for the large amplification of the dynamic internal loads at these frequencies could therefore be that the two software estimate completely different inertia loads.

9.2 Recommendations for future work

In the following, a number of recommendations for future work are given. An attempt has been made to rank the recommendations based on the author's opinion on how fundamental and

important they are to future research and practical application.

1. The method of implementing the loads from potential theory for sections of the hull gave good results for the TLPWT in this work. The applicability of the method should be tested for other types of structures too, such as spar-type or semi-submersible type floaters.
2. The investigation of amplification of internal dynamic loads due to hull elasticity gave highly unexpected results for certain wave frequencies. In the present work, it was suggested that a possible explanation could be large differences in estimated inertia loads induced by very large motion response amplifications at these frequencies. It is recommended that future work investigates where these large differences come from, and whether the WADAM results are inherently different from the SIMO-RIFLEX results due to fundamental inconsistencies, such as different modelling techniques and/or computation methods.
3. In the present work, the hydrodynamic loads for sections of the structure was based on first-order potential theory. Future work may do the same for higher-order potential theory for a more accurate estimation of the loads. Additionally, a higher-order panel method or a finer panel mesh would enable the model to better capture high-frequency waves.
4. Future work could investigate the elastic multi-body TLPWT's global response in a larger number of environmental conditions. First, including loads from currents and tidal variations, tower drag and turbulent wind would give a more realistic loading environment. Second, a more complete analysis should also consider the model's response in misaligned wind-waves, and the response to extreme weather conditions.
5. The global dynamic analysis did not account for the effects of soil-tendon interaction. Future work could include this, and thereby making the global dynamic analysis more complete.

6. Amplification of internal dynamic loads can be caused not only by structural elasticity, but also by the combined action of external loads. For an offshore wind turbine, the most obvious combined action would be that of wind and waves, and future work is therefore recommended to investigate the effects of this. Additionally, also accounting for current would allow the analysis to investigate the effects of current loads and the Doppler shift on the waves.
7. In the present study, the scantling design was evaluated based on the system's response in three environmental conditions only. The design should be evaluated based on the response in a larger number of conditions, including more external loads, such as current and turbulent wind.
8. The proposed scantling design is a ULS design. However, fatigue loads may be governing, especially for connections, such as the pontoon-base node connection. Furthermore, fatigue damage estimations in a number of environmental conditions are needed to check whether the design is susceptible to fatigue failure. Should a stronger design be needed, then a new design is recommended. Some proposed design modifications are a non-uniform wall thickness along the length of the pontoon and main column, assigning a larger proportion of the steel to the plating and stiffeners which are located close to the base node connection. Also, assigning a larger proportion of material to the plating and stiffeners at the bottom of the pontoons than to the plating and stiffeners at the top and side walls would increase the pontoons resistance to tendon induced compressive stresses.
9. The proposed equivalent beam model for the hull models the base node as rigid. Future work could complete the equivalent beam model by modelling the base node as elastic. This would make the model more realistic. The stiffness of the base node could be derived in the same way as for the pontoon and main column.

10. No scantling design was made for the base node. In order to make sure that the complete hull complies with industry stability requirements, a scantling design should be made for the base node too. This can be done by following guidelines in DNV-RP-C202, which was also used for the main column.

11. The equivalent stiffness estimations which were derived for the pontoon and main column in the equivalent beam model were not able to accurately represent the actual stiffness along the whole length when compared to the numerical results in the FE model. Future work could improve the equivalent beam model by modelling each part with a varying stiffness along the length.

12. In the elastic multi-body hull model, the current selection of the hydrodynamic section loads' point of application results in underestimated rotational loads. Future work could re-define the section loads' point of application to be at the middle of each section, instead of at one of the section's boundaries. This could improve the accuracy of the elastic multi-body model's rotational loads for the hull as a whole. Another option could be to increase the number of sections, and thereby reduce the size of each section. This would reduce the error which is made when neglecting rotational quantities within each section.

References

- [1] European Wind Energy Association, "<http://www.ewea.org/publications/reports/deep-water/>," [Online].
- [2] Y. H. Bae, M. H. Kim, S. W. Im and I. H. Chang, "Aero-Elastic-Control-Floater-Mooring Coupled Dynamic Analysis of Floating Offshore Wind Turbines," 2011.
- [3] "http://www.statoil.com/en/TechnologyInnovation/NewEnergy/RenewablePowerProduction/Offshore/Hywind/Downloads/Hywind_nov_2012.pdf," [Online].
- [4] "<http://www.meretmarine.com/fr/content/eolien-flottant-windfloat-veut-passer-la-vitesse-superieure>," [Online].
- [5] "<http://www.rechargenews.com/wind/1403335/ideol-seals-japan-floater-pact-with-hitachizosen>," [Online].
- [6] "<http://thefutureofthings.com/5981-deep-water-offshore-wind-turbine/>," [Online].
- [7] R. Laugesen and A. M. Hansen, "Experimental Study of the Dynamic Response of the DTU 10 MW Wind turbine on a Tension Leg Platform," DTU Wind Energy, 2015.
- [8] A. Myhr, C. Bjerkseter, A. Ågotnes and T. A. Nygaard, "Levelised cost of energy for offshore floating wind turbines in a life cycle perspective," *Renewable Energy - An International Journal*, vol. 66, pp. 714-728, 2014.
- [9] E. E. Bachynski, *Design and Dynamic Analysis of Tension Leg Platform Wind Turbines*, 2014.
- [10] Y. Zhao, J. Yang and Y. He, "Preliminary Design of a Multi-Column TLP Foundation for a," *Energies*, 2012.
- [11] J. E. Withee, *Fully Coupled Dynamic Analysis of a Floating Wind Turbine System*, 2004.
- [12] K. H. Lee, *Responses of Floating Wind Turbines to Wind and Wave Excitation*, 2005.

-
- [13] Y. H. Bae, M. H. Kim and Y. S. Shin, "Rotor-Floater-Mooring Coupled Dynamic Analysis of Mini TLP-Type Offshore Floating Wind Turbines," 2010.
- [14] D. Matha, "Model development and loads analysis of an offshore wind turbine on a tension leg platform, with a comparison to other floating turbine concepts," 2009.
- [15] R. B. Matten and M. J. Provost, "Typhoon SeaStar TLP," 2002.
- [16] G. K. V. Ramachandran, H. Bredmose, J. N. Sørensen and J. J. Jensen, Fully Coupled Three-Dimensional Dynamic Response of a TLPWT in Waves and Wind, 2014.
- [17] MARINTEK, RIFLEX Theory Manual, 2015.
- [18] J. Journee and W. Massie, Offshore Hydromechanics, 2001.
- [19] J. M. Jonkman, "Dynamics Modeling and Loads Analysis of an Offshore Floating Wind Turbine," 2007.
- [20] O. M. Faltinsen, Sea Loads on Ships and Offshore Structures, 1993.
- [21] J. N. Newman and C. H. Lee, "Computation of wave effects using the panel method".
- [22] S. Gueydon and S. Weller, "Study of a Floating Foundation for Wind Turbines," *Journal of Offshore Mechanics and Arctic Engineering*, vol. 135, 2013.
- [23] M. O. L. Hansen, Aerodynamics of Wind Turbines, 2008.
- [24] P. J. Moriarty and A. C. Hansen, AeroDyn Theory Manual, 2005.
- [25] J. Jonkman, S. Butterfield, W. Musial and G. Scott, "Definition of a 5 MW Reference Wind Turbine for Offshore System Development," 2009.
- [26] J. Yang and R. Michael, "TLP Hull Structural Design and Analysis".
- [27] R. Aggarwal, S. Bas and R. D'Souza, "The Tension Leg Platform - A Retrospective," 2013.
- [28] D. Zhang, "Parametric Study of Plate and Stiffening Arrangements for Non-Circular TLP Columns and pontoons," 2006.

-
- [29] Offshore Magazine, "<http://www.offshore-mag.com/articles/print/volume-56/issue-6/news/general-interest/tlp-technology-seastar-minimal-platform-for-small-deepwater-reserves.html>," [Online].
- [30] J. E. L. Lygren, "Dynamic response analysis of a tension-leg floating wind turbine," Norwegian University of Science and Technology, 2011.
- [31] W. L. Moon and C. J. Nordstrom, "Tension Leg Platform Turbine: A Unique Integration Of Mature Technologies," 2010.
- [32] A. Henderson, K. Argyriadis and J. Nichols, "Offshore Wind Turbines on TLPs - Assessment of Floating Support Structures for Offshore Wind Farms in German Waters," 2010.
- [33] A. Crozier, "Design and Dynamic Modelling of the Support Structure for a 10 MW Offshore Wind Turbine," 2011.
- [34] K. Suzuki, H. Yamaguchi, M. Akase, A. Imakita, T. Ishihara, Y. Fukumoto and T. Oyama, "Initial Design of TLP for Offshore Wind Farm".
- [35] R. W. Copple and C. Capanoglu, "Tension Leg Wind Turbine Conceptual Design Suitable for a Wide Range of Water Depths," 2012.
- [36] Det Norske Veritas, *Recommended Practice DNV-RP-C202, Buckling Strength of Shells*, 2013.
- [37] Det Norske Veritas, *Recommended Practice DNV-R-C201, Buckling Strength of Plated Structures*, 2010.
- [38] American Bureau of Shipping, "Rules for Building and Classing Mobile Offshore Drilling Units," 2015.
- [39] B. & Partners, "Islands for Offshore Nuclear Power Stations".
- [40] J. Jonkman, "Definition of the Floating System for Phase IV of OC3," NREL, 2010.
- [41] J. Spijkers, A. Vrouwenvelder and E. Klaver, "Part 1 - Structural Vibrations," in *Structural Dynamics CT 4140*, 2005.

-
- [42] J. M. Gere and B. J. Goodno, *Mechanics of Materials, 7th edition*, Cengage Learning, 2009.
- [43] MARINTEK, RIFLEX User Manual, 2009.
- [44] J. N. Newman, *Marine Hydrodynamics*, MIT, 1977.
- [45] Det Norske Veritas, *Recommended Practice DNV-RP-C205, Environmental Conditions and Environmental Loads*, 2007.
- [46] I. WAMIT, *WAMIT User Manual*, 2006.
- [47] S. S. Rao, *Mechanical Vibrations 5th edition*, Pearson, 2001.
- [48] R. E. D. Bishop and W. G. Price, *Hydroelasticity of Ships*, Cambridge University Press, 1979.
- [49] B. M. Sumer and J. Fredsoe, *Hydrodynamics around cylindrical structures*, 2006.
- [50] J. Fredsøe, *Hydrodynamics*, 2008.
- [51] G. R. Cowper, "The Shear Coefficient in Timoshenko's Beam Theory," *Journal of Applied Mechanics*, vol. 33, pp. 335-340, 1966.

Appendix

A. Potential flow and regular wave theory

This chapter summarizes the theory on potential flow and linear waves.

A.1 Potential flow essentials

A potential flow is a flow which has a velocity field that can be written as the gradient of the velocity potential [18]:

$$V = \nabla\phi \quad (\text{A-1})$$

where the gradient is defined as

$$\nabla = \left[\frac{\partial}{\partial x}, \frac{\partial}{\partial y}, \frac{\partial}{\partial z} \right] \quad (\text{A-2})$$

This implies that:

1. The flow is irrotational.
2. ϕ satisfies the Laplace equation if the flow is incompressible.

Irrotational flow:

For an irrotational flow, the curl of the velocity field is zero:

$$V = \nabla\phi \quad (\text{A-3})$$

$$\nabla \times V = \nabla \times \nabla\phi \quad (\text{A-4})$$

The curl of a gradient is always zero. The right hand side then becomes

$$\nabla \times V = 0 \quad (\text{A-5})$$

This proves that the curl of the velocity field is zero.

Incompressible flow:

The continuity condition for incompressible flow reads

$$\nabla \cdot \mathbf{V} = 0 \quad (\text{A-6})$$

Substituting the expression for the velocity in equation A-1 gives

$$\nabla \cdot \nabla \phi = 0 \quad (\text{A-7})$$

$$\nabla^2 \phi = 0 \quad (\text{A-8})$$

Equation A-8 is the Laplace equation. It is also referred to as the continuity equation. The wave body interaction problem is determined by solving the Laplace equation and corresponding boundary conditions. These boundary conditions are described in the following. Note that the boundary conditions have been linearized.

Sea bed boundary condition:

The vertical velocity component of the fluid particles at the sea bed must be zero. This is sometimes referred to as the no-leak condition. Mathematically, it can be expressed as follows:

$$\frac{\partial \phi}{\partial z} = 0 \quad \text{for } z = -h \quad (\text{A-9})$$

where h is the water depth, and z is the vertical coordinate, which has its origin at the MWL and is positive upwards.

Body boundary condition:

No fluid enters or leaves the body surface. For a body which is moving with velocity U , this can be expressed as

$$\frac{\partial \phi}{\partial n} = U \cdot \mathbf{n} \quad (\text{A-10})$$

where \mathbf{n} is the normal vector on the body surface. The positive normal direction is into the fluid domain.

Free-surface boundary condition:

The water pressure, p , at the free surface must be equal to the atmospheric pressure, p_a . This is called the dynamic free-surface boundary condition. The pressure follows from the Bernoulli equation. This can be expressed mathematically as

$$\frac{\partial \phi}{\partial t} + g \eta = 0 \quad \text{for } z = 0 \quad (\text{A-11})$$

There is also a free-surface kinematic boundary condition, which can be expressed as

$$\frac{\partial \eta}{\partial t} - \frac{\partial \phi}{\partial z} = 0 \quad \text{for } z = 0 \quad (\text{A-12})$$

The free-surface dynamic and kinematic boundary conditions in equations A-11 and A-12 can be combined to give

$$\frac{\partial^2 \phi}{\partial t^2} + g \frac{\partial \phi}{\partial z} = 0 \quad \text{for } z = 0 \quad (\text{A-13})$$

A.2 Linear wave theory for regular waves

It is assumed that the sea water can be described by a planar potential flow [20] and that the wave amplitude is small compared to the water depth. The figure below shows some key wave parameter definitions which are used in the following equations.

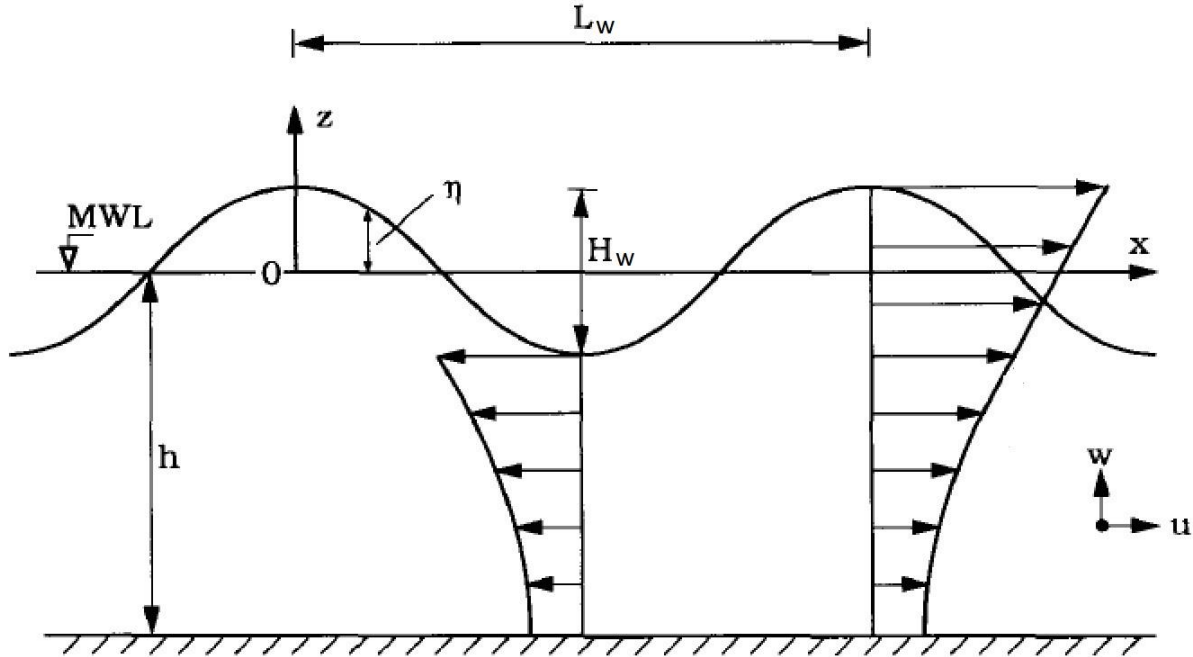


Figure A-1: Regular planar wave [48]

For a wave with wave length L_w and period T_w , the wave frequency and wave number are defined as:

$$\omega = \frac{2 \pi}{T_w} \quad (\text{A-14})$$

$$k = \frac{2 \pi}{L_w} \quad (\text{A-15})$$

The surface elevation of a regular wave with wave height H_w can be described by:

$$\eta = \frac{H_w}{2} \cos(kx - \omega t) \quad (\text{A-16})$$

The velocity potential and fluid particle velocities:

The corresponding velocity potential is given by the relation:

$$\phi(x, z, t) = \frac{H_w \omega}{2 k} \frac{\cosh(k(z+h))}{\sinh(kh)} \sin(kx - \omega t) \quad (\text{A-17})$$

With the velocity potential defined, the horizontal and vertical fluid particle velocities can be derived:

$$u = \frac{H_w \omega}{2} \frac{\cosh(k(z+h))}{\sinh(kh)} \cos(kx - \omega t) \quad (\text{A-18})$$

$$w = \frac{H_w \omega}{2} \frac{\sinh(k(z+h))}{\sinh(kh)} \sin(kx - \omega t) \quad (\text{A-19})$$

The dispersion relation:

The dispersion relation relates the wave frequency of a wave to its wave number:

$$\omega^2 = g k \tanh(kh) \quad (\text{A-20})$$

A.3 Irregular waves and wave spectra

Linear theory is used to model irregular sea. The wave elevation of an irregular sea can be described as the superposition of many wave components:

$$\eta = \sum_{j=1}^N a_j \cos(k_j x - \omega_j t + \epsilon_j) \quad (\text{A-21})$$

A wave spectrum can be used to express the wave amplitude:

$$\frac{1}{2} a_j^2 = S(\omega_j) \Delta\omega \quad (\text{A-22})$$

A wave spectrum expresses how the energy is distributed over the wave frequencies. Two of the most common wave spectra are the Pierson-Moskowitz (PM) and JONSWAP spectra. The PM spectrum is often used to describe a fully developed sea, which means that the waves have reached an equilibrium with the wind. The JONSWAP spectrum is a modified PM spectrum used to describe the sea state in the North Sea, which is fetch-limited and hence does not allow waves to fully develop. The JONSWAP spectrum is typically more “peaky” than the PM spectrum.

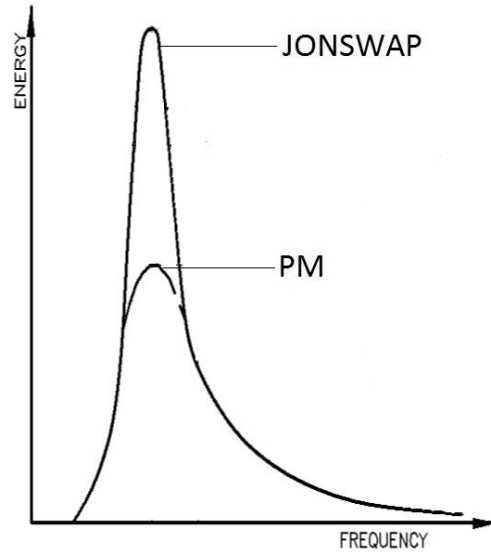


Figure A-2: The PM and JONSWAP spectra

A time series of the surface elevation of an irregular sea can be computed by taking the wave spectrum and using the inverse Fourier transform to go from the frequency domain to the time domain.

A.4 Wheeler stretching

Linear wave theory, also called Airy wave theory, is applicable only up to the MWL. One way to describe the wave kinematics above the MWL is to stretch the velocity profile. The wave kinematics are computed up to the MWL and then stretched (or compressed) by being mapped onto to the full water column from the sea bed to the instantaneous surface elevation.

B. Wind field

A description of the wind field is required in order to compute the aerodynamic loads. The wind field description should represent both spatial and temporal fluctuations in order to be realistic. In the following, three common contributors to such fluctuations are presented, namely wind shear, tower shadow and atmospheric turbulence.

B.1 Wind shear

The wind speed varies with altitude. This variation is represented by the vertical wind shear. Figure B-1 shows a typical wind shear variation.

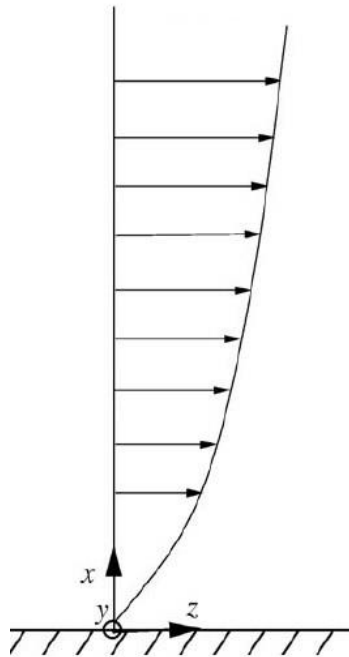


Figure B-1: Typical wind shear [23]

In the present study no wind shear was applied. Instead, the wind was approximated to be the same at every elevation.

B.2 Tower shadow

The presence of the tower disturbs the wind field and has an effect on the wind inflow also for an upwind turbine. Each time a blade passes a region in which the inflow is altered, the thrust varies. This in turn can lead to increased fatigue damage.

In the present study, the flow around the tower was based on a 2-D potential solution for constant flow around a cylinder, as depicted in Figure B-2. This also implicates that there is no drag on the tower.

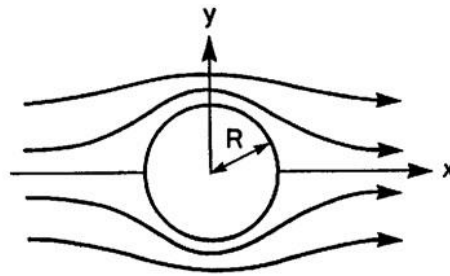


Figure B-2: Potential flow around a cylinder [49]

B.3 Atmospheric turbulence

Atmospheric turbulence refers to irregular small-scale changes in wind speed and direction. This causes spatial and temporal variations in the wind inflow seen by the rotor as depicted in Figure B-3.

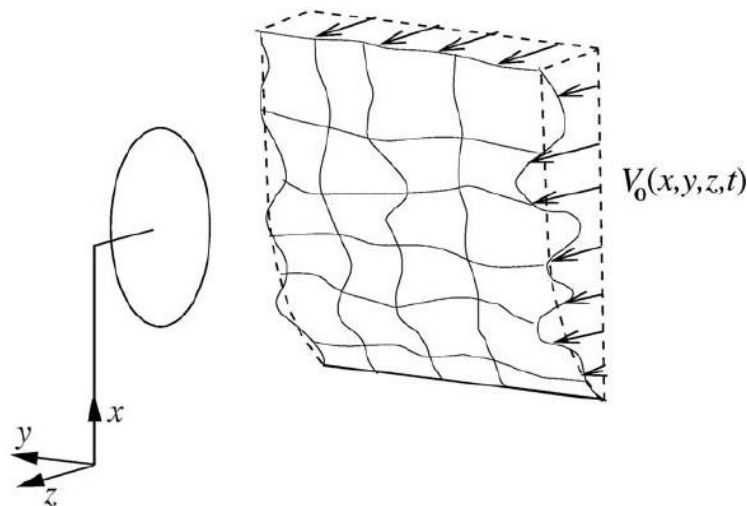


Figure B-3: Turbulent inflow seen by the rotor [23]

The turbulence is often accounted for by including parameters for the turbulence intensity and the turbulence length scale in the wind speed modelling. Turbulence was not accounted for in the simulations in this study.

C. Checking the final pontoon scantling design with the LRFD method accounting for tendon induced bending stresses and hydrostatic pressure

This appendix gives more details on the additional design check of the final pontoon scantling design. Paragraph 3.2.3.2 mentioned the outcome of the check and evaluated the design based on this. Here, all of the equations are presented. Also, comments are given on how the equations were used.

The design stress components estimations are presented first. Then the forces in the stiffened plate and the effective width are presented. Next, the characteristic buckling strength and resistance parameters of the stiffeners are treated. Last, the interaction formulas for axial compression and lateral pressure are treated. The outcome of the interaction formulas determine whether the design is complying with the stability requirements.

C.1 Design stress components

For plated structures, the following three stress components should be considered.

σ_{xd} : Design membrane stress in the x-direction

σ_{yd} : Design membrane stress in the y-direction

τ_{sd} : Design shear stress in x-y plane

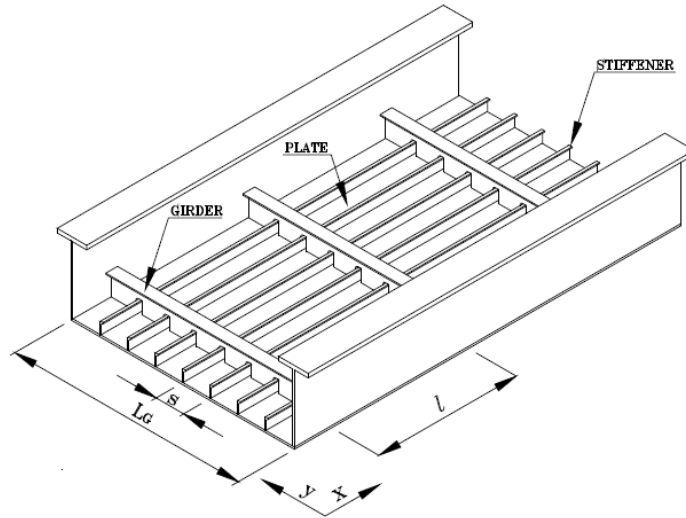


Figure C-1: Stiffened plate panel

The tendon force causes bending of the pontoon. This leads to compression of the plate and longitudinal stiffeners at the bottom of the pontoon. The bottom of the pontoon is thus compressed by the combined action of the tendon force and the hydrostatic pressure. The longitudinal stiffeners and plating at the bottom of the pontoon were therefore assumed to be the critical components. The girders are oriented perpendicularly to the direction of the compressive force induced by the tendons and are therefore assumed to not be critical components in this buckling scenario. The maximum compressive stress is at the bottom of the pontoon where the pontoon is connected to the base node. This was taken to be the design stress in the x-direction (longitudinal direction of pontoon) and is referred to as $\sigma_{x,sd}$ in the following paragraphs. The stress component in the y-direction, σ_{yd} , and the stress component in the x-y plane, τ_{sd} , were assumed to be negligible. Therefore, the considered stress components were $\sigma_{x,sd}$, which is caused by the tendon tension, and the design lateral pressure, p_{sd} , which is caused by the hydrostatic pressure.

Design stress in the x-direction caused by the tendon force

The stress in the x-direction, $\sigma_{x,sd}$, caused by the vertical tendon force was calculated with simple beam theory as previously described. To get the compressive stress from the tendon force, the moment of inertia of the cross section must be determined. This depends on the wall thickness,

the number of stiffeners and the stiffener dimensions. It was calculated using the parallel axis theorem.

Because of the girders and the bulkheads, the area moment of inertia is not constant over the length of the pontoon. In this first estimation, the contributions to the pontoon bending stiffness from the bulkheads and girders were assumed to be very small because of their relatively low thickness compared to the length of the pontoon. Therefore, only the walls and the longitudinal stiffeners were considered here. The area moment of inertia of the pontoon cross section is then the sum of the contribution from the wall and the stiffeners. The contribution from the wall was found from

$$I_{wall} = \frac{w_p h_p^3}{12} - \frac{(w_p - t_p) * (h_p - t_p)^3}{12} \quad (C-1)$$

where w_p , h_p and t_p are the pontoon width, height and wall thickness respectively.

The contribution from each stiffeners was found using the parallel axis theorem. Stiffeners at the horizontally oriented plates have a web which is oriented vertically. The contribution from such a stiffener is:

$$I_{stiffener,1} = \frac{1}{12} t_w h_w^3 + A_s d_{s,1}^2 \quad (C-2)$$

For a stiffener on one of the side walls, the contribution becomes

$$I_{stiffener,2} = \frac{1}{12} h_w t_w^3 + A_s d_{s,2}^2 \quad (C-3)$$

Here, t_w and h_w are the stiffener web thickness and height respectively, while A_s is the area of the stiffener. d is the distance from the centroid of the stiffener to the centroidal axis of the whole cross section. These parameters are indicated in Figure C-2 for a cross section with 8 equal flat bar stiffeners.

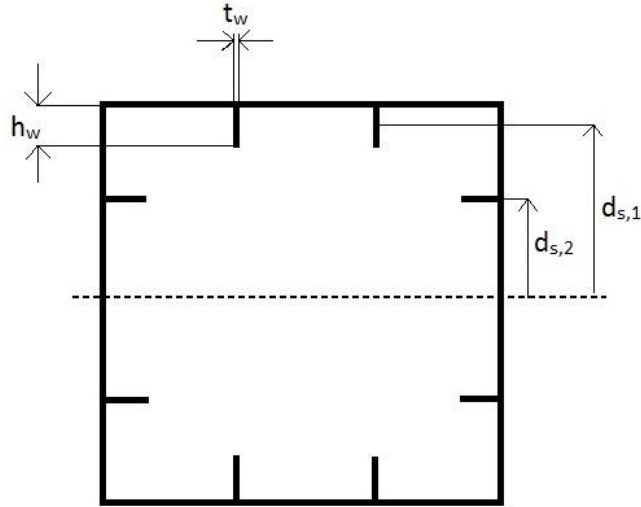


Figure C-2: Parameter definitions used for calculation of moment of inertia contribution from longitudinal stiffeners

The total area moment of inertia was found by summing up the contributions from the walls and each stiffener.

$$I_{pontoon} = I_{wall} + \sum I_{stiffeners} \quad (C-4)$$

Because of symmetry, the area moment of inertia is the same about both axes.

Design lateral pressure caused by hydrostatic pressure

The design lateral pressure was set equal to the design hydrostatic pressure. The bottom of the pontoon is located at a depth of 22 meters. With a sea water density of 1025 kg/m^3 , the hydrostatic pressure is approximately 2.21 bar. This is then also the value for the design lateral pressure, p_{sd} .

C.2 Forces in the stiffened plate and effective plate width

Because the pontoon is subjected to combined forces, the stiffened plates should be designed to resist an equivalent axial force and an equivalent lateral line load.

The equivalent axial force was calculated from the bending stress induced by the tendon tension:

$$N_{sd} = \sigma_{x,sd}(A_s + st_{plate}) \quad (C-5)$$

Here, A_s is the stiffener cross sectional area, s is the stiffener spacing and t_{plate} is the plate thickness. The equivalent axial force in the plate is thus proportional to the bending stress and also increases with plate thickness, stiffener spacing and stiffener cross sectional area.

The equivalent lateral line load is calculated with

$$q_{sd} = (p_{sd} + p_0)s \quad (C-6)$$

Here, p_0 is an equivalent lateral pressure which is proportional to the stress in the y-direction. Because this stress is neglected, p_0 is zero. Therefore, equation C-6 reduces to

$$q_{sd} = p_{sd}s \quad (C-7)$$

The equivalent line load is thus proportional to the design lateral pressure and the stiffener spacing.

Plate buckling is accounted for by the effective width method. Therefore, the plate between stiffeners is checked implicitly by the stiffener check, which is described further down. The effective plate width, s_e , for a continuous stiffener is calculated with the following formula

$$s_e = sC_{xs}C_{ys} \quad (C-8)$$

Here, C_{ys} and C_{xs} are reduction factors. C_{ys} is equal to 1 because the stresses in the y-direction have been neglected. C_{xs} depends on the reduced plate slenderness, which is defined as

$$\bar{\lambda}_p = 0.525 \frac{s}{t_{plate}} \sqrt{\frac{f_y}{E}} \quad (C-9)$$

The yield strength, f_y , and the modulus of elasticity, E , were set to 250 MPa and 210 GPa respectively. With the effective plate width, the stiffener check can be carried out to check both plate and stiffeners at the same time.

C.3 Characteristic buckling strength of stiffeners

The characteristic buckling strength of stiffeners depends on the yield strength and two additional parameters. It is found from the following equation

$$f_k = f_y \frac{1 + \mu + \bar{\lambda}^2 - \sqrt{(1 + \mu + \bar{\lambda}^2)^2 - 4\bar{\lambda}^2}}{2\bar{\lambda}^2} \quad (\text{C-10})$$

Here, μ is a geometric parameter which depends on the reduced slenderness and the effective radius of gyration. It also depends on whether the check is done at plate side or stiffener side. Eventually, f_k will then be different for plate and stiffener side. The reduced slenderness is found from the following formula

$$\bar{\lambda} = \sqrt{\frac{f_y}{f_E}} \quad (\text{C-11})$$

Here, f_E is the Euler buckling strength and f_r is the characteristic strength. The characteristic strength, f_r , depends on whether the check is done for buckling at plate side or at stiffener side. The Euler buckling strength is found from

$$f_E = \pi^2 E \left(\frac{i_e}{l_k} \right)^2 \quad (\text{C-12})$$

where i_e is the effective radius of gyration. This is for the stiffener and effective width of the wall combined. For flat bar stiffeners, the effective radius of gyration is then the radius of gyration of a t-section stiffener with flange dimensions equal to the effective plate width and the pontoon wall thickness. l_k depends on the lateral pressure and the girder spacing:

$$l_k = l \left(1 - 0.5 \left| \frac{p_{sd}}{p_f} \right| \right) \quad (\text{C-13})$$

Where p_f is a lateral pressure defined by

$$p_f = \frac{12W_e f_y}{l^2 S \gamma_M} \quad (\text{C-14})$$

This lateral pressure is the pressure that gives yield in the stiffener. Here, W_e is the smallest of the effective section modulus on the plate side and the effective section modulus on the stiffener side. Figure C-3 shows an L-section stiffener with effective plate flange.

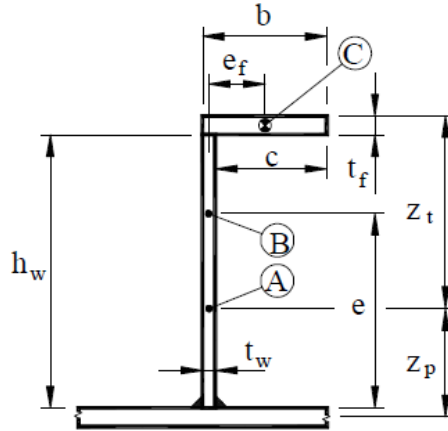


Figure C-3: L-stiffener with effective plate flange [37]

The effective section modulus on the plate side is then the moment of inertia divided by z_p , while the effective section modulus on the stiffener side is the moment of inertia divided by z_t .

Note that the design was made with simple flat bar stiffeners and not with L-section stiffeners.

C.4 Resistance parameters of stiffeners

The final goal of this procedure is to fulfill the interaction equations which are presented in paragraph C.5. To do this, the resistance parameters of the stiffeners must be determined first.

There are six resistance parameters.

The first resistance parameter is determined by the following relationship:

$$N_{Rd} = A_e \frac{f_y}{\gamma_M} \quad (\text{C-15})$$

Here, A_e is the effective area of stiffener and plate.

The second resistance parameter is the design stiffener induced axial buckling resistance:

$$N_{ks,Rd} = A_e \frac{f_{k,stiffener\ side}}{\gamma_M} \quad (\text{C-16})$$

The third parameter is the design plate induced axial buckling resistance:

$$N_{kp,Rd} = A_e \frac{f_{k,plate\ side}}{\gamma_M} \quad (C-17)$$

The fourth parameter is related to the design bending moment resistance on the stiffener side:

$$M_{s,Rd} = W_{es} \frac{f_y}{\gamma_M} \quad (C-18)$$

Here, W_{es} is the effective elastic section modulus on the stiffener side.

The fifth parameter is related to the design bending moment resistance on the plate side:

$$M_{p,Rd} = W_{ep} \frac{f_y}{\gamma_M} \quad (C-19)$$

Here, W_{ep} is the effective elastic section modulus on the plate side.

The sixth parameter is the Euler buckling strength:

$$N_E = \frac{\pi^2 E A_e}{\left(\frac{l_k}{i_e}\right)^2} \quad (C-20)$$

With these parameters defined, the interaction between compression and lateral pressure can be quantified.

C.5 Interaction formulas for axial compression and lateral pressure

Four interaction equations need to be fulfilled for lateral pressure on the plate side. Also on the stiffener side, four interaction equations need to be fulfilled. So in total, eight interaction equations must be fulfilled. Before presenting these equations, two design bending moments are introduced, which are induced by the equivalent lateral line load:

$$M_{1,Sd} = \left| \frac{q_{sd} l^2}{24} \right| \quad (C-21)$$

$$M_{2,Sd} = \left| \frac{q_{sd} l^2}{12} \right| \quad (C-22)$$

The first interaction equation is:

$$\frac{N_{Sd}}{N_{ks,Rd}} + \frac{M_{1,Sd} - N_{Sd}z^*}{M_{s,Rd} \left(1 - \frac{N_{Sd}}{N_E}\right)} \leq 1 \quad (C-23)$$

Here, z^* is the distance from the neutral axis of the effective stiffener section to the bottom of the pontoon. This is close to the value of z_p indicated in the figure above. Simplifying by setting z^* equal to zero is always allowed according to DNV. This was done here.

The second interaction equation is:

$$\frac{N_{Sd}}{N_{kp,Rd}} - 2 \frac{N_{Sd}}{N_{Rd}} + \frac{M_{1,Sd} - N_{Sd}z^*}{M_{p,Rd} \left(1 - \frac{N_{Sd}}{N_E}\right)} \leq 1 \quad (C-24)$$

All of the other six interaction equations are similar to the two presented here. To avoid unnecessary quoting of the DNV recommended practice, the reader is referred to the DNV document for further details in the definition of the remaining interaction equations.

D. Stiffness estimation for the reference design pontoon and main column

Here, the results from the FE cantilever beam tests for the reference pontoon and main column presented. Also, the deflection predicted by elementary beam theory is presented and compared to the FE solution.

D.1 Deflections of the reference pontoon and main column derived from FE analysis

The cantilever beam test for the reference pontoon and main column were carried out with the exact same loads as in paragraph 4.2. The same element type and characteristic mesh size was used as in the FE model of the flexible pontoon and main column. Table D-1 shows the deflection at the midpoint of the beam for the reference pontoon and main column. For comparison, the corresponding deflections found for the flexible pontoon and main column are shown too.

Table D-1: Deflections of both the reference and flexible pontoon and main column computed in ABAQUS

	Flexible pontoon	Reference pontoon	Flexible main column	Reference main column
Deflection in bending [mm]	1.75	1.3	1.26	1.39
Deflection in torsion [rad]	0.00083	0.000543	0.00015	0.000142

The deflections of the reference pontoon are smaller than those of the flexible pontoon. This can be explained by the lower cross section moments of inertia of the flexible pontoon, where material in principle has been removed from the walls and added to stiffeners, girders and bulkheads, effectively moving material closer to the centroidal axis of the cross section.

The flexible main column has a lower deflection in the bending test than the reference main column. This can be explained by the three bulkheads, which provide extra bending stiffness.

The torsional deflection of the flexible main column is slightly larger than that of the reference main column. This indicates that taking some material from the walls and adding bulkheads and ring stiffeners has reduced the main column's torsional stiffness. Last, it is important to keep in mind that even if the reference design gives a lower deflection in three of the four cantilever beam tests, it has a much lower resistance to external pressure due to the absence of stiffeners, girders and bulkheads.

D.2 Deflections of the reference pontoon and main column estimated with elementary beam theory

The numerical output of the FE models for the reference pontoon and main column (paragraph D.1) was verified with simple hand calculations and beam theory. First, the area moment of inertia and torsional constant of both cross sections (pontoon and main column) were estimated. Then, the deflections due to the applied loads at the free end were calculated and compared to the deflections derived from FE analysis.

First, Euler-Bernoulli beam theory was used for the comparison. However, this resulted in deflections which were 20-25 % higher than the numerical output. This can be explained by the relatively low slenderness of the two parts, which gives rise to shear deformations. Therefore, Timoshenko beam theory was used instead. The modulus of elasticity and shear modulus used are 210 GPa and 79.3 GPa respectively. The Poisson ratio is 0.3.

D.2.1 Estimation of the cross section properties

In the following, the area moment of inertia, torsional constant and Timoshenko shear coefficient are estimated with simple hand calculations for the reference pontoon and main column.

Cross section properties of the reference pontoon

The area moment of inertia of the hollow rectangular cross section of the reference pontoon is

$$I_{eq,p} = \frac{w_p h_p^3}{12} - \frac{(w_p - 2t_{eq,p})(h_p - 2t_{eq,p})^3}{12} = 4.7716 \text{ m}^4 \quad (\text{D-1})$$

The torsional constant is [42]

$$J_{eq,p} = \frac{2t_{eq,p} \left((w_p - t_{eq,p})(h_p - t_{eq,p}) \right)^2}{(w_p - t_{eq,p}) + (h_p - t_{eq,p})} = 7.1517 \text{ m}^4 \quad (\text{D-2})$$

The shear coefficient is [50]

$$\kappa_p = \frac{20(1 + \nu)}{48 + 39\nu} = 0.4355 \quad (\text{D-3})$$

Cross section properties of the reference main column

The area moment of inertia of the hollow circular cross section of the reference design main column is

$$I_{eq,mc} = \frac{\pi}{64} D_1^4 - \frac{\pi}{64} * (D_1 - 2 * t_{eq,mc})^4 = 58.6765 \text{ m}^4 \quad (\text{D-4})$$

The torsional constant is [42]

$$J_{eq,mc} = \frac{\pi}{2} \left(\frac{D_1}{2} \right)^4 - \frac{\pi}{2} \left(\frac{D_1 - 2 * t_{eq,mc}}{2} \right)^4 = 117.3531 \text{ m}^4 \quad (\text{D-5})$$

The shear coefficient is [50]

$$\kappa_{mc} = \frac{2(1 + \nu)}{4 + 3\nu} = 0.5306 \quad (\text{D-6})$$

where ν is the Poisson ratio.

D.2.2 Predicting deflections with beam theory

The vertical deflection for a cantilever Timoshenko beam loaded with a vertical force at the free end is given by

$$\delta = \frac{P_{load}(L_{beam} - x)}{\kappa A_c G} - \frac{P_{load}x}{2EI} \left(L_{beam}^2 - \frac{x^2}{3} \right) + \frac{P_{load}L_{beam}^3}{3EI} \quad (D-7)$$

Here, x is the distance from the wall, L_{beam} is the length of the beam, P_{load} is the load, A_c is the cross sectional area, G is the shear modulus, E is the elasticity modulus, I is the area moment of inertia and κ is the shear coefficient.

The rotation about the beam axis for a cantilever Timoshenko beam loaded in pure bending can be calculated with the usual formula for angle of twist (equation 4-2).

The deflections at the middle of the beam predicted by Timoshenko beam theory are presented in Table D-2.

Table D-2: Timoshenko beam theory predicted deflections of the reference pontoon and main column

	Pontoon	Main column
Vertical deflection due to the applied forces at the tip	1.34 mm	1.38 mm
Rotation due to the applied torque at the tip	0.000555 rad	0.000147 rad

When comparing with the deflections computed with FE analysis for the reference design (Table D-1), it can be seen that the finite element solution corresponds quite well with the analytical solution. For the chosen mesh, it deviates no more than 3.5 % from the analytical solution at the mid plane ($x=L_{beam}/2$).

E. Time series of simulations in environmental conditions 2 and 3

This appendix presents the motion time series, bending moment power spectrum and tendon tension power spectra for environmental conditions 2 and 3 in paragraph 7.4.

E.1 Condition 2

Motion response

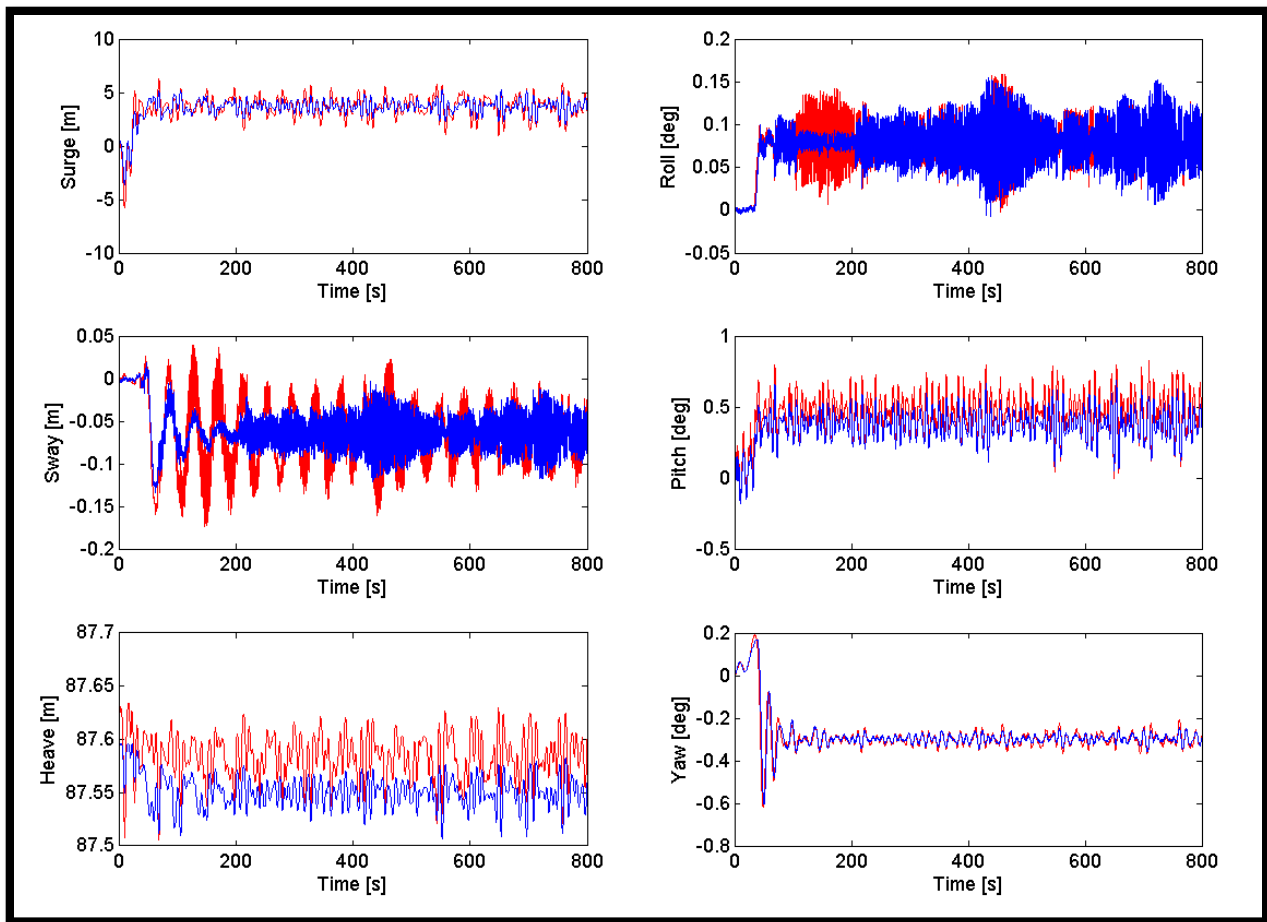


Figure E-1: Time series of motion response in condition 2

Table E-1: Mean and standard deviation of each steady state motion response in condition 2

		Surge [m]	Sway [m]	Heave [m]	Roll [deg]	Pitch [deg]	Yaw [deg]
Elastic multi-body model	Mean	3.698	-0.068	-0.016	0.080	0.459	-0.298
	Standard deviation	0.948	0.030	0.021	0.026	0.148	0.029
Rigid single-body model	Mean	3.699	-0.064	-0.05	0.079	0.379	-0.297
	Standard deviation	0.590	0.024	0.014	0.033	0.108	0.019

Bending moment about the y-axis at the tower base

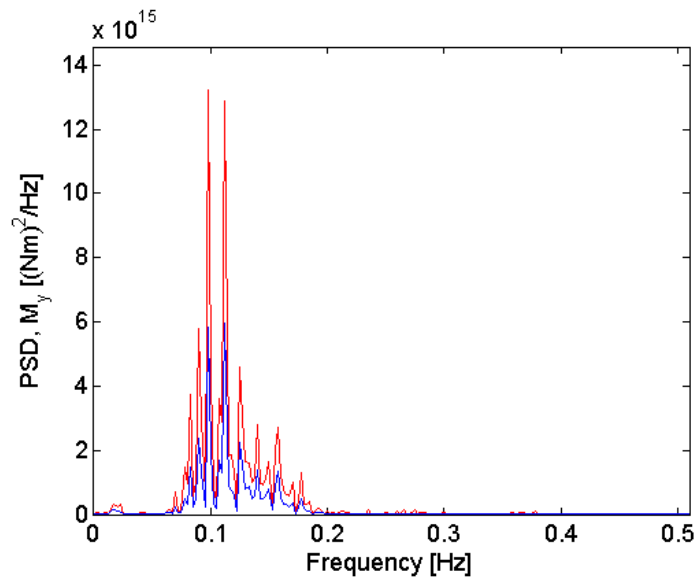


Figure E-2: Power spectrum for the bending moment about the y-axis at the tower base in condition 2

Tendon tension

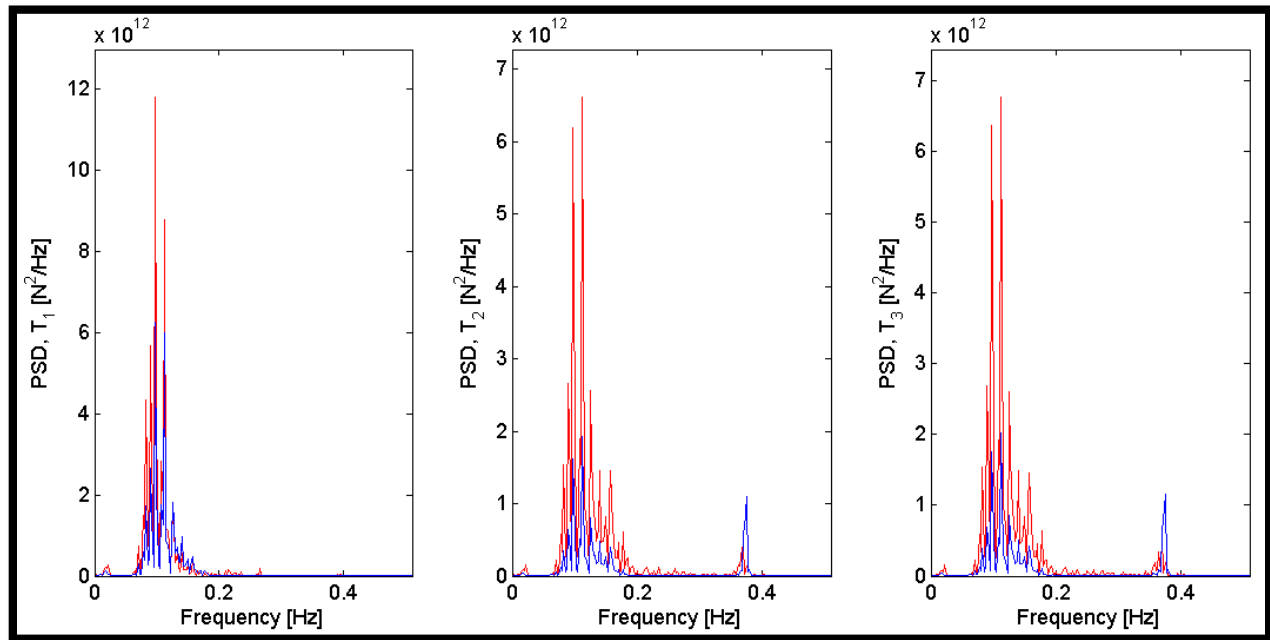


Figure E-3: Power spectrum for the tension at the top of each tendon in condition 2

In addition to what was seen in condition 1, tendons 2 and 3 now show a peak at 2.35 Hz for the rigid hull model. This is close to the tower bending natural frequency. Because the same peak is not seen for tendon 1, this could indicate that this peak is related to the roll motion.

E.2 Condition 3

Motion response

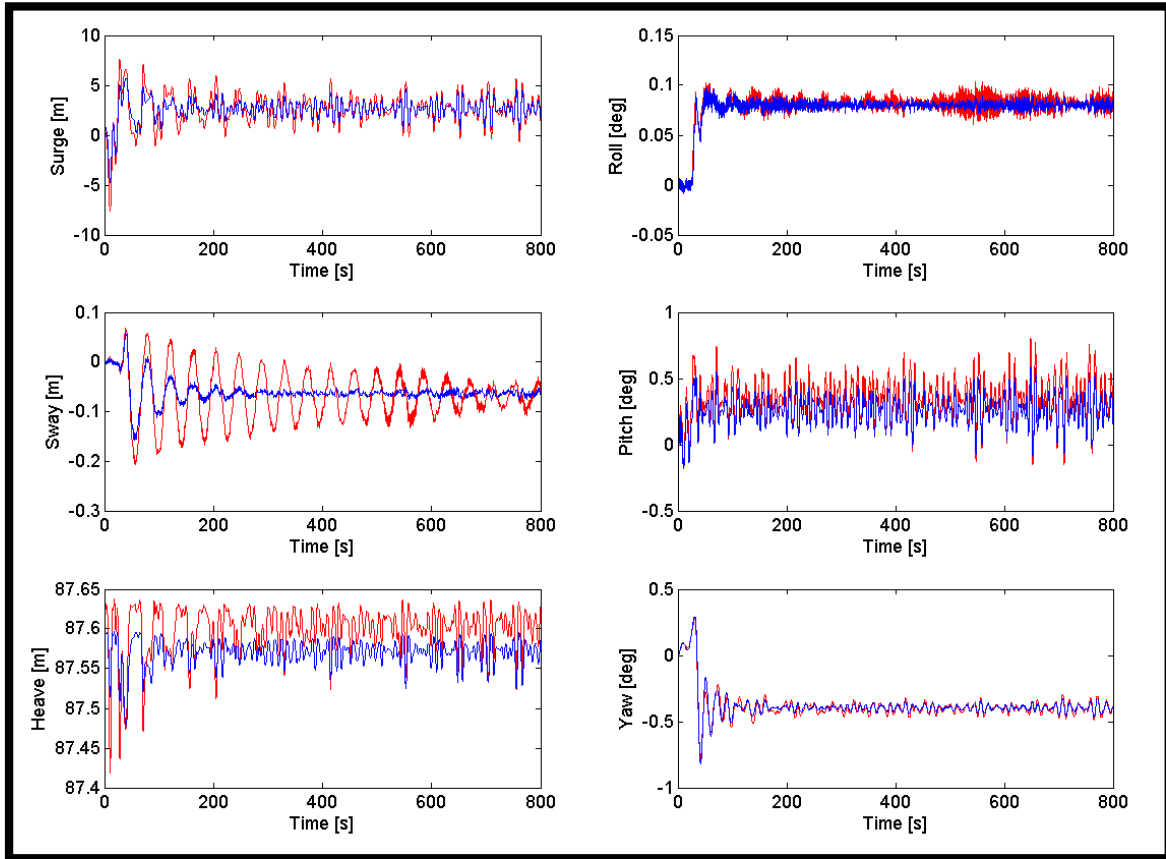


Figure E-4: Time series of motion response in condition 3

Table E-2: Mean and standard deviation of each steady state motion response in condition 3

		Surge [m]	Sway [m]	Heave [m]	Roll [deg]	Pitch [deg]	Yaw [deg]
Elastic multi-body model	Mean	2.714	-0.069	0.002	0.082	0.344	-0.399
	Standard deviation	1.121	0.030	0.020	0.007	0.162	0.035
Rigid single-body model	Mean	2.657	-0.064	-0.029	0.080	0.264	-0.395
	Standard deviation	0.749	0.005	0.013	0.003	0.117	0.024

Bending moment about the y-axis at the tower base

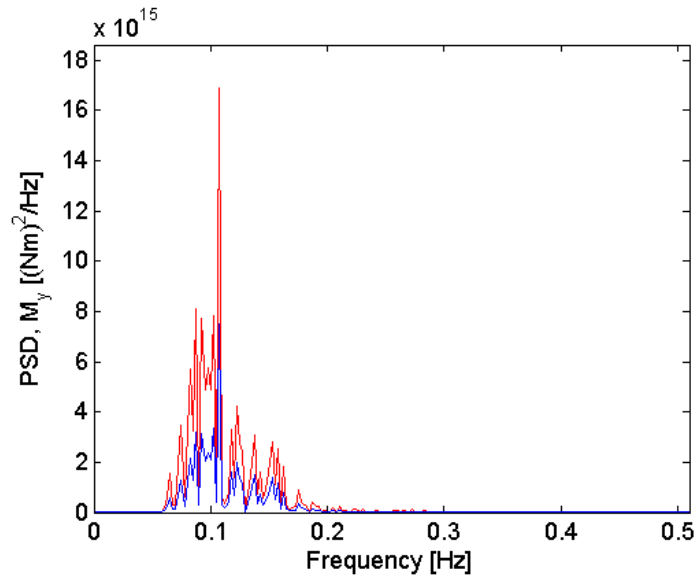


Figure E-5: Power spectrum for the bending moment about the y-axis at the tower base in condition 3

Tendon tension

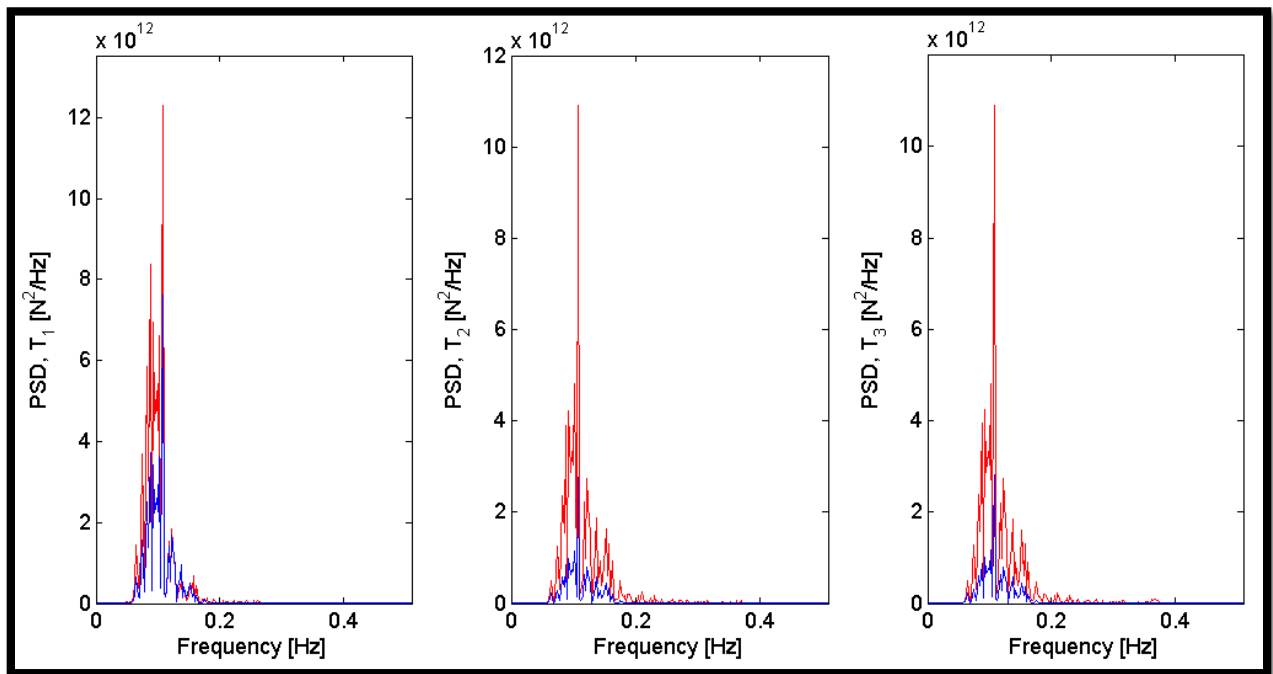


Figure E-6: Power spectrum for the tension at the top of each tendon in condition 3

F. Matlab code

This appendix presents the essentials of the Matlab code which was written as part of this work to:

- Divide the hull structure into sections.
- Associate each panel in the 3-D panel model with one of the sections.
- Compute the added mass, radiation and excitation coefficients for each section.
- Determine the hydrodynamic loads' point of application within each section.

```
%% Read WAMIT output

datGDF = dlmread('WAMIT_5S.GDF',' ',1,0); % geometric data file
datpnl = dlmread('wamit_5s.pnl'); % panel data file
dat1 = dlmread('t1pwt.1'); % added mass and damping coefficients
dat2 = dlmread('t1pwt.2'); % exciting forces from Haskind relations
dat3 = dlmread('t1pwt.3'); % exciting forces from diffraction potential
dat5p = dlmread('t1pwt.5p'); % Hydrodynamic pressure on body surface

%% Define basic parameters

ULEN = datGDF(1,1); g = datGDF(1,2);
XV = datGDF(4:end,1); YV = datGDF(4:end,2); ZV = datGDF(4:end,3);

Mpnl = datpnl(:,1); Kpnl = datpnl(:,2);
XCT = datpnl(:,3); YCT = datpnl(:,4); ZCT = datpnl(:,5);
AREA = datpnl(:,6);
nx = datpnl(:,7); ny = datpnl(:,8); nz = datpnl(:,9);

pers = flipud(unique(dat5p(:,1)));
Npers = length(pers); % number of periods
Npanels = length(Kpnl); % number of panels
Nbetas = length(unique(dat3(:,2))); % number of wave headings
betas = unique(dat5p(Npanels+1:Npanels+Npanels*Nbetas,2));

omega = 2*pi./pers;
rho = 1025;
L = ULEN;

%% Split TLP into column, base node and pontoons

heightC = 16; % column length
lengthP = 21; % pontoon length
radC = 7; % column radius
draft = min(ZCT); % TLP draft
dl = 2; % distance between SIMO bodies

crd_TLP = [XCT YCT ZCT]; % panel coordinates TLP
pnl_C = find( crd_TLP(:,3) > -heightC );
crd_C = crd_TLP(pnl_C,:); % panel coordinates column
pnl_BN = find( sqrt(crd_TLP(:,1).^2 + crd_TLP(:,2).^2) <= radC & crd_TLP(:,3) <= -heightC );
crd_BN = crd_TLP(pnl_BN,:); % panel coordinates base node
pnl_P1 = find( sqrt(crd_TLP(:,1).^2 + crd_TLP(:,2).^2) > radC & crd_TLP(:,3) <= -heightC & crd_TLP(:,1) > 0 );
crd_P1 = crd_TLP(pnl_P1,:); % panel coordinates pontoon 1
pnl_P2 = find( sqrt(crd_TLP(:,1).^2 + crd_TLP(:,2).^2) > radC & crd_TLP(:,3) <= -heightC & crd_TLP(:,2) > 0 &
crd_TLP(:,1) < 0 );
crd_P2 = crd_TLP(pnl_P2,:); % panel coordinates pontoon 2
pnl_P3 = find( sqrt(crd_TLP(:,1).^2 + crd_TLP(:,2).^2) > radC & crd_TLP(:,3) <= -heightC & crd_TLP(:,2) < 0 &
crd_TLP(:,1) < 0 );
crd_P3 = crd_TLP(pnl_P3,:); % panel coordinates pontoon 3

%% Define multi-body model
```

```

zC = linspace(0,-heightC,heightC/dl+1)';
xC = zeros(size(zC));           % node x-locations on column
yC = zeros(size(zC));           % node y-locations on column

zBN = linspace(-heightC,draft,(-draft-heightC)/dl+1)';
xBN = zeros(size(zBN));        % node x-locations on base node
yBN = zeros(size(zBN));        % node y-locations on base node

xP1 = linspace(radC,radC+lengthP,(lengthP-radC)/dl+1)';
yP1 = zeros(size(xP1));        % node y-locations on pontoon 1
zP1 = -19*ones(size(xP1));     % node z-locations on pontoon 1
xP2 = -cosd(60)*xP1;          % node x-locations on pontoon 2
yP2 = cosd(30)*xP1;          % node y-locations on pontoon 2
zP2 = -19*ones(size(yP2));    % node z-locations on pontoon 2
xP3 = xP2;                    % node x-locations on pontoon 3
yP3 = -yP2;                   % node y-locations on pontoon 3
zP3 = zP2;                    % node z-locations on pontoon 3

nodesC = [xC yC zC];          NnodesC = size(nodesC,1);
nodesBN = [xBN yBN zBN];     NnodesBN = size(nodesBN,1);
nodesP1 = [xP1 yP1 zP1];     NnodesP1 = size(nodesP1,1);
nodesP2 = [xP2 yP2 zP2];     NnodesP2 = size(nodesP2,1);
nodesP3 = [xP3 yP3 zP3];     NnodesP3 = size(nodesP3,1);
nodes = [nodesC ; nodesBN ; nodesP1 ; nodesP2 ; nodesP3];
Nnodes = length(nodes);

%% Generate SIMO body input for A, B and F from radiation and diffraction pressures

AB_C = zeros(Npers,NnodesC,6,6); F_C = zeros(Npers,Nbetas,NnodesC,6);
AB_BN = zeros(Npers,NnodesBN,6,6); F_BN = zeros(Npers,Nbetas,NnodesBN,6);
AB_P1 = zeros(Npers,NnodesP1,6,6); F_P1 = zeros(Npers,Nbetas,NnodesP1,6);
AB_P2 = zeros(Npers,NnodesP2,6,6); F_P2 = zeros(Npers,Nbetas,NnodesP2,6);
AB_P3 = zeros(Npers,NnodesP3,6,6); F_P3 = zeros(Npers,Nbetas,NnodesP3,6);

Lm = [L^2 L^2 L^2 L^3 L^3 L^3];
Lkn = [L^-3 L^-3 L^-3 L^-4 L^-4 L^-4];
count = 0;

for iper = 1:Npers % loop through periods

    nC_AB = 0;
    nBN_AB = 0;
    nP1_AB = 0;
    nP2_AB = 0;
    nP3_AB = 0;

    disp(['Run calculation period ' num2str(pers(iper))])

    for ipnl = 1:Npanels % loop through panels

        count = count + 1;

        if any(pnl_C==ipnl) % check if panel is located in column (ignore last node of column, this is the same
as first node of base node)
            for inode = 1:NnodesC-1
                if ZCT(ipnl) > zC(inode+1) && ZCT(ipnl) <= zC(inode)
                    p1 = dat5p(count,4)+1i*dat5p(count,5);
                    p2 = dat5p(count,6)+1i*dat5p(count,7);
                    p3 = dat5p(count,8)+1i*dat5p(count,9);
                    p = [p1 , p2 , p3 , 0 , 0 , 0]; clear p1 p2 p3
                    n = [nx(ipnl), ny(ipnl), nz(ipnl)];
                    rn = [0 0 0];
                    nrn = ([n rn].*Lkn)';
                    ABpan = nrn*p*AREA(ipnl)*g/(omega(iper))^2; % 6x6 matrix
                    AB_C(iper,inode,:) = squeeze(AB_C(iper,inode,:)) + ABpan;
                    nC_AB = nC_AB + 1;

                    for ibet = 1:Nbetas
                        f = dat5p(count+Npanels*ibet,5) + 1i*dat5p(count+Npanels*ibet,6);
                        Fpan = AREA(ipnl)./Lm.*[n rn]*f; clear f
                        F_C(iper,ibet,inode,1) = Fpan(1) + F_C(iper,ibet,inode,1); %Fx
                        F_C(iper,ibet,inode,2) = Fpan(2) + F_C(iper,ibet,inode,2); %Fy
                        F_C(iper,ibet,inode,3) = Fpan(3) + F_C(iper,ibet,inode,3); %Fz
                        F_C(iper,ibet,inode,4) = 0; %Mx
                        F_C(iper,ibet,inode,5) = 0; %My
                        F_C(iper,ibet,inode,6) = 0; %Mz
                    end
                end
            end
        end
    end
end

```

```

elseif any(pnl_BN==ipnl) % check if panel is located in base node
for inode = 1:NnodesBN-1
    if ZCT(ipnl) > zBN(inode+1) && ZCT(ipnl) <= zBN(inode)
        p1 = dat5p(count,4)+li*dat5p(count,5);
        p2 = dat5p(count,6)+li*dat5p(count,7);
        p3 = dat5p(count,8)+li*dat5p(count,9);
        p = [p1 , p2 , p3 , 0 , 0 , 0]; clear p1 p2 p3
        n = [nx(ipnl), ny(ipnl), nz(ipnl)];
        rn = [0 0 0];
        nrn = ([n rn].*Lkn)';
        ABpan = nrn*p*AREA(ipnl)*g/(omega(iper))^2; % 6x6 matrix
        AB_BN(iper,inode,:) = squeeze(AB_BN(iper,inode,:)) + ABpan;
        nBN_AB = nBN_AB + 1;

        for ibet = 1:Nbetas
            f = dat5p(count+Npanels*ibet,5) + li*dat5p(count+Npanels*ibet,6);
            Fpan = AREA(ipnl)./Lm.*[n rn]*f; clear f
            F_BN(iper,ibet,inode,1) = Fpan(1) + F_BN(iper,ibet,inode,1); %Fx
            F_BN(iper,ibet,inode,2) = Fpan(2) + F_BN(iper,ibet,inode,2); %Fy
            F_BN(iper,ibet,inode,3) = Fpan(3) + F_BN(iper,ibet,inode,3); %Fz
            F_BN(iper,ibet,inode,4) = 0; %Mx
            F_BN(iper,ibet,inode,5) = 0; %My
            F_BN(iper,ibet,inode,6) = 0; %Mz
        end

    elseif ZCT(ipnl) <= min(zBN)
        p1 = dat5p(count,4)+li*dat5p(count,5);
        p2 = dat5p(count,6)+li*dat5p(count,7);
        p3 = dat5p(count,8)+li*dat5p(count,9);
        p = [p1 , p2 , p3 , 0 , 0 , 0]; clear p1 p2 p3
        n = [nx(ipnl), ny(ipnl), nz(ipnl)];
        rn = [0 0 0];
        nrn = ([n rn].*Lkn)';
        ABpan = nrn*p*AREA(ipnl)*g/(omega(iper))^2; % 6x6 matrix
        AB_BN(iper,end,:) = squeeze(AB_BN(iper,end,:)) + ABpan;
        nBN_AB = nBN_AB + 1;

        for ibet = 1:Nbetas
            f = dat5p(count+Npanels*ibet,5) + li*dat5p(count+Npanels*ibet,6);
            Fpan = AREA(ipnl)./Lm.*[n rn]*f; clear f
            F_BN(iper,ibet,end,1) = Fpan(1) + F_BN(iper,ibet,end,1); %Fx
            F_BN(iper,ibet,end,2) = Fpan(2) + F_BN(iper,ibet,end,2); %Fy
            F_BN(iper,ibet,end,3) = Fpan(3) + F_BN(iper,ibet,end,3); %Fz
            F_BN(iper,ibet,end,4) = 0; %Mx
            F_BN(iper,ibet,end,5) = 0; %My
            F_BN(iper,ibet,end,6) = 0; %Mz
        end

        break % break for loop
    end
end

elseif any(pnl_P1==ipnl) % check if panel is located in pontoon 1
for inode = 1:NnodesP1-1
    lim1 = sqrt(xP1(inode)^2 + yP1(inode)^2);
    lim2 = sqrt(xP1(inode+1)^2 + yP1(inode+1)^2);
    if sqrt( XCT(ipnl)^2 + YCT(ipnl)^2 ) >= lim1 && sqrt( XCT(ipnl)^2 + YCT(ipnl)^2 ) < lim2
        p1 = dat5p(count,4)+li*dat5p(count,5);
        p2 = dat5p(count,6)+li*dat5p(count,7);
        p3 = dat5p(count,8)+li*dat5p(count,9);
        p = [p1 , p2 , p3 , 0 , 0 , 0]; clear p1 p2 p3
        n = [nx(ipnl), ny(ipnl), nz(ipnl)];
        rn = [0 0 0];
        nrn = ([n rn].*Lkn)';
        ABpan = nrn*p*AREA(ipnl)*g/(omega(iper))^2; % 6x6 matrix
        AB_P1(iper,inode,:) = squeeze(AB_P1(iper,inode,:)) + ABpan;
        nP1_AB = nP1_AB + 1;

        for ibet = 1:Nbetas
            f = dat5p(count+Npanels*ibet,5) + li*dat5p(count+Npanels*ibet,6);
            Fpan = AREA(ipnl)./Lm.*[n rn]*f; clear f
            F_P1(iper,ibet,inode,1) = Fpan(1) + F_P1(iper,ibet,inode,1); %Fx
            F_P1(iper,ibet,inode,2) = Fpan(2) + F_P1(iper,ibet,inode,2); %Fy
            F_P1(iper,ibet,inode,3) = Fpan(3) + F_P1(iper,ibet,inode,3); %Fz
            F_P1(iper,ibet,inode,4) = 0; %Mx
            F_P1(iper,ibet,inode,5) = 0; %My
            F_P1(iper,ibet,inode,6) = 0; %Mz
        end
    end
end

```

```

elseif sqrt( XCT(ipnl)^2 + YCT(ipnl)^2 ) >= lengthP+radC
    p1 = dat5p(count,4)+li*dat5p(count,5);
    p2 = dat5p(count,6)+li*dat5p(count,7);
    p3 = dat5p(count,8)+li*dat5p(count,9);
    p = [p1 , p2 , p3 , 0 , 0 , 0]; clear p1 p2 p3
    n = [nx(ipnl), ny(ipnl), nz(ipnl)];
    rn = [0 0 0];
    nrn = ([n rn].*Lkn)';
    ABpan = nrn*p*AREA(ipnl)*g/(omega(iper))^2; % 6x6 matrix
    AB_P1(iper,end,,:) = squeeze(AB_P1(iper,end,,:)) + ABpan;
    nP1_AB = nP1_AB + 1;

    for ibet = 1:Nbetas
        f = dat5p(count+Npanels*ibet,5) + li*dat5p(count+Npanels*ibet,6);
        Fpan = AREA(ipnl)./Lm.*[n rn]*f; clear f
        F_P1(iper,ibet,end,1) = Fpan(1) + F_P1(iper,ibet,end,1); %Fx
        F_P1(iper,ibet,end,2) = Fpan(2) + F_P1(iper,ibet,end,2); %Fy
        F_P1(iper,ibet,end,3) = Fpan(3) + F_P1(iper,ibet,end,3); %Fz
        F_P1(iper,ibet,end,4) = 0; %Mx
        F_P1(iper,ibet,end,5) = 0; %My
        F_P1(iper,ibet,end,6) = 0; %Mz
    end

    break % break for loop
end
end

elseif any(pnl_P2==ipnl) % check if panel is located in pontoon 2 and do the same as for pontoon 1

elseif any(pnl_P3==ipnl) % check if panel is located in pontoon 3 and do the same as for pontoon 1

else
    display('panel not found in any part of structure')
    stop
end

end

if nC_AB < size(crd_C,1) || nC_AB > size(crd_C,1)
    display('column panels are missing')
    stop
elseif nBN_AB < size(crd_BN,1) || nBN_AB > size(crd_BN,1)
    display('base node panels are missing')
    stop
elseif nP1_AB < size(crd_P1,1) || nP1_AB > size(crd_P1,1)
    display('pontoon 1 panels are missing')
    stop
elseif nP2_AB < size(crd_P2,1) || nP2_AB > size(crd_P2,1)
    display('pontoon 2 panels are missing')
    stop
elseif nP3_AB < size(crd_P3,1) || nP3_AB > size(crd_P3,1)
    display('pontoon 3 panels are missing')
    stop
end

count = count + Npanels*Nbetas;

end

%% Write results to files

% Column
disp('Write data to files for column')

for body = 1:size(nodesC,1)

    disp(['Cbody' num2str(body) ' ' num2str(nodesC(body,:))])
    countdiff = 0;
    countrad = 0;
    fileID = fopen([folderout 'Cbody' num2str(body) '.1'],'w');
    fileID2 = fopen([folderout 'Cbody' num2str(body) '.3'],'w');

    for iper2 = 1:Npers

```

```

for ibeta = 1:Nbetas
    for mode = 1:6

        % Print excitation forces to file
        countdiff = countdiff + 1;
        Mod = abs(F_C(iper2,ibeta,body,mode));
        Pha = angle(F_C(iper2,ibeta,body,mode))*180/pi;
        Re = real(F_C(iper2,ibeta,body,mode));
        Im = imag(F_C(iper2,ibeta,body,mode));
        fprintf(fileID2, '%.4e\t%.4e\t%i\t%.4e\t%.4e\t%.4e\t%.4e\n',[ pers(iper2) ,
betas(ibeta) , mode , Mod , Pha , Re , Im ]);

        % Print added mass and damping to file
        countrad = countrad + 1;
        for j = 1:6
            if abs(AB_C(iper2,body,mode,j)) > eps
                Aij = real(AB_C(iper2,body,mode,j));
                Bij = -imag(AB_C(iper2,body,mode,j));
                fprintf(fileID, '%.4e\t%i\t%i\t%.4e\t%.4e\n',[ pers(iper2) , mode , j , Aij ,
Bij ]);
            end
        end
        clear Mod Pha Re Im Aij Bij

    end
end
end

fclose(fileID);
fclose(fileID2);

copyfile([folder 'tlpbody0.mmx'],[folderout 'Cbody' num2str(body) '.mmx'])

% Replace all wamit_5s with CbodyX in file to get more readable simo body names
fileID = fopen([folder 'tlpbody0.out'],'r');
f = fread(fileID, '*char');
fclose(fileID);
f = strrep(f, 'wamit_5s', ['Cbody' num2str(body)]);
fileID = fopen([folderout 'Cbody' num2str(body) '.out'],'w');
fprintf(fileID, '%s', f);
fclose(fileID);

end

% Base Node
oncemat_BN = zeros(Npers*Nbetas*6,7);
oncerad_BN = zeros(Npers*36,5);

disp('Write data to files for base node')

for body = 1:size(nodesBN,1)

    disp(['BNbody' num2str(body) ' ' num2str(nodesBN(body,:))])
    countdiff = 0;
    countrad = 0;
    fileID = fopen([folderout 'BNbody' num2str(body) '.1'],'w');
    fileID2 = fopen([folderout 'BNbody' num2str(body) '.3'],'w');

    for iper2 = 1:Npers
        for ibeta = 1:Nbetas
            for mode = 1:6

                % Print excitation forces to file
                countdiff = countdiff + 1;
                Mod = abs(F_BN(iper2,ibeta,body,mode));
                Pha = angle(F_BN(iper2,ibeta,body,mode))*180/pi;
                Re = real(F_BN(iper2,ibeta,body,mode));
                Im = imag(F_BN(iper2,ibeta,body,mode));
                fprintf(fileID2, '%.4e\t%.4e\t%i\t%.4e\t%.4e\t%.4e\t%.4e\n',[ pers(iper2) ,
betas(ibeta) , mode , Mod , Pha , Re , Im ]);
            end
        end
    end
end

```

```

        % Print added mass and damping to file
        countrad = countrad + 1;
        for j = 1:6
            if abs(AB_BN(iper2,body,mode,j)) > eps
                Aij = real(AB_BN(iper2,body,mode,j));
                Bij = -imag(AB_BN(iper2,body,mode,j));
                fprintf(fileID,'%4e\t%i\t%i\t%.4e\t%.4e\n',[ pers(iper2) , mode , j , Aij ,
Bij ]);
            end
        end
        clear Mod Pha Re Im Aij Bij

    end
end

fclose(fileID);
fclose(fileID2);

copyfile([folder 'tlpbody0.mmx'],[folderout 'BNbody' num2str(body) '.mmx'])

% Replace all wamit_5s with BNbodyX in file to get more readable simo body names
fileID = fopen([folder 'tlpbody0.out'],'r');
f = fread(fileID,'*char');
fclose(fileID);
f = strrep(f,'wamit_5s',[ 'BNbody' num2str(body)]);
fileID = fopen([folderout 'BNbody' num2str(body) '.out'],'w');
fprintf(fileID,'%s',f);
fclose(fileID);

end

% Pontoon 1
oncemat_P1 = zeros(Npers*Nbetas*6,7);
oncerad_P1 = zeros(Npers*36,5);

disp('Write data to files for pontoon 1')

for body = 1:size(nodesP1,1)

    disp(['P1body' num2str(body) ' ' num2str(nodesP1(body,:))])
    countdiff = 0;
    countrad = 0;
    fileID = fopen([folderout 'P1body' num2str(body) '.1'],'w');
    fileID2 = fopen([folderout 'P1body' num2str(body) '.3'],'w');

    for iper2 = 1:Npers
        for ibeta = 1:Nbetas
            for mode = 1:6

                % Print excitation forces to file
                countdiff = countdiff + 1;
                Mod = abs(F_P1(iper2,ibeta,body,mode));
                Pha = angle(F_P1(iper2,ibeta,body,mode))*180/pi;
                Re = real(F_P1(iper2,ibeta,body,mode));
                Im = imag(F_P1(iper2,ibeta,body,mode));
                fprintf(fileID2,'%4e\t%.4e\t%i\t%.4e\t%.4e\t%.4e\n',[ pers(iper2) ,
betas(ibeta) , mode , Mod , Pha , Re , Im ]);

                % Print added mass and damping to file
                countrad = countrad + 1;
                for j = 1:6
                    if abs(AB_P1(iper2,body,mode,j)) > eps
                        Aij = real(AB_P1(iper2,body,mode,j));
                        Bij = -imag(AB_P1(iper2,body,mode,j));
                        fprintf(fileID,'%4e\t%i\t%i\t%.4e\t%.4e\n',[ pers(iper2) , mode , j , Aij ,
Bij ]);
                    end
                end
            end
        end
    end
end

```

```

        clear Mod Pha Re Im Aij Bij

    end
end
end

fclose(fileID);
fclose(fileID2);

copyfile([folder 'tlpbody0.mmx'],[folderout 'P1body' num2str(body) '.mmx'])

% Replace all wamit_5s with P1bodyX in file to get more readable simo body names
fileID = fopen([folder 'tlpbody0.out'],'r');
f = fread(fileID, '*char');
fclose(fileID);
f = strrep(f, 'wamit_5s', ['P1body' num2str(body)]);
fileID = fopen([folderout 'P1body' num2str(body) '.out'],'w');
fprintf(fileID, '%s', f);
fclose(fileID);

end

% Do the same for Pontoon 2 and 3 as for Pontoon 1

```